6 May 2011 | $10

Science

AAAS

EPITOMICS®
Better Antibodies · Better Science

Now Available
2500 RABBIT MONOCLONALS
Over 9000 Antibodies Total

THE RABBIT MONOCLONAL ADVANTAGE

	RABBIT MONOCLONAL	MOUSE MONOCLONAL
ANTIGEN RECOGNITION	Excellent response to a wide range of antigens	Limited immuno response
AFFINITIES	Picomolar (10^{-12} kD M) possible	Nanomolar (~10^{-9} kD M)
APPLICATIONS	Westerns, ELISA, Flow Cytometry, IP, IHC, ICC - Excellent results in IHC	Westerns, ELISA, Flow Cytometry, IP - Not suitable for mouse studies
IHC	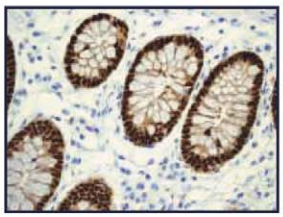	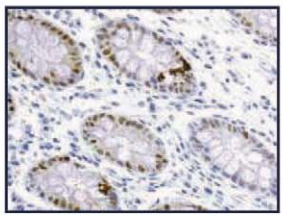

What is the Rabbit Monoclonal Advantage ?

Rabbit Monoclonal Antibodies (RabMAbs®) provide the combined benefits of superior antigen recognition of the rabbit immune system with the specificity and consistency of a monoclonal antibody, bringing you the highest quality antibody possible.

Find out more @ www.epitomics.com/comparison

Paraffin-embedded human colon tissue stained with Epitomics' CDX2 RabMAb (Cat.# 2475-1) and Vendor A's CDX2 Mouse Monoclonal under optimal conditions

SPECIAL OFFER

$99 ANTIBODY SPECIAL

Find out more @ www.epitomics.com/products/promo

For updates and special offers
Follow us on: twitter
www.twitter.com/epitomics_inc

www.epitomics.com

US & Canada | 1-877-772-2622
Outside NA | 650-583-6688

Limited by an outdated PCR system?

You can run 15 minute PCR protocols and use 50% less consumables and energy by getting away from the old standard. Choose Thermo Scientific Piko Thermal Cyclers, Phusion reagents, and ultra thin wall (UTW) plastic consumables for the most rapid and accurate PCR results. These technologically advanced components can be used individually to improve your current workflow, or as a complete solution for advanced PCR.

- Ultra fast PCR cycling protocols optimized to ‹15 minutes
- 96-well PCR runs using 50% less plastics, reagents and energy
- PCR kits that allow amplification directly from plant, blood, and tissue samples

Start your PCR experiment today
www.thermoscientific.com/advancedpcr

Everything for PCR
Thermo Scientific PCR portfolio has everything you need for successful PCR including industry leading reagents, high-quality instruments and trusted plastic consumables.

Moving science forward

Thermo SCIENTIFIC
Part of Thermo Fisher Scientific

Submission deadline August 1

Your name here.

The GE & Science Prize for Young Life Scientists. Because brilliant ideas build better realities.

Imagine standing on the podium at the Grand Hotel in Stockholm, making your acceptance speech for the GE & Science Prize for Young Life Scientists. Imagine having your essay read by your peers around the world. Imagine discussing your work in a seminar with other prize winners and Nobel Laureates. Imagine what you could do with the $25,000 prize money. Now stop imagining. If you were awarded your Ph.D. in molecular biology in 2010, then submit your 1000-word essay by August 1, and you can make it reality.

Want to build a better reality? Go to www.gescienceprize.org

GE & Science Prize for Young Life Scientists

imagination at work

Science AAAS

* For the purpose of this prize, molecular biology is defined as "that part of biology which attempts to interpret biological events in terms of the physico-chemical properties of molecules in a cell".

(McGraw-Hill Dictionary of Scientific and Technical Terms, 4th Edition).

28-9402-06AB

EDITORIAL

639 Indigenous Genomics
Vanessa Hayes

NEWS OF THE WEEK

646 A roundup of the week's top stories

NEWS & ANALYSIS

650 China's Population Growing Slowly, Changing Fast

651 NIH Wins in Appeals Court, But Legal Battle Continues

652 EPA Proposal Would Exempt Some GMOs From Registry

653 Anonymous Alcoholic Bankrolls Trial of Controversial Therapy

NEWS FOCUS

654 Red in Tooth and Claw Among the Literati
>> Science *Podcast*

657 Car-Crash Epidemiologist Pushes Systemic Attack on Bad Driving

658 Dating Duo Illuminates Modern Humans' Journey
New Light on Ancient Samples

LETTERS

662 An Unexpected Spotlight
A. Pollatsek

New University Plan Skips Crucial Steps
W. Zhong

Symmetrical Transparency in Science
K. Shrader-Frechette and N. Oreskes

Bringing Research into the Classroom
A. Krolik

664 CORRECTIONS AND CLARIFICATIONS

BOOKS *ET AL.*

665 Lab Coats in Hollywood
D. A. Kirby, reviewed by M. A. MacIver

666 Energy, People, and the Natural World

POLICY FORUM

670 Transforming U.S. Agriculture
J. P. Reganold et al.

PERSPECTIVES

672 Twisted Disks
H. Salo
>> Reports pp. 708 and 711

673 Ancient Neurons Regulate Immunity
K. J. Tracey
>> Report p. 729

674 Designing the Next Generation of Chemical Separation Membranes
D. L. Gin and R. D. Noble

676 Hot Electrons Cross Boundaries
M. Moskovits
>> Report p. 702

677 Flow Cytometry, Amped Up
C. Benoist and N. Hacohen
>> Research Article p. 687

679 Retrospective: Jürg Tschopp (1951–2011)
L. A. O'Neill

REVIEW

680 Scaffold Proteins: Hubs for Controlling the Flow of Cellular Information
M. C. Good et al.

CONTENTS continued >>

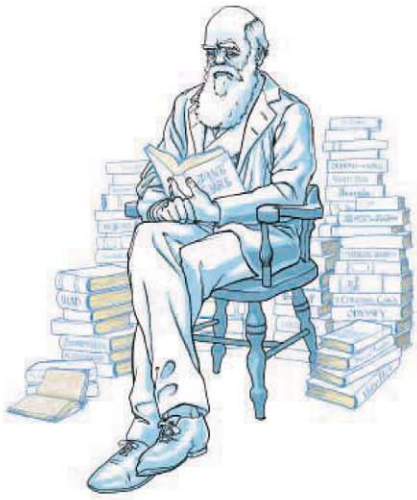

page 654

page 665

COVER

Skull of the theropod dinosaur *Velociraptor mongoliensis* (Mongolia) showing the eye socket (4 centimeters across). Analysis of the shape of the eye socket and scleral ring (a bone within the eye) of fossil and extant species suggests that Mesozoic archosaurs were active both day and night. See page 705.

Photo: Lars Schmitz, University of California, Davis

DEPARTMENTS

635 This Week in *Science*
641 Editors' Choice
644 *Science* Staff
739 New Products
740 *Science* Careers

SEE THE BIG PICTURE
WITHOUT MISSING THE SMALLEST DETAIL.

INTRODUCING THE NEW *WEB OF KNOWLEDGE*

The next generation of *Thomson Reuters Web of Knowledge*℠ has arrived. With new features, enhanced functionality, and additional content, it's everything you've been searching for. The streamlined interface and more precise search options ensure you will find all the information related to your topic — quickly and efficiently. And with powerful analysis tools, you can spend less time digging into the details and more time focusing on the big picture.

DISCOVERY STARTS HERE: TheNewWok.com

THOMSON REUTERS™

RESEARCH ARTICLE

687 Single-Cell Mass Cytometry of Differential Immune and Drug Responses Across a Human Hematopoietic Continuum
S. C. Bendall et al.
Simultaneous measurement of more than 30 properties in individual human cells is used to characterize signaling in the immune system.
>> *Perspective p. 677*

REPORTS

696 Observation of Orbital Currents in CuO
V. Scagnoli et al.
Resonant x-ray scattering is used to detect microscopic loop currents within the plane of cupric oxide.

698 Imaging Doped Holes in a Cuprate Superconductor with High-Resolution Compton Scattering
Y. Sakurai et al.
Inelastic x-ray scattering probed the doping dependence of the electronic environment within a cuprate superconductor.

702 Photodetection with Active Optical Antennas
M. W. Knight et al.
An active optical antenna-diode combines the functions of light-harvesting and excited-electron injection.
>> *Perspective p. 676*

705 Nocturnality in Dinosaurs Inferred from Scleral Ring and Orbit Morphology
L. Schmitz and R. Motani
Comparison of eye structures between fossils and modern species suggests that Mesozoic archosaurs were active day and night.

708 Saturn's Curiously Corrugated C Ring
M. M. Hedman et al.

711 The Impact of Comet Shoemaker-Levy 9 Sends Ripples Through the Rings of Jupiter
M. R. Showalter et al.
Spacecraft observations show that Saturn's and Jupiter's rings preserve records of recent interplanetary debris collisions.
>> *Perspective p. 672*

714 Single-Cell Genomics Reveals Organismal Interactions in Uncultivated Marine Protists
H. S. Yoon et al.
Marine protist cells from the wild environment contain DNA from several viruses and bacteria, but apparently lack plastids.

717 A Family of IFN-γ–Inducible 65-kD GTPases Protects Against Bacterial Infection
B.-H. Kim et al.
Guanylate-binding proteins coordinately regulate oxidative and autophagic responses to intracellular bacteria.

721 Normalization for Sparse Encoding of Odors by a Wide-Field Interneuron
M. Papadopoulou et al.
A single neuron is responsible for adaptive normalization in an olfactory circuit generating sparse odor representations.

726 Relationship Between Clinical Signs and Transmission of an Infectious Disease and the Implications for Control
B. Charleston et al.
Livestock experiments provide precise parameters for incubation and infectious periods for foot-and-mouth disease virus.
>> Science *Podcast*

729 Neuronal GPCR Controls Innate Immunity by Regulating Noncanonical Unfolded Protein Response Genes
J. Sun et al.
Two nematode worm neurons "smell" disease and promote resistance to pathogens.
>> *Perspective p. 673*

732 Transient Activation of the HOG MAPK Pathway Regulates Bimodal Gene Expression
S. Pelet et al.
Bimodal expression of genes is activated in response to osmotic stress.

CONTENTS continued >>

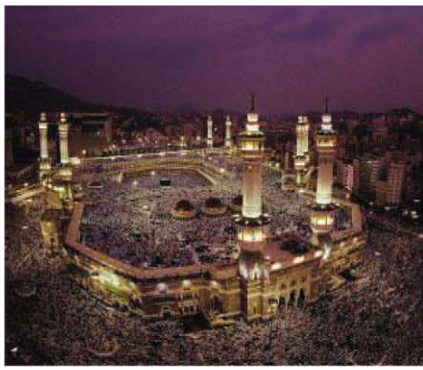

page 666

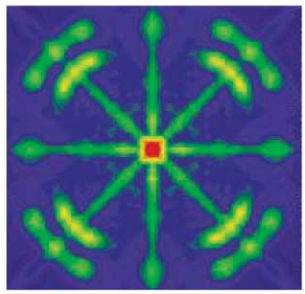

pages 696 & 698

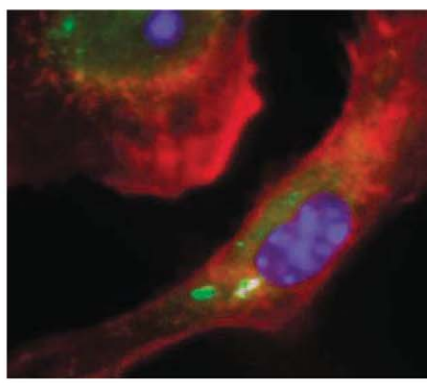

page 717

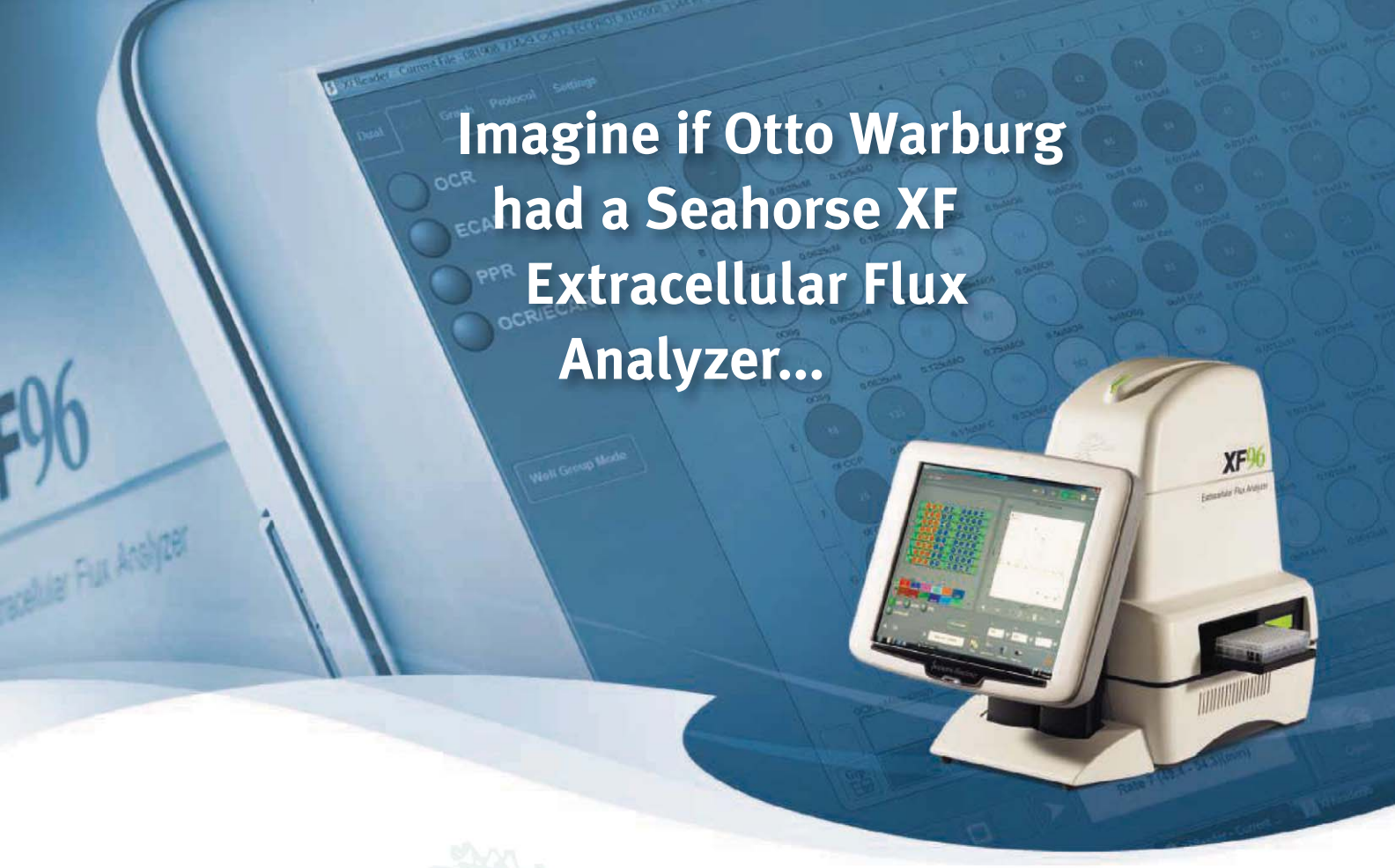

Finally, a real-time, kinetic measurement of the **Warburg Effect**, glucose & glutamine addictions, and fatty acid oxidation of cancer cells in a microplate.

Seahorse's award winning XF Extracellular Flux Analyzers provide an easy way to:

- Evaluate the role of oncogenes and tumor suppressor genes in energy metabolism and tumorigenesis
- Detect HIF-1 and drug mediated effects on mitochondrial respiration and glycolysis
- Determine which energy substrates are preferentially used by tumor cells
- Measure the dynamic contributions of OXPHOS & aerobic glycolysis
- Validate genes that target tumor metabolism

Webinars On-Demand
See our Cancer Related Webinars at seahorsebio.com/science

Measuring **cancer metabolism** is so easy now!

www.seahorsebio.com/science • 978 671 1600 • info@seahorsebio.com
16 Esquire Road, North Billerica, MA 01862

Seahorse *Bioscience*

SCIENCEONLINE

SCIENCEXPRESS
www.sciencexpress.org

The Compact Selaginella Genome Identifies Changes in Gene Content Associated with the Evolution of Vascular Plants
J. A. Banks et al.
The genome sequence of a lycophyte hints at ancient evolutionary transitions.
10.1126/science.1203810

Deciphering the Rhizosphere Microbiome for Disease-Suppressive Bacteria
R. Mendes et al.
A common plant pathogen induces the growth of disease-suppressive microbes in local soil communities.
10.1126/science.1203980

Realizing All-Spin–Based Logic Operations Atom by Atom
A. A. Khajetoorians et al.
Scanning tunneling microscopy is used to assemble and read out signals from a device based on atomic spins.
10.1126/science.1201725

Climate Trends and Global Crop Production Since 1980
D. B. Lobell et al.
Climate change has decreased global maize and wheat production, while soybean and rice production have remained stable.
10.1126/science.1204531
>> Science *Podcast*

SCIENCENOW
www.sciencenow.org
Highlights From Our Daily News Coverage

First Buildings May Have Been Community Centers
Large structures found in 12,000-year-old farming village were probably not homes.
http://scim.ag/first-buildings

Computer Algorithm May Speed Drug Discovery
A computational approach could simplify the quest for new HIV and cancer therapies.
http://scim.ag/drug-discovery

Scattering Microscope Peers Into the Nanoscale
A new frosted lens sees finer details than ever before.
http://scim.ag/nano-scale

SCIENCESIGNALING
www.sciencesignaling.org
The Signal Transduction Knowledge Environment
3 May issue: http://scim.ag/ss050311

RESEARCH ARTICLE: Male Fertility Depends on Ca^{2+} Absorption by TRPV6 in Epididymal Epithelia
P. Weissgerber et al.
Production of functional spermatozoa requires regulation of the Ca^{2+} concentration in epididymal fluid by TRPV6.

RESEARCH ARTICLE: Mechanism of Impaired NLRP3 Inflammasome Priming by Monophosphoryl Lipid A
C. A. Embry et al.

PODCAST
T. C. Mitchell and A. M. VanHook
Biased signaling by an immune receptor ligand underlies its inability to induce inflammatory responses.

PERSPECTIVE: New Roles for Lysosomal Trafficking in Morphogen Gradient Sensing
E. Rainero and J. C. Norman
The rate at which morphogen receptors move into lysosomes dictates the extent of downstream signaling during differentiation.

SCIENCECAREERS
www.sciencecareers.org/career_magazine
Free Career Resources for Scientists

Focus on Aging: Unlocking the Genome's Secrets to Long Life
M. Leslie
Liz Cirulli is seeking gene variants in centenarians that account for their longevity.
http://scim.ag/long_life_genome

Taken for Granted: When Will They Learn?
B. L. Benderly
Another needless death at a university research facility points up the scandal of lax safety standards in academe.
http://scim.ag/tfg_safety

SCIENCETRANSLATIONAL MEDICINE
www.sciencetranslationalmedicine.org
Integrating Medicine and Science
4 May issue: http://scim.ag/ss050411

PERSPECTIVE: The Inflammasome in Atherosclerosis and Type 2 Diabetes
S. L. Masters et al.
Type 2 diabetes and atherosclerosis might be linked through the inflammasome via obesity-related triggers.

RESEARCH ARTICLE: A Phosphorus-Based Dendrimer Targets Inflammation and Osteoclastogenesis in Experimental Arthritis
M. Hayder et al.
A phosphorus-based dendrimer suppresses inflammation and reduces bone erosion in mouse models of rheumatoid arthritis.

SCIENCESIGNALING
Epididymus, a site of calcium regulation.

RESEARCH ARTICLE: Immune and Genetic Correlates of Vaccine Protection Against Mucosal Infection by SIV in Monkeys
N. L. Letvin et al.
A vaccine protecting monkeys against mucosal infection by simian immunodeficiency virus sheds light on immune and genetic correlates of protection.

SCIENCEPODCAST
www.sciencemag.org/multimedia/podcast
Free Weekly Show

On the 6 May *Science* Podcast: the effects of climate on crop production, detecting infectious disease, Darwinian literary criticism, and more.

SCIENCEINSIDER
news.sciencemag.org/scienceinsider
Science Policy News and Analysis

SCIENCE (ISSN 0036-8075) is published weekly on Friday, except the last week in December, by the American Association for the Advancement of Science, 1200 New York Avenue, NW, Washington, DC 20005. Periodicals Mail postage (publication No. 484460) paid at Washington, DC, and additional mailing offices. Domestic individual membership and subscription (51 issues): $149 ($74 allocated to subscription). Domestic institutional subscription (51 issues): $990; Foreign postage extra: Mexico, Caribbean (surface mail) $55; other countries (air assist delivery) $85. First class, airmail, student, and emeritus rates on request. Canadian rates with GST available upon request, GST #1254 88122. Publications Mail Agreement Number 1069624. **Printed in the U.S.A.**

Change of address: Allow 4 weeks, giving old and new addresses and 8-digit account number. **Postmaster:** Send change of address to AAAS, P.O. Box 96178, Washington, DC 20090–6178. **Single-copy sales:** $10.00 current issue, $15.00 back issue prepaid includes surface postage; bulk rates on request. The identification code for *Science* is 0036-8075. *Science* is indexed in the *Reader's Guide to Periodical Literature* and in several specialized indexes.

AAAS
ADVANCING SCIENCE, SERVING SOCIETY

ENLIGHTENED BY SCIENCE

The 2011•12 NEB Catalog & Technical Reference

New England Biolabs introduces its latest award-winning Catalog and Technical Reference, featuring over 100 new products, up-to-date charts, protocols and troubleshooting tips. Our thought-provoking collection of mini-reviews explore the mysteries of the deep ocean.

Featured New Products

One*Taq*™ DNA Polymerase – ideal for a wide range of templates, One*Taq* offers robust amplification with minimal optimization

EpiMark™ Validated Reagents for Epigenetics – this suite of products is designed to simplify DNA and histone modification studies

NEBNext® Reagents for Sample Preparation – available for DNA or RNA, these reagents facilitate sample prep for next generation sequencing

High Fidelity (HF) Restriction Enzymes – engineered for reduced star activity, HF enzymes offer maximum convenience

Visit **www.neb.com/newcatalog** to request a copy.

NEW ENGLAND BioLabs® Inc.
enabling technologies in the life sciences

Photo above – Moon Jellies *(Aurelia labiata)*, Monterey Bay Aquarium, CA

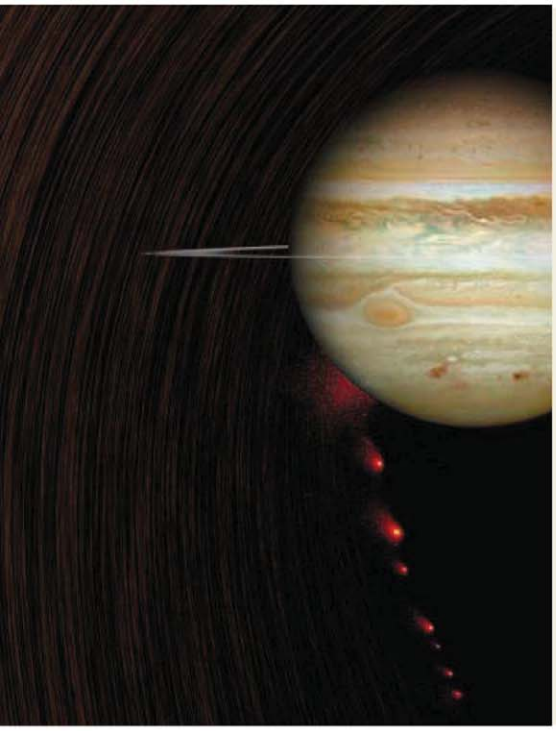

<< Ring-Tilting Events

Both Saturn's C ring and the rings of Jupiter show unexpected patterns of vertical corrugations (see the Perspective by **Salo**). **Hedman *et al.*** (p. 708, published online 31 March) show that in the case of Saturn, the patterns observed by the Cassini spacecraft in August 2009 were likely generated by an event in 1983 that caused part of the ring to tilt out of Saturn's equator plane. **Showalter *et al.*** (p. 711, published online 31 March) show that the features in Jupiter's rings observed in 1996 and 2000 by the Galileo spacecraft, and again in 2007 by the New Horizon spacecraft, are kinematically identical to those of Saturn's C ring. Jupiter's ring-tilting event occurred in 1994 and can be attributed to the impact of comet Shoemaker-Levy 9. Although the main fragments of the comet did not cross the ring, the associated dust debris may have caused the ring tilt.

CREDITS (TOP TO BOTTOM): SHOWALTER *ET AL.*; KNIGHT *ET AL.*

Building on Scaffold Proteins

One of the most fundamental insights into the mechanisms of cell signaling has been the recognition of the importance of scaffold proteins. These proteins hold in proximity components that function together. Such tethering of interacting molecules can have large effects on specificity and efficiency of signaling mechanisms. But as **Good *et al.*** (p. 680) explain in their review, scaffold proteins can have other effects on the behavior of bound proteins, which influence the sensitivity or time course of a signaling response. Scaffolds have thus allowed the evolution of complex regulatory mechanisms, and efforts are now under way to design molecules to produce therapeutically useful scaffold regulators.

Mass and Flow

Measurement of multiple parameters on individual cells in conventional flow cytometry is limited because of spectral overlap of the fluorophore markers that are detected. **Bendall *et al.*** (p. 687; see the Perspective by **Benoist and Hacohen**) describe a technique in which more than 30 measurements can be made through the use of distinct elemental isotopes detected by mass spectrometry. This technique allows the analysis of hundreds of cells per second. Each cell is vaporized at 5500 degrees kelvin, and the markers are monitored by inductively coupled plasma–mass spectrometry (ICP-MS). The technique was used to analyze the signaling properties of various cell types in the human hematopoietic system but should also be applicable to many other systems.

Nanoantenna Photodiode

Antennas are designed to collect electromagnetic radiation and focus it to a point where the signal can be read. Shrinking the size of the antenna to the nanometer-scale allows optical wavelengths to be collected and focused. Surface plasmons, which are collective electronic excitations that propagate near to the surface of a metal, allow the light to be converted to an electrical signal. **Knight *et al.*** (p. 702; see the Perspective by **Moskovits**) fabricated arrays of gold nanoantennas directly on a silicon surface, which then form a potential barrier between the nanoantenna and the semiconductor. If the assembly is subjected to polarization-sensitive photon absorption, electrons are injected across the antenna-semiconductor barrier into the semiconductor to create a photocurrent. Combining light-harvesting and "hot" electron injection in the same nanoscale device provides a mechanism for spectral and photon detection at energies below the semiconductor band gap.

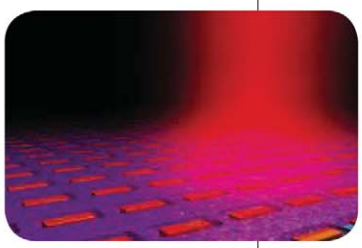

Probing the Cuprate Surface

Changing the positively charged carrier density of layered copper oxide materials transforms them from insulators into high-temperature superconductors. To discover what is happening within the bulk material, **Sakurai *et al.*** (p. 698) adopted an inelastic x-ray scattering technique to observe how the copper and oxygen orbitals shift with changes in the chemical environment. In a complementary study, **Scagnoli *et al.*** (p. 696, published online 7 April) used resonant x-ray scattering to image orbital currents in a copper oxide plaquette. Gaining a better understanding of how changes in the chemical environment affect the electronic behavior of the bulk material, combined with observations of (previously only theoretically predicted) loop currents, may be key to unlocking the mechanism of high-temperature superconductivity.

Dinosaurs in the Dark

Conventional wisdom has long held that physiological limitations meant that dinosaurs and pterosaurs were only active during the day, leaving the night to small, primitive mammals. Using characteristics of eye structure in extant species with known activity patterns, **Schmitz and Motani** (p. 705, published online 14 April; see the cover), suggest that these archosaurs were in fact active both day and night. Many similarities were observed between extant and extinct groups; flying animals are largely diurnal, carnivores largely nocturnal, and herbivores cathemeral (or active in bouts throughout a 24-hour cycle), indicating that paleozoic archosaurs, like mammals and birds, adopted daily activity patterns shaped by ecology.

Eat or Be Eaten—Alone

It is possible now to sequence the genomes of single cells, and of course anything else that might be on or within that cell. **Yoon *et al.*** (p. 714) shotgun-sequenced single cells of recently discovered picobiliphyte marine algae obtained directly from a wild environment, which

Continued on page 637

With the new easyCyte™ single-sample flow cytometer, more = less.

The new line of easyCyte™ single-sample flow cytometry instruments provides all the advantages and quality of the EMD Millipore guava® solution in an affordable single-sample device. With up to 8 parameters and 2 lasers, you have more analytical power, better quality data, validated reagents and full service support. You would expect to pay more for a similar instrument, but with the new **easyCyte** single-sample solution, **more = less.**

+ **MORE** PARAMETERS
+ **MORE** ANALYTICS
+ **MORE** INSIGHTFUL DATA
+ **MORE** BENCHTOP SPACE
+ **MORE** SIMPLICITY
+ **MORE** SOLUTIONS

= **LESS** $$$

www.millipore.com/easyCyte5

EMD Millipore is a division of Merck KGaA, Damstadt, Germany

Continued from page 635

provides a fascinating glimpse of possible virus infections and putative bacterial meals, with each cell displaying a different complement of genomes. Furthermore, this assumed photosynthetic genus apparently does not possess a complete plastid, and is thus more likely to be heterotrophic.

Priming the Intracellular Armory

The immune cytokine interferon gamma is capable of eliciting nearly 2000 host genes, including several families of guanosine triphosphatases such as the interferon-inducible, 65-kilodalton guanylate-binding proteins (Gbps). **Kim *et al.*** (p. 717) systematically assessed the effects of inactivating each member of the mouse family of Gbps and found that several were important in soliciting the machinery to combat intracellular bacterial infections by oxidative killing, phagocytosis, and autophagy.

Intriguing Insect Interneuron Normalization

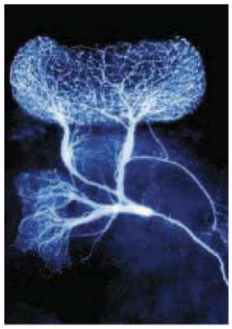

In the mushroom bodies that extend from of the brain of the locust, dense input signals from the antennal lobe are transformed into sparse representations in the intrinsic neurons of the mushroom bodies (the Kenyon cells). **Papadopoulou *et al.*** (p. 721) addressed the challenge of the distribution of sparse encoding in this system by applying a normalization function in which the network inhibits itself proportionally to the amplitude of the average input. In the locust, normalization is done by a single giant GABAergic neuron in each mushroom body, which receives input from virtually all the Kenyon cells and thereby acts to increase the dynamic range and overall encoding capacity of the system. This work has implications for understanding mechanisms underlying sensory representation in the mammalian brain.

Timing Infectiousness

Foot-and-mouth disease virus (FMDV) is a source of major economic loss for the livestock industry, not to mention the major logistical and animal welfare issues that accompany infection control. **Charleston *et al.*** (p. 726) have undertaken experiments in cattle to ascertain what the criteria should be for detecting infectiousness and thus how much leeway there is for modifying infection-control policies to limit cost and maximize animal welfare. They found that even if virus can be detected in a blood sample, it does not mean an animal is infectious. For successful transmission, certain symptoms also have to be apparent, and FMDV virus has to be excreted in mucus. But infectiousness is short-lived—1.7 days—because immune responses kick in and limit virus replication. The priority now is to develop rapid and accurate diagnostic tests as a precursor to reassessing infection-control policy.

Infectious Behavior

In the nematode worm *Caenorhabditis elegans*, three sensory neurons regulate resistance to pathogen infections by controlling the activation of a signaling pathway and promoting behavioral avoidance of certain pathogens. The neurons integrate behavioral responses to environmental oxygen, bacteria, and other animals within a neural circuit, and consequently their individual role in the control of immune responses has been difficult to assess. Now, **Sun *et al.*** (p. 729, published online 7 April; see the Perspective by **Tracey**) show that two of these neurons, which are located in chemosensory organs exposed to the environment, sense molecules related to disease or inflammation and regulate innate immunity via a pathway known as the unfolded protein response.

Remodeling Responses

The ability to measure responses of cellular signaling systems in single cells allows investigators to characterize the ways each cell optimizes responses to external cues. In studies on mitogen-activated protein kinase (MAPK) signaling in yeast cells, **Pelet *et al.*** (p. 732) discovered there was a linear relation between an osmotic stimulus and the amount of activated MAPK (in this case, Hog1) translocated to the nucleus and its retention time in the nucleus. Hog1 causes transcription of stress-response genes, but unlike the expected response of the kinase, gene activation was bimodal and varied even within the same cell. Further experiments and mathematical modeling showed that this variation corresponded to chromatin remodeling.

CREDIT: PAPADOPOULOU *ET AL.*

Eppendorf Consumables – it's Your sample

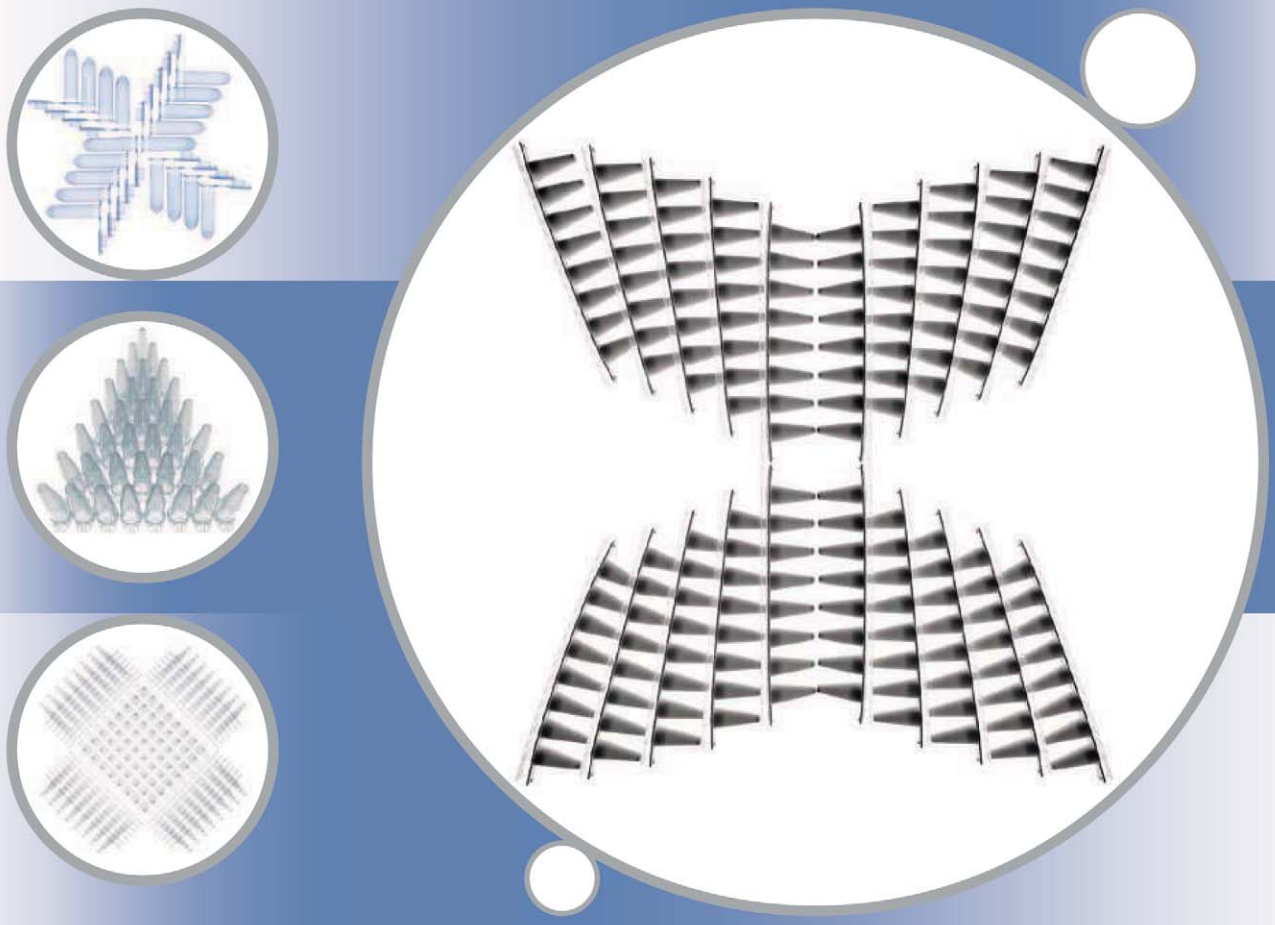

Go for Unaffected Assay Results!

Choose the right tubes for your experiments

Laboratory consumables can affect bioassays!
Reaction tubes for storing and processing samples should be selected carefully as they can influence the quality and reproducibility of your entire workflow. Original Eppendorf Tubes are produced without additives that have been shown to influence bioassay results, offer proven mechanical stability, superior technical performance and batch certified purity levels.

Original Eppendorf Tubes® :
Developed with your research results in mind!

- No slip agents, no plasticizers or biocides used at any time of the production process
- No leaching of UV-absorbing substances that can affect DNA quantifications
- Automated manufacturing under clean-room conditions to eliminate human interaction as source for contamination

Experience Eppendorf quality consumables and order your free sample on:
www.eppendorf.com/consumables

eppendorf
In touch with life

Your local distributor www.eppendorf.com/worldwide · Application Support: support@eppendorf.com
Eppendorf AG · Germany · Tel: +49 40 538 01-0 · Eppendorf North America, Inc. · USA · Tel: +1 800 645 3050
Eppendorf Asia Pacific Headquarters · Malaysia · Tel: +60 3 8023 2769

Vanessa M. Hayes is a professor of Genomic Medicine at the J. Craig Venter Institute, San Diego, CA. E-mail: vhayes@jcvi.org.

Indigenous Genomics

STUDIES OF INDIGENOUS PEOPLES ARE A CRUCIAL PART OF GENOMIC RESEARCH, NOT ONLY TO DEFINE the extent of human diversity but to provide medical benefit to all people. There are more than 370 million indigenous people living in almost half the countries of the world. Exploding interest in indigenous genomics and global population structure has raised debate about issues of informed consent and community benefit. As was evident in March 2011 during the African and Southern African Society of Human Genetics Meeting in Cape Town, South Africa, the inclusion of indigenous people in future genomic research is paramount, but ethical guidelines must address local concerns. Scientific practices and values must be integrated with indigenous governance so that such genomic research can continue, with the benefits fully realized by all.

The indigenous world, composed often of marginalized and impoverished populations, has experienced social injustices for the purposes of scientific advancement for centuries. Ranging from unethical experimental testing (such as of nuclear weapons in the deserts of Aboriginal-occupied Australia), to the "biopiracy" of traditional knowledge and resources (such as of endemic plants and their medicinal properties), exploitation has produced a sense of distrust in scientific endeavors. Concerns need to be addressed before establishing protocols and seeking ethical approvals. For example, informed consent is generally overseen by an institutional review board that lacks representation by, or understanding of, the local indigenous population of interest. This is frustrating for locals, who may understand the benefits of the research but may not have a clear understanding of the facts, implications, and consequences of participation.

Language concerns range from inadequate translations to a lack of written indigenous texts. Whereas modern societies emphasize literacy skills, indigenous cultures may communicate through sensory stimulations (visual action) and description (storytelling). For example, in the Khoesan languages, a single "western" word may have multiple descriptive narratives depending on the context in which it is used, by whom it is used, and to whom the narrative is directed. By including communities early in the process, one can ensure an adequate translation and adaptation of informed consent protocols. Cultural practices also must be respected. For many indigenous communities, for example, the practice of group ownership would call for a group-based informed consent for genomic property that may require extensive community discussions, as is the case in the nonhierarchical Khoesan communities.

Going forward, the scientific community must do more to ensure the full and effective participation of indigenous communities in the research process, ranging from correct data interpretation and acknowledgment in scientific publication, to negotiating potential long-term commercial benefits, to maintaining ties after the research is completed. Access to such communities requires a long-term social obligation that considers basic community needs, such as access to water, nutrition, education, and medicines.

My own experience in sequencing the first Southern Africans' genomes and exomes from Khoesan Namibian communities is perhaps illustrative.* The groups involved in this study have since communicated immense pride in the local and global recognition of their culture and history, and that this knowledge has had a positive impact on their youth. The project provided a platform for social empowerment by providing an opportunity for these voiceless communities to come together with local government, local media, and human rights leaders (including Archbishop Desmond Tutu) to enhance discussions about community needs. Indigenous genomic research must commit to bridging the communication and cultural differences between scientists and indigenes, creating additional knowledge-based capacities through bidirectional learning, while ensuring continued and sustained community benefit. **– Vanessa Hayes**

10.1126/science.1205999

*S. C. Schuster *et al., Nature* **18**, 943 (2010).

CREDITS: CHRIS BENNETT

EDITED BY KRISTEN MUELLER AND JAKE YESTON

CREDITS (TOP TO BOTTOM): NASA/KEPLER MISSION/WENDY STENZEL; A. M. BENAVIDES

ASTRONOMY

Seeking Distant Companions

The Kepler satellite searches for planets around other stars by detecting the dimming of light that occurs when a planet passes in front of its star. Between 2 May and 16 September 2009, in its first 4 months of operation, Kepler looked at 156,453 stars in our galaxy, 1489 of which were considered of interest because their light curves—the graph of their brightness as a function of time—bore the signatures of planetary candidates. Testing for false positives, such as binary star systems, eliminated 492 stars, leaving 1235 planetary candidates around 997 stars: 827 in systems of single transiting planets and 408 in systems where more than one planet transits the same host star. Although not all the candidates have been confirmed through follow-up observations, the rate of false positives within the list of singles is thought to be 5 to 10% and that within multiples even lower. Latham *et al.* compared the properties of planet candidates in single and multiple systems. Systems with single transiting planets are more likely to include a planet larger than Neptune, suggesting that Jupiter-like planets in short-period orbits disrupt the orbital inclinations of smaller planets, making them less likely to preserve the flatness of the disk from which they originated and thus less likely to transit the star. — MJC

Astrophys. J. **732,** L24 (2011).

OCEAN SCIENCE

All Gassed Up

Ocean sediments contain an immense quantity of methane and thus play a key role in the global methane cycle. There are enormous fluxes of methane into and out of the sediments, even though most of the methane produced within the sediments is oxidized anaerobically before it can be released to the ocean water column. Estimates of sedimentary methane production vary between about 85 and 300 Tg per year, although analytical difficulties have made the supporting measurements too imprecise to tell where in that range the true value lies. Zhang *et al.* employed an in situ technique to measure methane concentrations in sediments, in order to avoid the sampling issues that have plagued other methods. They find concentrations as much as 10 to 20 times higher than those determined by shipboard measurements and conclude that production rates are near the high end of past estimates. — HJS

Geophys. Res. Lett. **38**, L08605 (2011).

EDUCATION

All Together Now

The recent explosion of citizen science activities has been accompanied by informal science education efforts aimed at fostering partnerships between students, academics, and industrial scientists. Gebbels *et al.* brought students and employees from Merck, Sharp and Dohme (MSD) together to participate in an environmental management project in coastal northeast England. Students, ages 13 to 14, spent a day in the field surveying flora of sand dunes and the rocky shore, small mammals, birds, and invertebrates and presented their findings to MSD employees. Students reported a rich and varied ecosystem but noted that an abundance of an invasive ragwort plant in the dunes was a cause for concern. Students also noted the effects of human impact, specifically the number of access points and the resulting paths where vegetation had been destroyed. MSD employees took seriously the management recommendations made by the students and, along with student assistance, brought one to fruition (reconstruction of a bird hide). All participants claimed that involvement in the project increased their awareness of environmental issues and motivated them to become involved in further conservation projects. As an additional incentive for other industrial firms looking to embark on similar education projects, students reported a more positive outlook on the ways in which companies act as environmental stewards. — MM

J. Biol. Educ. **45**, 13 (2011).

ECOLOGY

Elucidating Epiphyte Diversity

In tropical forests, an important fraction of the total plant species diversity is composed of epiphytes: plants that are rooted for part or all their life on the trunks and branches of trees and lianas. The patterns of epiphyte diversity are still poorly understood relative to those of trees, however, because of logistical challenges, such as tree height. Benavides *et al*. performed a comparative analysis of the epiphyte communities in lowland forest in Colombian Amazonia, aiming to understand how landscape unit (swamp forest, floodplain forest, and well-drained upland) and host tree species influenced the composition of their epiphyte communities, using a combination of collecting by tree climbing and binocular observations. They recorded 154 epiphyte species on 411 tree species. There were clear associations between tree/liana species

Continued on page 643

Continued from page 641

assemblages and epiphyte species assemblages, but there were few significant associations between individual host species and epiphyte species. The high diversity of both groups of plants in the sampled plots made testing for individual host preferences difficult, suggesting the need for further studies. — AMS

J. Trop. Ecol. **27**, 223 (2011).

EPIDEMIOLOGY

Knowlesi Enters the Malaria Mix

What if a new and devastating form of malaria emerges? This scenario may be occurring in Southeast Asia, where a significant number of reported malaria cases were identified as being caused by *Plasmodium knowlesi*, until recently thought to be a monkey infection. This parasite has recently been recognized to cause a wide spectrum of human diseases that can result in complications and death. Lee *et al.* surveyed monkeys in Sarawak, Malaysia, and found very high levels of *P. knowlesi* infection in long-tailed macaques. Genetic analysis of human cases and macaques did not show any clustering or distinct lineages associated with host species. A relatively recent population expansion of the parasite occurred about 30,000 to 40,000 years ago, roughly coincident with major human settlement in Southeast Asia. The genetic data thus indicate that this is a previously unrecognized parasite rather than a newly emerging one, and that infection is zoonotic, arising when humans penetrate macaque habitats during forestry activities. Caution is necessary because further forest destruction might prompt the parasite and its mosquito vector to adapt to a future more numerous primate host species. — CA

PLoS Pathol. **7**, e1002015 (2011).

CELL BIOLOGY

Tagged for Delivery

Localized translation of mRNA in eukaryotes is essential for regulating gene expression. Localized mRNAs contain specific sequences that target them for recognition and incorporation into messenger ribonucleoprotein particles (mRNPs) and also recruit motor proteins; however, how selective transport is achieved remains unclear. Müller *et al.* used in vitro reconstitution assays and in vivo experiments to investigate how *Saccharomyces cerevisiae ASH1*-mRNA, which is transported from the mother to the daughter cell during mitosis, is incorporated into mRNPs. Surprisingly, two RNA-binding proteins, She2p and Puf6p, implicated in escorting *ASH1* mRNA from the nucleus to the cytoplasm, were found to display little specificity for cargo RNAs. Instead, She3p, which was previously identified as an adaptor that brings the motor myosin V into the mRNAp, bound to She2p and also bound weakly to cargo RNAs. The RNA binding of She2p and She3p was synergistic, so that together the two form a specific ternary complex with the mRNA, stabilizing the She2p:She3p interaction. These data suggest that the mRNA cargos are bound with only limited specificity for nuclear export. A stable and specific transport complex then forms in the cytoplasm and mediates appropriate localization of the cargo mRNA. — VV

PLoS Biol. **9**, e1000611 (2011).

STRUCTURAL BIOLOGY

Seahorse Versus Pathogen

Just like us, prokaryotes—bacteria and archea—must also protect themselves against pathogenic microbes, such as viruses and plasmids. Prokaryotes use the CRISPR (clustered regularly interspaced short palindromic repeats) system, an adaptive immune response whereby sequence snippets from the invading pathogen's genome are collected and stored by the host, which then uses them to target the pathogen for destruction.

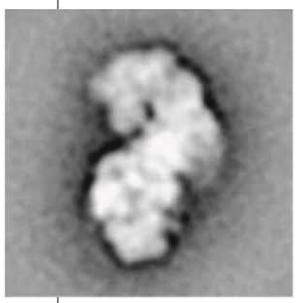

Jore *et al.* have analyzed the composition and low-resolution structure of the Cascade complex, which lies at the heart of the CRISPR immune response. The snippets of invader sequence are transcribed and converted into CRISPR RNA (crRNA), which is bound by the Cascade complex. Thus loaded, the Cascade complex is able to bind sequences complementary to the crRNA either as double-stranded (ds) DNA or single-stranded DNA. With a dsDNA target, Cascade-complex binding displaced the noncomplementary target strand as an R loop, in an ATP-independent reaction. The overall structure of the Cascade complex surprisingly resembled the shape of a seahorse, with the spine and head consisting of a tightly curved polymer of six CasC protein subunits, which might bind the crRNA. — GR

Nat. Struct. Mol. Biol. **18**, 10.1038/nsmb.2019 (2011).

CREDIT: JORE *ET AL.*, *NAT. STRUCT. MOL. BIOL.* **18**, 10.1038/NSMB.2019 (2011)

www.sciencemag.org

Science

1200 New York Avenue, NW
Washington, DC 20005
Editorial: 202-326-6550, FAX 202-289-7562
News: 202-326-6581, FAX 202-371-9227
Bateman House, 82-88 Hills Road
Cambridge, UK CB2 1LQ
+44 (0) 1223 326500, FAX +44 (0) 1223 326501

Subscription Services For change of address, missing issues, new orders and renewals, and payment questions: 866-434-AAAS (2227) or 202-326-6417, FAX 202-842-1065. Mailing addresses: AAAS, P.O. Box 96178, Washington, DC 20090-6178 or AAAS Member Services, 1200 New York Avenue, NW, Washington, DC 20005

Institutional Site Licenses please call 202-326-6755 for any questions or information

Reprints: Author Inquiries 800-635-7181
Commercial Inquiries 803-359-4578

Permissions 202-326-7074, FAX 202-682-0816

Member Benefits AAAS/Barnes&Noble.com bookstore www.aaas.org/bn; AAAS Online Store www.apisource.com/aaas/ code MKB6; AAAS Travels: Betchart Expeditions 800-252-4910; Apple Store www.apple.com/eppstore/aaas; Bank of America MasterCard 1-800-833-6262 priority code FAA3YU; Cold Spring Harbor Laboratory Press Publications www.cshlpress.com/affiliates/aaas.htm; GEICO Auto Insurance www.geico.com/landingpage/go51.htm?logo=17624; Hertz 800-654-2200 CDP#343457; Office Depot https://bsd.officedepot.com/portalLogin.do; Seabury & Smith Life Insurance 800-424-9883; Subaru VIP Program 202-326-6417; VIP Moving Services www.vipmayflower.com/domestic/index.html; Other Benefits: AAAS Member Services 202-326-6417 or www.aaasmember.org.

science_editors@aaas.org	(for general editorial queries)
science_letters@aaas.org	(for queries about letters)
science_reviews@aaas.org	(for returning manuscript reviews)
science_bookrevs@aaas.org	(for book review queries)

Published by the American Association for the Advancement of Science (AAAS), *Science* serves its readers as a forum for the presentation and discussion of important issues related to the advancement of science, including the presentation of minority or conflicting points of view, rather than by publishing only material on which a consensus has been reached. Accordingly, all articles published in *Science*—including editorials, news and comment, and book reviews—are signed and reflect the individual views of the authors and not official points of view adopted by AAAS or the institutions with which the authors are affiliated.

AAAS was founded in 1848 and incorporated in 1874. Its mission is to advance science, engineering, and innovation throughout the world for the benefit of all people. The goals of the association are to: enhance communication among scientists, engineers, and the public; promote and defend the integrity of science and its use; strengthen support for the science and technology enterprise; provide a voice for science on societal issues; promote the responsible use of science in public policy; strengthen and diversify the science and technology workforce; foster education in science and technology for everyone; increase public engagement with science and technology; and advance international cooperation in science.

Information for Authors
See pages 784 and 785 of the 11 February 2011 issue or access www.sciencemag.org/about/authors

WEBINAR

Identifying Novel Cancer Therapeutic Targets

Real-time, Label-free Cell Monitoring in RNAi Profiling

PARTICIPANTS:

Kristina Cole, M.D., Ph.D.
Children's Hospital of Philadelphia
Philadelphia, PA

David Azorsa, Ph.D.
Translational Genomics
Research Institute (TGen)
Scottsdale, AZ

REGISTER NOW!

Sign Up At:
www.sciencemag.org/webinar

May 18, 2011
12 noon ET, 9 am PT, 4 pm GMT, 5 pm UK

The identification of novel molecular targets for cancer can be a challenge. Such targets have recently been discovered in cell lines derived from aggressive childhood tumors using phenotypic profiling and RNAi screening. Further, studies have shown real-time, label-free cell monitoring using electrical impedance technology to be a viable technique to perform these assays and identify and validate novel cancer targets. Two current publications highlight the power of such an unbiased genetic screen to identify potential therapeutic targets from the protein kinome for Ewing's sarcoma and neuroblastoma through the use of RNAi profiling combined with real-time, label-free technology. In this webinar, a panel of experts will discuss their research and describe the use of real-time, label-free cell monitoring in their investigation of novel cancer targets and the impact of their work on translational research and drug development.

During the webinar, viewers will:

- Discover how these scientists are incorporating real-time, label-free cell analysis in screening and validation to identify therapeutic targets
- Learn about the application of kinetic monitoring of cell growth
- Hear how label-free technology can be an enabling tool for cellular analysis
- Have the opportunity to ask questions of the experts live!

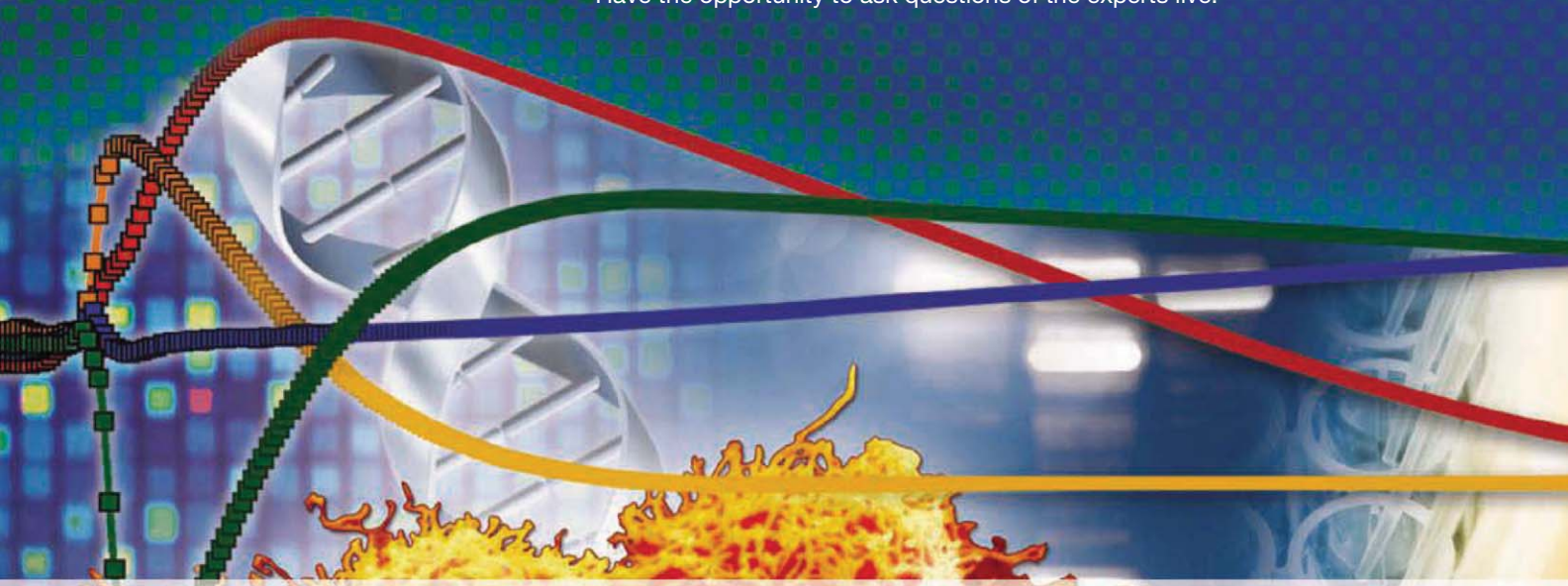

Brought to you by the AAAS/*Science* Business Office

Science
AAAS

Webinar sponsored by

Roche
xCELLigence

xCELLigence is a trademark of Roche

AROUND THE WORLD

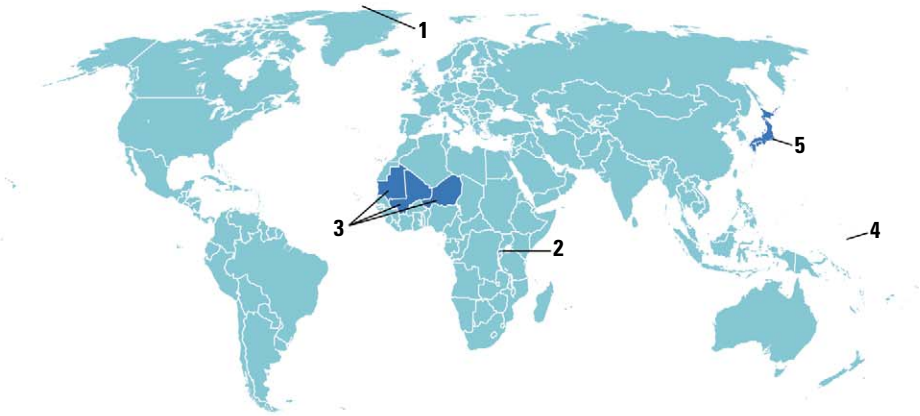

Arctic Ocean **1**

Scientists Urge Greater Protection For Arctic as Ice Recedes

Scientists and representatives of indigenous Arctic communities have identified areas around the Arctic Ocean that they say should be protected as sea ice recedes, opening the way for industry. The report, released last week by the Natural Resources Defense Council (NRDC) and the International Union for Conservation of Nature, maps out 77 areas, 13 of which they identify as high priority regions. These range from the Bering Strait to perennial gaps in the ice off the coasts of Russia and Greenland.

The predictable retreat of Arctic sea ice under global warming presents one last opportunity to adopt effective marine management practices before industry gets going, says Lisa Speer of NRDC in New York City, who co-authored the workshop report. Once development starts, "it becomes much more difficult to protect key ecosystems," she says. "Now we have a short window of opportunity to do it right."

That will require cooperation among the eight Arctic nations, which include the United States and Russia. Foreign ministers of the Arctic Eight meet next week in Nuuk, Greenland, where the agenda will include management practices in the melting Arctic.

Rwanda **2**

Africa's First Cervical Cancer Prevention Program Launched

The Rwandan government, in collaboration with two companies, launched the first national cervical cancer prevention program in Africa on 25 April. The companies, Merck and Qiagen, will make substantial donations to help vaccinate girls against the human papillomavirus (HPV), which causes cervical cancer, and screen adult women for infection with the virus.

Many countries in the western world have implemented HPV vaccination programs. But the vaccines' cost—more than $300 for three doses—has been a major obstacle to their use in developing countries. Under the deal, Merck will donate more than 2 million doses of its vaccine, Gardasil, for the first 3 years of a nationwide program targeting girls 12 to 15 years old. Qiagen will contribute 250,000 of its DNA-based HPV screening tests, which are easier to administer than traditional Pap smears, for women ages 35 to 45.

After 3 years, Rwanda will pay for the products at discounted prices that have yet to be revealed. The companies say they are talking to other poor countries about similar programs.

Mauritania, Mali, and Niger **3**

French Researchers Balk At Limits on African Travel

French scientists are up in arms about a freeze on field work in Mauritania, Mali, and Niger, triggered by the deteriorating security situation in those countries. French citizens in the region have become frequent targets of Al-Qaeda in the Islamic Maghreb—the terrorist group believed to be behind last week's bomb attack in Marrakesh—leading the French government to issue a travel warning for the three countries in January. In response, universities and research agencies such as the National Center for Scientific Research (CNRS) and the Institute for Research for Development have told their scientists to stay home indefinitely.

The freeze is a severe blow to research and is isolating local scientists, says Sébastien Boulay, an anthropologist at the University of Paris Descartes. Boulay, who works in Mauritania, started an online petition to relax the measures; it has drawn more than 650 signatures, including many from African scientists.

CNRS security expert Joseph Illand says that his agency can't ignore government advisories but that exceptions are possible if scientists justify the importance of their mission and have detailed security plans. "The death of Osama bin Laden won't contribute to pacification in the short term," Illand predicts. **http://scim.ag/travel-ban**

Conservationists are hurrying to protect Arctic regions, such as Canada's Lancaster Sound, as global warming opens them up to industry.

CREDIT: CHRISTOPHER DEBICKI/*MCCLATCHY-TRIBUNE* VIA GETTY IMAGES

NOTED

>Stanford University in Palo Alto, California, will begin a new **Ph.D. program in stem cell science** in 2012. Officials there say it will be the first such program in the nation, if not the world. Prospective students can apply this fall for three to six spots in the inaugural class.

A purse seiner offloads its frozen catch of skipjack onto a refrigerator ship in Pohnpei, Federated States of Micronesia, a member of PNA.

Western and Central Pacific Ocean **4**

Fishery Certification Boosts Tuna Conservation

A group of Pacific Ocean island states known as the Parties to the Nauru Agreement (PNA) have scored a victory in their battle with distant fishing nations to preserve the world's last major stocks of tuna. Last week, the London-based Marine Stewardship Council announced its intention to certify as sustainable about half the skipjack tuna caught by purse-seine vessels in waters surrounding the eight member nations, which include Papua New Guinea and Kiribati. The certification, a first among purse-seine fisheries, recognizes PNA's aggressive efforts to limit tuna fishing in its waters.

Skipjack, the most abundant of the tunas, is sold mostly for canning. The certification will apply only to the half of skipjack caught in free-swimming schools. The other half is caught with floating devices that attract other species as well, notably the prized bigeye tuna, whose numbers have dwindled so much that scientists who monitor the fishery have called for a 30% reduction in the take. The certification dovetails with PNA's decision last month to extend a ban on the floating devices from 3 months a year this year to 6 months next year. PNA plans eventually to ban them entirely, and has already prohibited nearly all purse-seining in an area the size of India.

CREDITS: C. PALA; UNIVERSITY OF CAMBRIDGE; (GRAPH SOURCE) NIH, J. R. POHLHAUS *ET AL.*, *ACADEMIC MEDICINE* 86 (ADVANCE EDITION, JUNE 2011)

Tokyo, Japan **5**

Radiation Standards Draw Protests

Toshiso Kosako, a radiation safety expert at the University of Tokyo, resigned his governmental advisory post last week in protest over what he calls "inexcusable" standards for schoolchildren exposed to radiation from the ravaged Fukushima Daiichi Nuclear Power Plant.

On 19 April, the ministry of education announced a "provisional idea" for contaminated schoolyards. It cited a recommendation by the International Commission on Radiological Protection that exposure be kept at the lower end of a range between 1 and 20 millisieverts (mSv) per year for individuals living long-term in contaminated areas. The education ministry figured that children could spend 8 hours a day in a schoolyard with as much as 3.8 microsieverts per hour of radiation and then 16 hours a day inside a building with 1.52 microsieverts per hour and stay within a 20 mSv per year limit.

Some 800 groups and 3400 individuals have signed a petition, presented to the government 2 May, demanding the proposal's withdrawal. Kosako's resignation is expected to put additional pressure on the government to rethink its decision.

NEWSMAKERS

The $23 Million Textbook

The Making of a Fly, by **Peter Lawrence** of the University of Cambridge in the United Kingdom, is a classic in the field of developmental biology. But is a single copy really worth $23,698,655, the price one seller was asking last month on Amazon.com?

University of California, Berkeley, evolutionary biologist Michael Eisen noticed the skyrocketing price when a postdoc in his lab wanted to order an extra copy. The book, written in 1992, is out of print, but third-party sellers on Amazon still had 17 copies in stock. When Eisen looked, one copy was being hawked for $1,730,045.91 (+$3.99 shipping).

The culprit? An algorithm used by two competing sellers to automatically adjust their prices depending on the other's offer, which had created an upward spiral. The price peaked on 18 April before a human being intervened and the prices came >>

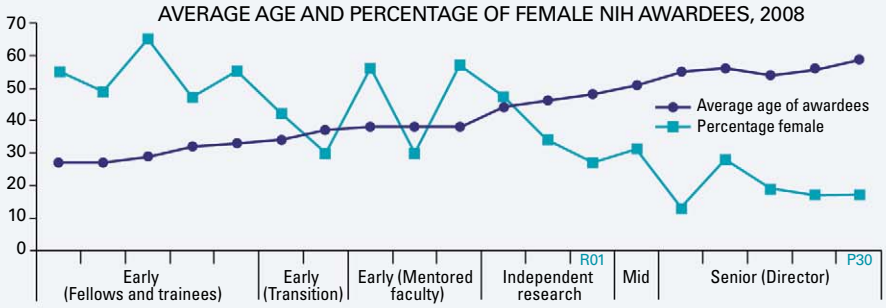

Biomedical Research's Shaky Ladder

A new analysis puts in stark relief the widening imbalance between men and women biomedical researchers as they move up the career ladder. National Institutes of Health (NIH) staff members examined women's share in 2008 of 19 types of training grants and research awards arranged by career stage (see graph). Women held about half of the training grants. But they received only 27% of R01s, NIH's basic independent research grants, and only 17% of all P30s, which are large center grants.

The numbers are a snapshot of a single year and say nothing about the progression of a particular cohort. The data come from a paper published online 20 April in *Academic Medicine* that also explores success rates for men and women. For the most part, they are the same. But experienced male scientists submit more R01 applications, and they are more successful at renewing these grants than women.
http://scim.ag/_grants

>>NEWSMAKERS

back to Earth. (As *Science* went to press, however, the price had sneaked back up to $10,000.00.)

"It's funny, isn't it," Lawrence says. "I was hoping it would go up to a billion."

He says Eisen's desire to order a copy of the 1992 textbook suggests that he succeeded in his intention to "write a book that lasts."

USDA Research Leader Departs

Roger Beachy, the top scientist for extramural research at the U.S. Department of Agriculture (USDA), is leaving his post this month after serving less than 2 years. A pioneer in the genetic engineering of plants at Washington University in St. Louis (WUSTL), Beachy was recruited to increase the profile and success of agricultural research.

Congress had already boosted USDA's budget for competitive research grants by 30% in FY 2010, to $260 million. Beachy put roughly half those funds into larger, multidisciplinary grants focused on "grand challenges," such as dealing with the impact of climate change. The number of grant applications rose significantly and included researchers beyond the department's traditional constituency of land-grant universities. "I feel pretty good that we've been able to do as much as we have," Beachey told *Science*.

This year's pot for competitive grants is down by about 1%. But Beachy says his decision to leave on 20 May is "strictly for personal reasons"—a desire to be with his family, which has remained in St. Louis. He will return to WUSTL as a professor in the biology department. **http://scim.ag/_Beachy**

FINDINGS

First Stars Were Spinning Tops

The first stars, which were up to hundreds of times bigger than the sun, were also whirling at incredible speeds, suggests a new study.

Consisting of hydrogen and helium, these early stars burned out by the time the universe was 1 billion years old. But they produced heavier elements that, after their death, were incorporated into new stars. To gather clues about the first generation, a team led by Cristina Chiappini of the Leibniz Institute for Astrophysics in Potsdam, Germany, looked at a member of the second:

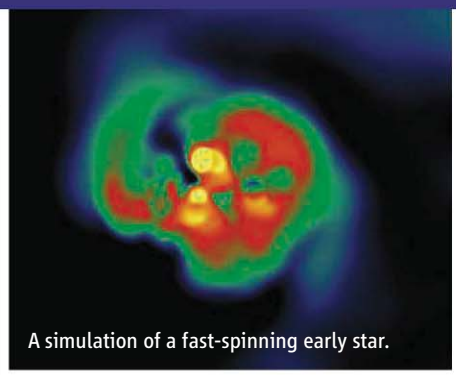

A simulation of a fast-spinning early star.

stars from a 12-billion-year-old Milky Way cluster named NGC 6522.

The stars' spectra indicated high abundances of the heavy elements strontium and yttrium, which rotating stars can create at high rates. To produce the ratios seen in this cluster, an ancestor star would have to be spinning at 500 km per second, Chiappini and her colleagues reported online last week in *Nature*. That's 250 times as fast as the sun.

If the first stars were indeed rapid spinners, they probably went out with a high-energy bang known as a Gamma Ray Burst. These flashes can be seen much farther away than individual stars. That augurs well for astronomers hoping to watch the first stars in the act of dying. **http://scim.ag/spin-stars**

Computer Algorithm May Speed Drug Discovery

In 2007, researchers noticed that the anti-HIV drug nelfinavir, developed in the 1990s, also reduced tumors. Now scientists say they've figured out how nelfinavir works its double magic. The finding could open up a new route for drug discovery.

Pharmacologist Philip Bourne of the University of California, San Diego, and colleagues used a structure-based algorithm to find all the proteins to which nelfinavir might bind, 92 in all. Most were protein kinases, which have been linked to tumor growth because they can speed up cell division. Their shapes' similarity to HIV enzymes allowed nelfinavir to bind and disrupt them. And because improper kinase activity strongly dampens the signals that tell the tumor cell to divide, nelfinavir's weak action against many kinases shrank tumors.

This computational approach can be used to identify numerous drug targets more cheaply and easily than traditional experimental methods, the researchers reported 28 April in *PLoS Computational Biology*. Selecting one enzyme and screening libraries of drugs for one that targets it is laborious, says Bourne; computation can save time

A Tree Expert in Your Back Pocket

As spring unfolds and leaves unfurl, it's time to take the iPhone for a walk in the woods. Just as there are mobile applications for identifying constellations, there's now Leafsnap, a free electronic field guide to trees. Point and shoot at a leaf, and the iPhone—and soon the iPad and phones running Android—will compare the image to a central database of 8000 leaves, providing the closest matches using face recognition software. The answer comes with facts about the species as well as pictures of the leaf, flower, bark, and fruit. The application also sends the image, identity, and location to another database that scientists can use to track how the numbers and ranges of trees are changing through time.

Leafsnap currently includes 191 tree species in Washington, D.C., and New York City. By the year's end, the app's 50-plus creators from Columbia University; the University of Maryland, College Park; and the Smithsonian Institution expect to have the 250 species needed to identify trees throughout the northeastern United States. Covering the continental United States needs more funding and 2 to 3 years to complete.

CREDITS (TOP TO BOTTOM): ADAPTED FROM A. STACY *ET AL.*, *MNRAS*, **413** (2011); USDA; COLUMBIA UNIVERSITY, UNIVERSITY OF MARYLAND, AND SMITHSONIAN INSTITUTION

BY THE NUMBERS

2511 Artifacts, including prototype helmets from NASA's early shuttle research, in Syracuse University's Plastics Collection, most of which is now perusable at http://plastics.syr.edu.

>1000 Entries submitted to the European Commission's contest to name its next science and technology funding program. The current program, called Framework 7, ends in 2013. The contest closes 10 May. **http://scim.ag/name-game**

88% Percentage of respondents to the U.K.'s Public Attitudes to Science 2011 survey who agreed that "scientists make a valuable contribution to society." Fifty-four percent, however, agreed that "rules will not stop scientists doing what they want behind closed doors." **http://scim.ag/_attitudes**

and money. And with pipelines for drug discovery running dry, searching for substances that weakly interact with many targets provides a welcome fresh strategy for finding effective drugs, say other researchers. **http://scim.ag/drug-discovery**

At Long Last, Gravity Probe B Satellite Proves Einstein Right

Fifty years after it was conceived, a $760 million NASA spacecraft has confirmed general relativity, Einstein's theory of gravity, albeit less precisely than hoped. Gravity Probe B circled Earth from pole to pole for 15 months starting 20 April 2004 and used gyroscopes to measure two aspects of general relativity, which states that gravity arises when mass bends space and time. The satellite confirmed to 0.25% precision the geodetic effect in which the circumference of a circle around Earth is slightly shorter than 2π times the circle's radius, researchers reported this week at NASA headquarters in Washington, D.C. It also confirmed to 20% precision the frame-dragging effect, in which the rotating Earth twists spacetime much as turning a heavy bowl twists a table cloth beneath it. In 2004, a team from Italy reported a similar result.

Researchers aimed to measure frame dragging to 1% precision, but were thwarted by electrostatic imperfections in the gyroscopes—rapidly spinning, almost perfectly round quartz spheres covered in superconducting niobium. Just to reach 20% precision, they spent 5 years figuring out how to correct for the slight tugs caused by those imperfections, says Francis Everitt, a physicist at Stanford University in Palo Alto, California.

But the experiment's full value goes beyond the results, Everitt says: "Just the element of challenge, the element of invention in it" made it worthwhile.

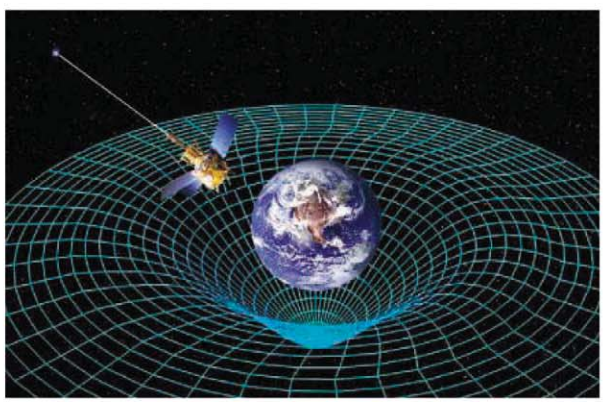

CREDITS (TOP TO BOTTOM): NEWSCOM; NASA

Random Sample

Young, But How Innocent?

Decked with colorful poster boards and potted lima bean plants, school science fairs are a rite of passage for budding researchers. But a new survey by two Kentucky teenagers suggests the events might also be cradles of scientific misconduct.

Michael Moorin and Tyler Smith, both 17, of duPont Manual High School in Louisville found that more than half of science fair competitors at their school cheated. The results have propelled the pair to next week's Intel International Science and Engineering Fair in Los Angeles.

One hundred students—about one-third of the participants in Manual's science fair—answered Moorin and Smith's anonymous online questionnaire. Sixty percent admitted to some form of scientific misconduct. Most had falsified data (55% of respondents), while others had changed hypotheses to fit results or had lied on fair entry forms. Fifteen percent of respondents acknowledged doing all three, and seven students admitted to cheating on Intel competition projects.

With nearly $4 million in awards at stake, Intel fair entries are rigorously scrutinized, says Michele Glidden, director of science education programs for the Society for Science & the Public in Washington, D.C., which oversees the Intel competitions. Still, she called the survey results "disturbing."

Moorin and Smith's findings have prompted Manual to add an ethics component to courses next year. But Bruce Shore, an education researcher at McGill University in Montreal, Canada, who has published his own paper on science fair cheating, says what students really need is more instruction on how to conduct the projects. "High-performing students cheat less," Shore says. "Part of the reason is they've learned to learn."

On the move. China's migrant population has grown by 81% in the past decade.

DEMOGRAPHY

China's Population Growing Slowly, Changing Fast

China's population has long been something of a magic number for the rest of the world. Marketers rhapsodize about selling to 1.3 billion consumers, while agronomists worry about whether those 1.3 billion mouths will have enough to eat. Preliminary figures from the 2010 census released last week show that the country is still growing. But the census also reveals trends that could reshape the world's view of China—and perhaps even trigger changes in the government's controversial one-child policy.

After adhering to that policy for 3 decades, the world's most populous country is aging, and fast. China grew by only 5.8% in the past decade, from 1.27 billion to 1.34 billion. That's less than half the growth rate of 11.7% for the previous decade, as recorded in the 2000 census. Meanwhile, the proportion of Chinese aged 14 and under fell to 16.6%, compared with 22.9% in the previous census, while the share of those 60 and over increased to 13.3%—some 2.9 percentage points higher than in 2000.

Those statistics suggest a low fertility rate, "confirm[ing] what demographers in China have long anticipated," says Wang Feng, a demographer and director of the Brookings-Tsinghua Center for Public Policy in Beijing. Wang estimates the fertility rate at below 1.5 children per couple, although others say it's too early to know.

Either way, China may soon lose the title of most populous country. Projections from the U.S. Census Bureau predict that India, which last month reported a total population of 1.21 billion, will overtake China in 2025. Now that preliminary results from both the Indian and Chinese censuses have come out, Census Bureau demographer Daniel Goodkind wrote in an e-mail, those projections "hold up fairly well."

Of greater concern to Chinese demographers are the social and economic effects of these trends. The low birth rate points to labor shortages and the aging population to more challenges for an already overburdened social service system. If current trends continue, says Zhongdong Ma, a demographer at Hong Kong University of Science and Technology, China's fertility rate is in danger of falling below 1.3 children per couple. That would place it among countries with "lowest-low" fertility such as South Korea and Japan.

Citing these disruptions to society, Chinese demographers have become increasingly vocal in pushing for an end to the one-child policy adopted in 1980 (*Science*, 17 September 2010, p. 1458). They hope the census results will bolster their arguments. In a speech broadcast on state television last week, President Hu Jintao stated that China will stick to its birth planning program but talked of tweaking the program—a comment Wang says could mean a "crack at the top."

This year's census suggests a growing imbalance in China's sex ratio at birth. It's gone from 116.9 boys to 100 girls in 2000 to 118.1 to 100 in the latest census, a change most likely explained by an increase in sex-selective abortion. The effects of the imbalance will only worsen as those in the youngest birth cohorts become adults, Ma says: "In 2 to 3 years, you'll see the number of females in the marriage market substantially decrease."

And yet, even as the sex ratio at birth increased, the country's overall sex ratio—including adults and seniors—fell, from 106.7 males per 100 females in 2000 to 105.2 per 100 now. That drop is puzzling, says Cai Yong, a demographer at the University of North Carolina, Chapel Hill. The 2000 census found that Chinese females were living an average of 3 years longer than males. The 2010 results suggest that the life expectancy gap has widened to about 8 years—a shift Cai calls "almost impossible." He hopes more detailed data, expected later this year, will explain the mystery.

On another note, the census revealed that 49.7% of Chinese now live in cities, compared with 36.2% in the previous census. This decade was the fastest period of urbanization in China's history. The country's population is moving eastward, into booming cities like Beijing, while the less developed western provinces of Sichuan, Gansu, and Shaanxi recorded drops in their share of the overall population. Leading the pack is Shanghai, whose 23 million people now account for 1.7% of China's population.

Kam Wing Chan, a geographer at the University of Washington, Seattle, who studies migration in China, wrote in an e-mail that some of the rise could be explained by a new method of counting people that supplemented registration data with a head count and comprehensive interviews in an effort to track down more temporary residents (*Science*, 22 October 2010, p. 436). The census found 261.4 million unregistered people who have lived at their current residence for at least 6 months—a whopping 81% increase over 10 years ago. But the shift also reflects China's booming economy, he added.

CREDIT: CHINA PHOTOS/GETTY IMAGES

As China urbanizes, its population is also rapidly becoming more educated. The number of Chinese with a college degree more than doubled since 2000, to 119.6 million, and the literacy rate rose slightly, to 95.9%. And for the first time the survey, in addition to mainlanders, counted foreigners and residents of Hong Kong and Macau. They total 1 million, including 71,000 Americans. About half of that population has stayed for longer than 2 years.

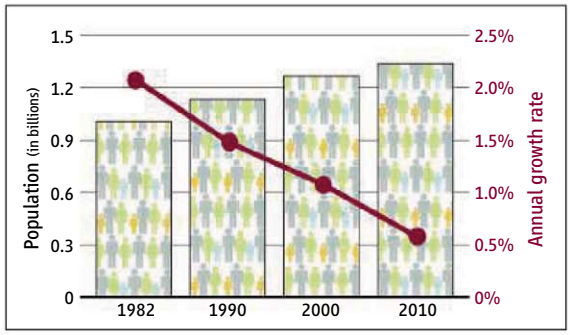

Going down. Although China's population is still growing, the rate (shown here as the annual average since the previous census) has been slowing since the first modern census.

Demographers are waiting to see the full census results before drawing conclusions about data quality. But China's National Bureau of Statistics, at least, is confident about the survey. Its reported undercounting rate dropped to 0.12%, down from 1.81% in 2000, a year the census is thought to have missed 22.5 million Chinese.

Chan says the new counting method may have contributed to the drop. Ma, meanwhile, chalks up the change to good publicity and an army of 6.5 million census takers. Such a low undercounting rate, he says, is "amazing for such a large country." And even as India is closing in on the title of most populous nation, there's no debate that "large" still applies to China.

–MARA HVISTENDAHL

GRAPH SOURCE: NATIONAL BUREAU OF STATISTICS OF CHINA

STEM CELLS

NIH Wins in Appeals Court, But Legal Battle Continues

Stem cell research supporters are elated—but still worried—after an appeals court last week threw out a temporary ban on the use of federal funds for human embryonic stem cell (hESC) research. The case now returns to the trial court, where the outcome is unpredictable. And appeals of the trial court's decision could drag out the legal process for many more months.

Some onlookers hailed the victory for the Obama Administration as the beginning of the end of the case. "This was a very good day for the [hESC] research community. The best chance plaintiffs had was with this [appeals court] panel, and everything from here out is low probability for them," says Stanford University law professor Hank Greely. But others aren't so confident. "This will be a protracted fight," predicts Anthony Mazzaschi of the Association of American Medical Colleges.

The appeals court's 2–1 decision does lift some of the gloom hanging over scientists since U.S. District Judge Royce Lamberth issued a preliminary injunction halting hESC research last August. Lamberth had ruled in favor of James Sherley and Theresa Deisher, scientists who study adult stem cells. They claimed in a 2009 suit that the National Institutes of Health's (NIH's) new guidelines expanding research on hESCs violated the Dickey-Wicker Amendment, a 1996 law barring the use of federal funds for research that destroys embryos. The Lamberth ban held for 17 days, until the U.S. Court of Appeals for the D.C. Circuit blocked the injunction while a three-judge panel deliberated.

In that panel's 21-page majority ruling, written by Judge Douglas Ginsburg, the judges disagree with Lamberth's view that a ban wouldn't seriously harm hESC scientists. The effects "would be certain and substantial," and for those with ongoing grants, "their investments in project planning would be a loss, their expenditures for equipment a waste, and their staffs out of a job," the decision says.

The judges also weighed in on whether the plaintiffs are likely to win the underlying case. The government had argued in part that Dickey-Wicker does not clearly ban research using hESCs because it is written in the present tense: It prohibits funds for "research in which a human embryo or embryos are destroyed," not "for which" embryos "were destroyed." The judges agreed that this wording "strongly suggests" that the statute "does not extend to past actions."

Their bottom line: "We conclude the plaintiffs are unlikely to prevail because Dickey-Wicker is ambiguous and the NIH seems reasonably to have concluded that, although Dickey-Wicker bars funding for the destructive act of deriving an ESC [embryonic stem cell] from an embryo, it does not prohibit funding a research project in which an ESC will be used."

In a dissenting opinion, Judge Karen LeCraft Henderson wrote that "the majority opinion strains mightily to find the ambiguity the Government presses." She calls her colleagues' separation of the derivation of hESCs and research on the cells themselves "linguistic jujitsu."

The split decision has given the plaintiffs some hope that the full appeals court would be willing to rehear the preliminary injunction case, even though such *en banc* hearings are rare, says Samuel Casey of the pro-life Law of Life Project in Washington, D.C., one of the plaintiffs' attorneys. More likely, action will shift to the lower court, where both the plaintiffs and the government have asked Lamberth to rule quickly without a trial.

Because the appeals court found that NIH properly interpreted Dickey-Wicker, "it's much harder now" for Lamberth to rule to the contrary because his decision would likely be overturned by the same appeals court, Greely says. But John Robertson of the University of Texas School of Law in Austin says the appeals decision "will not necessarily have any influence on Lamberth." Casey also notes that neither court has yet ruled on two other arguments made by the plaintiffs: that the NIH guidelines violate Dickey-Wicker because they give scientists an incentive to destroy embryos, and that NIH didn't follow proper procedures when it developed the guidelines.

Lamberth could rule at any time, but he might first give both sides 30 days to file briefs responding to the appeals court ruling, Casey says. He thinks a written opinion from Lamberth could take up to 6 months. If Lamberth sides with the plaintiffs again and issues a permanent injunction, the appeals court will likely issue another stay while it considers the appeal, onlookers say. Any decision by the appeals court is expected to be appealed to the U.S. Supreme Court.

–JOCELYN KAISER

BIOTECHNOLOGY

EPA Proposal Would Exempt Some GMOs From Registry

Many forest ecologists dream of restoring the once-great American chestnut tree to the Appalachian range. For decades, researchers have been trying to transfer the natural blight-resistance genes of the closely related Chinese chestnut by crossbreeding the two trees, with varying degrees of success. If the Chinese chestnut's resistance genes were known—and forest geneticist Charles Maynard at the State University of New York (SUNY) in Syracuse says his group is close to identifying a few—using existing transgenic techniques to transfer them directly into the American variety would be a welcome shortcut.

But this high-tech solution would come with considerable drawbacks. Even though the new and improved chestnut would not contain any DNA that it couldn't have acquired naturally through conventional breeding, its chestnuts would be considered a transgenic crop. That means anyone who wanted to plant it outside would have to jump through costly and time-consuming hoops to satisfy regulatory agencies' concerns about safety.

Definitions of Key Terms

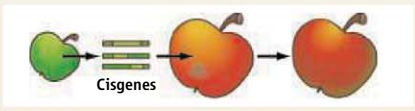

Cisgenics. Genetic modification of a recipient plant with a gene from a sexually compatible species.

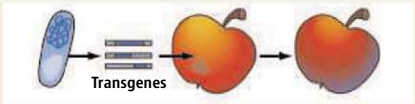

Transgenics. Genetic modification of a recipient plant with one or more genes from a sexually incompatible plant or other organism.

Traditional breeding. Conventional crossbreeding.

The time is ripe, some researchers are arguing, for a distinction here. They propose that plants dubbed "cisgenic," that is, containing only genetic material from sexually compatible species, be exempted from the scrutiny and safety tests that agencies currently demand for transgenic plants on a case-by-case basis. In March, the U.S. Environmental Protection Agency opened a request for comments on a draft rule that would exempt cisgenic organisms from the requirement to be registered with EPA before being field-tested or marketed. The comment period closed 15 April.

Opinions in the comments ran hot, echoing a 2006 controversy in which Dutch researchers proposed regulatory exemption in Europe for cisgenic plants in the journal *EMBO reports*. There is nothing intrinsically dangerous about such plants, the authors argued, despite their provenance in a biotech lab. They and other proponents of this new classification, like forest biotechnologist Steven Strauss of Oregon State University, Corvallis, point out that during traditional breeding, plants swap huge chunks of DNA, and a breeder doesn't know what other genes might be transferred along with the gene of interest. Similarly, classical mutagenesis methods, which involve treating pollen with radiation or chemicals and then screening for desirable mutants, are unregulated. By contrast, moving a specific gene or gene using biotech methods—say, injecting the new DNA directly into plants' germ cells—would let researchers track precisely what is being transferred. There's no scientific reason to think moving just one piece of DNA might be a problem, says biologist Wayne Parrott of the University of Georgia in Athens, "but if you chop a chromosome up by blasting a cell with radiation, that's not going to be a problem."

But the proposal has angered scientists on both sides of the broader debate about genetically modified organisms (GMOs). Cell biologist David Schubert of the Salk Institute for Biological Studies in San Diego, California, who believes that GMOs deserve more regulation, calls cisgenics "semantics and illusions to scam the public into thinking they are eating a 'natural' product."

Some biotech allies who would like to see less regulation of GM crops scorn the idea for different reasons. Giving cisgenics special treatment would unfairly impugn the safety of transgenics, says population geneticist and independent biotech consultant L. Val Giddings, adding that the process by which DNA is manipulated in a plant tells one nothing about the potential hazard of the resulting product.

SUNY molecular biologist William Powell, who works with Maynard on the American Chestnut Research and Restoration Project, said in an e-mail that he thinks EPA's proposed rule is "a step in the right direction." But he cautions that a host of technical issues must be resolved before cisgenic plants would be ready for prime time. No cisgenic plants have yet been presented for EPA scrutiny.

Family tree. Researchers hope that deregulating cisgenic techniques will help speed development of a blight-resistant American chestnut tree.

At the University of California, Davis, plant biologist Charles Gasser is working on another genetic modification approach that may also be considered under EPA's proposed rule: improving plants by tweaking their own genes instead of introducing foreign genes. Strauss calls such an approach "intragenic." In a March paper in the *Proceedings of the National Academy of Sciences*, Gasser and colleagues described a gene called *INO* that, when disrupted in natural mutants, causes Spanish sugar apples to be seedless. *INO* is the first known gene for seeds and is likely present in popular fruits such as regular apples and avocados, Gasser says. In addition to conventional crossing experiments, his group is testing whether gene targeting approaches could be used to delete the gene in these other fruits, leaving no foreign DNA behind.

Getting any cisgenic or intragenic crop to market would require their approval by the U.S. Department of Agriculture (USDA): EPA steps in only if a GM plant has genes that act as pesticides. Researchers would likely want approval from the Food and Drug Administration (FDA) as well to lessen their susceptibility to lawsuits. Strauss says EPA tends to be the strictest regulator: If EPA exempts cisgenics from registration, USDA and FDA may follow suit. But the legal issues will take some work. Freeing such plants from registration would complicate USDA's job when exporting them to countries with GM labeling laws. The next step is for EPA to present a final proposed rule for entry in the *Federal Register*.

–SARA REARDON

CREDITS (LEFT TO RIGHT): ADAPTED FROM H. J. SCHOUTEN *ET AL.*, *EMBO REPORTS* **7** (1 AUGUST 2006); COURTESY CHARLES MAYNARD/SUNY

ADDICTION RESEARCH

Anonymous Alcoholic Bankrolls Trial of Controversial Therapy

AMSTERDAM—For 6 years, French cardiologist Olivier Ameisen has tried to persuade addiction researchers to set up a large clinical trial of what he claims is a safe and highly effective cure for alcoholism: high doses of a decades-old muscle relaxant called baclofen.

Ameisen's main argument: his own case. There was a time when he could down a bottle of Scotch a day and, in his bestselling 2008 book *The End of My Addiction*, the cardiologist describes how baclofen broke that habit and saved his life.

Now, Ameisen may finally get the study he wants. As a gesture of thanks to Ameisen, a Dutch donor has given the University of Amsterdam half-a-million euros to conduct a rigorous placebo-controlled study of the drug, to be led by psychopathologist and addiction researcher Reinout Wiers. The philanthropist's name is being kept secret, but Ameisen, who met him at a lecture, says the man was a "hopeless alcoholic" until he gave his physician a copy of Ameisen's book and received baclofen.

The study could help settle what Markus Heilig, clinical director of the National Institute on Alcohol Abuse and Alcoholism, calls a "controversy in a low-key way." Ameisen's advocacy for baclofen—which mimics the action of a neurotransmitter called gamma-aminobutyric acid (GABA) in the brain—has generated a lot of publicity, and increasing numbers of alcoholics demand a prescription from their doctors. But hard evidence for its efficacy has been lacking. A handful of trials have generated conflicting evidence; all were small and used much lower doses of baclofen than Ameisen recommends. The anonymous gift is a "fantastic opportunity," says alcoholism researcher Giovanni Addolorato of Catholic University of Rome.

A successful cardiologist working in Manhattan, Ameisen saw his life and career coming apart in the 1990s, when his binges frequently landed him in the emergency room. Highly motivated to kick his habit, he tried all sorts of treatments, attended thousands of Alcoholics Anonymous meetings, and checked into rehab centers. Yet he always relapsed. Then he read a story about baclofen, a drug that in animal models of alcoholism appeared to suppress craving. He devised a study protocol in which he took escalating doses of baclofen. At 270 milligrams a day, he wrote in a rare first-person case study published in a 2005 issue of *Alcohol and Alcoholism*, "I experienced no craving or desire for alcohol for the first time in my alcoholic life." He still takes lower doses of baclofen daily to keep his anxiety in check and hasn't taken a drink since 2003.

Scientists believe that GABA may play a role in addiction, and another drug candidate for alcoholism, topiramate, also targets the GABA receptor (*Science*, 11 April 2008, p. 168). The anecdotal stories about miraculous recoveries with baclofen extend beyond addiction to alcohol to people with cocaine and other drug problems. The few randomized controlled trials—the gold standard in medicine—have shown mixed results, however.

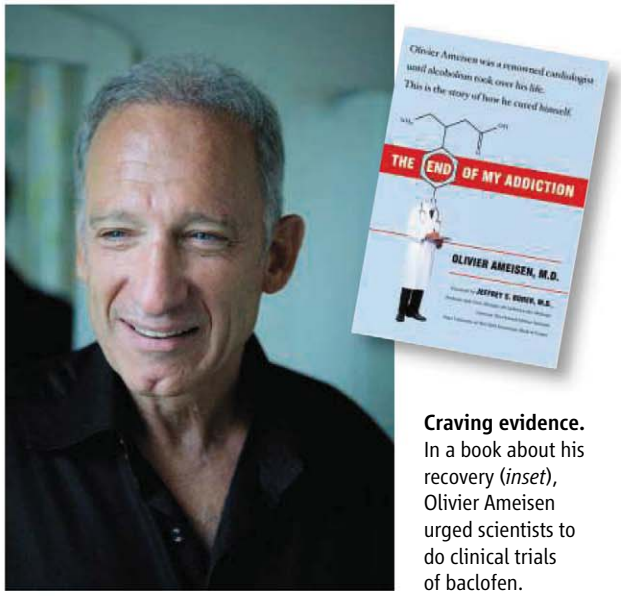

Craving evidence. In a book about his recovery (*inset*), Olivier Ameisen urged scientists to do clinical trials of baclofen.

In a study among 84 heavy drinkers with liver damage, published in *The Lancet* in 2007, Addolorato showed that 30 milligrams of baclofen a day helped 71% abstain from drinking, versus 29% of those on placebo. But in a 2010 study of the same dose among 80 diagnosed alcoholics by James Garbutt of the University of North Carolina, Chapel Hill, baclofen did not outperform placebos.

Ameisen says dosing is crucial. Another study by Addolorato's group published in April showed that alcoholics who take 60 milligrams of baclofen do better, suggesting that 30 milligrams is below the optimal dose. Ameisen says both 30 and 60 milligrams are "ridiculously low:" Neurologists who use the muscle relaxant to treat spasms have long treated patients with up to 300 milligrams daily without serious side effects except sleepiness, he says.

But other scientists say it's prudent to be careful with a drug whose side effects have not been studied systematically. The U.S. Food and Drug Administration's limit for treating spasticity is 80 milligrams. The Amsterdam study now on the drawing board will escalate the dose while carefully monitoring patients, Wiers says; the researchers might put the study's ceiling at 150 or 200 milligrams. Others say that's quite high. Garbutt has proposed a new trial that would go up to 90 milligrams a day, which is "already pretty aggressive," he says. Addolorato says he would not go beyond 100 milligrams.

Ameisen is frustrated with the slow pace of research, but his zeal to convince the world is rubbing some the wrong way. "When people know all the answers before having the data, it's usually not worth listening to," Heilig says. Nor has Ameisen's treatment of skeptics—in interviews with *Science*, he described several scientists as "stupid"—made the cardiologist any friends. An adviser to the Amsterdam study, Ameisen says he's already disappointed in the communication with Wiers's team. That may be because he often fires off multiple long e-mails per day, Wiers counters.

Yet even those who are skeptical about baclofen, such as Heilig, applaud the new study because it may help bring doctors and patients some answers. The study will aim to enroll at least 200 diagnosed alcoholics, Wiers says, and will also aim to find out whether the drug is most effective in people also suffering from anxiety disorders, as some studies suggest. Functional magnetic resonance imaging will help establish whether the drug affects brain circuits involved in anxiety.

Wiers is "a highly respected investigator in the field of alcohol dependence," says Lorenzo Leggio of Brown University's Center for Alcohol and Addiction Studies. "I am sure it will be a very good study."

–MARTIN ENSERINK

CREDITS (LEFT TO RIGHT): ©FRANCK FERVILLE; COURTESY FARRAR, STRAUS AND GIROUX

Red in Tooth and Claw Among the Literati

Upset by the isolation of their field, some critics are trying to bring Darwin's ideas and recent science to the study of literature. They haven't been popular

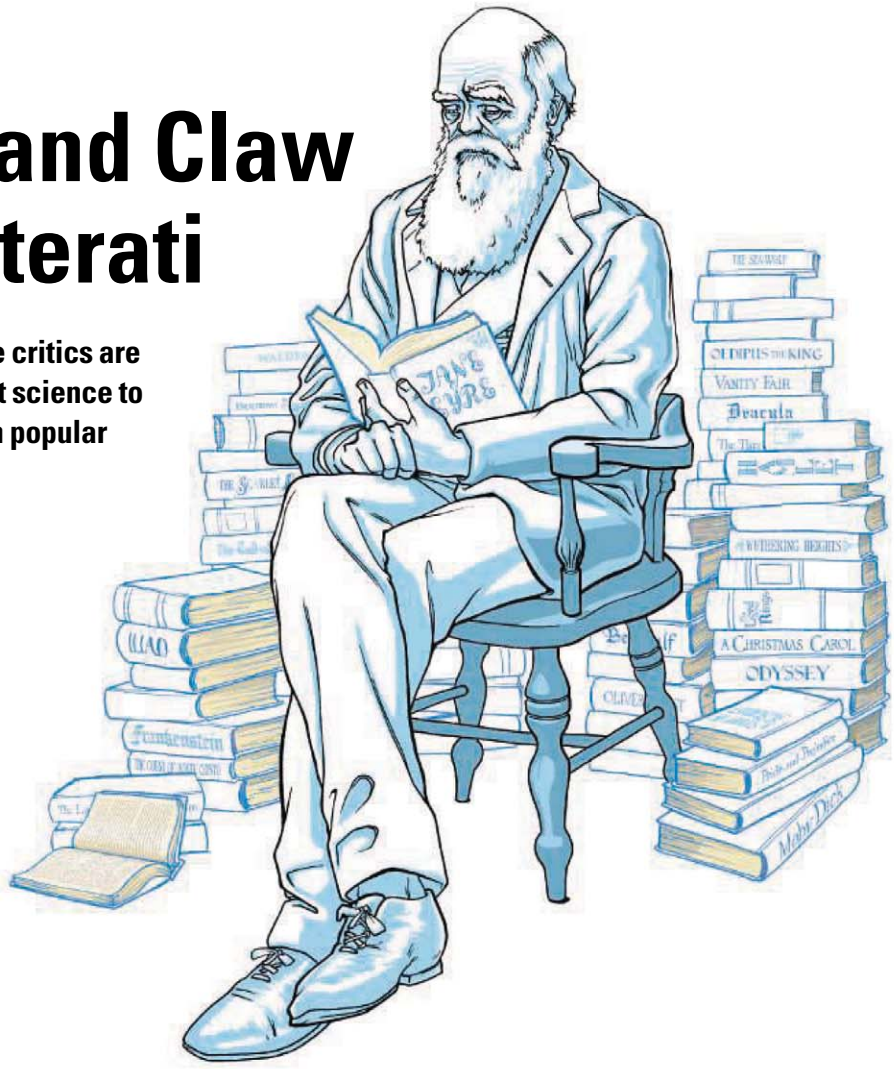

IN THE EARLY 1990s JOSEPH CARROLL, AN English professor at the University of Missouri, St. Louis, presented a paper on the possibility of studying literature through the lens of Darwinian evolution. Not long afterward, he heard from a colleague that the paper had generated lots of discussion, though not for the most flattering reason. "People didn't think that anyone in literary studies cared about such things," Carroll recalls. "There was an argument over whether it was a hoax."

Carroll was indeed serious. For 2 decades prior, Freudianism, Marxism, poststructuralism, postcolonialism, and other fashionable "isms" had dominated the academic study of literature. These schools dismissed the idea that evolutionary pressures have shaped human nature, attributing all human nature to culture instead. Frustrated by this thinking, which he has grumbled is "unable to contribute in any useful way to the serious world of adult knowledge," Carroll rebelled. In 1994, he helped found a new field by publishing his self-described "big, baggy monster," *Evolution and Literary Theory*, a 536-page book promoting an approach to literature based on evolution science.

Carroll wasn't alone in his despondency. Other literary scholars have described their field as "a backwater" and "embarrassingly out of step" with science. Following Carroll, some began incorporating neuroscience, cognitive science, anthropology, and—most prominently and controversially—evolutionary psychology into their work.

Some of that work reads like traditional, pre-1970s English scholarship: discussions of tone, style, context, and theme. But it also explores how evolution might have shaped aspects of literature. On a deeper level, writers investigate the potential adaptive benefits of storytelling for our Pleistocene ancestors and the mystery of why humans spend so much time immersed in it. (By one measure, we spend 4 hours per day consuming, discussing, and creating stories, and 4 minutes per day having sex.)

Most scientific lit scholars incorporate at least some evolution into their work because evolution provides a framework for understanding human behavior. And many focus on evolutionary psychology because it explores the origins of mental phenomena, including narratives and aesthetics, and can bridge evolutionary biology and the humanities. Some recent evopsychology also emphasizes the plasticity of the human mind, which helps explain how universal human behaviors (such as storytelling) can exist but can nevertheless be expressed in different ways in different cultures.

Online
sciencemag.org
Podcast interview with author Sam Kean.

Straddling multiple fields, this analysis has earned a mixed response. Carroll says most scientists encourage his work: Supporters include evolutionary psychologist Steven Pinker and biologist Edward O. Wilson of Harvard University and biologist David Sloan Wilson of Binghamton University in New York state. In contrast, applying evolutionary thought to the human mind has never been popular in the humanities, and scientific lit crit has met with bemusement and occasional hostility. (Three scholars who used scientific ideas in their analyses were denounced as "protofascists" at a prominent academic meeting for literary scholars in the 1990s by a critic who admitted he hadn't read their work.)

But since 2007, the number of books and articles incorporating Darwinian and other scientific thought into literary studies has more than doubled, Carroll says. Carroll himself released a new book in March, *Reading Human Nature*, which summarizes the accomplishments of evolutionary criticism and anticipates where it might be headed. It's not a unified field; some of its members in fact distance themselves from Carroll. But these scholars are united in one sense: They're convinced not only that evolution-

CREDIT: M.TWOMBLY/*SCIENCE*

ary thought can improve literary research but also that literature can teach scientists a thing or two about human evolution.

Out with Freud, in with Darwin

Humanities scholars have criticized scientific lit crit as too general or too reductive to say anything meaningful about individual works. Pinker makes a similar argument, saying that although the approach may help us identify how our craving for fiction evolved, he's not convinced it will enrich our understanding of specific texts.

In his new book, Carroll contests these claims, saying that science can offer insight into even the most pored-over works in the canon. In a chapter devoted to *Hamlet*, he explores the neuroscience of depression, among other topics. Carroll also cites the work of Michelle Scalise Sugiyama, a cognitive scientist at the University of Oregon, Eugene, who reinterpreted the Oedipus tragedies. Standard commentary has been dominated by Freudian theories about people's repressed desires to have sex with their parents, but she argues that, in light of widespread anthropological evidence of cultural taboos against incest, that reading simply isn't tenable.

Another examination of the classics is *The Rape of Troy* by Jonathan Gottschall, an English professor at Washington and Jefferson College in Washington, Pennsylvania, who completed his Ph.D. thesis under the aegis of David Sloan Wilson. The book examines *The Iliad* and *The Odyssey* and employs anthropological work on warfare and evolutionary work on polygyny to show, Gottschall argues, that "patterns of violence in Homeric society are tantalizingly consistent with … acute shortages of available young women relative to young men." In this reading, whatever reasons the Greek mythic heroes invoked for waging war—status, money, honor—they were fundamentally fighting for marriages and their evolutionary legacy.

Gottschall has also looked outside the Western canon, by studying hundreds of ancient fairy tales worldwide. Although the tales differed in some ways, Gottschall concluded that the same basic underlying characters—handsome young males, pretty maidens, and shrewish older women—appear pervasively in all cultures. This counters, he says, the popular feminist argument that such stereotypes appear only in the fairy tales of Western societies and merely reinforce Western patriarchy.

Carroll and Gottschall have examined more modern fiction as well. In a paper they wrote with psychologists John A. Johnson and Daniel Kruger, they asked hundreds of literary experts to rate their attitudes toward antagonists and protagonists in 201 Victorian novels and then tabulated the numbers. They found that experts rated antagonists as overtly dominant and selfish, whereas protagonists displayed altruistic and selfless behavior. In one sense this is trivial: Good guys are good, bad guys bad. But the authors argue that experts overwhelmingly perceived consistent "prosocial" behavior among characters that people root for.

Carroll and his colleagues then drew on anthropological research to argue why this behavior appeals. In our fraught hunter-gatherer days, when humans roamed about in small bands, people had to sacrifice selfish interests and work together, or they'd perish. In contrast, self-aggrandizing or dominant behavior threatened group survival. Victorian novels, in this view, merely dress up these ancient, evolved preferences in crinolines and top hats.

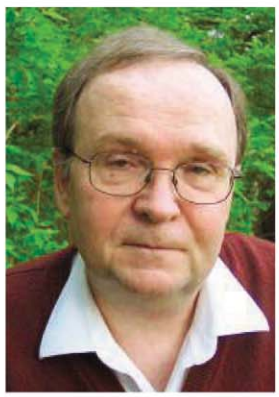

Most humanities scholarship today is "unable to contribute in any useful way to the serious world of adult knowledge."

—JOSEPH CARROLL, UNIVERSITY OF MISSOURI, ST. LOUIS

If fiction does reinforce cooperative and egalitarian behavior, and if that behavior did ensure the survival of hunter-gatherers, then perhaps the ability to create and understand literature gave our ancestors a survival advantage; it is what evolutionary scientists call adaptive. It's an appealing theory—it makes literature essential to life—but it has proved contentious.

First, most scholars distinguish between modern, written literature and more fundamental forms, such as oral stories. And stories can indeed be adaptive in human culture because they work "like a flight simulator" for social life, says Brian Boyd, a Nabokov scholar at the University of Auckland in New Zealand. His 2009 book, *On the Origin of Stories*, examines works as diverse as *Horton Hears a Who!* and *The Iliad*. Boyd argues that animals often chase, frisk, and playfight, and in a similar way, humans "refine their most important cognitive skills through art." In fiction, "we learn to understand events and shift perspectives at a faster clip than usual, to enjoy simulations of a wide range of social situations, and to generate a wider range of options."

Storytelling could also have an evolutionary benefit by bringing societies, especially oral societies, closer together and fostering cohesion. Ellen Dissanayake, a professor of music at the University of Washington, Seattle, has argued that all the arts generally fulfill this purpose and are therefore adaptive.

Evolutionary biologist Geoffrey Miller of the University of New Mexico, Albuquerque, has argued instead that literature and other arts arose through sexual selection. In brief, in his view, a talent for storytelling provided evidence of a big brain and language skills, which make someone a more attractive mate. Literature was our peacock tail.

Boyd sees some truth in both the social-cohesion and sexual-selection models, though he's less keen on the latter. Sexual selection usually results in divergent behavior between the sexes, and both males and females (despite some differences in taste) indulge just as readily in fiction. Boyd calls sexual selection "another gear, but not the engine" that drove the evolution of storytelling.

Although receptive to the idea, Boyd and other scholars don't necessarily believe that literature itself (in contrast to simple storytelling) is adaptive. Their case is subtle.

William Flesch, a professor of comparative literature at Brandeis University in Waltham, Massachusetts, distances himself from "literary Darwinists" like Carroll. But the finding that self-aggrandizers are villains in Victorian fiction meshes with Flesch's own work on evolutionary game theory and literature, in which rogues are generally punished. Game theory (the prisoner's dilemma is the classic scenario) explores how people cooperate with or screw each other over in various situations, and how they respond to later interactions with the same people. Flesch focuses on "altruistic punishment": situations in which bystanders will punish a rogue, even if the rogue never hurt them personally.

"There has to be a reward for altruistic punishment," Flesch says; otherwise human cooperation can't evolve. And he argues that the ability to grasp narratives and keep track of people's reputations probably helped

to distribute punishments and rewards and therefore proved adaptive. What's more, if there were conflicting interests among people, he says, those who crafted persuasive narratives—perhaps by fictionalizing them—would have gained advantages as well. But even if certain components of literature are adaptive, Flesch says, it doesn't follow that the ability to create or understand literature itself—the full, flowery, emotionally charged production—is adaptive. Flesch instead calls literature a mental spandrel, an epiphenomenon of various evolved traits that happen to work well together.

This resembles the "cheesecake" analogy put forth by Pinker in *How the Mind Works*. Evolution gave us cravings for the concentrated calories in fats and sugars, and cheesecake happens to deliver fats and sugars in concentrated doses. Similarly, we might crave ingredients of literature for sound evolutionary reasons, and novels might simply mainline those components to our minds. Pornography is another example.

Still, arguments like that haven't dissuaded some literary Darwinists. Carroll still believes literature (or at least its oral predecessors) had adaptive value. So does Gottschall, although he admits he lacks sufficient data to prove this: "Right now all I can do is tell a just-so story." But instead of arguing, he wants to import methods from the sciences to frame this hypothesis and test it. "We need help from experimentalists," he says, "expertise beyond what most of us [literary scholars] have."

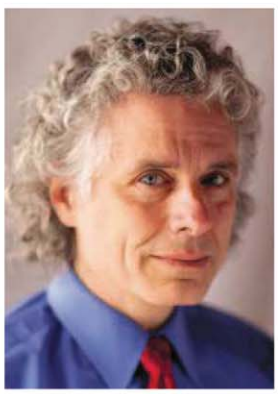

"Evolutionary psychology has concentrated on lurid and fraught aspects of human nature … all the juicy stuff that dominates people's lives" and makes for lively fiction.

—STEVEN PINKER, HARVARD UNIVERSITY

What science can learn

Pinker has criticized Darwinian lit crit for focusing so heavily on evolutionary psychology and neglecting general psychology, linguistics, and other disciplines. But he says the focus makes sense. "Evolutionary psychology has concentrated on lurid and fraught aspects of human nature," he says, including sex, beauty, jealousy, dominance, status—"all the juicy stuff that dominates people's lives" and makes for lively fiction.

But evolutionary literary scholars have criticized evolutionary psychology as well—especially what they call "narrow" or "orthodox" evolutionary psychology. In fact, they feel their work can bend back and improve evolutionary psychology's understanding of the human mind.

Carroll and Gottschall point out that textbooks of evolutionary psychology often omit art and other aspects of imagination. "Survival, mating, parenting, kin networks, and adaptations for social interactions within groups—[those books] think that that pretty much covers it" for human nature, Carroll says. "What they're missing is that art, religion, and ideology regulate and direct behavior," he adds. "Those imaginative features regulate people's birthing systems and kinship networks, or whether they practice polygamy or monogamy." Without those nuances, "you're just missing the subject, you're not talking about human beings."

Blakey Vermeule, a professor of English at Stanford University in Palo Alto, California, approaches literature more from a cognitive science than an evolutionary perspective, but she argues that literature can still illuminate how the mind evolved. For instance, we impose narrative patterns on the world, which reveals how our minds work. Children and Alzheimer's victims both tend to find deep, ultimate causes in random events: They tend to say things like, "Clouds are really 'for' raining." Stories offer an entry point for understanding how these narrative tendencies emerge, Vermeule says: "Literature is a massive database people can look at and figure out what questions to ask" about human cognition.

Literary criticism might even inform biology generally by showing how the mind can open up new avenues for evolution. For example, Flesch says studying literature might help explain how altruistic behavior can develop among nonkin. "The emotions that good stories are particularly effective at eliciting, outrage and indignation" over unfair treatment, he says, are exactly the responses that lead to altruistic punishment and cooperation.

Still, although literature might illustrate the roots of cooperation, many literary scholars themselves remain wary of cooperating with evolutionary literary critics. A few months ago, *Critical Inquiry*, a leading journal for literary theory, published a 33-page article with the blunt title "Against Literary Darwinism." And although Carroll and Gottschall have a book-length manuscript on their Victorian novels study (titled *Graphing Jane Austen*), they've had difficulty finding a publisher.

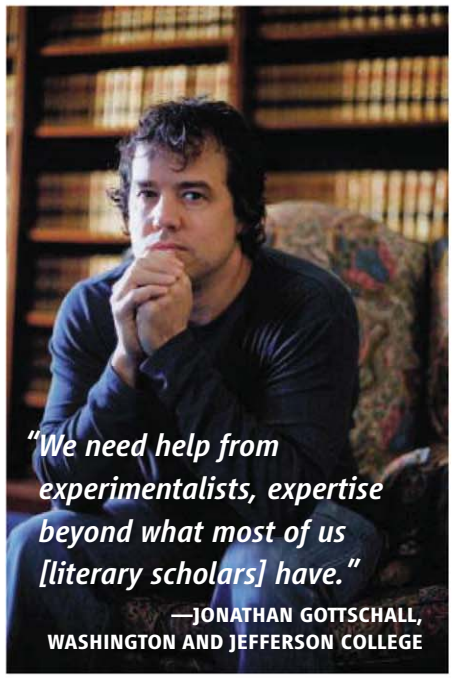

"We need help from experimentalists, expertise beyond what most of us [literary scholars] have."

—JONATHAN GOTTSCHALL, WASHINGTON AND JEFFERSON COLLEGE

Gottschall says the resistance to Darwinian lit crit among literary scholars reminds him of resistance among religious groups to evolution itself. "There's the fear that if you were able to explain the arts and their power scientifically, you'd explain them away," he says. "Humanities are the last bastion of magic."

Yet ideas have emerged recently that might help reconcile the divergent worldviews of scientific and traditional literary studies. Edward O. Wilson and others now argue that human beings might have evolved not only specific mental skills—like language—but also a general tendency for mental flexibility. Our minds, in other words, evolved to be plastic. Carroll and others have taken up the idea and argue that literature has adaptive value precisely because it promotes and enhances this plasticity.

If that's true, the notion may someday provide a bridge between the two cultures. "I try to stress that evolution has shaped human minds to be reshapable more than other minds," Boyd says. "It's really not so far from things said for a long time in some areas of the humanities."

–SAM KEAN

CREDITS (TOP TO BOTTOM): ROSS MANTLE; REBECCA GOLDSTEIN

PROFILE: JIN HUIQING

Car-Crash Epidemiologist Pushes Systemic Attack on Bad Driving

China, burdened with traffic casualties, is trying a "three-line defense"

JINAN, CHINA—As he mulled over topics for a master's dissertation in the mid-1980s, Jin Huiqing made a fateful decision. He had studied medicine at Anhui Medical College in Hefei and saw in graphic detail how car crashes can wreck lives. It dawned on Jin that insights into why some drivers are accident-prone could have a huge impact on society. He floated the idea past his thesis adviser, who tried to dissuade him from the seemingly quixotic quest. "He told me that I may not be able to finish the degree. No one supported me," Jin says.

Jin proved his professor wrong and went on to pioneer a new field in China: traffic-accident epidemiology. A quarter-century later, the fruits of that research are ripening. Based on Jin's findings, the U.N. Global Compact Cities Programme in 2006 anointed Jinan, capital of Shandong Province, a traffic safety pilot city. The $70 million project is due for a 5-year review, and the statistics are tilting in favor of its chief scientist and mastermind: On Jinan's roads, the rates of traffic accidents and fatalities have declined steadily. "Jin's ideas have had a powerful effect in Jinan," says Frederick Dubee, a former auto-industry captain and executive director of the MBA Center and Global Management Education Institute at Shanghai University. Experts have called for extending the safety program to other cities.

Jin has a track record of venturing into uncharted territory—and beating the odds. At his base in Hefei, capital of Anhui Province, Jin in 1990 opened the Sanlian Accident Prevention Institute, one of the earliest private R&D centers in China. He expanded his road-safety empire 9 years later when he founded Anhui Sanlian College, which launched the country's first degree program on traffic-accident prevention. "It's a rare example of a good private college in China," says Zhu Qingshi, former president of Hefei's University of Science and Technology of China.

More daringly, Jin, 54, is now fishing for genes associated with accident-prone behavior. At his disposal is a unique resource that he has amassed: thousands of blood samples and psychological profiles of safe and accident-prone Chinese drivers.

After being banished to the countryside during the Cultural Revolution, Jin enrolled at Anhui Medical University in the late 1970s and began thinking about how to reduce the incidence of noncommunicable diseases. "I thought, 'Why not view traffic accidents as a disease,' " he says. Car crashes are a major cause of preventable deaths. Worldwide each year, approximately 1.2 million people die and 50 million are injured on the roads. China has more casualties than any other country.

At the time, Jin says, China's public security bureaus "were unwilling to disclose data about traffic accidents." And academics were not inclined to pursue such data. "No one cared about the human factors of accidents," Jin says. He persisted and befriended several security commanders. From data on 17,124 registered drivers, Jin gleaned that 6% to 8% were repeat offenders, causing around 40% of crashes involving more than one car. Compared with safe drivers, he found that levels of two neurotransmitters—dopamine and serotonin—were significantly lower in accident-prone drivers, defined as those causing three accidents or more within 5 years. In a case-control study, Jin found that they scored much worse than safe drivers on a battery of tests measuring everything from depth perception and night vision to attitude toward risk taking.

These findings led Jin to develop what he calls "Three Lines of Defense" against traffic accidents: using written tests and physical exams of, for example, visual acuity and mental alertness, to screen truck drivers and other professional drivers for accident-proneness; using simulators and other methods to train drivers and correct poor driving habits; and installing cameras to monitor dangerous intersections and road conditions for driver behavior and road safety. "Three Lines of Defense is a powerful concept. It looks at accident prevention in a holistic way," says Dubee, a 35-year veteran of the auto industry who ran Porsche's operations in Canada. Jin has collaborated with scientists at the University of Kansas, and in 2005 he was a visiting scholar at Harvard University.

At the Traffic Command Center here in Jinan, the third of Jin's three defense lines occupies an entire wall of a two-story room, displaying video feeds from intersections and computers alongside a map of the city's road network lit to indicate traffic flow. Traffic police carry GPS receivers so the officer nearest an accident scene can be dispatched without delay. Jinan may be the safest place in China to hit the road. Even as the number of private cars in the city rose from 929,000 in 2006 to more than 1.2 million in 2010, the death toll from traffic accidents in that period fell from 343 to 263. Although Jinan averages more than 100 traffic accidents each day, it is the only major Chinese city that hasn't had a single traffic accident in the past 5 years with more than one fatality, says Lu Dehe, commander of the Jinan Municipal Traffic Police Department, who credits Jin's methodology for making Jinan safer.

Jin is now writing a second dissertation, on Daoism, for a Ph.D. in philosophy. And his latest accident-prevention research is more exploratory. In a genomewide association study, he has found tentative links between three genes and accident-prone driving. The preliminary work is "very interesting," says Yang Huanming, director of BGI, China's genomics institute in Shenzhen, who notes that unraveling susceptibility to behaviors is fraught with challenges. Genetic studies "will offer a solution to the mystery of why some drivers are accident-prone," predicts Jin, clearly relishing the possibility of blazing another new trail. **–RICHARD STONE**

"I thought, 'Why not view traffic accidents as a disease.' " **—JIN HUIQING**

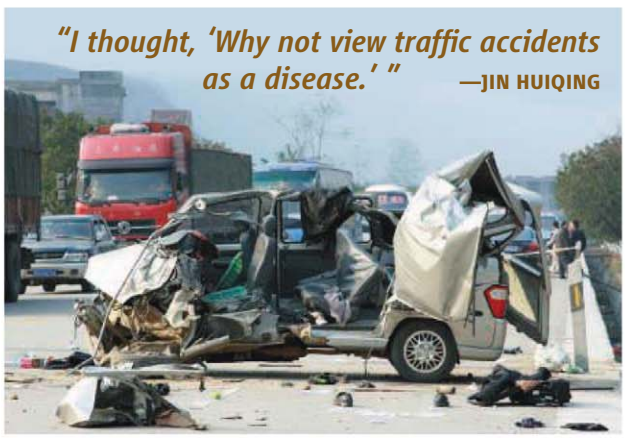

CREDITS (LEFT TO RIGHT): MO XIANTAO/XINHUA/LANDOV; COURTESY OF JIN HUIQING

Double daters. Zenobia Jacobs and Richard Roberts work together.

PROFILE: ZENOBIA JACOBS AND RICHARD ROBERTS

Dating Duo Illuminates Modern Humans' Journey

By improving a powerful dating technique, a professional and personal couple fills in the blanks of human evolution

WOLLONGONG, AUSTRALIA—When University of Pennsylvania archaeologist Harold Dibble was reopening excavations at the Grotte des Contrebandiers (Smuggler's Cave) in Morocco a few years ago, he looked for experts to help him figure out when prehistoric humans had occupied the cave, which is a key site for understanding the spread of *Homo sapiens*. Dibble knew our species had been there more than 50,000 years ago—beyond the practical limit of radiocarbon dating. So he recruited two dating aces from the University of Wollongong in Australia, Zenobia Jacobs and Richard Roberts, experts in the technique of optically stimulated luminescence (OSL) dating. That method determines how long buried sand grains have been hidden from sunlight and can peer back 200,000 or more years in time.

Dibble had never met Roberts and Jacobs, but he invited them to Contrebandiers. In contrast to radiocarbon dating labs that simply process samples taken by others, the pair spent 2 weeks at the site, discussing the stratigraphy and the research questions, and working at night so their samples wouldn't be spoiled by exposure to sunlight. "I was impressed with how totally professional they were," Dibble says. They were so professional that more than a week passed before Dibble spotted Roberts with his arm around Jacobs and realized that they were romantically involved.

Jacobs and Roberts, who married last December—"You can call us the double daters," Roberts says—eventually dated a skull at Contrebandiers to an impressive 100,000 years ago (*Science*, 7 January, p. 20). Today they, and the powerful method they wield (see sidebar), are much in demand to help settle a wide range of questions in archaeology. "[Their] laboratory is widely acknowledged to be the world's premier [OSL dating] facility," says dating expert Thomas Higham of the University of Oxford in the United Kingdom.

Radiocarbon has long been the leading dating method in archaeology, but it requires organic material such as charcoal or bone. And many of today's hottest research questions center on events that took place more

New Light on Ancient Samples

WOLLONGONG, AUSTRALIA—When you walk into the lab run by Zenobia Jacobs and Bert Roberts at the University of Wollongong, you will have a hard time seeing anything at all: The lab is illuminated only by dim red lights. But as your eyes get used to the dark, the shapes of computer-operated instruments fitted with lasers and light detectors come into view, along with large revolving metal plates that carry disks on which tiny sand grains are mounted.

This sophisticated equipment lets Roberts and Jacobs look far back into the past. The pair are pioneers in the technique of optically stimulated luminescence (OSL) dating, a method that measures the time since grains of either quartz or feldspar were exposed to light. The equipment measures the energy of electrons trapped in the grain's crystal lattices. If the lab lights were any brighter, they would prematurely kick out the extra energy of those electrons and spoil the samples.

Roberts and Jacobs's joint lab is in high demand these days (see main text), as is OSL dating itself. The reason? "Unlike any other technique," says dating expert Thomas Higham of the University of Oxford in the United Kingdom, "OSL is able to date the actual sediments in which archaeological materials are found." Radiocarbon dating, which can be used only for samples up to about 50,000 years old, is normally used to date pieces of bone or charcoal, which can move up and down in sediments. Electron spin resonance spectroscopy is used to date teeth, which can also easily shift position in archaeological layers; and uranium series dating, often used to date cave formations, frequently leads to debates over the stratigraphic relationship between those formations and artifacts.

OSL can be used to date the sediments themselves, in caves or now-buried open-air sites, back to at least 200,000 years ago. And a series of OSL dates can reveal whether sediments at a site have been mixed or perturbed. That's crucial for archaeologists, geologists, and paleoecologists—anyone studying ancient worlds, Higham says.

The principle behind OSL dating is fairly simple. The quartz grains serve as natural clocks, because the longer they are buried the more natural radiation they absorb from their surroundings. The energy of this radiation is stored in electrons in the quartz crystals and released again in the form of a detectable light signal when a laser shines on the grains.

OSL dating got its start in the mid-1980s and took some time to become accepted, although by now dating experts have successfully checked its reliability against dates obtained using other techniques. But until the late 1990s, the accuracy of OSL dating was limited by the fact that researchers dated hundreds or thousands of sand grains in one sample. The OSL signal was thus an average of all of those grains, which might not give the same result because of differences in their crystal structures or because they came from archaeological sediments that had been mixed. Then in 1997,

CREDITS (TOP TO BOTTOM): SEAN MAGUIRE/UNIVERSITY OF WOLLONGONG; ISTOCKPHOTO

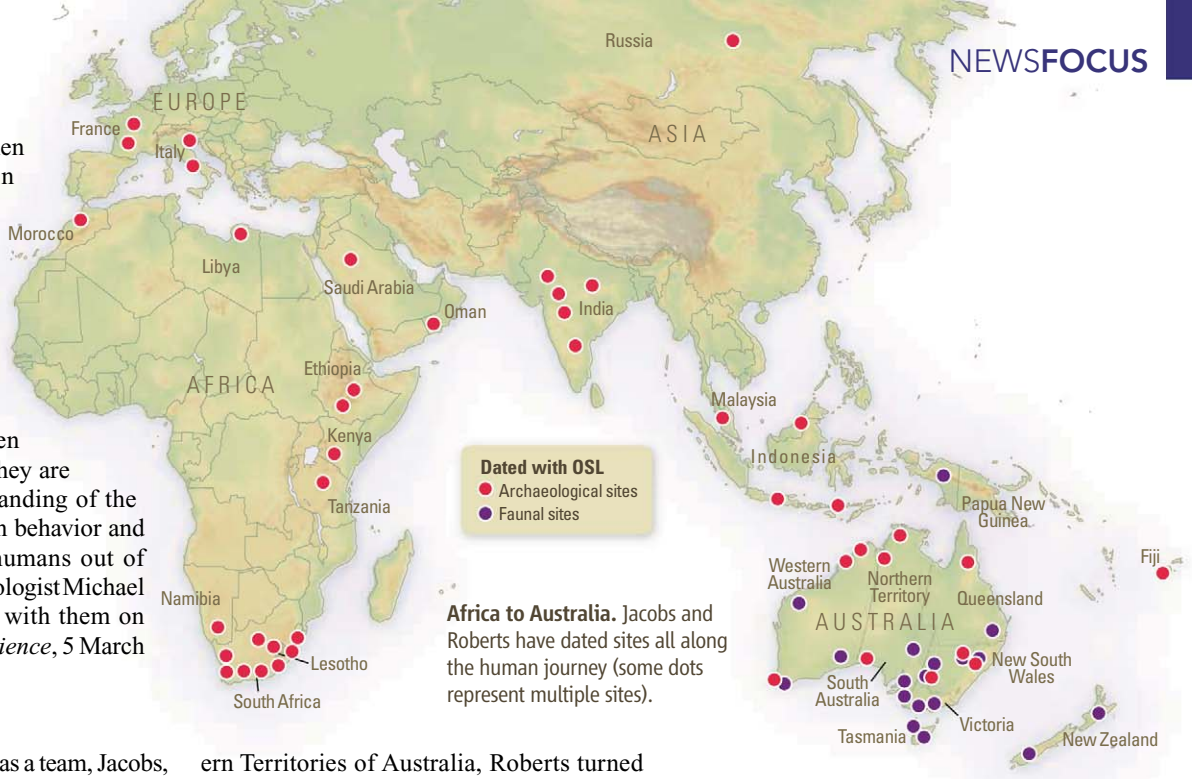

Africa to Australia. Jacobs and Roberts have dated sites all along the human journey (some dots represent multiple sites).

than 50,000 years ago: When did modern humans begin to use symbols? When, and along what routes, did they leave Africa? Jacobs and Roberts are putting time stamps on some of these key events in modern human evolution, whose dates have long been uncertain. In the process, they are "transforming our understanding of the evolution of modern human behavior and the dispersal of modern humans out of Africa," says Oxford archaeologist Michael Petraglia, who is working with them on sites in India and Arabia (*Science*, 5 March 2010, p. 1187).

Coming together

Although the pair now work as a team, Jacobs, 34, and Roberts, 51, come from very different backgrounds and followed divergent career paths. And yet they sometimes ended up at the same place at different times.

Roberts, universally called Bert and known for his sense of humor, is a lanky Englishman who now also has Australian nationality. He grew up in the suburbs of London amid the traces of Roman forts, "surrounded by old things," he says. But before turning to archaeology, he began as a geologist.

While doing his Ph.D. work at the University of Wollongong on the effects of uranium mining on a creek in the Northern Territories of Australia, Roberts turned to thermoluminescence (TL) dating to find out how quickly the landscape near the mine was changing. Buried sediments absorb energy from background radiation until they are exposed to heat or light. TL dating uses heat to release that stored energy, which provides a measure of how long the sediments have been buried. Roberts soon realized that TL could date archaeological sites too old for radiocarbon dating. With colleagues, he roamed across Australia, for the first time applying both TL and the then-new OSL technique—which uses laser light instead of heat to release the stored energy—to ancient human sites. "It was my first introduction to archaeology, and I've never dug my way out of it since," he says.

Roberts began to work to improve the OSL method with Andrew Murray, now director of the Nordic Centre for Luminescence Research in Roskilde, Denmark. Rather than taking the measure of an entire sample and so averaging the grains within it, Roberts and Murray focused on determining when single grains had last been exposed to light.

With the single-grain method, Roberts demonstrated that Australia had first been occupied by modern humans between 45,000

Seeing the light. Wollongong's lab dates single grains of sand.

Roberts and dating expert Andrew Murray, now director of the Nordic Laboratory for Luminescence Dating in Roskilde, Denmark, published the first attempts to date single grains of quartz.

"This was a fundamental contribution," says OSL dating pioneer Ann Wintle of Aberystwyth University in the United Kingdom, "even if in the early days Bert had to mount them by hand, grain by grain, onto metal disks." Today, OSL daters can mount 100 grains onto small aluminum disks, expose them to laser light, and record the resulting signals automatically.

And researchers keep improving the method. Jacobs has developed techniques that allow the pair to reject quartz grains that are not likely to give an accurate age signal; she chooses grains that are easily "bleached" of their stored radiation and thus give the most reproducible results. Higham notes that the single-grain technique not only gives an age for a site but also reveals the degree to which its sediments "are potentially mixed, which in many ways is just as important."

But some dating experts have reservations. Jean-Luc Schwenninger of Oxford praises Roberts and Jacobs as a "formidable team" but says that the single-grain method is best used where sediments are suspected to have been mixed or exposed to light before they could be dated. "A large majority of grains, often more than 95%, are removed from the analyses on the basis of various rejection criteria," Schwenninger notes, adding that the "obsessive search for perfectly behaved grains" might result in "involuntary bias." Schwenninger also says that OSL dating is currently limited by difficulties in determining how much radiation a quartz grain was originally exposed to during a set period of time, a parameter often gathered by directly measuring radiation at sites.

Roberts agrees that single-grain dating is "not a panacea" and adds that "unlike radiocarbon dating, where you send your sample to a lab and pay your money, OSL is not a one-stop shop." Nevertheless, for many researchers studying the past, OSL dating, and particularly the single-grain approach, represents a major step forward.

The method succeeds, says Curtis Marean, director of excavations at 165,000-year-old Pinnacle Point in South Africa, "where so many other techniques fail." **–M.B.**

CREDITS (TOP TO BOTTOM): (SOURCE) R. ROBERTS; SEAN MAGUIRE/UNIVERSITY OF WOLLONGONG

Eppendorf & *Science* Prize for

Neurobiology

Be the 10th winner!

2010 Winner
Christopher Gregg, Ph.D.
Postdoctoral Fellow
Harvard University

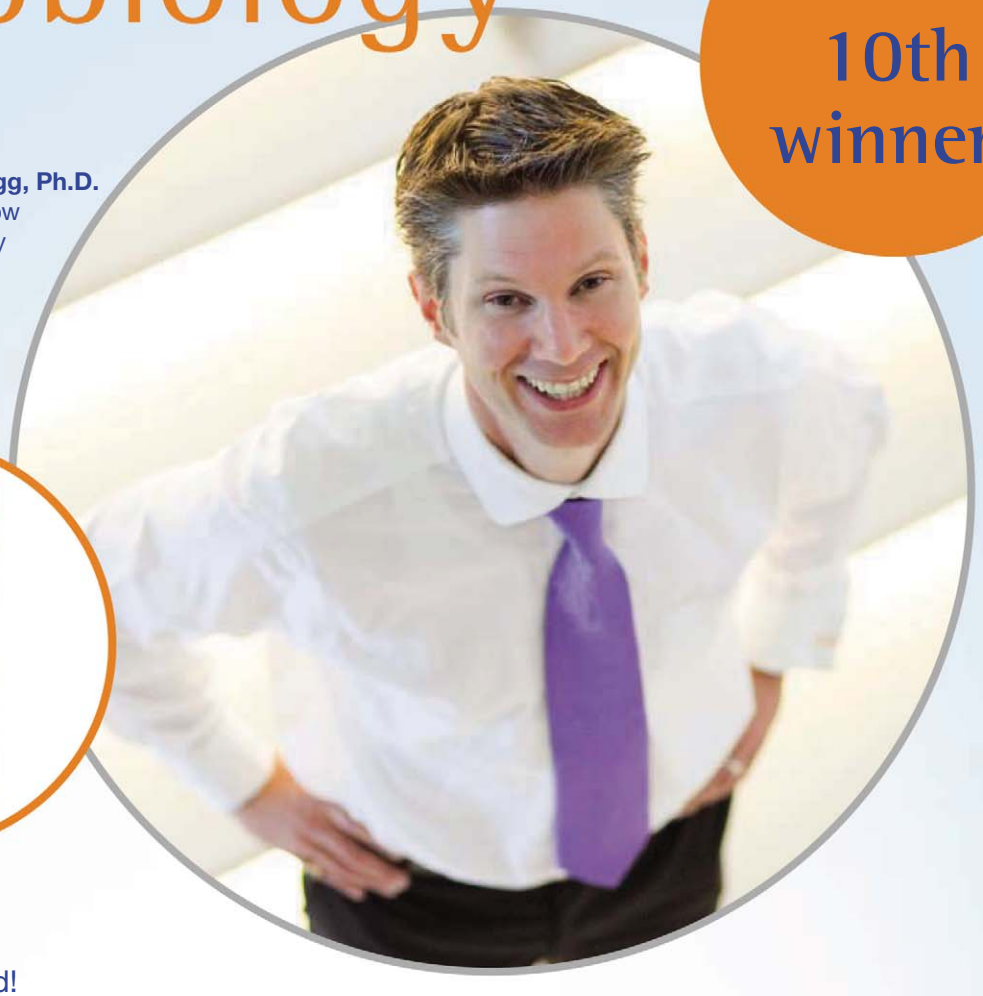

Kurstin Roe Photography

eppendorf & Science PRIZE FOR NEUROBIOLOGY

Get recognized!
US$ 25,000 Prize

Deadline for entries
June 15, 2011

It´s easy to apply! Learn more at
www.eppendorf.com/prize

Congratulations to Dr. Christopher Gregg on winning the 2010 Eppendorf & *Science* Prize for his studies on genes that alter their expression in the brains of offspring according to whether they were inherited from the father versus the mother. His findings suggest new pathways that may help to understand brain diseases such as autism, schizophrenia and eating disorders.

The annual international US$ 25,000 Eppendorf & *Science* Prize for Neurobiology honors young scientists for their outstanding contributions to neurobiological research based on methods of molecular and cell biology. The winner and finalists are selected by a committee of independent scientists, chaired by *Science's* Senior Editor, Dr. Peter Stern.

To be eligible, you must be 35 years of age or younger. If you're selected as this year's winner, you will receive US$ 25,000, have your work published in *Science* and be invited to visit Eppendorf in Hamburg, Germany. Past winners and finalists have come from as far a field as China, Chile, India and New Zealand. Yes, it *can* happen to you!

eppendorf
In touch with life

Science
AAAS

and 50,000 years ago, in contrast to earlier claims of up to 60,000 years ago. These dates, which could not have been achieved using radiocarbon, also suggest that humans were largely responsible for the extinction of Australia's giant birds and supersized kangaroos, which disappeared about 40,000 years ago (*Science*, 22 January 2010, p. 420).

While Roberts was working to improve OSL dating, Jacobs was a student in South Africa just discovering the technique. She grew up speaking Afrikaans, the daughter of a minister in a small mining town in Kruger National Park. As a child, Jacobs says, "life was all about nature." She explored early iron smelting furnaces that dotted the landscape. "That made me quite curious about how old things were and where things came from," she says.

Jacobs, who spoke no English until she spent a year in Australia on an exchange program at age 17, was taught by leading archaeologists and dating experts. She says she "fell in love with archaeology from the first class" in South Africa. As an undergraduate, Jacobs began exploring several methods to date the South African site of Blombos, famed for its ancient beads and etched ochre, possibly the earliest known art. For her Ph.D. work on Blombos and other sites, she teamed up with OSL pioneer Ann Wintle of Aberystwyth University in the United Kingdom, where Roberts had been an undergraduate many years earlier. Jacobs "doesn't suffer fools gladly and has very high standards that she applies to herself and to other people," Wintle says.

Jacobs found herself grappling with a key question in human evolution: when symbolic behavior began. Some researchers had argued that symbolism, such as art and jewelry, made its first appearance in Europe 50,000 years ago or later. But others countered that symbolism had its roots much earlier in Africa. Jacobs used OSL to date the layers containing ochre and beads at Blombos, using both single and multigrain techniques. She found that these apparently symbolic objects were created at least 75,000 years ago (*Science*, 11 January 2002, p. 247), settling the debate for a majority of researchers. Her widely cited study "revolutionized our understanding," says archaeologist Curtis Marean of Arizona State University, Tempe.

Jacobs and Roberts first learned about each other through their research. Roberts had reviewed her papers; she knew him from afar as an OSL dating pioneer. Soon after they finally met, in 2004, Roberts began recruiting her to the University of Wollongong, where he had moved permanently in 2001. In 2006, Jacobs came to Wollongong,

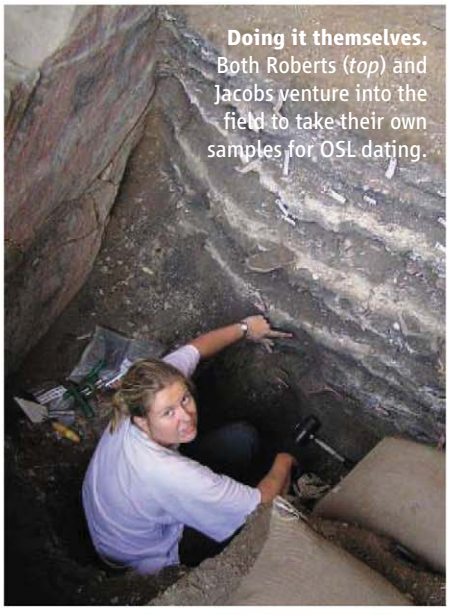

Doing it themselves. Both Roberts (*top*) and Jacobs venture into the field to take their own samples for OSL dating.

and not long afterward the daters began to date. Jacobs and Roberts are each other's "perfect partners," Higham says.

More than technicians

Jacobs and Roberts now work as a close-knit team from their lab in Wollongong. One of them usually does the fieldwork for a given project—Roberts in Australia, India, and Arabia; Jacobs in Africa and Europe—but lab analysis is a fully joint operation. Jacobs has taken the lead in projects designed to improve OSL, for example in decisions about which grains are best for single-grain dating and which should be rejected because they may give erroneous results. She also serves as the lab's manager, leaving her imprint with sternly worded signs at each workstation spelling out the dos and don'ts.

Not content to be dating technicians, the pair is pursuing their own research agenda and often offers to date sites with their own funding. They have received more than $7 million from the Australian Research Council in the past decade. "Right from the research design stage, we had discussions about how new dating results would be integrated into our project," says Petraglia, whose team is tracing human migrations from Africa into southern Asia.

For example, in a key 2008 *Science* paper (31 October 2008, p. 733), the pair pinpointed dates for two innovative stone tool technologies found across southern Africa. Known as the Still Bay and the Howieson's Poort, these advanced toolkits, including tools hafted to spears or arrows, were thought to be associated with symbolic behavior. But researchers weren't sure about how long each lasted, the relationship between them, or why they seemed to give way to less sophisticated stone tools soon afterward.

In a paper Higham calls "hugely important," the pair was able to get very tight time resolution on these tools, showing that modern humans were simultaneously engaging in similar behavior across vast territorial expanses. This work also demonstrated one of the key advantages of single-grain OSL dating. "We can see if things are contemporaneous, or relatively older or younger," Dibble says. "That is just as important as knowing their actual ages."

Jacobs and Roberts showed that the Still Bay was extremely limited in time, between 71,000 and 72,000 years ago, while the Howieson's Port lasted from 60,000 to 65,000 years ago. Thus the technologies did not overlap, and their appearances were not correlated with climate change, as some had thought. "OSL is key to our understanding of behavior" in this critical period, says archaeologist Lyn Wadley of the University of the Witwatersrand, Johannesburg, in South Africa. "Previously, we didn't even know whether the Still Bay definitely came before the Howieson's Poort."

Roberts and Jacobs's work so far has focused mostly on Africa, Asia, and Australia, but they have more plans for Europe, where limited OSL dating has been done. Working beyond radiocarbon's limits, the pair will use the single-grain technique at both Neandertal and modern human sites in an attempt to pinpoint when sophisticated behaviors arose in each group. "They will get a resolution that otherwise would not be possible," Dibble says.

Says Petraglia: "I feel fortunate to be associated with them. … Luminescence dating has the potential to transform our understanding of human evolution in these places, and Bert and Zenobia are at center stage in this work."

–MICHAEL BALTER

LETTERS

edited by Jennifer Sills

An Unexpected Spotlight

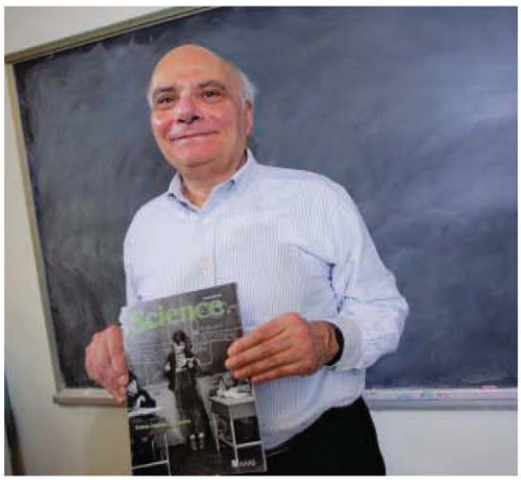

ON 22 MARCH 1948, *LIFE* MAGAZINE RAN AN ARTICLE titled "Genius school," about Hunter College Elementary School, then the only special elementary school in New York City for "gifted" children. Accompanying the article was a photograph of a 7-year-old boy with a chemistry book in hand, standing in front of a blackboard covered in chemistry equations. That little boy was me.

I had not thought about my brief moment of childhood fame in decades, when recently I received an e-mail from an elementary school friend, Judith Shulman Weis. From Judith, I learned that my 7-year-old self had earned a second moment of glory: *Science* magazine had run a version of the *Life* magazine photograph on the cover of the 23 April 2010 issue on Science, Language, and Literacy.

Upon seeing this snapshot of the past, I couldn't help thinking about my years at Hunter and how the school may have affected the path my life has taken. The photograph seems to imply that I learned those chemical equations at school. This was not the case. The staff at Hunter did not teach me advanced chemistry, but they did provide something even more important: an environment that encouraged independent learning and rewarded interest in science. With support from my teachers, I taught myself the chemistry displayed in the photograph by reading the high-school review book shown in my hand. My father had given me the book; he was a high school graduate but had always been interested in chemistry and was one of the smartest people I have ever known.

Throughout my childhood, I dreamed of being another Beethoven, but when reality set in, I turned back to my interest in chemistry. I majored in chemistry at the University of Michigan and then earned a master's degree in chemistry from Harvard. However, because of the way chemistry was taught at the time, I became frustrated with the subject. Even after my first year of graduate school, I did not understand what a chemist did. I changed course again and returned to the University of Michigan to get a master's in mathematics and a Ph.D. in psychology.

In the years since, my primary research has been measuring eye movements to gain insight into the reading process. I have also been involved in funded research on the understanding and misunderstanding of statistics, and more recently I have studied driving and driving safety, also using eye movements as a primary variable of attention.

I am still active in all three areas at age 70. I like to think that the inquisitive little boy that graced the cover of *Science* last year is still a part of me.

ALEXANDER (SANDY) POLLATSEK

Department of Psychology, University of Massachusetts, Amherst, MA 01003, USA. E-mail: pollatsek@psych.umass.edu

New University Plan Skips Crucial Steps

I WAS SHOCKED BY THE NEWS & ANALYSIS story "Daring experiment in higher education opens its doors" (8 April, p. 161), in which R. Stone describes Zhu Qingshi's effort to build a new university, the Southern University of Science and Technology of China (SUSTC). I laud the goal of exploring new models to challenge China's education system, as educators and students alike in China believe the current system is inadequate for training independent and innovative thinkers. However, what President Zhu Qingshi is doing, while indeed daring, defies common sense.

Well-regarded and successful universities educate students by offering both a curriculum that comprises the collective wisdom of the faculty and a course selection that reflects the knowledge and style of individual faculty members. SUSTC currently meets neither of these criteria; Zhu has chosen to enroll undergraduates to his university before establishing a formal curriculum and permanent faculty. It is no surprise that the government will not promptly approve SUSTC's authority to grant undergraduate and graduate degrees.

The first step in building a new university—especially a research university with an overarching emphasis on undergraduate and graduate education, as SUSTC aspires to become—is not to enroll students but to build the necessary infrastructure and use it to recruit a diverse group of highly qualified faculty members. Faculty recruitment itself is an extremely challenging and time-consuming endeavor, and money often plays only a limited role in its success. Once the faculty has been assembled, the professors should be given a few years to establish their own research programs and develop the cur-

riculum and individual courses. Students, especially undergraduates, should only be admitted after these are in place, so that they can make an informed decision as to whether the university is suitable for them.

SUSTC appears to be doing things backwards. There are many ills that need to be cured in China's education system, but, to borrow a phrase from medicine, "first, do no harm."

WEIMIN ZHONG

Department of Molecular, Cellular and Developmental Biology, Yale University, New Haven, CT 06520–8103, USA. E-mail: weimin.zhong@yale.edu

Symmetrical Transparency in Science

IN RECENT MONTHS, THERE HAS BEEN CONsiderable discussion in the scientific community of the need for increased transparency, openness, and data access [Dealing with Data special section, 11 February, "Making data maximally available," B. Hanson *et al.*, Editorial, p. 649, and "Climate data challenges in the 21st century," J. T. Overpeck *et al.*, Perspective, p. 700, as well as (*1*–*4*)]. Missing from the discussion, however, is recognition that a good deal of science relevant to public and environmental health and welfare is done in the private sector and, largely because of the 1999 U.S. Data Access Act and the 2001 U.S. Data Quality Act, this private science is not subject to the same scrutiny as public science. Much or even most private science may well be of high quality, but it is difficult to judge because private science does not face the same transparency requirements as public science, even when it assesses public health, safety, or environmental threats; supports product licenses or pollution permits; or is supposed to support industry's regulatory compliance. This constitutes a seriously tilted playing field.

Ideally, both the Data Access and Data Quality Acts would be amended to apply equitably to public and private science. Because this is unlikely in the near term, we suggest that the scientific community, perhaps through the National Research Council, provide guidance for best practices regarding data access and transparency for private science affecting public health and the environment. For example, privately funded science used for public or regulatory purposes should be subject to the same transparency requirements as publicly funded science, and industry requests to protect data, under claims of confidential business interests, should be granted only when public health and safety are demonstrably not at stake (*5*, *6*).

Of course, some data requests may well be harassing or malicious, designed to block sound public policy rather than promote it. The scientific community should therefore also suggest criteria to evaluate when data requests, under the Freedom of Information Act or other federal statutes, constitute an unreasonable burden on researchers.

KRISTIN SHRADER-FRECHETTE[1]* AND NAOMI ORESKES[2]

[1]Department of Biological Sciences and Department of Philosophy, University of Notre Dame, Notre Dame, IN 46556, USA. [2]Department of History and Program in Science Studies, University of California, San Diego, La Jolla, CA 92093–0104, USA.

*To whom correspondence should be addressed. E-mail: kshrader@nd.edu

References

1. M. Russell, "The independent climate change e-mails review" (July 2010); www.cce-review.org/pdf/FINAL%20REPORT.pdf.
2. R. A. Pielke Jr., "Major change is needed if the IPCC hopes to survive" (Yale Environment 360, 25 February 2010); http://e360.yale.edu/feature/major_change_is_needed_if_the_ipcc_hopes_to_survive/2244/.
3. M.-E. Carr, R. F. Anderson, K. Brash, "Climate change: Addressing the major skeptic arguments" (September 2010); www.dbcca.com/dbcca/EN/_media/DBCCAColumbiaSkepticPaper090710.pdf.
4. Q. Schiermeier, *Nature* **467**, 891 (2010).
5. M. O. McGarity, W. E. Wagner, *Bending Science: How Special Interests Corrupt Public Health Research* (Harvard Univ. Press, Cambridge, MA, 2008).
6. D. Michaels, *Doubt Is Their Product: How Industry's Assault on Science Threatens Your Health* (Oxford Univ. Press, Oxford, 2008), pp. 9–16.

Bringing Research into the Classroom

AS A HIGH SCHOOL STUDENT LOOKING TO pursue science, I was happy to read J. Durant and A. Ibrahim's Editorial "Celebrating the culture of science" (11 March, p. 1242). I feel that engaging the public in Science, Technology, Engineering, and Math (STEM) is an often-overlooked aspect of bringing STEM into the mainstream.

I believe that before there can be a revolution in STEM education, there needs to be a paradigm shift in the way our culture and society embrace STEM, beginning with the youngest age groups. STEM taught in the classroom should be reinforced at the dinner table and on the school bus. Presently STEM is regarded by both students and teachers as a static subject, instead of appreciated as an interactive and dynamic field.

To help cultivate an infectious interest in STEM, I believe that the idea of celebrating STEM should proliferate into the classroom. I propose a graduate school–style approach to primary and secondary school STEM education.

This curriculum would not focus only on the core material, but would also emphasize current research in each subject. I think that a freely available journal publication that takes groundbreaking current STEM reports and edits them for a younger audience should be created and integrated into the classroom.

Incorporating journal discussions in the classroom would stimulate the teachers who choose the papers and pique the curiosity of the students. Only then, when students are self-motivated by curiosity to study STEM, will they go on to achieve STEM excellence.

AARON KROLIK

Chapel Hill, NC 27514, USA. E-mail: aaron.b.krolik@gmail.com

CORRECTIONS AND CLARIFICATIONS

News Focus: "Early farmers went heavy on the starch" (22 April, p. 416). The research detailed in the story was led by Cheryl Makarewicz at Germany's Christian-Albrechts University at Kiel. Sadie Weber, who presented the research, is an undergraduate on Makarewicz's team. In the HTML version online, the last sentence of the second paragraph has been corrected and two instances of "Weber" have been changed to "Makarewicz."

Review: "Beyond predictions: Biodiversity conservation in a changing climate" by T. P. Dawson *et al*. (1 April, p. 53). When originally published, Fig. 2 was incorrect due to an editorial error. The third column in Fig. 2 was mislabeled as "Habitat shift." The PDF and HTML versions were corrected on the day of publication.

News & Analysis: "Waves of destruction" by D. Normile (18 March, p. 1376). Geologist Kazuhisa Goto is at Chiba Institute of Technology, not Chiba University.

Reports: "Aryl hydrocarbon receptor antagonists promote the expansion of human hematopoietic stem cells" by A. E. Boitano *et al*. (10 September 2010, p. 1345). Microarray data for this paper were not immediately available but have now been deposited in the National Center for Biotechnology Information's Gene Expression Omnibus (GEO) with accession numbers GSM701153, GSM701154, GSM701155, GSM701156, GSM701157, GSM701158, GSM701159, and GSM701160.

Reports: "A topoisomerase IIβ–mediated dsDNA break required for regulated transcription" by B.-G. Ju *et al*. (23 June 2006, p. 1798). In Fig. 1B, ChIP assays were performed using the same samples as in Fig. 1A. The TopoIIβ track from Fig. 1A is reproduced in Fig. 1B to facilitate direct comparison to TopoIIα. Mer treatments in Fig. 2C were performed as part of the same experiment shown in Fig. 1, A and B, with the 0- and 30-min time points for E2-only data from Fig. 1, A and B, reproduced in Fig. 2C to facilitate comparison to E2+Mer data. These details, not delineated on the images, should have been clearly described in the legends.

Letters to the Editor

Letters (~300 words) discuss material published in *Science* in the past 3 months or matters of general interest. Letters are not acknowledged upon receipt. Whether published in full or in part, Letters are subject to editing for clarity and space. Letters submitted, published, or posted elsewhere, in print or online, will be disqualified. To submit a Letter, go to www.submit2science.org.

SCIENCE IN FILM

Fitting Science and Screen

Malcolm A. MacIver

In the mid-1920s, the great German film director Fritz Lang decided to make a movie about going to the Moon that would be more scientifically accurate than previous movies on space flight such as Holger-Madsen's *The Sky Ship* (Denmark, 1918) and Yakov Protazanov's *Aelita* (Soviet Union, 1924). So he did what every Hollywood director in the same position would now do: he hired some scientific consultants, among them rocket scientist Hermann Oberth. (A young Wernher von Braun also helped out on set.) To Oberth's dismay—so great that he threatened to quit the job—Lang insisted that his characters walk around on the Moon without space suits, despite the scientific consensus that the Moon had no atmosphere. Lang had his reasons: this was a silent film about a love story. It's hard to show affection through a space suit—and with no audio, it was especially important to be able to see the expressions on the actors' faces. Today, such an obvious transgression of scientific truth would provoke ridicule. But in 1929 the public didn't know any better. Lang knew that, and he made a shrewd calculation that the (then minor) benefit of being accurate was outweighed by the difficulties of silently expressing love through a deep-sea diving suit.

Lang's *Woman in the Moon* is one of the many examples of potential tensions between science and fiction that David Kirby discusses in *Lab Coats in Hollywood*. It illustrates a useful rubric for science-versus-art decision-making that he sets up, one I'll be applying in my own consulting work in the future. Kirby (whose work at the University of Manchester centers on science communication) defines "public science" as the kind of science that the majority of the public is likely to know. "Expert science" involves facts that, if disregarded, only provoke irate letters from people like readers of *Science*. "Folk science" is science that people think is true but isn't. Lastly, "unsettled science" covers the vast area where science is either silent or has not reached consensus.

The reviewer is at the Department of Mechanical Engineering, Northwestern University, 2145 Sheridan Road, Tech B224, Evanston, IL 60208, USA. E-mail: maciver@northwestern.edu

Lab Coats in Hollywood
Science, Scientists, and Cinema
by David A. *Kirby*
MIT Press, Cambridge, MA, 2011. 279 pp. $27.95, £20.95. ISBN 9780262014786.

If something in a film violates public science, there's a substantial risk of the film seeming implausible. Because that could hurt the film's commercial success, a consultant who makes a good argument on this score can usually ensure a change toward scientific fidelity. If a movie violates expert science, however, many other considerations come into play: Does the director value scientific accuracy? Is the suggested change expensive? Will it reduce the drama of the film? Here, Kirby argues that the consultant has to be creative in providing a scenario where fidelity to truth will enhance, rather than detract from, the narrative. On this score, Oberth's logic was no match for Lang's narrative wisdom.

When it comes to folk science, the default position is to sacrifice scientific accuracy. Kirby gives the example of people's expectation that a lab will contain bubbling flasks of colored liquids. The directors he talked with know this stereotype to be false, but they often find that violating the expectations of the audience isn't worth the price. Sometimes directors decide that disagreeing with folk science is worthwhile. *Jurassic Park* broke with the popular belief that dinosaurs were large, slow, and stupid animals, and Kirby details the extraordinary publicity efforts to prepare the audience. When it comes to unsettled science, consultants get the freedom to be creative—or, in some fascinating and ethically thorny cases Kirby describes, put forward their own pet theories as settled truth.

In the book, Kirby balances thoughtful analysis with a wealth of well-researched anecdotes that reveal a previously hidden but important part of the culture of science. These stories will appeal not just to those involved in science and cinema, but to anyone who is curious about the ways scientists have contributed to popular culture. We learn, for example, that Kubrick's obsession with scientific realism in *2001* brought him to employ people from a vast array of technical disciplines, including space science (Frederick Ordway), artificial intelligence (Marvin Minsky), and supercomputing (the statistician I. J. Good, originator of the idea that we now call "technological singularity").

Perhaps the most intriguing point Kirby makes is that science consultants should choose their battles more wisely than they have in the past. He suggests focusing less on transgressions of scientific accuracy and more on the cultural meanings of science conveyed by the work. Seeing movies as a vehicle for improving science literacy, he claims, is a lost cause. There are too many ways in which scientific accuracy (particularly in the realm of expert science) has to give way to storytelling expediency. However, as Kirby illustrates with a number of cases, the cultural meaning of science offers an area where the science consultant has the potential to powerfully influence writers or directors. Showing scientists as creative people, or its process of inquiry as our most effective approach to understanding nature, for example, can have far more impact than ensuring that a particular dinosaur is depicted with the correct body shape.

As France's art-roboticist extraordinaire François Delarozière has written, "dreams are what fuel the greatest human adventures" (*1*). For those of us wanting to work with story makers to bring those dreams into cinematic reality, *Lab Coats in Hollywood* is an invaluable guide for how to do it with the right measure of scientific validity. For movie-lovers everywhere, it provides a fascinating behind-the-scenes look at how art and science meet in producing motion pictures we find delightful.

CREDIT: UFA/THE KOBAL COLLECTION

Consultants overruled. Space suit–free travelers in Fritz Lang's *Woman in the Moon*.

References

1. F. Delarozière, *Carnets de croquis et réalisations: Edition bilingue français-anglais* (Actes Sud, Paris, 2010).

10.1126/science.1205130

FILM: ENVIRONMENT

Energy, People, and the Natural World

The 19th annual Environmental Film Festival in the Nation's Capital offered a broad sample of movies on the natural world and people's relations with it. This year, many of the films highlighted aspects of the crucial links between energy and the environment. Audiences were often encouraged to stay afterward to discuss the films and issues with the filmmakers, activists, and experts. Brief descriptions of the 148 films can be found at www.dcenvironmentalfilmfest.org/films. Here our reviewers comment on ten.

Oil Rocks: City Above the Sea (La Cité du Pétrole). Marc Wolfensberger, director. Intermezzo Films and Thin Line Productions, Switzerland/Azerbaijan. 2009. 52 minutes. www.thin-line.net/thinline/Documentaries.html

In grainy black-and-white footage, lumbering waves smash into pylons that support fragile-looking trestle bridges. Two men crawl precariously along a horizontal pipe, past wrecked planking, to a joint pulsing an arterial spray of oil into the tearing wind. They creep into the spray and grapple the joint shut. In another scene from the same devastating 1957 storm, workers, so completely soaked in oil that they appear shiny and metallic, manhandle more burst and gushing pipes.

Many of the platforms, roads, and bridges of Neft Daslari ("Oil Rocks" in Azeri) collapsed that day, killing an unknown number of workers. In Marc Wolfensberger's documentary *Oil Rocks*, the storm is a harbinger of the future, a metaphorical warning that Stalin's "ludicrous" scheme to build a fully functioning metropolis directly over what would become one of the most productive oil fields in the then–Soviet Union must end in ruin.

The film portrays the history of this unique construction and the community that still lives and works on it through interviews with present-day workers (some of whom are older than the city itself) intercut with Soviet-era propaganda footage (complete with triumphal music parping in the background): We see Khrushchev visiting the island, jocular and rotund in his pork-pie hat, grinning like a buck-toothed mafia boss; members of the Bolshoi Theatre, bravely performing for the workers on a wind-swept dock; and the workers themselves, swimming and diving, quaffing beer, eating on neat tablecloths, or beaming at the camera.

Oil Rocks is a strange spider's web of hundreds of oil derricks linked by trestles radiating from the central hub of a tiny artificial island. Built on the scuttled hulks of seven ships, the island is a monument, in microcosm, to both the socialist idealism and brutal concrete architecture of the Soviet era. In its day, the complex was a technological triumph, becoming one of the most productive oil fields in the Caspian Sea region and pumping over 170 million tons of oil. But the Soviet Union collapsed, and—in the face of the elements and neglect from its new owners, the Azerbaijan government—so has much of Oil Rocks.

The propaganda-fueled euphoria of the Soviet era ("Wherever the Party sends me, I will go!") is long gone, and the memories of the workers belie that artfully constructed and mostly fictional past: "What did we have in the Soviet era? Bread, and that was it … now, there are plenty of sausages." The remaining workers, cramped three or more in squalid crumbling dorm rooms, working with rusting, junkyard equipment, on tottering piers, remain only because of the salaries oil brings.

The film's depiction of the flayed and decaying city—and the words of those who work there—give veracity and a strangely uplifting pathos to the story of a once truly audacious engineering project that is sinking slowly back into the sea.

–Guy Riddihough

The Pipe. Risteard Ó Domhnaill, director. Underground FIlms, Ireland, 2010. 83 minutes. www.thepipethefilm.com

Following the members of a small, remote fishing village in western Ireland, *The Pipe* offers a microcosm of the choices that increasingly confront communities around the world when meeting the rising global demands for energy interferes with local livelihood—and of what happens when the ability to make a choice is taken away. When residents of Rossport and neighboring villages were faced with the prospect of a large oil company constructing a 9-km-long pipeline through their coastal fishing waters and farmland, many thought they had the option of keeping the energy development away. Despite numerous protests, litigation, and even a hunger strike, the objecting residents lost. Although the pipeline, a new refinery, and offshore drilling activities will likely bring economic benefits to some, many locals—and the environment—may soon bear untold costs.

The story begins after a large natural gas field was discovered off the Irish coast in 1996. The new supply could provide temporary relief from diminishing supply along with a potential reduction in gas prices beyond Ireland, but the oil company's construction plans encountered substan-

CREDITS (LEFT TO RIGHT): © THIN LINE PRODUCTIONS; © UNDERGROUND FILMS

tial local protest. Ó Domhnaill's strategy of entraining himself among the outraged citizens is highly effective at demonstrating the emotional side of the all-too-common "not in my backyard" dilemma. Viewers can easily empathize with the community as they see protests that result in violence, arrests, and the division of towns.

The film's approach of not explicitly stating an opinion on the subject matter contrasts with the style and tone of the final product. It is clear that Ó Domhnaill bonded with and felt deeply for the fishermen and farmers. Indeed, it would be difficult not to when he himself was beaten by police as he was filming one particular protest. The film exhibits some lack of perspective in that it fails to contextualize the conflict in Rossport with the larger problem of a world growing thirstier for oil and gas. Similar stories will assuredly continue to arise in Ireland and beyond as oil and gas companies choose to invest in reservoirs previously considered too difficult or too expensive to tap. For now, *The Pipe* illustrates the lack of choices many communities with resources have as the rest of the world continues to consume. **–Nicholas S. Wigginton**

Windfall. Laura Israel, director. Cat Hollow Films, USA, 2010. 83 minutes. http://windfallthemovie.com

Wind energy is clean and therefore good, right? Filmmaker Laura Israel thought so and decided that she might want a wind turbine installed on her property. So began a journey from rosy general impression to harsh reality that Israel herself experienced and that she leads us through in *Windfall*.

As Israel began to investigate the details of erecting a power-generating windmill on her property, she encountered the citizens of Meredith, New York, who were struggling with the same question. They were caught up in an increasingly divisive debate over whether wind turbines should be allowed within the town boundaries. Through interviews with the residents on both sides of the argument, she adeptly demonstrates how knowledge is a powerfully important thing. Gradually the residents of this Catskills community, and we the viewers, come to realize that wind turbines are not purely an environmentally clean, domestic solution to our energy woes. The technology is also imposing, loud, extremely hazardous to birds and bats, and a potential risk to human health. People from Meredith compellingly describe their transition from believers in wind as a green energy solution to skeptics fighting for the health of their town, neighbors, and environment.

Even more striking are the testimonies from residents of Tug Hill, in western New York. There wind turbines were initially welcomed, but people now live surrounded by hundreds of them and feel their physical and psychological effects daily. In the end, the film leaves us with feelings of disappointment that wind energy is not the benign solution it is often made out to be—and a bit of dread for what the future may hold if others don't learn what these New Yorkers have discovered. *Windfall* serves as a reminder that there is no perfect solution to our energy problems and should inspire us to conserve and innovate. **–Sacha Vignieri**

Arabia 3D. Greg MacGillivray, director. MacGillivray Freeman Films, USA, 2010. 45 minutes. www.arabia-film.com

With scenes ranging from windswept desert sand dunes to the dusk-colored corals of the Red Sea, *Arabia* melds striking images from an exotic and fascinating land. Greg MacGillivray films his three-dimensional IMAX movie from the perspective of Hamzah Jamjoom, a young Saudi filmmaker studying in Chicago who sets out to learn more about the geography, history, and culture of his homeland. The magnificent cinematography, recorded at 20 different sites around Saudi Arabia, includes footage of Bedouin tribesmen riding their camels across the desert, the celestial minarets of Mecca, and the kingdom's surprisingly modern capital city, Riyadh. The filmmakers clearly wanted to inform viewers not only about the beauty of the often harsh landscape but also about the peoples of the Arabian peninsula. They used animations and historical reenactments to depict aspects of two golden ages of Arabia. The first, two millennia ago, was built on wealth derived from trading the rare costly spice frankincense. Guided by archaeologists, Jamjoom explores a great Nabataean city of that era, Madain Saleh, now a World Heritage site. A second golden age, spanning 800 years, began in the 7th century with the prophet Muhammad, whose followers reshaped the peninsula and spread their religion east to Persia and India and west to Spain. Reading and learning flourished in the Islamic world, which made great strides in mathematics, physics, and chemistry. The narrator suggests somewhat wistfully that Saudi Arabia, with its fabulous oil wealth, may be about to embark on a third golden age, as evidenced by the government's efforts to build several new state-of-the-art universities and to boost student enrollment.

MacGillivray and his collaborators have worked hard to bridge the cultural divide between Saudi Arabia and the United States. They show us Jamjoon at home with his family, discussing the making of the movie with his father, talking to a celebrated female Saudi poet, and sharing a meal with a Bedouin tribesman. Combining travelogue, history lesson, and cultural outreach, the film certainly should entice any tourist to spend time in this desert kingdom. Perhaps the movie's most enduring image is that of the *Hajj*, the annual pilgrimage to Mecca during which two to three million Muslims from around the world converge on the Grand Mosque in the largest gathering of people on Earth. The breathtaking aerial footage of hundreds of thousands of pilgrims walking in unison seven times around the Kaaba (the holy center of their faith) serves as a powerful reminder that a peaceful, prosperous, and more open Arab world will benefit us all. **–Orla Smith**

Contact. Bentley Dean and Martin Butler, directors. Contact Films, Australia, 2009. 80 minutes. www.contactfilms.com.au

Although there have been many stories of first meetings between isolated indigenous groups and members of the modern world, *Contact* is unusual in that the filmmakers not only had photographs and movies of the first encounter but were able, more than 40 years later, to find the people involved. In 1964, 20 women and children of the Martu people were living in a remote section of desert in Western Australia that was about to be used as the impact zone for a series of rocket tests. There they were stumbled upon by a patrol from the Weapons Research Establishment sent to check that the zone was clear. The aborigines had never seen a truck, and Yuwali (who was 17 at the time and 62 when the movie was made) thought at first that a boulder had come to life and was chasing them. Bentley Dean and Martin Butler based their award-winning documentary on a book by Sue Davenport,

Peter Johnson, and Yuwali, *Cleared Out: First Contact in the Western Desert* (Aboriginal Studies Press, Canberra, 2005). The filmmakers relate a poignant tale, showing the "evacuation"of the aborigines to a mission village and the irreversible changes in their lives that followed. The officials involved, however, are presented as real people, not villains. For example, Terry Long of the Native Welfare Patrol wishes that he had done better, but he noted that the aborigines were starving and there were no men in the region to teach the young boys or to marry the young women. The film ends with the Martu visiting their old watering holes and watching films of themselves as children. They are very well aware of how much they have changed: laughing at themselves when they bend down to lap water from a puddle as they used to and commenting on how they would no longer care to walk around naked. Nonetheless, Yuwali remarks, "We were carried away by something we never knew before. We left out hearts in our country." She explains that they had brought their own children and grandchildren back to the desert so they would know where their stories had come from. **–Barbara Jasny**

Henry A. Wallace: An Uncommon Man. Joan D. Murray, director. Video Takes, USA, 2011. 57 minutes. www.henryawallace.com

Although many retired politicians write books, Henry A. Wallace must be unique for also devoting time to improving brown-egg chickens, strawberries, and minature gladiolus. Even so, that is probably the most trivial distinction Joan Murray includes in this "film tribute" to her grandfather.

Wallace's father and grandfather were prominent Iowa farmers. His early achievements included the recognition that the appearance of corn ears did not predict crop yields, an econometric analysis of farm prices, and the founding of the first (and incredibly successful) hybrid-seed company, Pioneer. While Secretary of Agriculture during Franklin D. Roosevelt's first two terms, he helped plan and implement the New Deal. He proved a very effective administrator despite not fitting into the culture of Washington. (He abhorred political patronage; did not smoke, drink alcohol, or eat meat; and declined his official car, preferring to walk the 10-km round trip to and from his office.) His innovative department developed emergency measures to stabilize crop prices, the Soil Conservation Service, rural electrification, food stamps, and school lunches. Convinced that increasing crop yields would provide great benefits to the people of Latin America, Wallace encouraged the Rockefeller Foundation to sponsor what became the International Maize and Wheat Improvement Center. (Norman Borlaug's research there helped fuel the Green Revolution in agricultural productivity.)

FDR chose Wallace for his running mate in 1940, seeing him as the potential successor who would be most likely to continue the New Deal reforms. As vice president, Wallace expanded the scope of the office's duties and during World War II chaired important economic and production boards. He entered the 1944 Democratic Convention as the delegates' choice for reelection, but party bosses and Southern conservatives (opposed to his positions on poverty and race) engineered his replacement by Harry Truman. When FDR died in office and Truman assumed the presidency, Wallace remained as Secretary of Commerce. The next year he was forced to resign due to disagreements over policy toward the Soviet Union. As the Progressive Party's candidate in the 1948 presidential election, he was widely accused of links to communists and finished fourth. However, many of the planks of his then-radical platform have subsequently been enacted (although not universal government health care).

The film weaves together excerpts from Wallace's speeches and writings; historic news footage and photographs; and interviews with historians, biographers, conservationists, and others. The portrait Murray offers is clearly a friendly one. Nonetheless, she makes a convincing case for the broad, lasting, and beneficial impact of Wallace's science and public service.

–Sherman J. Suter

Plastic Planet. Werner Boote, director. Neue Sentimental Film Entertainment and Brandstorm Entertainment, Austria/Germany. 2009. 95 minutes. www.plastic-planet.at

Anyone who still doubts that we live in the age of plastics should be dissuaded by the convincing arguments Werner Boote presents in *Plastic Planet*. The filmmaker, whose grandfather worked in a plastics factory, traveled to 14 countries to learn how plastics are manufactured, used, and discarded. In one of the film's most striking story lines, he asks people around the world to place every plastic item from their households in front of their homes, an eye-opening exercise for both participants and viewers. Even a small dwelling in Kolkata, India, holds a surprisingly large amount of plastic. Another narrative begins when Boote buys an inexpensive plastic globe and tries to discover its origins. Although the Chinese factory that makes the toy grants him a tour, once the guide realizes that Boote is a filmmaker (complete with camera crew) and not a potential customer, she quickly ends the interview.

Few who have been following concerns about the safety of plastics will learn much new here. Some of the scientists who appear in the film emphasize bisphenol A (BPA)—found in polycarbonate plastics and epoxy resins—as the primary enemy, but Boote freely extends the hazards of BPA to any and all forms of plastic. In one scene, he travels the aisles of a grocery store sticking labels with negative slogans (for example, "PLASTIC CAUSES BRAIN DEFECTS") on various items, including a nonpolycarbonate bottle of shampoo. Industry representatives appear as familiar villains, refusing to address negative effects,

and government officials are their usual foes, wanting further regulations. Boote does suggest a third way in mentioning a company that has developed biodegradable plastics from plant-derived as well as petroleum-based materials. Their manufacturer deems these bioplastics completely safe, much as traditional plastics were seen when they were first introduced. Although the film provides a detailed account of plastic's extended life cycle, Boote does not offer much in the way of constructive suggestions for mitigating the material's many problems. Instead, viewers are simply left wary about what lies ahead in a world awash with plastic. **–Trista Wagoner**

Mother Nature's Child. Camilla Rockwell, director. Fuzzy Slippers Productions, USA, 2011. 57 minutes. www.mothernaturesmovie.com
Play Again. Tonje Hessen Schei, director. Ground Productions, USA, 2010. 80 minutes. www.playagainfilm.com

As a child I spent my free time climbing trees, catching insects, and exploring my neighborhood, largely only in the company of other children. Today, most girls and boys experience much different childhoods. Technological advances and increasing concerns over children's safety have led to them spending their spare moments indoors, in front of television or computer screens, or being shuttled by adults to organized and supervised activities. A recent estimate placed the average amount of time a child in the United States spends in front of a screen at 44 hours a week and the average weekly total spent outdoors in unstructured play at less than 40 minutes. *Mother Nature's Child* and *Play Again* explore the physical, psychological, and societal consequences of a generation of children growing up in the absence of free interaction with the natural world around them.

By following organizations designed to foster contact with nature, *Mother Nature's Child* leads viewers through the important impacts that free play in nature has on childhood development. Preschool children develop their senses, understanding of cause and effect, creativity, and early sense of self as they explore and interact with the natural environment. School-age children build forts to establish their independence; acquire the ability to observe, reflect, and make decisions; and develop empathy for other living things. As adolescents, the natural world becomes a place to bond with peers, foster prosocial behavior, and gain self-confidence and self-reliance. At all ages, contact with nature reduces aggression and improves physical health.

In *Play Again*, we see the profound influence direct contact with nature has on a group of adolescents whose earlier years largely lacked such experiences and whose childhoods were instead shaped by screens and media. Young teens who usually spent 6 to 15 hours a day planted in front of televisions and computers were asked to give up their screens and disconnect from their online networks for a 4-day camping trip in the woods. Through the teens' own words and actions, we witness initial withdrawal followed by profound transformations in confidence, interaction, and engagement.

Both films note important points about the influence of the media and advertising on children's development and desires for the future. Both pose a crucial question: Will children raised without contact with the natural world work to protect it? In the end, both demonstrate the essential fact that the risks of raising a generation of children away from nature are much larger—for the young, society, and the planet—than those that await them in the great outdoors. **–Sacha Vignieri**

Inside the Firestorm. Jacob Hickey, director. Renegade Films for Australian Broadcasting Company, Australia, 2010. 110 minutes. www.renegade.com.au

With the seasonal drought, a stretch of daily highs above 40°C, record low humidity, and gale-force continental winds, bush fire indices in the countryside around Melbourne, Australia, reached levels of 140 to 190 (where 100 is extreme) on 7 February 2009. Fire officials warned the public to prepare for the worst. But the course of events on "Black Saturday" far exceeded anyone's expectations. By 3 p.m., 10 uncontrolled major fires (several ignited by electrical power lines, others of suspicious origin) were burning across Victoria. They would consume nearly a half million hectares of bushland, leave 7000 people homeless, and claim 173 lives.

Many factors contributed to the catastrophe. Driving the fires to the southeast, winds dropped flaming material up to 20 km ahead. One blaze rushed 50 km in a few hours. Fires roared up slopes, and locations nestled in valleys came under intense attack from falling embers. Prompt initial responses were overwhelmed, access routes were closed, and fire-fighting resources were exhausted. A late-afternoon shift of winds to the southwest turned long northeast flanks into active fronts. Existing policy urged rural residents to "prepare, stay, and defend or leave early." The rapid spread of the fires and communications breakdowns (some messages warning particular locations of imminent danger were prepared but then neither broadcast nor posted) meant many people, and entire towns, were caught unaware, having insufficient time to flee or to take shelter. And often even the best-prepared structures were destroyed in the intense firestorms.

Inside the Firestorm uses impressive computer graphics to map the progression of the fires. Jacob Hickey incorporates amazing, often frightening, footage captured on cameras (and cell phones) by people caught among the flames, fire fighters, and the news media. But the power of this commemoration of Black Saturday stems from the captivating, moving, and frequently heart-breaking personal stories told by those who fought and escaped the fires—many losing their homes and possessions; others, much more.

Like people who inhabit wildfire landscapes elsewhere around the world, most residents of Australia's bush do not wish to leave. Recognizing that fact, the Royal Commission charged with investigating the February 2009 fires in Victoria (www.royalcommission.vic.gov.au) returned an extensive list of recommendations for policy, procedural, and organizational changes that could help reduce the risks to lives in future fires. But it is impossible to disagree with the conclusion of a 97-year-old veteran of the devastating bushfires of 1939 who came close to losing his life on Black Saturday. Noting the continuing arguments over who's to blame and what should be done, he commented, "on a day like that, nature will take over." **–Sherman J. Suter**

10.1126/science.1206845

AGRICULTURE

Transforming U.S. Agriculture

Achieving sustainable agricultural systems will require transformative changes in markets, policies, and science.

J. P. Reganold,[1]* D. Jackson-Smith,[2] S. S. Batie,[3] R. R. Harwood,[3] J. L. Kornegay,[4] D. Bucks,[5] C. B. Flora,[6] J. C. Hanson,[7] W. A. Jury,[8] D. Meyer,[9] A. Schumacher Jr.,[10] H. Sehmsdorf,[11] C. Shennan,[12] L. A. Thrupp,[13] P. Willis[14]

Agriculture in the United States and many other countries is at a critical juncture. Public investments and policy reforms will inform landscape management practices to be used by farmers and ranchers for sustaining food and ecosystem security. Although U.S. farms have provided growing supplies of food and other products, they have also been major contributors to global greenhouse gases, biodiversity loss, natural resource degradation, and public health problems (*1*). Farm productivity and economic viability are vulnerable to resource scarcities, climate change, and market volatility (*2*). Concerns about long-term sustainability have promoted interest in new forms of agriculture that (i) enhance the natural-resource base and environment, (ii) make farming financially viable, and (iii) contribute to the well-being of farmers, farm workers, and rural communities, while still (iv) providing abundant, affordable food, feed, fiber, and fuel.

A 2010 report by the U.S. National Research Council (NRC) (*1*) identified numerous examples of innovative farming systems that contribute to multiple sustainability goals but noted they are not widespread. This report joins others [e.g., (*3*–*6*)] critical of aspects of mainstream, conventional farming systems. We argue that the slow expansion of such innovative farming systems in the United States is as much a policy and market problem as a science and technology problem. Incentives for appropriate markets, reform of U.S. farm-related policies, and reorientation of publicly funded agricultural science are needed to hasten implementation of more sustainable agricultural systems.

[1]Washington State University, Pullman, WA 99164, USA. [2]Utah State University, Logan, UT 84322, USA. [3]Michigan State University, East Lansing, MI 48824, USA. [4]North Carolina State University, Raleigh, NC 27695, USA. [5]Bucks Natural Resources Management, Elkridge, MD 21075, USA. [6]Iowa State University, Ames, Iowa 50011, USA. [7]University of Maryland, College Park, MD 20742, USA. [8]University of California, Riverside, CA 92521, USA. [9]University of California, Davis, CA 95616, USA. [10]SJH and Company, Washington, DC 20007, USA. [11]S&S Homestead Farm, Lopez Island, WA 98261, USA. [12]University of California, Santa Cruz, CA 95064, USA. [13]Fetzer Vineyards, Hopland, CA 95449, USA. [14]Niman Pork Ranch Company, Thornton, IA 50479, USA.

*Author for correspondence. E-mail: reganold@wsu.edu

Incremental, Transformative Approaches

To improve sustainability of U.S. agriculture, the NRC report proposes both incremental and transformative approaches. The former are practices and technologies that address specific production or environmental concerns associated with mainstream, conventional farming systems. Examples include 2-year crop rotations, precision agriculture using geospatial technologies that describe field variation, classically bred or genetically engineered crops, and reduced or no tillage. Although incremental approaches offer improvements and should be continued, in aggregate, they are inadequate to address multiple sustainability concerns.

In contrast, the transformative approach builds on an understanding of agriculture as a complex socioecological system. Transformative change looks to whole-system redesign rather than single technological improvements. Examples of such innovative systems make up a modest, but growing, component of U.S. agriculture and include organic farming, alternative livestock production (e.g., grass-fed), mixed-crop and livestock systems, and perennial grains (*1*). Such systems integrate production, environmental, and socioeconomic objectives; reflect greater awareness of ecosystem services; and capitalize on synergies between complementary farm enterprises, such as between crop and livestock production.

The existence of innovative agricultural systems in the United States suggests that technical obstacles are not the greatest barrier. Rather, change is hindered by market structures, policy incentives, and uneven development and availability of scientific information that guide farmers' decisions (see the figure).

Market Structures

Most U.S. farmers sell products to a highly consolidated global agri-food industry rewarding primarily the provision of large volumes of low-cost food, feed, fiber, and fuel, often constrained by contract requirements of food processors and retailers. Meanwhile, consumer food consumption habits associated with modern life-styles have sustained mainstream farming systems and food markets and have contributed to a national obesity and health crisis. Part of transforming U.S. agriculture is educating more consumers to take responsibility for what they eat and how much they eat (*7*).

Consumer demand is also growing for more environmental and social accountability from farmers, including considerations of animal welfare, ecosystem services, worker safety and welfare, and resource conservation. In response, "value-added trait" foods and "sustainability brands" have emerged in the marketplace, e.g., U.S. Department of Agriculture Certified Organic and Food Alliance Certified. U.S. and global markets for these value-added trait products have driven the spread of local, organic, and grass-fed livestock systems. Market forces could be accelerated through public-policy incentives.

Policy Incentives

Many international, federal, state, and local agricultural, credit, energy, risk-management, and environmental policies influence farmer decisions (see the figure). A major policy driver for U.S. agriculture is the Farm Bill, traditionally renewed by the U.S. Congress every 4 to 5 years, with the next version expected in 2012. The best-funded provisions of the Farm Bill include financial assistance for low-income families to purchase food; commodity subsidies paid to farmers (mostly for corn, cotton, rice, soybeans, and wheat); crop insurance and disaster relief; and conservation programs (*8*). Although only roughly a third of U.S. farmers receive commodity or conservation payments under the Farm Bill, it has a major influence on what, where, and how food is produced.

Most elements of the Farm Bill were not designed to promote sustainability. Subsidies are commonly criticized for distorting market incentives and making our food system overly dependent on a few grain crops mainly used for animal feed and highly processed food, with deleterious effects on the environment and human health (*9*, *10*). Redesigning the bill will be a complex undertaking in light of political and budgetary constraints, as well as knowledge gaps. However, much of the information necessary for Farm Bill redesign is available and

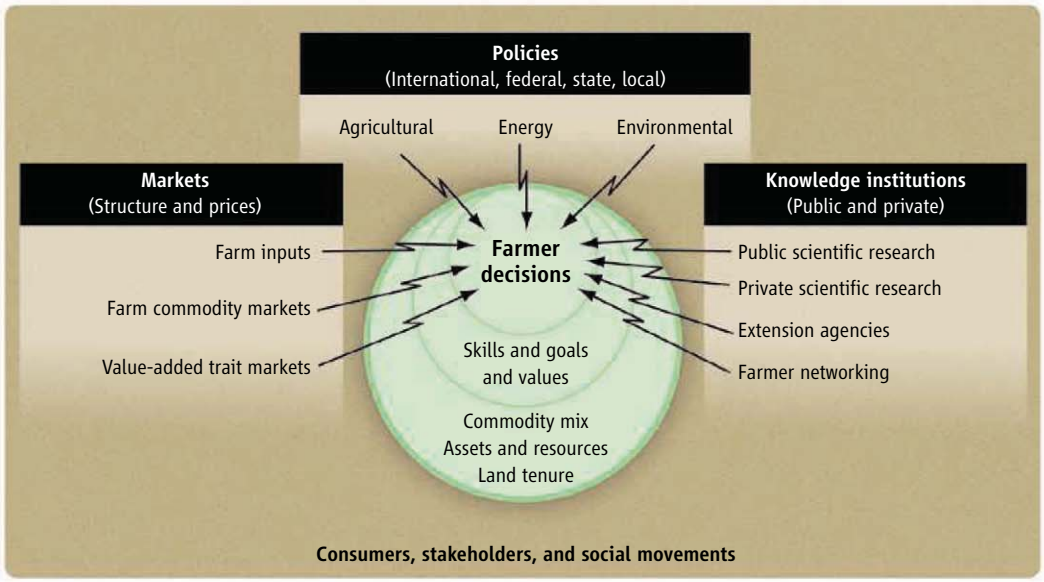

Drivers and constraints that affect farmers' decisions. Farmers make choices based on market structures, policy incentives, and knowledge institutions—all affected by consumers, stakeholders, and social movements [Modified from (*1*)]

not being used (*11*). Spending needs to be reduced on programs, such as subsidies, that mask market, social, and environmental risks associated with conventional production systems. Funding needs to be reallocated to encourage markets for sustainability brand products (e.g., by standardizing and defining sustainable product attributes) and to increase support for farming systems that balance all four sustainability goals and are more resilient to resource scarcities and global market variability.

With a new version of the Farm Bill due next year, we think the time to start reform is now. In addition, progress in other policy arenas is needed to address conflicting incentives and unintended consequences. Unless we integrate agricultural sustainability into debates over biofuels and other energy policies, climate change, trade agreements, immigration reform, and environmental regulation, we are unlikely to see major changes in policies that created and continue current production systems.

Agricultural Science and Knowledge

The publicly funded agricultural science portfolio could be reoriented toward agricultural sustainability, as this research is less likely to yield marketable inventions for private agribusinesses. The bulk of public and private agricultural science in the United States is narrowly focused on productivity and efficiency, particularly on technologies that fit into existing production systems and lead to private benefits (*1*, *12*). A major vehicle for public agricultural research is the National Institute for Food and Agriculture (NIFA). Despite NIFA efforts to solicit proposals addressing sustainability, most NIFA and other federal research grant programs still primarily support incremental research. What is needed is reallocation of public funds to support transdisciplinary systems research that explores such interlocking issues as farm productivity and resilience at field, farm, and landscape scales (*13*).

Transition toward transformative agricultural systems currently relies on a smaller, emerging knowledge base developed largely by farmers and nonprofit organizations independent of traditional scientific institutions. Agricultural science and farmers would benefit from an easily accessible information database of farm innovations. Moreover, pilot projects could be funded by reallocation of Farm Bill subsidies to measure multiple sustainability indicators on conventional and innovative farming systems at the landscape or watershed scale (*11*, *14*).

Final Recommendations

To make difficult choices among competing goals requires public dialogue about what kind of food and agriculture we want, in addition to identifying the roles of markets, policies, and science in delivering them (*15*). Successful implementation will require organizations spanning political and institutional boundaries and integrating complex components of agricultural transformation—from research to on-farm implementation, to markets, and to the dinner table. The Green Lands Blue Waters Initiative (*16*) to achieve "systemic transformation in the agricultural systems" in the Mississippi River basin is an example of such an effort. This involves community organizers, policy experts, scientists, and farmers from more than a dozen nonprofit organizations, five universities, and multiple government agencies from the Upper Midwest to the Gulf of Mexico.

The goals of agricultural sustainability are not unique to the United States. Although specific market, policy, and science solutions will need to be appropriate to diverse contexts, the importance of viewing sustainability as more than a technical problem applies to developed and less-developed countries. Lessons from experiences in developed countries can help less-developed countries avoid some problems associated with contemporary, industrialized agricultural systems and can reduce exposure to market volatility and climate-change risks. Likewise, U.S. farmers can learn from sustainable agricultural practices of less-developed nations.

References and Notes

1. National Research Council, *Toward Sustainable Agricultural Systems in the 21st Century* (The National Academies, Washington, DC, 2010).
2. D. S. Battisti, R. L. Naylor, *Science* **323**, 240 (2009).
3. International Assessment of Agricultural Science and Technology for Development, *Agriculture at a Crossroads: Global Report* (Island Press, Washington, DC, 2009).
4. J. Rockström *et al.*, *Nature* **461**, 472 (2009).
5. O. De Schutter, *Report Submitted by the Special Rapporteur on the Right to Food* (United Nations, Geneva, 2010).
6. H. C. J. Godfray *et al.*, *Science* **327**, 812 (2010).
7. U.S. Department of Agriculture and U.S. Department of Health and Human Services, *Dietary Guidelines for Americans, 2010*. (U.S. Government Printing Office, Washington, DC, 2010).
8. J. Monke, R. Johnson, *CRS Report for Congress* (R41195, Congressional Research Service, Washington, DC, 2010).
9. T. L. Dobbs, J. N. Pretty, *Rev. Agric. Econ.* **26**, 220 (2004).
10. C. Cox, in *Managing Agricultural Landscapes for Environmental Quality II: Achieving Effective Conservation*, P. Nowak, M. Schnepf, Eds. (Soil and Water Conservation Society, Ankeny, IA, 2011), pp. 81–94.
11. S. S. Batie, *Front. Ecol. Environ*. **7**, 380 (2009).
12. W. E. Huffman, R. E. Evenson, *Science for Agriculture: A Long-Term Perspective* (Blackwell Publishing, Ames, IA, ed. 2, 2006)
13. G. P. Robertson *et al.*, *Bioscience* **58**, 640 (2008).
14. J. Sachs *et al.*, *Nature* **466**, 558 (2010).
15. L. Busch, *Nat. Sci. Soc.* **17**, 241 (2009).
16. Green Lands Blue Waters, www.greenlandsbluewaters.org.
17. The authors comprise the Committee on Twenty-First Century Systems Agriculture of the National Research Council who wrote the 2010 NRC report (*1*). We thank L. Klein, J. Glover, and E. Sorensen for comments.

10.1126/science.1202462

ASTRONOMY

Twisted Disks

Ripple patterns in Saturn's and Jupiter's rings result from collisions with comets.

Heikki Salo

Astrophysical disks come in many sizes but, as vertically thin rotation-supported systems, are all susceptible to both external perturbations and internal instabilities. One spectacular form of deformation is vertical bending. For decades, it has been clear that many galactic disks, including our own Galaxy (*1*), are warped. This manifests as up and down bends of the outer disks of edge-on galaxies and, in more face-on galaxies, by distortions in the neutral hydrogen velocity fields (*2*, *3*). Warps are also seen in circumstellar dust disks [e.g., β Pictoris (*4*)] and are hypothesized to be present in accretion disks around massive objects (*5*). Nevertheless, the most striking twisted disks reside in our solar system. This is vividly demonstrated by Hedman *et al*. (*6*) and Showalter *et al*. (*7*) on pages 708 and 711 of this issue, analyzing the vertical corrugation patterns in the rings of Saturn and Jupiter with imaging data from the Cassini and Galileo/New Horizon spacecrafts, respectively. The new data confirms the previously suspected (*8*) vertical undulations in Jupiter's main ring. In Saturn's rings, the coherent pattern extends over hundreds of wavelengths, covering not only parts of the D ring (*9*) but also the entire C ring with an inferred vertical amplitude on the order of a few meters.

There is a simple kinematic description for a warp pattern. Particles orbiting in a spherical potential maintain fixed orbital planes. However, if the potential is flattened with respect to a central plane (e.g., around an oblate planet), the vertical motion with respect to this plane has a shorter period than the azimuthal rotation. Imagine a swarm of particles on inclined orbits, each initially crossing the central plane along a common nodal line. On each orbit, the particles cross the central plane earlier and earlier, indicating that their orbital nodes regress in the direction opposite to rotation. This twisting of orbits is faster closer to the planet, leading to a warp, and if the twisting goes on, to a wavelike vertical corrugation pattern (see the figure). Such a pattern, with wavelengths decreasing inversely proportional to time, describes well the corrugations reported (*6*, *7*), although the small amplitude of the patterns requires the advantage of very special observational geometries.

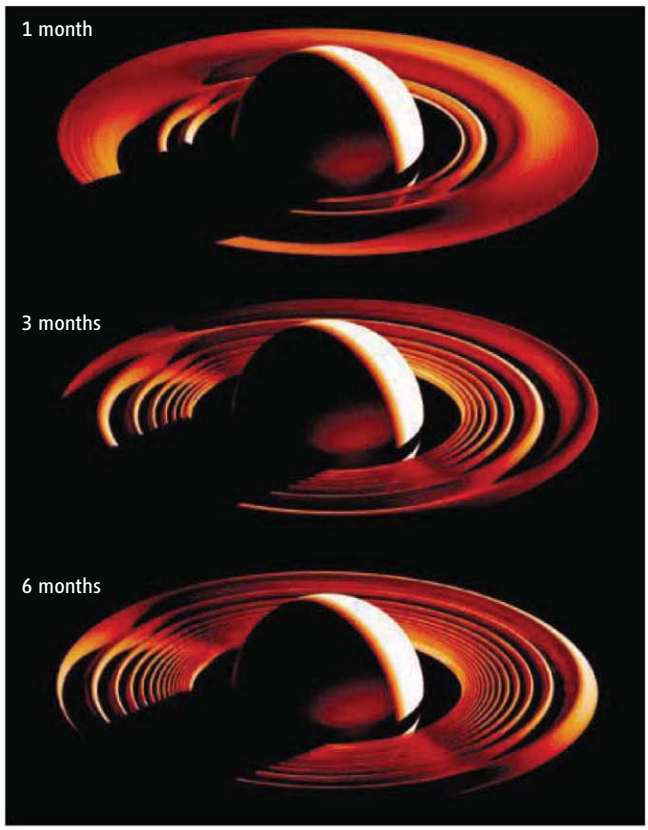

Rippling through. Evolution of a corrugation pattern after the entire toy ring has been tilted along a constant line by 0.5°. A leading one-armed spiral pattern forms due to the winding of orbital planes. Realistic values for Saturn's gravity moments are used, and after ~30 years the pattern would appear as tight as observed in Saturn's rings. However, the vertical amplitude is exaggerated by a factor of ~100,000. The bending of the local ring plane leads to brightness variations: In the plot, the slopes exceed the 5° illumination elevation, and parts of the ring are in its own shadow (alternating darker zones lit by multiple reflections). In Saturn's rings, the slopes are a factor ~2000 smaller (and limited to the D and C rings), indicating very subtle brightness variations discernible only when the Sun is shining near the ring plane (*6*). In Jupiter's tenuous rings, there is no shadowing, and brightness variations arise due to the larger number of scatters when the line-of-sight is along the local slopes, made possible when the rings are viewed near edge-on (*7*).

CREDIT: HEIKKI SALO

The origin of galaxy warps, with their small amount of winding, is poorly understood (*10*). The warps are common and are thus either very long-lived or continuously regenerated. Current explanations invoke a tilt between the disk and triaxial dark matter halo, or a continuous infall of material with angular momentum misaligned with that of the disk. Galaxy disks can also sustain vertical oscillations due to their self-gravity, but no permanent global mode can be maintained (*11*) unless fed by external forcing. Again, Saturn's rings provide the best example of externally forced permanent warp: the spiral bending waves (*12*) associated with resonance locations of Saturn's slightly inclined moons, known since the Voyager fly-bys in 1981. In contrast, the present corrugation patterns are truly transient features whose origin can be dated to within a few months, based on their observed degree of winding. Furthermore, this winding will proceed to make them eventually indiscernible.

Hedman *et al*. make a thorough analysis of how to provide the initial tilt responsible for the pattern. They argue that a sudden turning of Saturn's rotation axis is improbable and conclude that the rings themselves have been inclined, in a hit by an interplanetary debris cloud in Fall 1983. Such debris clouds, whose off-axis angular momentum transfers much more effectively to the ring than that of a single solid body, could be produced by comets disrupted in close planetary passages. The study by Showalter *et al*. adds a crucial piece of evidence by linking the Jupiter ring corrugations directly to the debris associated with the comet Shoemaker-Levy 9, which disintegrated during its close passage with Jupiter in 1992 and whose largest fragments hit the planet in 1994.

Besides providing fresh examples of the rapid dynamic processes in planetary rings (*13*), the implications of the vertical cor-

Department of Physics, Astronomy Division, University of Oulu, Oulu, FI-90014 Finland. E-mail: heikki.salo@oulu.fi

rugations are that they add a valuable tool for measuring the local ring properties: Although the ring's self-gravity has no role in exciting or maintaining the corrugations, the local nodal regression rate due to Saturn's oblateness increases by the extra gravity of ring particles. Hedman *et al*. verify this feeble effect and obtain a new estimate of the C ring's surface density. Concerning the dynamical evolution of the outer solar system, the amount of cometary debris is probably larger than previously anticipated. The rings, with their enormous surface area, thus provide an effective flypaper detector for interplanetary debris.

References

1. J. H. Oort *et al*., *Mon. Not. R. Astron. Soc.* **118**, 379 (1958).
2. R. Sancisi, *Astron. Astrophys.* **53**, 159 (1976).
3. A. Bosma, thesis, Groningen University, Groningen, Netherlands (1978).
4. D. Mouillet *et al*., *Mon. Not. R. Astron. Soc.* **292**, 896 (1997).
5. J. E. Pringle, *Mon. Not. R. Astron. Soc.* **281**, 357 (1996).
6. M. M. Hedman *et al*., *Science* **332**, 708 (2011); 10.1126/science.1202238.
7. M. Showalter *et al*., *Science* **332**, 711 (2011); 10.1126/science.1202241.
8. M. Ockert-Bell *et al*., *Icarus* **138**, 188 (1999).
9. M. M. Hedman *et al*., *Icarus* **188**, 89 (2007).
10. J. Binney, *Annu. Rev. Astron. Astrophys.* **30**, 51 (1992).
11. C. Hunter, A. Toomre, *Astrophys. J.* **155**, 747 (1969).
12. F. H. Shu *et al*., *Icarus* **53**, 185 (1983).
13. J. N. Cuzzi *et al*., *Science* **327**, 1470 (2010).

10.1126/science.1205672

CELL BIOLOGY

Ancient Neurons Regulate Immunity

The innate immune system of multicellular animals is regulated by the nervous system.

Kevin J. Tracey

The most evolutionarily ancient type of immunity, called "innate," exists in all living multicellular species. When exposed to pathogens or cellular damage, cells of an organism's innate immune system activate responses that coordinate defense against the insult, and enhance the repair of tissue injury. There is a modern-day cost associated with these processes, however, because innate mechanisms can damage normal tissue and organs, potentially killing the host. Human life is a balance between dual threats of insufficient innate immune responses—which would allow pathogens to prevail—and overabundant innate immune responses—which would kill or impair directly. What has been the key to maintaining this balance throughout years of mammalian evolution? On page 729 of this issue, Sun *et al*. (*1*) report that neurons in a nematode worm can regulate innate immunity, a mechanism dating back to the early origins of the nervous system itself.

Research on the pathophysiology of infection in the late 20th century revealed that molecules produced by the innate immune system, not pathogens, account for the major physiological, metabolic, and pathological responses to infection in mammals. Cytokines and other molecules were associated with the signs and symptoms of infection, ranging from fever, anorexia, and fatigue, to lethal shock and tissue injury. By understanding the "cytokine theory of disease," it became possible to develop highly selective drugs that neutralize cytokines and experimentally modify the pathophysiology of infection (*2*). This same approach subsequently revolutionized the treatment of inflammatory disease in humans with other, noninfectious, but inflammatory conditions. Today, millions of patients with arthritis, colitis, and other inflammatory syndromes have benefited from therapy with cytokine-blocking agents.

These advances also underscored the importance in understanding mechanisms that control innate immunity and restrain it from injuring the host. Early work focused on soluble factors that control innate immune responses by inhibiting the synthesis or action of cytokines. This "protective mediator" list grew to include glucocorticoid hormones, soluble cytokine receptor fragments, and other anti-inflammatory factors (*3*). More unexpected, however, were later findings that information propagated in neurons controls the magnitude of the mammalian innate immune response. Action potentials traveling in the vagus nerve to the spleen and other organs culminate in the release of acetylcholine, an evolutionarily ancient molecule that effectively inhibits cytokine production by innate immune cells. The cytokine-blocking mechanism requires signal transduction through α7 nicotinic acetylcholine receptors expressed on macrophages and other cytokine-producing immune cells (*4*). Signals generated via this neural circuit tonically suppress innate immunity, because lesions in this pathway enhance the innate immune response to pathogens and injury

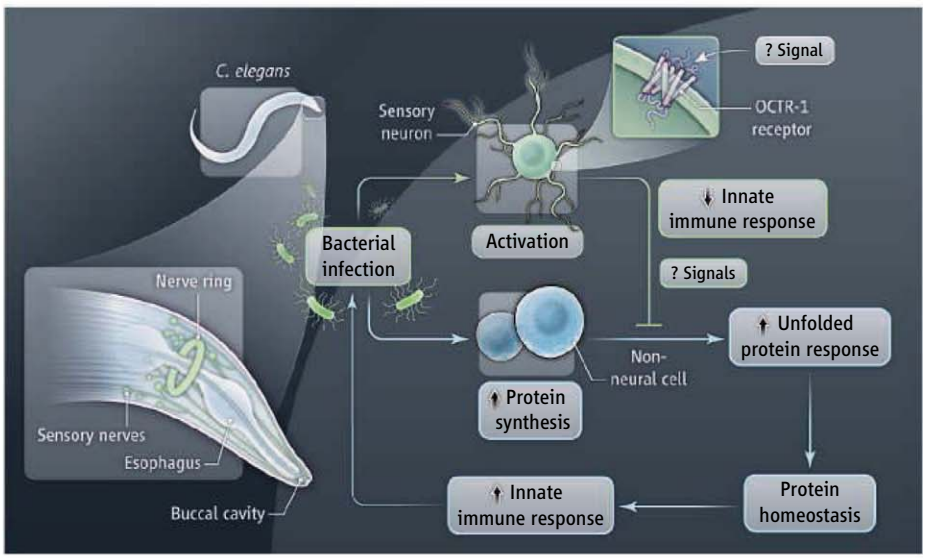

Innate innervation. Infection of *C. elegans* with a pathogen stimulates the innate immune response and activates the synthesis of new proteins, potentially causing the accumulation of unfolded proteins in host cells. To restore protein homeostasis, the unfolded protein response is activated. ASH and ASI sensory neurons negatively regulate the innate immune response to infection by blocking the unfolded protein response in nonneuronal cells. The OCTR-1 receptor in the sensory neurons is required for this effect.

CREDIT: Y. HAMMOND/*SCIENCE*

Feinstein Institute for Medical Research, Manhasset, NY 11030, USA. E-mail: kjtracey@nshs.edu

(*5*). It may be possible to use this inhibitory pathway to therapeutic advantage, because selective electrical stimulation of the vagus nerve inhibits the production of tumor necrosis factor, interleukin-1 and other cytokines, and prevents the pathology associated with arthritis, colitis, ischemic tissue injury, and other syndromes in experimental models.

Sun *et al*. reveal that neural control of innate immunity in mammals is present in *Caenorhabditis elegans*, one of the simplest organisms with a nervous system. This indicates that the regulatory mechanism dates back to the origins of the nervous system. *C. elegans* is a soil nematode, ~1 mm in length, that feeds on bacteria in decaying vegetable matter. Its nervous system consists of only 302 sensory neurons, motor neurons, and interneurons. The neurotransmitters include acetylcholine and γ-aminobutyric acid, which facilitate locomotion and pathogen avoidance. The authors found that worms lacking a cell surface receptor called OCTR-1 in two types of neurons exhibit substantially improved survival against the bacterial pathogen *Pseudomonas aeruginosa*. These neurons—the "ASH" and "ASI" sensory neurons—extend processes into an opening at the anterior end of the worm, where they are exposed to the environment. The protection was observed in the presence of living, but not dead bacteria, indicating that these neurons inhibit the innate immune response to bacterial pathogens. The protection was not attributed to enhanced pathogen avoidance, or pathogen accumulation. Rather, the neurons targeted, in nonneuronal cells, the molecular basis of the unfolded protein response, a mechanism that regulates organellar (endoplasmic reticulum) accumulation of unfolded proteins during periods of heightened protein synthesis, as in infection. Together, these results show that the tonic output of innate immunity is negatively regulated by signals originating in ASH and ASI sensory neurons in the worm (see the figure). Hence, in worms, as in mammals, the innate immune system is not autonomous; it is innervated. Additional work is needed in the worm model of Sun *et al*. to determine the nature of the signals that activate OCTR-1, a putative catecholamine receptor, in sensory neurons. Further work should also reveal how the sensory neurons regulate the unfolded protein response pathway in nonneuronal cells.

How might such a neural controlling system operate, and what are the possible therapeutic implications? A general principle in physiology is that innervation of a system enables reflex control mechanisms to provide a regulatory framework that can fine tune responses over time and space. The inflammatory reflex, a prototypical circuit in mammals, is activated by exposure to pathogens or injury and modulates the innate immune response (*5*). Neurons express Toll-like receptors and cytokine receptors, which detect the presence of pathogens (and perhaps damaged tissue as well) and cytokines, respectively (*6*, *7*). This activates action potentials that ascend to the central nervous system, which in turn sends efferent signals out to the immune system to dampen the responses. Such circuits provide control precision and integration not possible with diffuse, humoral control systems. Thus, the innate immune system is both the origin of signals that are converted to action potentials in the sensory arc, and it is the target of signals descending in the motor arc (*5*).

We have learned much about the efferent pathways controlling innate immunity, and there is now great interest in understanding more about how inflammatory and injurious factors activate the afferent input into this immunological and neurological system. Understanding these mechanisms as a function of "top-down" neurological regulatory processes—that is, as immune responses that are the result of action potentials originating in neurons—should stimulate the identification of new molecular targets and the development of therapeutic alternatives. From worms to humans, there is a consistent evolutionary theme that the immune system detects changes in the environment, and its actions modify the behavior of the animal. The loop is closed by reflex signals originating in the nervous system that modify innate immune responses to maintain homeostasis.

References

1. J. Sun, V. Singh, R. Kajino-Sakamoto, A. Aballay, *Science* **332**, 729 (2011); 10.1126/science.1203411.
2. K. J. Tracey, *J. Clin. Invest.* **117**, 289 (2007).
3. C. Nathan, *Nature* **420**, 846 (2002).
4. H. Wang *et al*., *Nature* **421**, 384 (2003).
5. K. J. Tracey, *Nat. Rev. Immunol.* **9**, 418 (2009).
6. F. Y. Tanga, N. Nutile-McMenemy, J. A. DeLeo, *Proc. Natl. Acad. Sci. U.S.A.* **102**, 5856 (2005).
7. M. K. Boettger *et al*., *Arthritis Rheum.* **58**, 2368 (2008).

10.1126/science.1206353

CHEMISTRY

Designing the Next Generation of Chemical Separation Membranes

New materials can be prepared as membranes that may allow their performance to beat long-standing limits.

Douglas L. Gin and Richard D. Noble

Synthetic membranes are used in many separation processes, from industrial-scale ones—such as separating atmospheric gases for medical and industrial use, and removing salt from seawater—to smaller-scale processes in chemical synthesis and purification. Membranes are commonly solid materials, such as polymers, that have good mechanical stability and can be readily processed into high–surface area, defect-free, thin films. These features are critical for obtaining not only good chemical separation but also high throughput. Membrane-based chemical separations can have advantages over other methods—they can take less energy than distillation or liquefaction, use less space than absorbent materials, and operate in a continuous mode. In some cases, such as CO_2 separations for CO_2 capture, their performance must be improved. We discuss how membranes work, and some notable new approaches for improving their performance.

Membranes work by forming a barrier between two phases (e.g., salt water and fresh water) that restricts the movement of some molecules while letting others through (*1*). Separation is driven by a difference in concentration or pressure (or both) across the membrane—pressurization is the main energy input. Membranes are either dense or porous, depending on how the molecules move across the barrier. In dense membranes, molecules dissolve into the material and diffuse through it (*1*). The product of a molecule's solubility and diffusivity is its perme-

Department of Chemical and Biological Engineering, University of Colorado, Boulder, CO 80309–0424, USA. E-mail: douglas.gin@colorado.edu

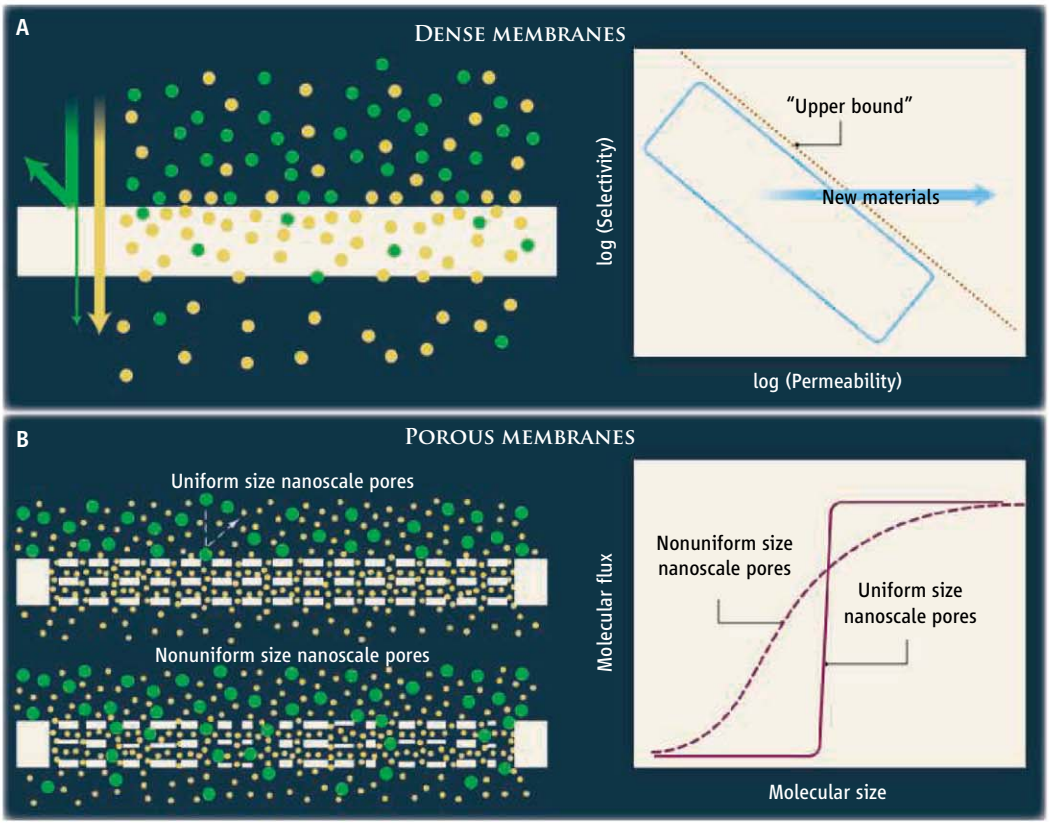

Chemical separation with dense and porous membranes. (**A**) For dense membranes, orange and green molecules move through the membranes at different rates because they have different permeabilities *P*. The Robeson plot shows that conventional dense membranes separate mainly via differences in diffusivity, and performance is limited by an "upper bound." (**B**) Nanoporous membranes separate via molecular size differences. The examples shown are for pores that interconnect into a 3D network. With uniform pore sizes, it is possible to get complete separation (smaller molecules pass through—they have a higher molecular flux; larger ones are completely blocked). With nonuniform pores, the largest pore sizes (i.e., a distribution) dictate the selectivity, and both molecules can pass through.

ability *P*, and membranes are designed so that two (or more) molecules have different *P* values (see the figure, panel A).

In contrast, porous membranes for chemical separations should have pores that are ideally the size of single small molecules (≤1 nm), and molecules pass through as a gas or a liquid solution. Molecules can be separated by size because the nanopores act as a screen or sieve (*1*). Uniform nanopores with the correct size must be continuous across the membrane. If there is a distribution of pore sizes, most of the molecules will pass through the largest pores first (path of least resistance), thereby compromising selectivity (see the figure, panel B).

The limitation of conventional dense polymer membranes is best illustrated by gas separations. Differences in *P* mainly arise from diffusion differences of each gas component in the polymer film—solubilities tend to be similar. Materials that are more permeable (i.e., that have higher throughput and would process gas faster) also have a more open structure and thus have lower selectivity. This compromise leads to an upper bound for separation performance that is shown graphically by plots generated by Robeson (*2*).

A new approach in the design of dense membranes is to use room-temperature ionic liquids (RTILs) in various morphologies. RTILs are liquid-phase organic salts (i.e., ionic compounds) with negligible vapor pressure (avoiding evaporation losses), high thermal stability, and intrinsic solubility for certain gases. Unlike conventional polymers, RTILs perform gas separations via solubility differences. They have been applied to CO_2 separations, but the wide variety of RTILs allows for many candidate separations. Also, RTIL derivatives can be prepared that allow the molecules to be polymerized to form solids so that membranes can be prepared in various morphologies, such as films (*3*), solid composite structures with RTIL within the structure (*3*), and gels (*4*). For RTIL morphologies, the limit on a Robeson plot is determined by the performance of the liquid itself as a membrane because the other morphologies have the same solubility selectivity but different diffusion rates.

Poly(RTIL) films have recently been tested for gas separations up to 40 atm pressure for mixtures of CO_2 and CH_4. The conditioning or morphology change caused by the incorporation of gases such as CO_2 at these high pressures is reversible compared to conventional polymers that exhibit irreversible conditioning at these pressures (*5*). Examples of improved separations include CO_2 from N_2 for postcombustion cleanup of flue gas from power plants.

For nanoporous membranes, several methods have recently been developed that afford materials with uniform molecular-size pores. For example, deposition techniques have been successfully used to reduce the pore size of commercial nanoporous polymer and ceramic membranes down to molecular dimensions (*6*). Recent advances in blending organic polymers with inorganic zeolites have afforded viable composite membranes with uniform pore sizes in the 0.3- to 0.7-nm range for light gas separations, such as CO_2, N_2, and CH_4 (*7*).

Similar approaches for making polymer-based composite membranes containing metal-organic framework compounds (*8*), carbon nanotubes (*9*), and peptide nanotubes (*10*) as the porous component have also been found to be promising for separating different-size ions in water and mixtures of light gases. "Molecular square" coordination compounds (*11*) and macrocyclic surfactants (*12*) also form membranes with molecular-size pores when applied as ordered thin layers on membrane supports. Ordered surfactant liquid crystal assemblies formed in water have successfully been polymerized into membranes with three-dimensional (3D) interconnected pores, smaller than 1 nm in diameter, that act as molecular sieves for water desalination (*13*). Selectively etched phase-segregated block copolymers (*14*) and colloidal crystal assemblies (*15*) are two promising platforms with uniform pores in the 10- to 100-nm range. Such materials are useful for macromolecular or protein separations, but methods are needed to bring the pore sizes down to molecular dimensions if they are to be useful for small-molecule separations.

Other factors are also important for making practical membranes with high through-

put, including high pore density, pore continuity, and the ability to form defect-free thin films. Several of the approaches listed above form 1D columnar pores (*6*, *9*–*12*) that need to be aligned in the flow direction and packed closely together for high membrane flux. Materials with 3D-interconnected pores (*7*, *8*, *13*–*15*) have the advantage that the pores need not be aligned to be continuous across the membrane, and are not easily blocked. These materials also often have better overall pore densities. Although many of the above materials can be processed into films, only a handful have been formed into films thin enough (*6*, *8*, *11*, *12*, *14*) to achieve high fluxes (i.e., thinner membranes have less flow resistance). For researchers working on new dense or porous materials for membrane applications, it is important to consider not only the design factors that afford better separation selectivity but also the factors that afford good productivity.

The future directions for these new membrane materials are very promising, primarily because of the enormous chemical flexibility of their base structures. The separation properties for the application of interest can be tuned, as can operational parameters such as stability and longevity. In addition, functional additives such as selective complexing agents can be incorporated into these new classes of membrane materials, providing exciting new opportunities for enhancing separation performance.

References

1. W. J. Koros, *Chem. Eng. Prog.* **91**, 10 (1995).
2. L. M. Robeson, *J. Membr. Sci.* **320**, 390 (2008).
3. J. E. Bara, D. E. Camper, D. L. Gin, R. D. Noble, *Acc. Chem. Res.* **43**, 152 (2010).
4. B. A. Voss, J. E. Bara, D. L. Gin, R. D. Noble, *Chem. Mater.* **21**, 3027 (2009).
5. K. Simons, K. Nijmeijer, J. E. Bara, R. D. Noble, M. Wessling, *J. Membr. Sci.* **360**, 202 (2010).
6. M. Wirtz *et al.*, *Int. J. Nanosci.* **1**, 255 (2002).
7. Y. C. Hudiono, T. K. Carlisle, A. L. LaFrate, D. L. Gin, R. D. Noble, *J. Membr. Sci.* **370**, 141 (2011).
8. T.-H. Bae *et al.*, *Angew. Chem. Int. Ed.* **49**, 9863 (2010).
9. B. J. Hinds *et al.*, *Science* **303**, 62 (2004).
10. T. Xu *et al.*, *ACS Nano* **5**, 1376 (2011).
11. K. F. Czaplewski, J. T. Hupp, R. Q. Snurr, *Adv. Mater.* **13**, 1895 (2001).
12. X. Yan, V. Janout, J. T. Hsu, S. L. Regen, *J. Am. Chem. Soc.* **124**, 10962 (2002).
13. M. Zhou *et al.*, *J. Am. Chem. Soc.* **129**, 9574 (2007).
14. D. A. Olson, L. Chen, M. A. Hillmyer, *Chem. Mater.* **20**, 869 (2008).
15. M. R. Newton, A. K. Bohaty, H. S. White, I. Zharov, *J. Am. Chem. Soc.* **127**, 7268 (2005).

10.1126/science.1203771

APPLIED PHYSICS

Hot Electrons Cross Boundaries

Devices based on gold nanostructures that convert absorbed light into electrical current can be used to detect near-infrared light.

Martin Moskovits

When light hits the surface of gold or silver, it can excite collective oscillations of the conduction electrons called surface plasmons. The sensitivity of surface plasmons to changes in the surface region forms the basis of analytical tools such as surface plasmon resonance detection, which can be used in lab-on-a-chip applications to detect biomolecules. The excitation of surface plasmons also underlies surface-enhanced Raman spectroscopy. The surface plasmon of silver and gold surfaces that are rough at a nanoscale greatly increases local electric fields and boosts the signal from adsorbed molecules. The wavelength that excites surface plasmons can also be tuned by creating nanoparticles of different sizes, and on page 702 of this issue, Knight *et al*. (*1*) exploit this effect to create a detector for near-infrared light. They fabricated a device consisting of rod-like nanoantennas that harvest light and convert a portion of the resulting plasmonic energy into an electric current without the need for an applied bias voltage.

The fundamental mode of the surface plasmons is similar to that of a quantum harmonic oscillator—a sea of electrons oscillates and creates alternating regions of higher electron density (that is relatively negatively charged) and lower electron density (that is relatively positively charged; see the figure, panel A). Many quanta of

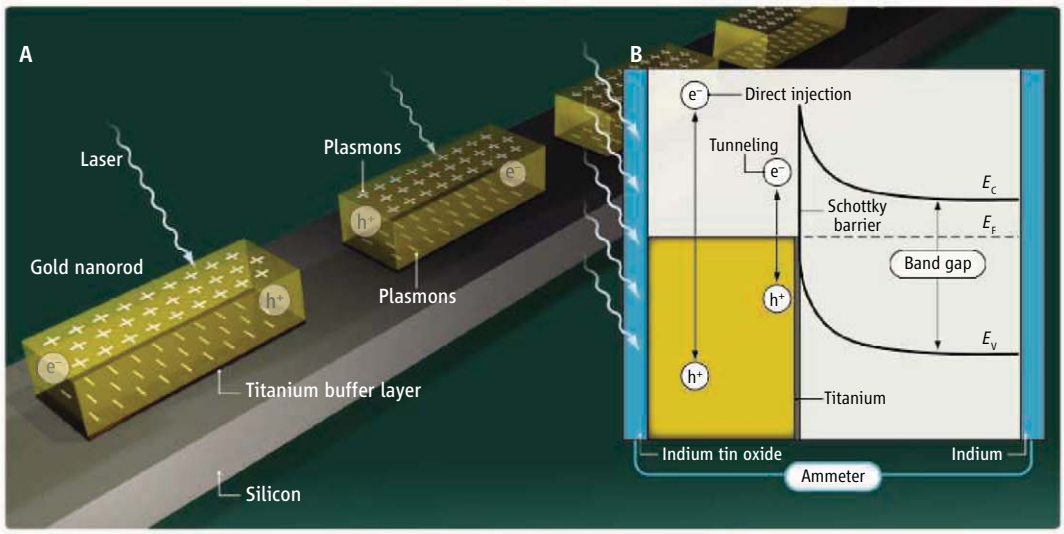

Plasmons to electricity. (**A**) Light excites surface plasmons (depicted as regions of positive and negative charge, top and bottom) that can decay into charge carriers, electrons e^- and holes h^+. Plasmons in shorter nanorods are excited at shorter wavelengths. The nanorods were grown on a titanium (Ti) buffer layer, 1 nanometer thick, on n-type silicon. (**B**) An energy diagram showing how excited electrons created by plasmon decay encounter a Schottky barrier at the metal-silicon interface, which share a common Fermi energy E_F. Highly energetic electrons are either directly injected into the conduction band of silicon above its band edge, E_C, or tunnel through the barrier. The barrier is less than the band gap energy (the difference between E_C and valence band edge, E_V). Holes and electrons produce a measurable photocurrent collected at the indium tin oxide and indium electrodes.

CREDIT: P. HUEY/*SCIENCE*

Department of Chemistry and Biochemistry, University of California, Santa Barbara, Santa Barbara, CA 93106–9510, USA. E-mail: moskovits@chem.ucsb.edu

the incoming light can be stored in the plasmonic oscillator, even when it is illuminated with dim light. In the tetragonal gold nanorods used by Knight *et al*., the plasmon resonance wavelengths are in the near-infrared, and shorter nanorods will have a shorter peak wavelength.

The light quanta stored in the plasmons can be re-emitted as light, but some of the plasmons can also decay into two charge carriers, an electron and a "hole." It has been known for some time that plasmon decay can create "hot" electrons that have high kinetic energy (*2*). However, to create a photocurrent, the electron and hole must be separated. Knight *et al*. extracted the electron into n-type silicon, which has high conductivity for electrons (see the figure, panel B). Normally, these hot electrons would still not have enough energy to enter the conduction band of silicon if they were starting their journey in the occupied molecular orbitals (valence band) of silicon—the energy gap is 1.1 electron volts. The electrons only need to clear a barrier set up at the metal-silicon interface (known as a Schottky barrier; in this case, a barrier of 0.5 electron volt is created by a thin layer of titanium metal used to adhere the gold nanorods). The most energetic fraction of the hot electrons either clear the Schottky barrier, or quantum-mechanically tunnel through it into the conduction band of silicon.

Quantum-mechanical tunneling depends not only on barrier height but also on its breadth. Tunneling is enhanced in this device because the barrier decreases as the electron moves into the silicon, an effect called conduction-band bending. Because the electrons have high kinetic energy, they need travel only a short distance beyond their point of generation before they become conduction electrons in silicon—too short a distance for them to lose energy through other relaxation processes. They then become trapped in the semiconductor by the barrier.

Plasmonic systems can be designed to cover much of the solar spectrum, so this approach suggests a photosensitization strategy, much like the one exploited by Grätzel in dye-sensitized photovoltaics (*3*), but avoiding the problem of easily photodegradable organics. Although Knight *et al*. report very low quantum efficiencies, there is no physical reason why efficiencies cannot be much larger and lead to applications in energy conversion and photodetection.

References

1. M. W. Knight, H. Sobhani, P. Nordlander, N. J. Halas, *Science* **332**, 702 (2011).
2. V. M. Shalaev, C. Douketis, J. T. Stuckless, M. Moskovits, *Phys. Rev. B* **53**, 11388 (1996).
3. M. Grätzel, B. O'Regan, *Nature* **353**, 737 (1991).

10.1126/science.1205312

IMMUNOLOGY

Flow Cytometry, Amped Up

The novel technique of mass cytometry opens a new chapter in single-cell biology.

Christophe Benoist[1,2] and Nir Hacohen[2,3]

In multicellular organisms, cells carry out a diverse array of complex, specialized functions. This specialization occurs mostly through the expression of cell type–specific genes and proteins that generate the appropriate structures and molecular networks. A central challenge in the biomedical sciences, however, has been to identify the distinct lineages and phenotypes of the specialized cells in organ systems, and track their molecular evolution during differentiation. On page 687 of this issue, Bendall *et al*. (*1*) offer a brilliant proof of principle for a novel technology—mass cytometry—and provide a uniquely detailed view of cell differentiation in the human hematopoietic system. They used this technology to simultaneously examine 34 attributes of human bone marrow cells and then create a superimposed map showing the complex interactions of cell signaling molecules, all at an unprecedented level of resolution. This opens a new chapter in single-cell biology.

Since the 1970s, fluorescence-based flow cytometry has been the leading technique for studying and sorting cell populations (*2*). It involves passing cells through flow chambers at high rates (>20,000 cells/s) and using lasers to excite fluorescent tags ("fluorochromes") that are usually attached to antibodies; different antibodies are tagged with different colors, enabling researchers to quantify molecules that define cell subtypes or reflect activation of specific pathways. Progress in instrument design, multilaser combinations, and novel fluorochromes has led to experimental configurations that simultaneously measure up to 15 markers. This has enabled very detailed description of cell subtypes, perhaps most extensively in the immune system, where the Immunological Genome Project is profiling >200 distinct cell types. Fluorescence cytometry seems to have reached a technical plateau, however: In practice, researchers typically measure only 6 to 10 cell markers because they are limited by the spectral overlap between fluorochromes (see the figure).

To escape this plateau, a group led by Scott Tanner of the University of Toronto in Canada devised the radically new approach of mass cytometry (CyTOF) (*3*), and teamed with a group led by Garry Nolan of Stanford University in California, who has long been a leader in developing higher-dimensional multicolor flow cytometry, especially for studying intracellular signaling components (*4*). In mass cytometry, fluorochrome tags are replaced by a series of rare earth elements (e.g., lanthanides), which are attached to antibodies through metal-chelator coupling reagents. Cells are labeled by incubation in a cocktail of tagged antibodies; as the cells flow through the instrument, they are vaporized at 5500 K, and the released tags are identified and quantified by time-of-flight mass spectrometry (MS). Rates are reasonable, at 1000 cells/s. The beauty of the approach stems from three factors: the precision of MS detection, which eliminates overlap between tags (a dream for any investigator who has battled this problem, known as fluorescence compensation); the number of detectable markers (34 here, but easily more); and the absence of background noise (because rare earth elements are essentially absent from biological materials, there is no equivalent of "autofluorescence"). Because the software tools commonly used for flow cytometry data would be woefully inadequate for analyzing dozens of dimensions, Bendall *et al*. used software that clusters cell populations into "minimum-spanning trees" that reproduce known hematopoietic differentiation, but with much finer granularity. As a result, cells that once would

[1]Department of Pathology, Harvard Medical School, Boston, MA 02115, USA. [2]Broad Institute, Cambridge, MA 02142, USA [3]Center for Immunology and Inflammatory Diseases, Massachusetts General Hospital, Charlestown, MA 02129, USA. E-mail: cb@hms.harvard.edu, nhacohen@partners.org

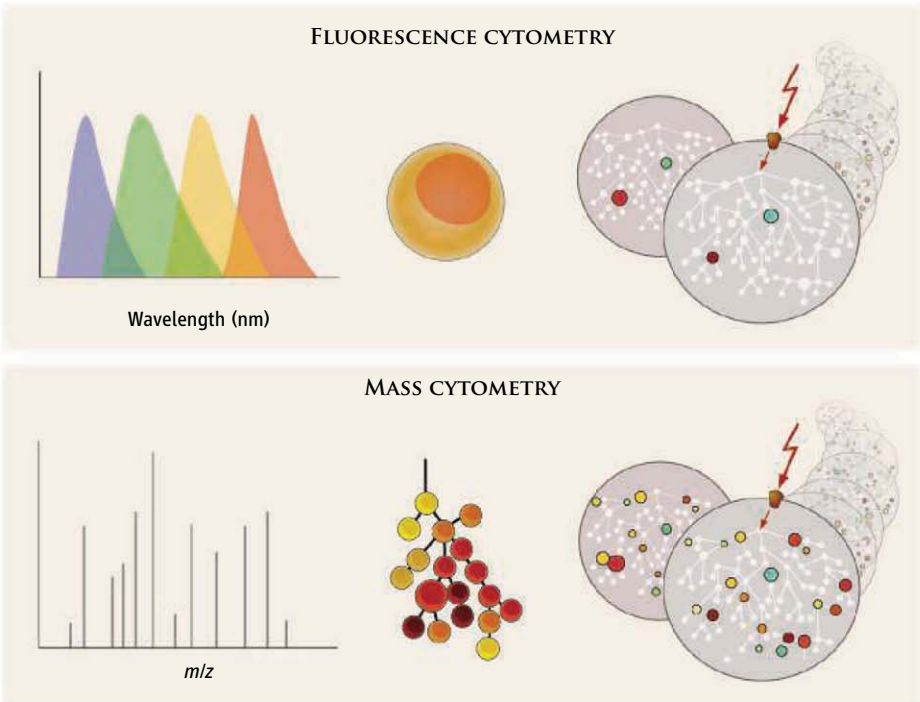

Fluorescence versus mass cytometry. Mass-tagging of antibodies allows for unfettered resolution of more labels (**bottom**, **left**) when compared with conventional detection of fluorescent antibody tags (**top**, **left**), which is hampered by overlap between emission spectra. Mass cytometry thus increases the discrimination power for cell subset analysis (**top and bottom**, **center**) and allows a far more comprehensive perspective on intracellular signaling pathways (**top and bottom**, **right**). *m/z*, mass/charge ratio.

have been grouped into one population are now divided into many more; for example, naïve $CD4^+$ T lymphocytes, a priori considered a homogeneous population, are now split into more than 10 subsets.

Like any new technology, mass cytometry has limitations. Most obviously, cells vaporized in a CyTOF cannot be recovered for further analysis or growth, as with conventional flow cytometry. A combination of techniques may evolve, with researchers using mass cytometry for broad initial analyses, from which they will define a minimal set of markers for fluorescence-based sorting. In addition, the procurement of labeled reagents will undoubtedly be a hurdle. Assembling and testing a set of labeled antibodies for a 35-plex experiment is no small feat. Unlike nucleic acid probes, which have reasonably uniform properties and can be synthesized cheaply in massively parallel formats, monoclonal antibodies are expensive, and each has a different affinity, stability, and resistance to conjugation chemistries. The range of antibodies that bind to specific proteins also is limited, in particular for their posttranslational, modified forms. Hopefully, researchers and commercial suppliers, with support from funding agencies, will tackle the challenge of developing panels of reagents. Standardized sets of conjugated antibodies that bind with surface molecules and intracellular signaling intermediates (across many known pathways) would be invaluable for studies of human inflammatory diseases.

Why is this technology a game-changer? One might argue that increasing from 15 to 35 simultaneous parameters is not in itself a dramatic conceptual leap. It is conceivable that the fine parsing of lymphocyte subsets by Bendall *et al*. could have been achieved by iterative application of conventional flow cytometry. Yet there is no doubt that the broader perspective given by this single CyTOF experiment greatly accelerated this parsing. It will be important, however, to determine whether the finer and finer cell subsets identified by mass cytometry merely represent an artifact of the clustering algorithm, or are both "real" (reproducible) and have functionally relevant differences. Although the physiological functions of different cell subsets may take a long time to work out, CyTOF can be used to test whether signaling pathways behave differently in each subset. After placing cells in different contexts (e.g., a range of stimuli), CyTOF can measure tens of signaling intermediates and determine if each cell subset uses subtly distinct cascades of signaling events. For example, differences in NF-κB activation were detected by Bendall *et al*. Quantitation of RNA or other molecular species, which should also be possible by mass spectrometry, may further help to anchor these subphenotypes.

It is perhaps in the emerging field of "single-cell biology" that CyTOF may make a unique contribution to dissecting intracellular networks. Much of biochemistry and molecular biology rests on the assumption that the behavior of cells in a population (in a culture, in an organ) can be reliably approximated by the population average that results when cells are lysed and their molecules analyzed as a pool. Increasingly, however, investigators realize that stochastic fluctuations in gene or protein expression, between cells of an otherwise identical group, can lead to major differences in their behavior. This "noise" in gene expression (*5*, *6*) can have profound consequences for cell differentiation (*7*), the response to apoptosis-inducing stimuli (*8*), or T lymphocyte triggering at the initiation of immune responses (*9*).

Mass cytometry can help researchers both take this stochasticity into account, and benefit from it. The secret is that, in flow cytometry, every cell acts as an independent "test tube." The ability to generate millions of independent datapoints, simultaneously measuring the activation of many signaling nodes in each cell, together with expression levels of key sensors or controlling factors, will enable researchers to infer connections within these biochemical networks (*10*).

It is easy to see how this technology will be used to analyze disease states or an individual's response to therapeutics. A problem in disease exploration is often to study the "correct" cell subtype or pathway. Most often, RNA or protein is analyzed from pooled cells, obscuring disease-related signals that might show up in specific cells or pathways. Mass cytometry is poised to revolutionize our studies of disorders in the human immune system by probing multiple critical parameters in parallel, across a broad range of cells and pathways.

References

1. S. C. Bendall *et al*., *Science* **332**, 687 (2011).
2. L. A. Herzenberg *et al*., *Clin. Chem.* **48**, 1819 (2002).
3. D. R. Bandura *et al*., *Anal. Chem.* **81**, 6813 (2009).
4. O. D. Perez, G. P. Nolan, *Nat. Biotechnol.* **20**, 155 (2002).
5. A. Sigal *et al*., *Nature* **444**, 643 (2006).
6. J. M. Pedraza, A. van Oudenaarden, *Science* **307**, 1965 (2005).
7. T. Kalmar *et al*., *PLoS Biol.* **7**, e1000149 (2009).
8. S. L. Spencer, P. K. Sorger, *Cell* **144**, 926 (2011).
9. O. Feinerman, J. Veiga, J. R. Dorfman, R. N. Germain, G. Altan-Bonnet, *Science* **321**, 1081 (2008).
10. K. Sachs, O. Perez, D. Pe'er, D. A. Lauffenburger, G. P. Nolan, *Science* **308**, 523 (2005).

10.1126/science.1206351

RETROSPECTIVE

Jürg Tschopp (1951–2011)

A scientist's basic research into cell death and inflammation will continue to have a clinical impact.

Luke A. O'Neill

Jürg Tschopp—biochemist, pioneer in the study of inflammation, researcher par excellence—died suddenly of a heart attack on 22 March while hiking with his wife and son in the Swiss Alps. He was 60 years old. Jürg was a hero to so many colleagues and the wider research community. His work on programmed cell death (apoptosis) and inflammation over the past 20 years made him the most important biochemist in these fields. His discoveries led to therapies for inflammatory diseases, which he described to me as the most satisfying outcome of his career.

The goal of every biochemist is to find and define the function of the biochemicals and proteins that participate in biological processes. Jürg discovered major players that control immune responses and in the competitive business of naming new molecules, his names for some of these have stuck—names that will last as long as immunology does. Some scientists gain fame for discovering new molecules, some for working out the functions of molecules discovered by others. Jürg is one of the few scientists who can rightly claim both of these achievements. The clinical impact of this work is now beginning to be felt, notably in autoimmune diseases such as systemic lupus erythematosus [where an inhibitor for a molecule that he discovered, called B cell–activating factor (BAFF), was recently approved by the U.S. Food and Drug Administration], and autoinflammatory diseases such as gout, where targeting interleukin-1β is proving effective. For these translational achievements, Jürg was awarded in 2010, along with Charles Dinarello, the Novartis Clinical Immunology Prize. Jürg told me he was especially proud to win this award with Charles, the discoverer of IL-1. With typical modesty, Jürg felt that he was a latecomer to the field of IL-1 research and didn't deserve the prize, having first reported on the inflammasome complex that regulates this cytokine in 2001. The discovery of this complex, along with those of Dan Kastner and Hal Hoffman in inflammasome-mediated hereditary fevers, however, ignited a renaissance of interest in IL-1 that continues to blaze.

Jürg received his Ph.D. in biophysics in 1979 from the University of Basel. He then joined the group of Hans Müller-Eberhard at the Scripps Clinic in La Jolla, California, to work on the membrane attack complex of complement. This spurred his interest in cell death, and he went on to discover granzymes and perforins (both of which he named) as key mediators of cytolytic T cell killing of virally infected cells. By this stage he was back in Switzerland, and he spent the rest of his professional life at the University of Lausanne (since 2003, he was co-director of the Department of Biochemistry). His research focused on signaling pathways that control apoptosis and inflammation. Biochemists traditionally purify components using chromatography, and Jürg was an extremely capable biochemist. He was also, however, one of the first to realize the potential of bioinformatics for finding new molecules and used this approach to great effect. His work on apoptosis continued, with important findings in the area of Fas-mediated cell death, on members of the tumor necrosis factor (TNF) cytokine family [most notably TNF-related apoptosis-inducing ligand (TRAIL) and BAFF], and on complex signaling pathways elicited by TNF. His work on the kinase receptor–interacting protein 1 (RIP1) and cell death can be seen in retrospect as an important forerunner of the process now called "necroptosis." He also named a protein complex involved in cell death, the "PiDDosome."

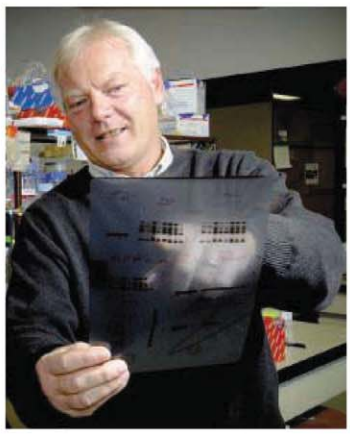

His talent for naming things continued, perhaps most notably in his naming of the inflammasome. I vividly remember the first time he described the inflammasome complex. We were both speaking at a session of the International Cytokine Society–Society of Leukocyte Biology joint meeting in 2001 on the island of Maui. I gave my talk ahead of Jürg and recollect being asked a few questions. Jürg was next and I sat, amazed, as he described for the first time the purification and characterization of what he called the inflammasome. There wasn't a single question. After the session I expressed my excitement about what he had just introduced and said it was strange that there were no questions. Jürg just replied with a wry smile,"Maybe they didn't understand my Swiss accent." However, we now know that in this case, as in many others, Jürg's thinking was simply far ahead of his peers.

I have so many memories of Jürg's interesting presentations and talking with him afterwards that I feel his loss especially acutely at conferences. One particular memory stands out. We were both at a Keystone Symposium in Colorado, and I asked if he would like to join a few of us for a drink. We had a few beers, and as the meeting venue was at high altitude, the effects were keenly felt. He continually teased me for making him drink so much beer, giving him an appalling headache. I took this to be an example of Swiss humor.

Like many scientists, Jürg had an interest in commercializing his research and founded two campus companies. A company that I cofounded licensed some technology around NLRP3 from one of his companies that developed NLRP3 inhibitors. This was greatly amusing to Jürg, who felt that I might benefit from his NLRP3 discoveries, although I promised to always buy the drinks should there be any financial rewards. He had a realistic view, to say the least, regarding the world of venture capitalists.

The film director Orson Welles famously noted that Italy, under the Borgias, had 30 years of warfare, terror, murder, and bloodshed, but had produced Michelangelo, Leonardo da Vinci, and the Renaissance. In Switzerland, they had brotherly love, 500 years of democracy, and peace, yet what did that produce? The cuckoo clock. Well, Switzerland gave us Jürg Tschopp, the most important scientist in the field of inflammation to have come out of Europe in our lifetime. He was a wonderfully generous scientist with a strong view that science is a hugely collaborative exercise whose key goal is to benefit humanity. His impact will continue to be felt, and we will miss him greatly.

School of Biochemistry and Immunology, Trinity College Dublin, Dublin-2, Ireland. E-mail: laoneill@tcd.ie

10.1126/science.1207046

CREDIT: BIOCHEMISTRY DEPARTMENT/UNIVERSITY OF LAUSANNE

Scaffold Proteins: Hubs for Controlling the Flow of Cellular Information

Matthew C. Good,[1]* Jesse G. Zalatan,[1] Wendell A. Lim[1,2,3]†

The spatial and temporal organization of molecules within a cell is critical for coordinating the many distinct activities carried out by the cell. In an increasing number of biological signaling processes, scaffold proteins have been found to play a central role in physically assembling the relevant molecular components. Although most scaffolds use a simple tethering mechanism to increase the efficiency of interaction between individual partner molecules, these proteins can also exert complex allosteric control over their partners and are themselves the target of regulation. Scaffold proteins offer a simple, flexible strategy for regulating selectivity in pathways, shaping output behaviors, and achieving new responses from preexisting signaling components. As a result, scaffold proteins have been exploited by evolution, pathogens, and cellular engineers to reshape cellular behavior.

Mammalian cells contain an estimated 1 billion individual protein molecules, with as many as 10% of these involved in signal transduction (*1*). Given this enormous number of molecules, it seems remarkable that cells can accurately process the vast array of signaling information they constantly receive. How can signaling proteins find their correct partners—and avoid their incorrect partners—among so many other proteins?

A principle that has emerged over the past two decades is that cells achieve specificity in their molecular signaling networks by organizing discrete subsets of proteins in space and time (Fig. 1A) (*2*–*4*). For example, functionally interacting signaling components can be sequestered into specific subcellular compartments (e.g., organelles) or at the plasma membrane. Another solution is to assemble functionally interacting proteins into specific complexes. More than 15 years ago, the first scaffold proteins were discovered—proteins that coordinate the physical assembly of components of a signaling pathway or network (*5*–*10*). These proteins have captured the attention of the signaling field because they appear to provide a simple and elegant solution for determining the specificity of information flow in intracellular networks (*2*, *11*, *12*). We review our current understanding of these organizational proteins: the types of pathways that they coordinate, the ways that they shape signaling responses, their biochemical and structural mechanisms, and how they are used in evolution or engineering to change signaling behaviors.

Scaffold Proteins: Versatile Tools to Assemble Diverse Pathways

Scaffolds are extremely diverse proteins, many of which are likely to have evolved independently. Nonetheless they are conceptually related, in that they are usually composed of multiple modular interaction domains or motifs (see Box 1A for an example). Their exact domain composition and order, however, can vary widely depending on the pathways that they organize.

In some cases, homologous individual interaction motifs can be found in scaffolds associated with particular signaling proteins. For example, the AKAPs (A-kinase anchoring proteins), which

[1]Department of Cellular and Molecular Pharmacology, University of California, San Francisco, CA 94158, USA. [2]Center for Systems and Synthetic Biology, University of California, San Francisco, CA 94158, USA. [3]Howard Hughes Medical Institute, University of California, San Francisco, CA 94158, USA.

*Present address: Department of Molecular and Cellular Biology, University of California, Berkeley, CA 94720, USA.
†To whom correspondence should be addressed. E-mail: lim@cmp.ucsf.edu

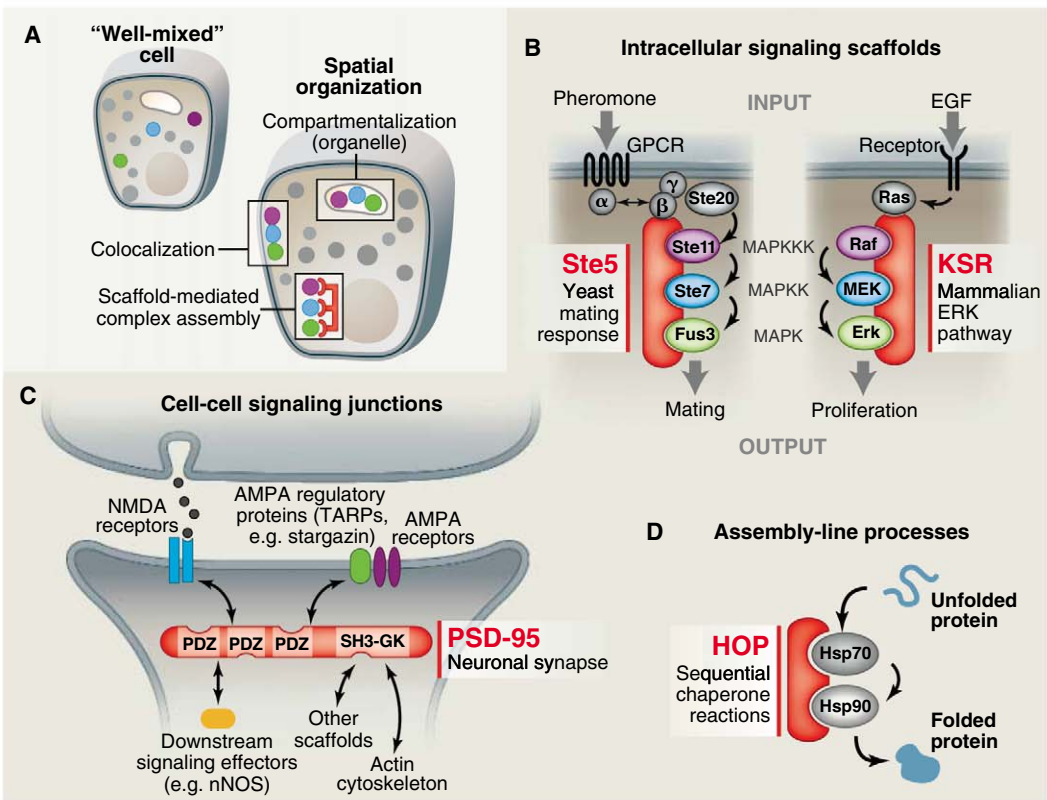

Fig. 1. Scaffold proteins organize cellular information flow. (**A**) Spatial organization is necessary to achieve high-fidelity intracellular information transfer. Proteins can be assembled into specific complexes by compartmentalization (organelle targeting), by membrane localization, and by scaffold proteins. (**B**) Intracellular signaling pathways often use scaffold proteins. Canonical examples include Ste5, essential to the yeast mating MAPK pathway, and KSR, which directs signaling in the mammalian Ras-Raf-MEK-MAPK pathway. (**C**) Scaffold proteins also play an important role in organizing cell-cell communication junctions, such as neuronal synapses. The PDZ scaffold, PSD-95, controls NMDA and AMPA glutamate receptor targeting to the synapse. (**D**) Assembly-line processes such as protein folding use scaffold proteins. The HOP protein promotes transfer of unfolded proteins between Hsp70 and Hsp90 chaperones.

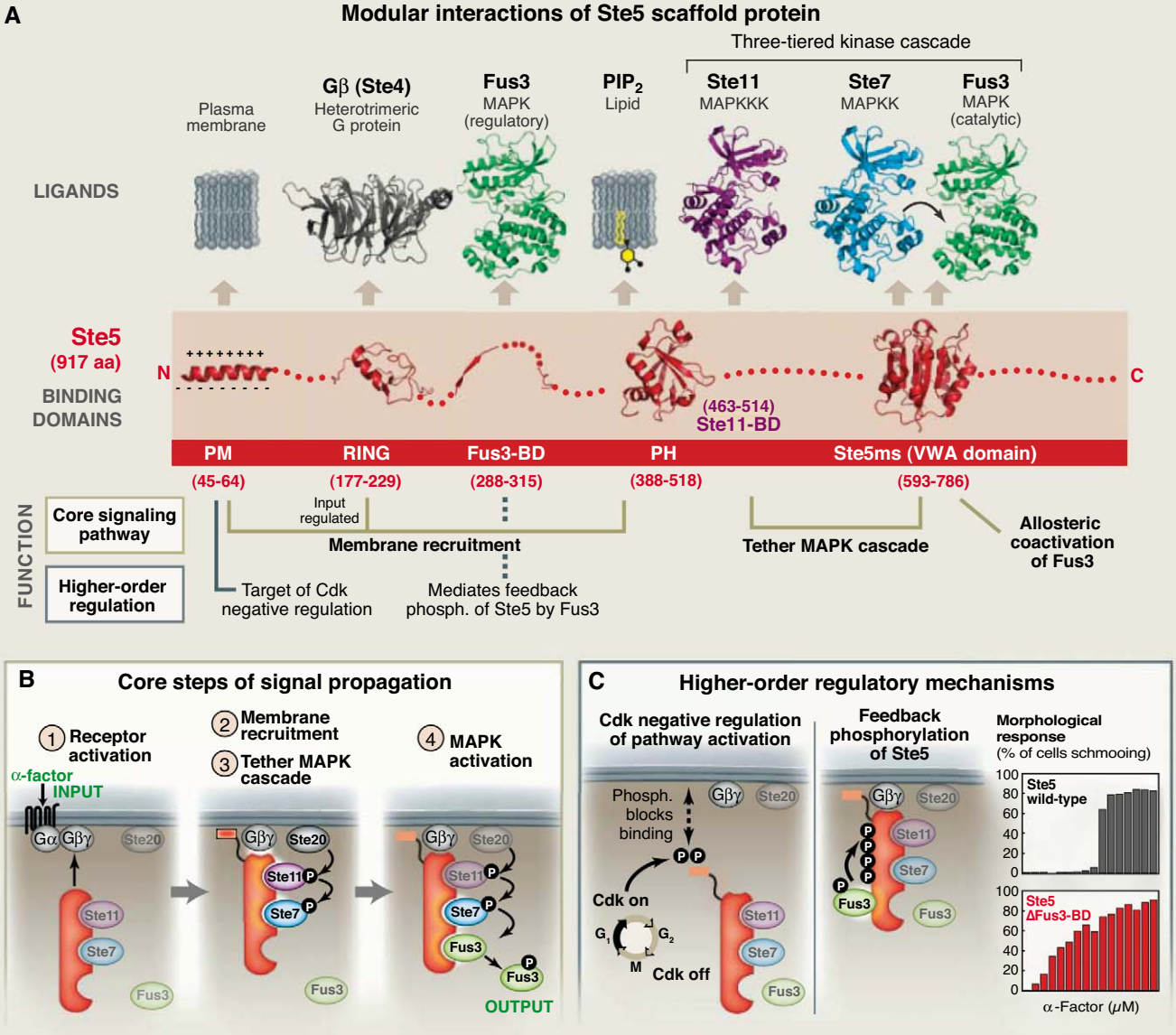

Box 1. Structure and mechanisms of a canonical scaffold: the MAPK scaffold protein Ste5. (**A**) The Ste5 scaffold protein is composed of modular interaction domains, some of which mediate essential steps in the three-tiered mating MAPK signaling cascade, and some of which function in higher-order regulatory behaviors. (**B**) Core steps of mating pathway (see also movie S1): Binding of α-factor peptide to its receptor (Ste2) leads to activation of the guanine nucleotide binding protein (G protein) and dissociation of Gβγ (Ste4 and Ste18) from the Gα subunit (Gpa1). The Ste5 RING domain binds to the free Gβγ complex (*54*, *55*), triggering rapid recruitment of the scaffold to the membrane. Stabilization and discrete localization of Ste5 at the plasma membrane also require the interaction of its PM domain (an amphipathic helix) (*14*, *25*) and a cryptic pleckstrin homology (PH) domain with the lipid bilayer or anchored phosphoinositides (*13*). A region on Ste5 that overlaps with the PH domain binds to the MAPKKK Ste11 (*5*, *56*) and, upon pathway activation, colocalizes the MAPKKK Ste11 with its activator, Ste20 [a MAPKKKK, similar to the p21-activated kinase (PAK)], which is localized to the membrane in a preactivated state. Phosphorylation of the MAPKKK Ste11 by Ste20 initiates the MAPK cascade. The MAPKK Ste7 is assembled into the mating signaling complex through the VWA domain of Ste5 (PDB ID 3FZE), and can be efficiently phosphorylated by the colocalized and activated MAPKKK Ste11. The minimal VWA also functions as a coactivator that permits Ste7 activation of the MAPK Fus3, which is tethered to Ste7 via docking motifs (PDB ID 2B9H) (*18*, *57*) (see Fig. 4C). (**C**) The Ste5 scaffold also takes part in higher-order regulatory processes. Phosphorylation of the PM helix by Cdk blocks Ste5 membrane binding (*25*), thus preventing activation of the mating response at specific stages of the cell cycle. The Fus3-binding domain (Fus3-BD; PDB ID 2F49) appears to be important for regulatory feedback phosphorylation of Ste5 by Fus3, rather than for core signal transmission through the MAPK cascade (*27*). Phosphorylation of at least four sites on the Ste5 scaffold is dependent on recruitment of Fus3 though the Fus3-BD. These regulatory phosphorylation sites on the scaffold inhibit pathway activity and are thought to help shape the ultrasensitive cell morphology response (shmooing) that occurs during mating. Mutation of the Fus3-BD does not prevent mating but rather leads to a much more graded shmooing response when stimulated by α-factor (*27*, *28*, *39*). Thus, this regulatory interaction may shape this switch-like cell-fate decision. Structures not denoted by PDB numbers in (B) and (C) were created using homology models.

link protein kinase A (PKA) to diverse signaling processes, all share a common short peptide motif that binds to the regulatory subunit of PKA (*4*). However, the other domains in individual AKAPs are highly variable, depending on what inputs and outputs the scaffold protein coordinates with PKA. Thus, scaffold proteins are flexible platforms assembled through mixing and matching of interaction domains.

There are a number of examples of convergent scaffold evolution. For example, the Ste5 protein in yeast and the KSR (kinase suppressor of Ras) protein in mammals (Fig. 1B) both coordinate mitogen-activated protein kinase (MAPK) pathways but do not appear to be related in sequence. The Ste5 and KSR scaffold proteins both carry out a similar set of functions: They physically assemble the individual kinases that make up their cognate MAPK cascades (as well as upstream regulators) (Fig. 1B) (*5*, *7*, *8*); they control MAPK pathway localization (e.g., membrane anchoring) (*8*, *13*, *14*); they can insulate MAPK signaling proteins from competing inputs, such as components from functionally distinct MAPK pathways (*15*, *16*); and they are required for efficient signaling (*17*, *18*). Box 1 summarizes the mechanisms used by the Ste5 scaffold protein to control yeast MAPK signaling. Thus different molecular implementations of scaffolds can be used to play a similar role in signaling.

Scaffold proteins that direct intracellular signaling are not limited to coordinating kinase cascades; they can organize other classes of molecules, such as those involved in guanosine triphosphatase (GTPase) signaling. For example, the yeast protein Bem1 directs the interaction between the guanine nucleotide exchange factor (GEF) Cdc24 and its downstream GTPase substrate, Cdc42 (*19*). Such coordinated GTPase regulation controls precise morphological behaviors such as polarized budding of yeast cells.

Scaffold proteins can also coordinate communication at cell-cell signaling junctions such as neuronal synapses. Synaptic scaffolds, such as the PDZ domain–containing protein PSD-95, contain a set of domains that bind to neuronal receptors [such as *N*-methyl-D-aspartate (NMDA) receptors], to other scaffold proteins, and to the actin cytoskeleton. They build preformed assemblies that are precisely anchored at sites of cell-cell contact (e.g., the postsynaptic density), thus allowing cells to respond efficiently to stimuli (e.g., neurotransmitter release from the partner cell) (*20*). PSD-95 also helps to determine the output of synaptic activation by colocalizing key downstream effectors, such as neuronal nitric oxide synthase (nNOS) (which is activated by local calcium influx upon NMDA receptor activation) (Fig. 1C). These scaffolds also mediate key functional changes at the synapse: They coordinate the stimulus-induced recruitment of α-amino-3-hydroxy-5-methyl-4-isoxazolepropionic acid (AMPA) receptors to synapses, a process thought to be required for long-term potentiation and memory. These critical regulatory changes at properly stimulated synapses are mediated by direct interaction of PSD-95 and other scaffolds with a class of proteins known as transmembrane AMPA receptor regulatory proteins (TARPs) (*21*). The scaffold proteins that function in cell-cell communication not only coordinate the signaling molecules that they interact with, but also target or anchor the complexes at the appropriate cellular location for receiving specific inputs. For example, the related PDZ domain scaffold, InaD,

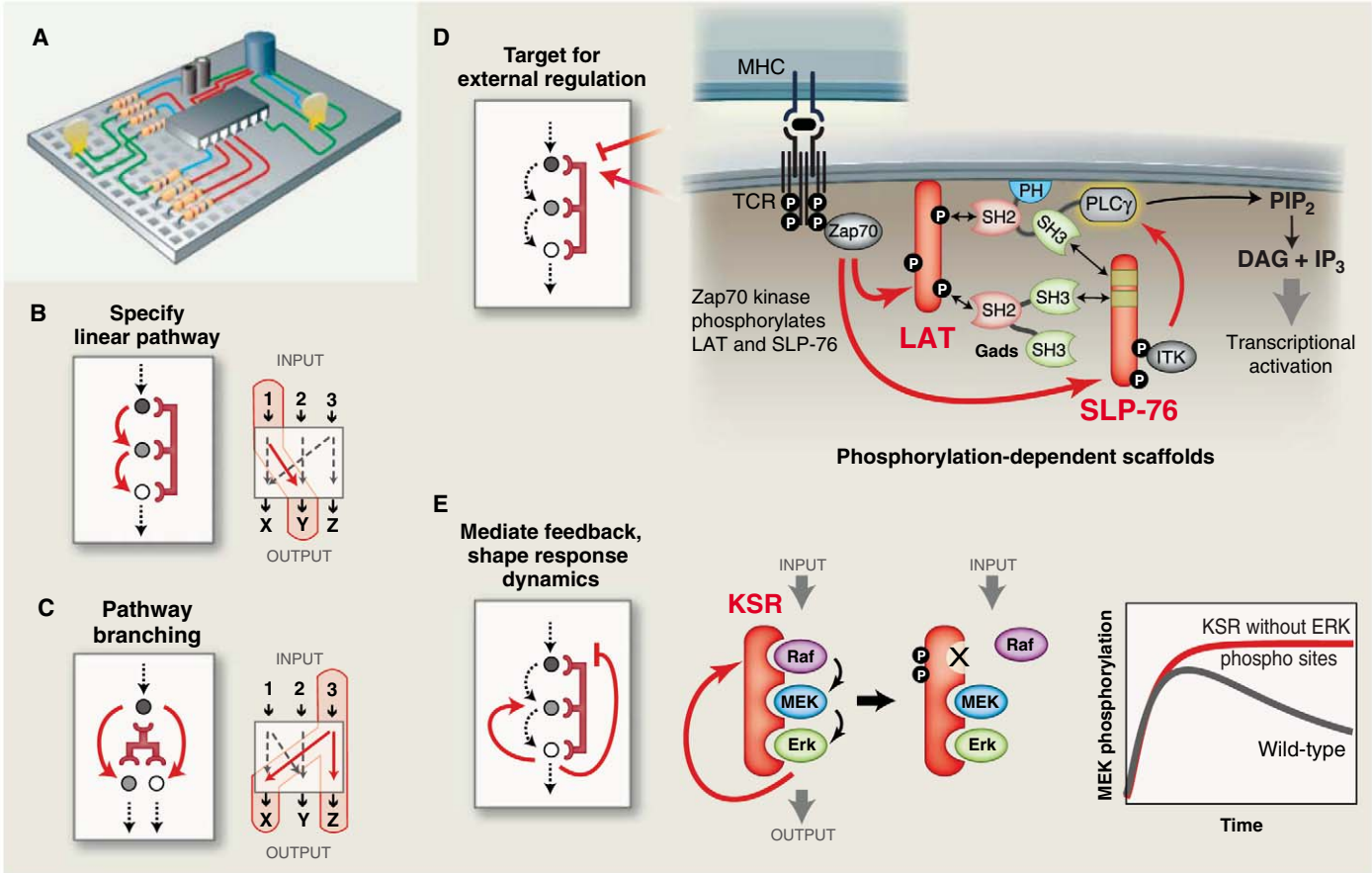

Fig. 2. Scaffold proteins can mediate pathway regulation and feedback to shape complex signaling responses. (**A**) Scaffold proteins are analogous to circuit boards—modular platforms that wire together components and direct the flow of information—and can program complex signaling behaviors. (**B**) Scaffold proteins function to wire pathway input and output through alternative possible routes. (**C**) Scaffold proteins can mediate branching of pathways to multiple outputs. (**D**) Scaffold proteins are themselves the targets of regulation. In T cell signaling, activation of the T cell receptor causes phosphorylation of the LAT and Slp76 scaffolds by Zap70, and phosphorylation-dependent recruitment of substrates leads to phospholipase C–γ (PLCγ) activation and PIP_2 hydrolysis. (**E**) Scaffold proteins can be the target of feedback phosphorylation that tunes pathway responses. Feedback phosphorylation of the KSR scaffold by activated ERK blocks Raf (MAPKKK) binding and attenuates MEK activation, thereby decreasing pathway output. [Plot adapted from (*24*)]

organizes the visual response cascade in the fruit fly (*9*, *22*).

Scaffold proteins can also coordinate assembly-line processes—situations where a molecule must be passed from one partner to another in a sequential manner. Proper folding of some client proteins, such as steroid hormone receptors, appears to require a sequential handoff from Hsp70 to Hsp90 chaperones, a process that is coordinated by the scaffold HOP (Hsp70 and Hsp90 organizing protein) (Fig. 1D) (*23*). Thus, scaffold proteins can have functions in controlling the flow of different classes of biological information that extend beyond what is traditionally considered signal transduction.

Circuit Boards for Wiring Pathway Connectivities and Shaping Pathway Responses

Scaffold proteins can be thought of as molecular circuit boards that can organize a wide variety of circuit relationships between signaling proteins (Fig. 2A). There appear to be common themes to the types of functional circuit topologies organized by scaffold proteins, despite the diversity of their molecular implementation.

The conceptually simplest scaffold proteins determine a specific linear input-output pathway among a set of potential partner proteins (Fig. 2B). Scaffold proteins can also mediate pathway branching—the fanning out of signaling information to multiple outputs that are part of the assembled complex (Fig. 2C).

In an increasing number of cases, scaffold proteins have been found to be direct targets for regulation: Pathways can be turned on or off by inputs that modify the scaffold protein rather than the actual signaling enzymes (Fig. 2D) (*24*, *25*). One of the clear benefits of using scaffold proteins to organize signaling complexes is that protein recruitment, and thus pathway function, can be easily regulated by external signals that modify association of other proteins with the scaffold. The scaffold proteins LAT and SLP-76, which help organize T cell signaling (Fig. 2D), provide an elegant example of this positive regulation. Under basal conditions, LAT and SLP-76 do not assemble active signaling complexes. However, upon T cell activation, the tyrosine kinase Zap70 is activated and recruited to the T cell receptor and phosphorylates a number of tyrosine motifs within the scaffold proteins LAT and SLP-76. These phosphorylated sites act as docking motifs for several Src homology 2 (SH2) domain–containing proteins (*10*, *26*). The phosphorylation-induced assembly of this complex triggers the major downstream pathways of T cell activation.

Scaffold phosphorylation can also be inhibitory and can block protein-protein and protein-lipid interactions. Phosphorylation of the yeast Ste5 scaffold protein by the cell cycle–regulated kinase Cdk1 (cyclin-dependent kinase 1) blocks association of the scaffold with the plasma membrane, thereby specifically attenuating mating signaling after cells have committed to the "start" (G_1-S transition) of the cell cycle (Box 1C) (*25*).

Perhaps the most sophisticated role of scaffold proteins is to coordinate complex feedback loops in signaling pathways by, for example, coordinating mechanisms that can turn off the pathway (Fig. 2E) (*27*, *28*). In these cases, the scaffold appears to play a central role in precisely shaping signaling response properties, such as dynamics or dose response. For example, the KSR scaffold protein assembles a three-tiered MAPK pathway in mammalian cells, and activation of the terminal MAPK creates a feedback loop that phosphorylates the KSR scaffold and the MAPK kinase kinase (MAPKKK) Raf (Fig. 2E). These modifications disrupt binding of the MAPKKK to the KSR scaffold and shut down pathway activation (Fig. 2E) (*24*). Mutation of the KSR phosphorylation sites results in dissociation of the scaffold from the plasma membrane and abnormal pathway dynamics, including sustained pathway activation.

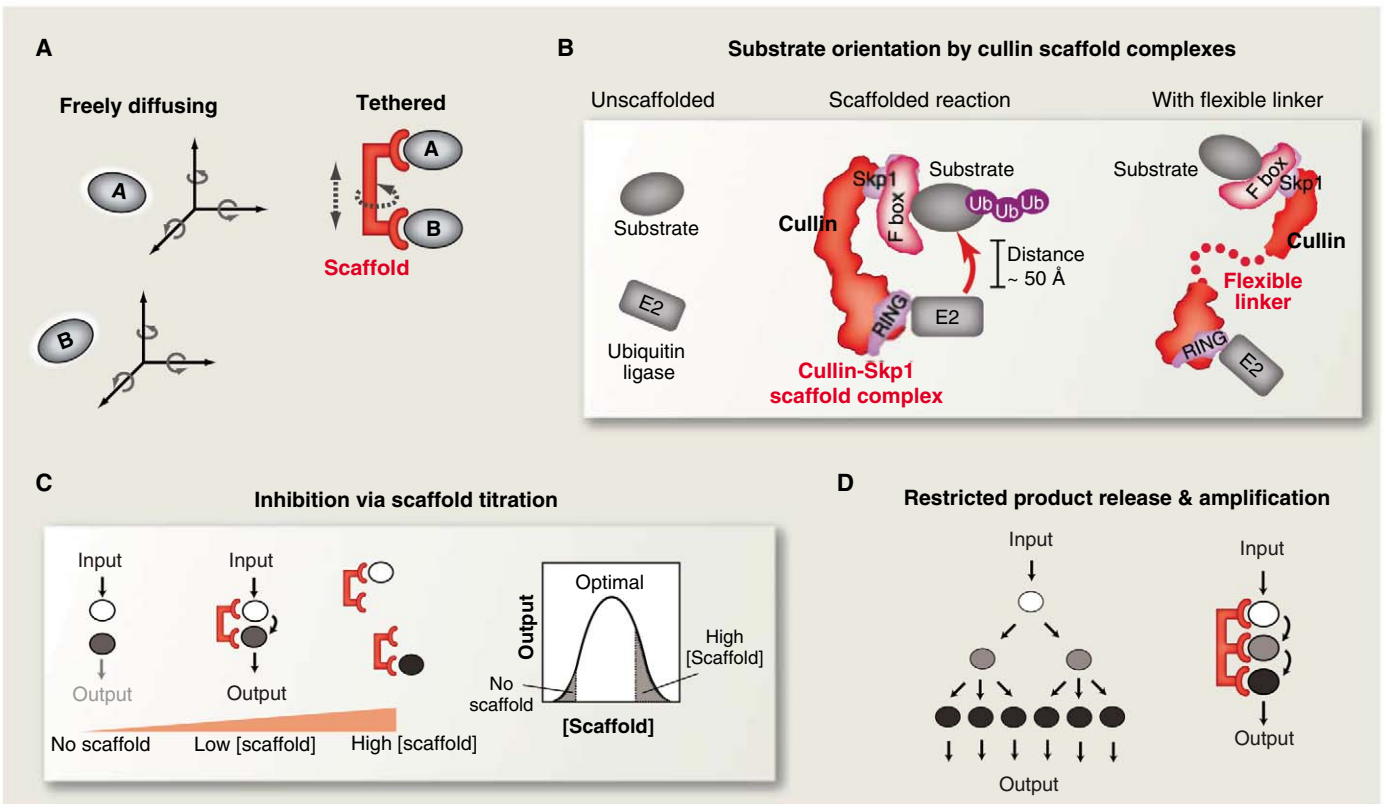

Fig. 3. Benefits and costs of scaffold tethering mechanisms. (**A**) By colocalizing enzyme and substrate, scaffold proteins can lower the entropic cost of signaling interactions; the loss of independent translational and rotational degrees of freedom is paid through binding interactions with the scaffold. The size of the advantage gained depends on the flexibility of the scaffold structure. (**B**) By restricting the conformational freedom of interacting proteins, scaffolds can orient these molecules to enhance the rate of signal transfer. The rigid cullin scaffold proteins tether E2 ubiquitin-conjugating enzymes and their substrates. If the cullin backbone is made flexible by mutation, the rate of substrate ubiquitination is greatly decreased. (**C**) Tethering has potential drawbacks: At high concentrations, scaffolds may titrate enzyme and substrate away from one another. (**D**) Increased affinities can restrict substrate release and diffusion throughout the cell, potentially limiting signal amplification and spatial redistribution (e.g., nuclear localization).

A recurring theme is that scaffold proteins increase the flexibility of a cell's signaling responses. Scaffold proteins can serve as targets for many forms of regulatory modulation, thereby allowing the cell to achieve a wide range of behaviors from a limited set of components.

Molecular Mechanisms of Scaffold Proteins: Tethering, Orientation, and Allosteric Regulation

How do scaffolds physically direct communication between the appropriate signaling partners? The most primitive scaffold proteins likely exert their effects through simple tethering of partner molecules. Tethering increases the effective concentration of enzymes and their substrates (Fig. 3A). For an enzyme that brings together two small-molecule substrates, the effective concentration may be as large as 10^8 M (*29*). This large effect is a consequence of avoiding the entropic penalty (the loss of translational and rotational degrees of freedom) for the molecules finding one another in solution, made possible by an enzyme that binds and pre-positions its substrates. Similarly, a scaffold protein that binds and orients two weakly interacting protein substrates is expected to provide a large entropic advantage. However, theoretical and experimental estimates for the entropic penalty for bringing two protein molecules together vary widely (*30*, *31*). The length and flexibility of the scaffold tether will also affect reaction rates, and these factors are only beginning to be systematically explored.

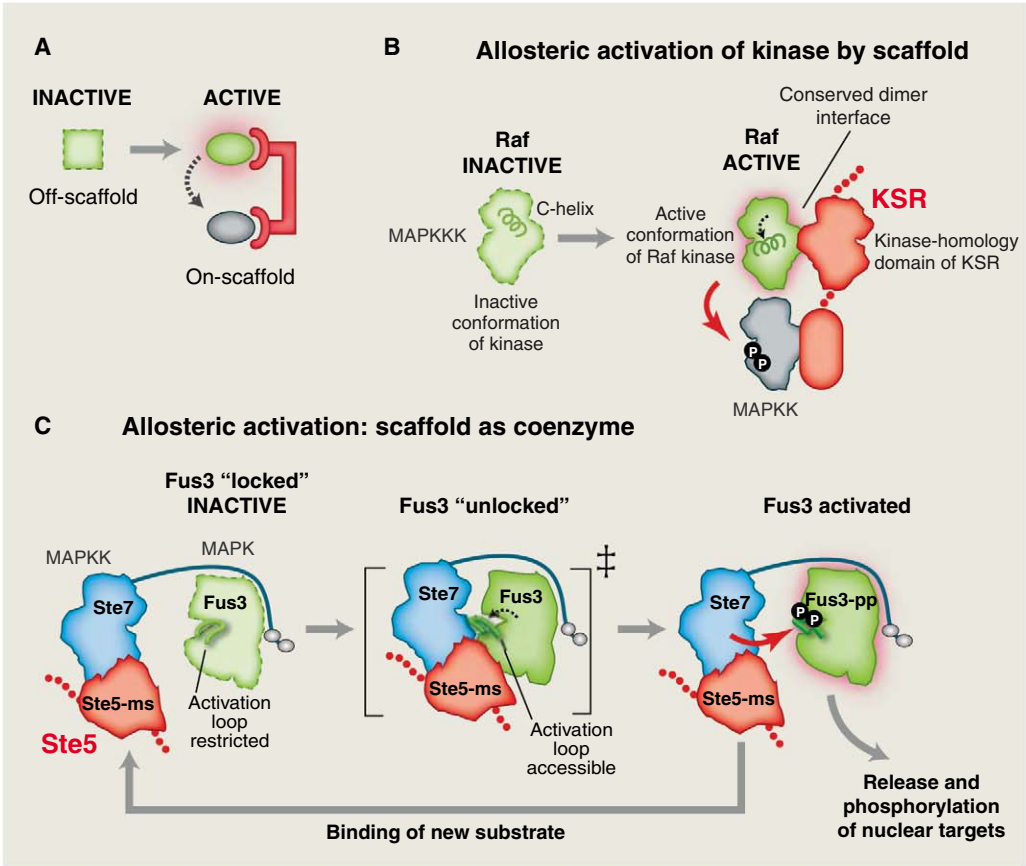

Fig. 4. Allosteric regulation by scaffold proteins. (**A**) Scaffolds can allosterically modulate the conformation of enzymes and substrates to gate information flow. (**B**) In MAPK ERK signaling, KSR can directly bind to the MAPKKK Raf and influence its activity toward the MAPKK MEK. The kinase-homology domain of KSR dimerizes with Raf, altering the conformation of the C-helix on Raf so that its kinase domain becomes catalytically active (thereby allowing Raf to phosphorylate MEK). (**C**) The VWA domain of Ste5 promotes phosphorylation of the MAPK Fus3 by the MAPKK Ste7. The scaffold may unlock the activation loop of the MAPK Fus3 to make it a better substrate for MAPKK Ste7.

Scaffold proteins that direct protein ubiquitination appear to function in part through properly orienting target proteins with upstream enzymes. Efficient ubiquitination of target substrates for proteasomal degradation requires the cullin-RING–F box complex, which acts as a scaffold to tether the target substrate and the E2 ubiquitin-conjugating enzyme together. However, simple tethering alone is not sufficient to stimulate substrate ubiquitination; the cullin scaffold backbone must be rigid to function properly (Fig. 3B) (*32*). Mutations that introduce flexibility into the scaffold greatly limit substrate ubiquitination (*33*), presumably because of loss of orientational specificity.

Although nearly all evidence suggests that simple enforced proximity is an important mechanism for scaffold proteins, there are functional tradeoffs that emerge when only this type of mechanism is used for wiring the interactions of signaling components. For example, a simple tethering scaffold can exhibit concentration-dependent titration effects. Mathematical models predict that increasing the concentration of scaffold protein will first favor increased interaction between partner proteins, but then, at higher concentrations (in excess of the component partner proteins), will titrate partner proteins into separate complexes, thus inhibiting their interaction (Fig. 3C) (*34*). Some hint of this biphasic effect has been demonstrated experimentally for the scaffold protein Ste5 in the yeast mating MAPK pathway response (*35*), although the degree of inhibition at high scaffold protein concentration is small. Inhibition of c-Jun N-terminal kinase (JNK) MAPK signaling due to overexpression of the JNK interacting protein 1 (JIP1) scaffold also demonstrates the biphasic effect (*36*).

A second potential tradeoff in using a simple tethering scaffold is the potential reduction in signal amplification. Many pathways are thought to amplify input signals by having multiple stages of signal transfer, as in a kinase cascade. Because each enzyme can modify many substrates, a single input signal (such as a peptide or hormone binding to a receptor) can be converted through a three-tiered kinase cascade into a greatly magnified output response. But if a tethering scaffold protein is required for the cascade, substrate turnover and signal amplification could be substantially reduced (Fig. 3D) (*37*), assuming that binding to individual components is tight and dissociation is slow. A related problem is that high-affinity tethering could prevent the diffusion of substrates away from their site of activation.

In principle, scaffold proteins could use more sophisticated mechanisms to overcome the tradeoffs of tethering. Cooperative or allosteric assembly of pathway components on the scaffold, for example, could mitigate the biphasic effect. Biochemical and structural studies of scaffold proteins are beginning to reveal that these proteins often make use of allosteric mechanisms that can minimize the tradeoffs of tethering (Fig. 4A). The MAPK scaffold protein KSR promotes signaling through the three-tiered ERK MAP kinase cascade through both tethering and allosteric mechanisms. In addition to colocalizing the MAPKKK Raf and the MAPKK MEK, the KSR scaffold protein also allosterically activates the kinase domain of Raf (Fig. 4B) (*38*). This allosteric effect of KSR is mediated by a kinase-homology domain in KSR that binds to and activates Raf. This scaffold function appears to be distinct from canonical tethering because there is no indication that Raf activity biphasically decreases with in-

creasing concentrations of KSR (*38*). Instead, binding of increased amounts of KSR to Raf monotonically increases the amount of active Raf enzyme. Recent studies further suggest that the Raf/KSR interaction is reciprocal: While KSR stimulates Raf, Raf also appears to stimulate kinase activity of the KSR kinase-homology domain, which may play a role in signaling to the MAPKK MEK (*39*, *40*). These allosteric mechanisms may increase the efficiency of signal transmission relative to that which occurs simply through tethering the MAPKKK and MAPKK proteins together.

Allosteric regulation has also been observed for the yeast mating response MAPK scaffold protein Ste5. In Ste5, a VWA (von Willebrand factor type A) domain is required to allosterically unlock the MAPK Fus3 so that it becomes a good substrate for the MAPKK Ste7; in the absence of scaffold, activated Ste7 cannot phosphorylate the MAPK Fus3, although it is catalytically competent to phosphorylate other potential substrates (Fig. 4C and Box 1) (*18*). This scaffold mechanism may be important for signaling specificity in *Saccharomyces cerevisiae* because the MAPKK Ste7 can be activated by inputs other than mating pheromone stimulation. The Ste5 scaffold VWA domain functions as a coactivator: It does not appear to modulate the association of the MAPKK Ste7 with the MAPK Fus3; instead, it specifically enhances the phosphorylation of Fus3 by Ste7 (Fig. 4C). This type of allosteric control may be physiologically important for the pathway: Because this mechanism does not appear to require tight binding between the scaffold and the MAPK Fus3, it may avoid problems associated with substrate release, thus allowing both signal amplification and MAPK translocation to the nucleus (*18*, *41*).

Scaffolds Can Be Used as Platforms for Redirecting Information Flow in Evolution and Engineering

Perhaps the most powerful feature of scaffold proteins is their potential to facilitate the evolution of new pathways. A scaffold is a separate, genetically encoded entity controlling the interaction of signaling components, and the creation of new or recombined scaffold proteins could

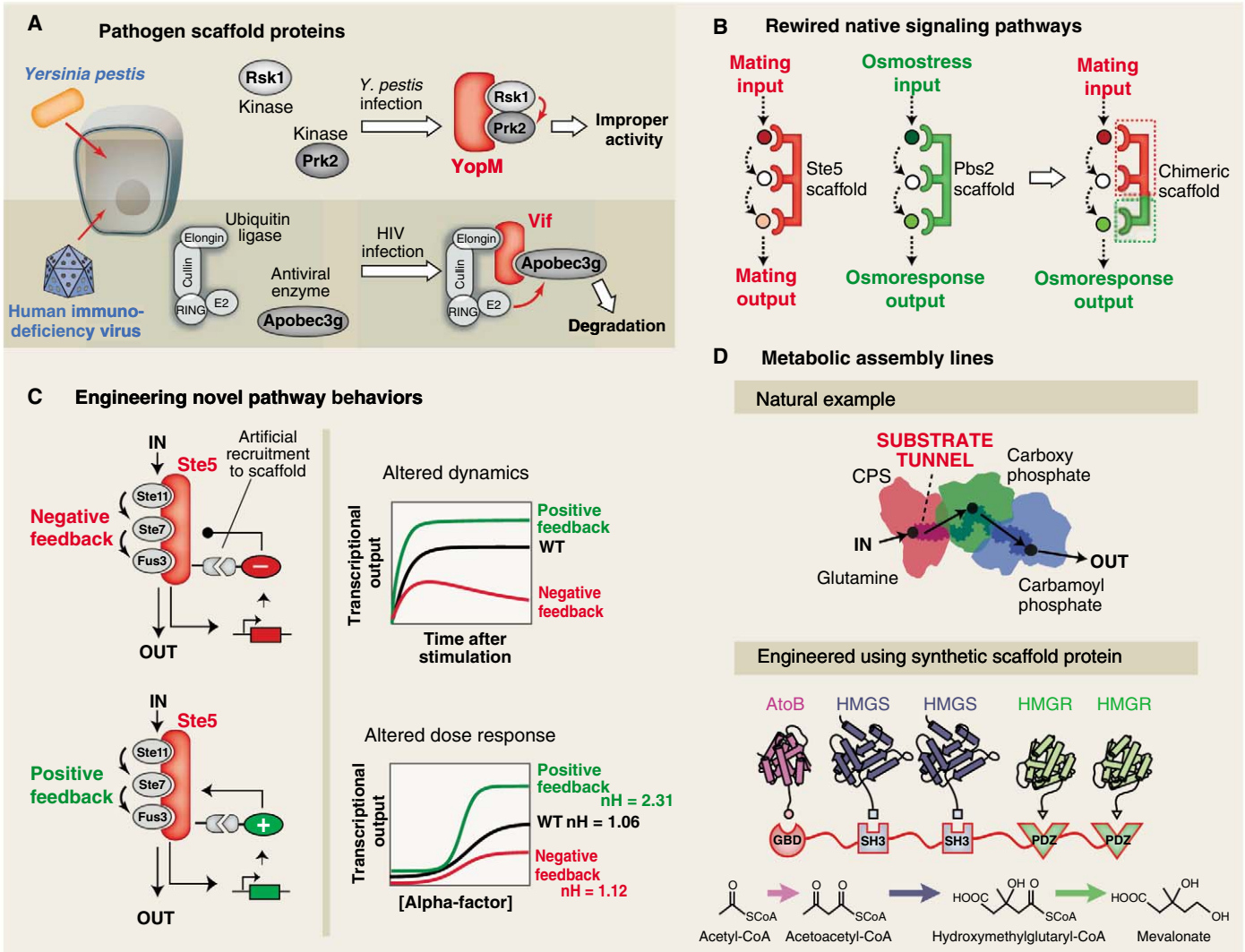

Fig. 5. Scaffold proteins are modular and can be used as platforms for redirecting information in evolution and engineering. (**A**) Pathogens can use scaffold-like proteins to rewire host signaling responses. The YopM scaffold from *Y. pestis* forces the interaction of the host Rsk1 and Prk2 kinases. The inappropriate activation is necessary for virulence. Viral scaffold proteins, such as HIV Vif, can target antiviral host proteins, such as the cytidine deaminase APOBEC3G, for degradation by targeting them to cullin-E2 ubiquitin ligases. (**B**) Engineered scaffolds can direct new cell signaling behaviors. A chimera of the Ste5 and Pbs2 yeast MAPK scaffold proteins can redirect mating pathway input to osmolarity pathway output. (**C**) Synthetic feedback loops can be engineered by controlling recruitment of positive and negative effectors to the Ste5 MAPK scaffold protein. Such loops can be used to precisely shape the dynamics and dose response of the yeast mating MAPK pathway to produce a wide range of signaling behaviors. (**D**) Natural metabolic pathways are often organized into multienzyme complexes that function like an assembly line to enhance the rate and yield of metabolite production. Engineered scaffold proteins can link together novel combinations of metabolic enzymes to more efficiently synthesize desired chemical products. [Adapted from (*53*)]

provide a simple mechanism for linking pre-existing components in novel ways (*2*). The ability to recombine pathways and regulate signaling behaviors with scaffolds can be likened to how the modular architecture of promoters gives rise to the diverse transcriptional responses that differentiate cell and tissue types.

The modular structure of most scaffold proteins implies an evolutionary history involving recombination of interaction domains. Although we are just beginning to trace the evolution of scaffold proteins through genomic comparisons, one example of rapid evolution of new pathway linkages through scaffolds is in pathogen-host interactions. Pathogens often hijack and rewire host signaling pathways, and pathogen scaffold proteins have been described (*42*). The pathogenic bacteria *Yersinia pestis* produces a scaffold-like protein (YopM) that artificially links together two kinases (Rsk1 and Prk2) that do not normally interact (Fig. 5A). YopM is secreted into host immune cells, and although the exact consequence of linking these two kinases is unclear, the binding and activation of the Rsk1 and Prk2 kinases by YopM is necessary for *Y. pestis* virulence (*43*, *44*). Similarly, a number of viruses encode scaffold proteins that act to target specific host antiviral proteins for ubiquitination and degradation. The human immunodeficiency virus (HIV) destroys the host APOBEC3G protein (a cytidine deaminase that interferes with viral replication) by producing a scaffold protein, Vif, which binds both APOBEC3G and a cullin-E2 complex (Fig. 5A) (*45*). A similar mechanism is used by the respiratory syncitial virus (RSV) to down-regulate the host STAT2 protein (*46*).

In principle, cellular engineers could also mimic evolution and wire new signaling pathways and cellular behaviors by building synthetic scaffolds. One simple approach to rewiring native signaling pathways is to fuse the functional elements of two different scaffold proteins into a chimeric scaffold protein. This strategy was successfully used in *S. cerevisiae* to link the mating and high-osmolarity stress MAPK pathway scaffold proteins so that a mating input resulted in an osmolarity response (Fig. 5B) (*47*).

More complex signaling behaviors can theoretically be achieved by engineering the recruitment of pathway regulators, thus generating feedback. A design strategy using modular recruitment of positive and negative effectors to the Ste5 scaffold generated feedback loops that result in a diverse array of MAPK pathway responses (*48*). The dynamics and dose-response behavior of the yeast mating MAPK pathway were greatly altered by tethering components such as phosphatases to a scaffold-kinase signaling complex (Fig. 5C).

Like cellular signaling, metabolic pathways are composed of a series of enzymes that are often assembled into complexes. Although these assemblies might not be considered true scaffold complexes, they use the same principle of enforced proximity. Substrate channeling in carbamoyl phosphate synthase, polyketide synthase, and tryptophan synthase is used to prevent loss of low-abundance intermediates, to protect unstable intermediates from interacting with solvent, and to increase the effective concentration of reactants (Fig. 5D) (*49*, *50*). Moreover, pathway flux can be controlled by regulating the assembly of these complexes, just as signaling can be regulated by assembly of a scaffolded complex (*51*). Given these parallels, an important question for industry and medicine is whether metabolic enzymes can be wired together into functional assemblies by engineered scaffolds, yielding designer metabolic pathways and small-molecule products. Remarkably, an artificial scaffold protein that tethered together three enzymes in a synthetic metabolic pathway in *Escherichia coli* was found to enhance mevalonate production by a factor of ~100 (Fig. 5D) (*52*). Thus, the principles of modular complex assembly can be used to flexibly control the flow of information in both signaling and metabolic pathways.

Conclusions

Scaffold proteins function in a diverse array of biological processes. Simple mechanisms (such as tethering) are layered with more sophisticated mechanisms (such as allosteric control) so that scaffolds can precisely control the specificity and dynamics of information transfer. Scaffold proteins can also control the wiring of more complex network configurations—they can integrate feedback loops and regulatory controls to generate precisely controlled signaling behaviors.

The versatility of scaffold proteins comes from their modularity, which allows recombination of protein interaction domains to generate new signaling pathways. Cells use scaffolds to diversify signaling behaviors and to evolve new responses. Pathogens can create scaffold proteins that are to their advantage: Their virulence depends on rewiring host signaling pathways to turn off or avoid host defenses. In the lab, scaffolds are being used to build new, predictable signaling or metabolic networks to program useful cellular behaviors.

References and Notes

1. R. Milo, P. Jorgensen, U. Moran, G. Weber, M. Springer, *Nucleic Acids Res.* **38**, D750 (2010).
2. R. P. Bhattacharyya, A. Reményi, B. J. Yeh, W. A. Lim, *Annu. Rev. Biochem.* **75**, 655 (2006).
3. B. N. Kholodenko, *Nat. Rev. Mol. Cell Biol.* **7**, 165 (2006).
4. J. D. Scott, T. Pawson, *Science* **326**, 1220 (2009).
5. K.-Y. Choi, B. Satterberg, D. M. Lyons, E. A. Elion, *Cell* **78**, 499 (1994).
6. H. C. Kornau, L. T. Schenker, M. B. Kennedy, P. H. Seeburg, *Science* **269**, 1737 (1995).
7. J. A. Printen, G. F. Sprague Jr., *Genetics* **138**, 609 (1994).
8. M. Therrien, N. R. Michaud, G. M. Rubin, D. K. Morrison, *Genes Dev.* **10**, 2684 (1996).
9. S. Tsunoda *et al*., *Nature* **388**, 243 (1997).
10. W. Zhang, J. Sloan-Lancaster, J. Kitchen, R. P. Trible, L. E. Samelson, *Cell* **92**, 83 (1998).
11. D. K. Morrison, R. J. Davis, *Annu. Rev. Cell Dev. Biol.* **19**, 91 (2003).
12. A. S. Shaw, E. L. Filbert, *Nat. Rev. Immunol.* **9**, 47 (2009).
13. L. S. Garrenton, S. L. Young, J. Thorner, *Genes Dev.* **20**, 1946 (2006).
14. M. J. Winters, R. E. Lamson, H. Nakanishi, A. M. Neiman, P. M. Pryciak, *Mol. Cell* **20**, 21 (2005).
15. J. C. Patterson, E. S. Klimenko, J. Thorner, *Sci. Signal.* **3**, ra75 (2010).
16. M. A. Schwartz, H. D. Madhani, *Curr. Genet.* **49**, 351 (2006).
17. L. J. Flatauer, S. F. Zadeh, L. Bardwell, *Mol. Cell. Biol.* **25**, 1793 (2005).
18. M. Good, G. Tang, J. Singleton, A. Reményi, W. A. Lim, *Cell* **136**, 1085 (2009).
19. L. Kozubowski *et al*., *Curr. Biol.* **18**, 1719 (2008).
20. L. Funke, S. Dakoji, D. S. Bredt, *Annu. Rev. Biochem.* **74**, 219 (2005).
21. E. Schnell *et al*., *Proc. Natl. Acad. Sci. U.S.A.* **99**, 13902 (2002).
22. R. Ranganathan, E. M. Ross, *Curr. Biol.* **7**, R770 (1997).
23. M. Taipale, D. F. Jarosz, S. Lindquist, *Nat. Rev. Mol. Cell Biol.* **11**, 515 (2010).
24. M. M. McKay, D. A. Ritt, D. K. Morrison, *Proc. Natl. Acad. Sci. U.S.A.* **106**, 11022 (2009).
25. S. C. Strickfaden *et al*., *Cell* **128**, 519 (2007).
26. J. Lin, A. Weiss, *J. Biol. Chem.* **276**, 29588 (2001).
27. R. P. Bhattacharyya *et al*., *Science* **311**, 822 (2006); 10.1126/science.1120941.
28. M. K. Malleshaiah, V. Shahrezaei, P. S. Swain, S. W. Michnick, *Nature* **465**, 101 (2010).
29. M. I. Page, W. P. Jencks, *Proc. Natl. Acad. Sci. U.S.A.* **68**, 1678 (1971).
30. A. V. Finkelstein, J. Janin, *Protein Eng.* **3**, 1 (1989).
31. Y. B. Yu, P. L. Privalov, R. S. Hodges, *Biophys. J.* **81**, 1632 (2001).
32. A. Saha, R. J. Deshaies, *Mol. Cell* **32**, 21 (2008).
33. N. Zheng *et al*., *Nature* **416**, 703 (2002).
34. A. Levchenko, J. Bruck, P. W. Sternberg, *Proc. Natl. Acad. Sci. U.S.A.* **97**, 5818 (2000).
35. S. A. Chapman, A. R. Asthagiri, *Mol. Syst. Biol.* **5**, 313 (2009).
36. M. Dickens *et al*., *Science* **277**, 693 (1997).
37. J. W. Locasale, A. S. Shaw, A. K. Chakraborty, *Proc. Natl. Acad. Sci. U.S.A.* **104**, 13307 (2007).
38. T. Rajakulendran, M. Sahmi, M. Lefrançois, F. Sicheri, M. Therrien, *Nature* **461**, 542 (2009).
39. D. F. Brennan *et al*., *Nature* **472**, 366 (2011).
40. J. Hu *et al*., *Proc. Natl. Acad. Sci. U.S.A.* **108**, 6067 (2011).
41. C. I. Maeder *et al*., *Nat. Cell Biol.* **9**, 1319 (2007).
42. A. S. Selyunin *et al*., *Nature* **469**, 107 (2011).
43. M. W. McCoy, M. L. Marré, C. F. Lesser, J. Mecsas, *Infect. Immun.* **78**, 2584 (2010).
44. C. McDonald, P. O. Vacratsis, J. B. Bliska, J. E. Dixon, *J. Biol. Chem.* **278**, 18514 (2003).
45. X. Yu *et al*., *Science* **302**, 1056 (2003); 10.1126/science.1089591.
46. J. Elliott *et al*., *J. Virol.* **81**, 3428 (2007).
47. S.-H. Park, A. Zarrinpar, W. A. Lim, *Science* **299**, 1061 (2003); 10.1126/science.1076979.
48. C. J. Bashor, N. C. Helman, S. Yan, W. A. Lim, *Science* **319**, 1539 (2008).
49. E. W. Miles, S. Rhee, D. R. Davies, *J. Biol. Chem.* **274**, 12193 (1999).
50. J. B. Thoden, H. M. Holden, G. Wesenberg, F. M. Raushel, I. Rayment, *Biochemistry* **36**, 6305 (1997).
51. S. An, R. Kumar, E. D. Sheets, S. J. Benkovic, *Science* **320**, 103 (2008).
52. J. E. Dueber *et al*., *Nat. Biotechnol.* **27**, 753 (2009).
53. M. P. DeLisa, R. J. Conrado, *Nat. Biotechnol.* **27**, 728 (2009).
54. C. Inouye, N. Dhillon, J. Thorner, *Science* **278**, 103 (1997).
55. P. M. Pryciak, F. A. Huntress, *Genes Dev.* **12**, 2684 (1998).
56. C. Inouye, N. Dhillon, T. Durfee, P. C. Zambryski, J. Thorner, *Genetics* **147**, 479 (1997).
57. A. Reményi, M. C. Good, R. P. Bhattacharyya, W. A. Lim, *Mol. Cell* **20**, 951 (2005).

58. We thank P. Pryciak, A. Weiss, R. Nicoll, R. Phillips, N. Pierce, J. Iwasa, J. Dueber, A. Remenyi, M. Borovinskaya, S. Peisajovich, J. Garbarino, A. Won, C. Bashor, N. Helman, S. H. Park, S. Coyle, P. Wei, J. Toettcher, and other members of the Lim lab for helpful discussions and comments. Supported by a Miller Fellowship (M.C.G.), a Damon Runyon Fellowship (J.G.Z.), NIH grants RO1GM055040, RO1GM062583, PN2EY016546, and P50GM081879 (W.A.L.), the NSF Synthetic Biology and Engineering Research Center (W.A.L.), the Packard Foundation (W.A.L.), and the Howard Hughes Medical Institute (W.A.L.).

Supporting Online Material

www.sciencemag.org/cgi/content/full/332/6030/680/DC1
Movie S1

10.1126/science.1198701

Single-Cell Mass Cytometry of Differential Immune and Drug Responses Across a Human Hematopoietic Continuum

Sean C. Bendall,[1]* Erin F. Simonds,[1]* Peng Qiu,[2] El-ad D. Amir,[3] Peter O. Krutzik,[1] Rachel Finck,[1] Robert V. Bruggner,[1,7] Rachel Melamed,[3] Angelica Trejo,[1] Olga I. Ornatsky,[4,5] Robert S. Balderas,[6] Sylvia K. Plevritis,[2] Karen Sachs,[1] Dana Pe'er,[3] Scott D. Tanner,[4,5] Garry P. Nolan[1]†

Flow cytometry is an essential tool for dissecting the functional complexity of hematopoiesis. We used single-cell "mass cytometry" to examine healthy human bone marrow, measuring 34 parameters simultaneously in single cells (binding of 31 antibodies, viability, DNA content, and relative cell size). The signaling behavior of cell subsets spanning a defined hematopoietic hierarchy was monitored with 18 simultaneous markers of functional signaling states perturbed by a set of ex vivo stimuli and inhibitors. The data set allowed for an algorithmically driven assembly of related cell types defined by surface antigen expression, providing a superimposable map of cell signaling responses in combination with drug inhibition. Visualized in this manner, the analysis revealed previously unappreciated instances of both precise signaling responses that were bounded within conventionally defined cell subsets and more continuous phosphorylation responses that crossed cell population boundaries in unexpected manners yet tracked closely with cellular phenotype. Collectively, such single-cell analyses provide system-wide views of immune signaling in healthy human hematopoiesis, against which drug action and disease can be compared for mechanistic studies and pharmacologic intervention.

Fluorescence-based flow cytometry has been fundamental to the discovery and definition of major and minor cell subsets of the immune system. Although the outline of hematopoiesis is generally understood (*1*), a comprehensive framework of its system-wide properties remains to be determined (*2*). Technological developments in flow cytometry and cell sorting [the introduction of new fluorophores, such as quantum dots (*3*)] have paralleled appreciation of the compartmentalization of function in the hematopoietic system and contributed to diverse fields, including immunology, stem cells (*4*, *5*), HIV (*6*), cancer (*7*), transcription (*8*, *9*), intracellular signaling (*10*, *11*), apoptosis, cell cycle (*12*), and development of cytometry-based clinical diagnostics (*13*, *14*). However, use of flow cytometry remains practically confined to the measurement of 6 to 10 simultaneous parameters (*15*). Analysis at the 11- to 15-parameter range is possible but limited by compensation needed to correct for spectral overlap that can create a source of confounding variability (*16*).

We used transition element isotopes not normally found in biological systems as chelated antibody tags in atomic mass spectrometric analysis of single cells to create a detailed response profile of the healthy primary human hematopoietic system with 34 simultaneously measured cellular parameters. This allowed us to take full advantage of the measurement resolution of mass spectrometry and apply it to single-cell analysis. Because the method is largely unhampered by interference from spectral overlap, it allows for the detection of considerably more simultaneous parameters than does traditional flow cytometry (*17*, *18*). Combined with its quantitative nature, atomic mass spectrometry measurement creates a platform with which to conduct multiplexed measurement of single-cell biological parameters that can exhibit vastly different dynamic ranges during signaling or over time (such as signaling changes indicated by shifts in protein phosphorylation).

We simultaneously measured 34 parameters in each single cell in human bone marrow (BM) samples to provide an in-depth analysis of normal human hematopoietic and immunological signaling overlaid onto a detailed template of cell phenotype. Cell subset–specific signaling phenotypes of drug action in the face of clinically meaningful physiologic stimuli were localized to pathway and cell-specific boundaries, with examples in B cell signaling shown. These provide a system-wide view of signaling behaviors, expanding our view of drug action while allowing us to limit the functions that certain drugs might have on complex tissues. Given that this technology can reasonably be expected to allow for as many as 100 parameters per cell (*18*, *19*), it affords an opportunity to increase our understanding of cell type–specific signaling responses in complex, distributed organs such as the immune system.

[1]Baxter Laboratory in Stem Cell Biology, Department of Microbiology and Immunology, Stanford University, Stanford, CA 94305, USA. [2]Department of Radiology, Stanford University, Stanford, CA 94305, USA. [3]Department of Biological Sciences, Columbia University, New York, NY 10027, USA. [4]University of Toronto, Toronto, ON M5S 3H6, Canada. [5]DVS Sciences, Markham, ON L3R 6E7, Canada. [6]BD Biosciences, San Diego, CA 95131, USA. [7]Biomedical Informatics Program, Stanford University, Stanford, CA 94305, USA.

*These authors contributed equally to this work.
†To whom correspondence can be addressed. E-mail: gnolan@stanford.edu

Performance assessment of mass cytometry. The workflow for mass cytometry is comparable with that of fluorescence flow cytometry (Fig. 1A). Antibodies coupled to distinct, stable, transition element isotopes were used to bind target epitopes on and within cells. Cells, with bound antibody-isotope conjugates, were sprayed as single-cell droplets into an inductively coupled argon plasma (created by passing argon gas through an induction coil with a high radio-frequency electric current) at approximately 5500 K. This vaporizes each cell and induces ionization of its atomic constituents. The resulting elemental ions were then sampled by a time-of-flight (TOF) mass spectrometer and quantified. The signal for each transition element isotope reporter was integrated as each cell's constituent ions reached the detector. Currently, TOF sampling resolution enables the measurement of up to 1000 cells per second. We compared mass cytometry with conventional nine-parameter fluorescence flow cytometry in analysis of cytokine signaling through responses in human peripheral blood mononuclear cells (PBMCs) from two healthy donors (Fig. 1, B to E, and fig. S1). Seven surface antigens (CD3, CD4, CD8, CD45RA, CD56, CD20, and CD33) and two intracellular phosphoprotein epitopes [phosphorylated signal transducer and activator of transcription 3 and 5 (pSTAT3 and pSTAT5)] were measured by means of fluorescence cytometry on two human PBMC samples treated with interleukin-2 (IL-2), IL-6, IL-10, granulocyte-monocyte colony stimulating factor (GM-CSF), or interferon-α (IFNα) to measure cytokine-mediated signaling responses in specific cell subsets. In traditional flow cytometry, forward scatter (FSC) and side scatter (SSC) measurements of laser light are used to detect the presence of a cell and to "trigger" the electronics in order to collate information as a cell "event" (the window of time during which a cell is measured). Because FSC and SSC are not currently implemented on the CyTOF platform, alternative parameters providing analogous utility were included to assist with the discrimination of single-cell events: (i) an antibody to the surface epitope CD45 (expressed on most cells measured in this study), (ii) a metal-encoded DNA intercalator to identify nucleated cells (*20*), and (iii) a derived parameter ("cell length") indicating the duration of each cell's measurement window (*18*).

Fluorescence (Fig. 1B and fig. S1A) and mass (Fig. 1C and fig. S1B) cytometry analysis provided comparable results when analyzed via traditional dot plots (fig. S2). Pertinent qualities, such as reduced CD45RA expression on $CD4^+$ T cells relative to that on $CD8^+$ cells, were reproduced between platforms (Fig. 1, B and C). Despite use of different metrics for identifying cell events, both platforms yielded quantitatively similar frequencies ($P < 0.000001$) for 12 manually gated cell populations in the parallel analysis of two separate door samples (fig. S1C and table S1). Patterns of specific induction of STAT protein phosphorylation within the $CD4^+CD45RA^+$

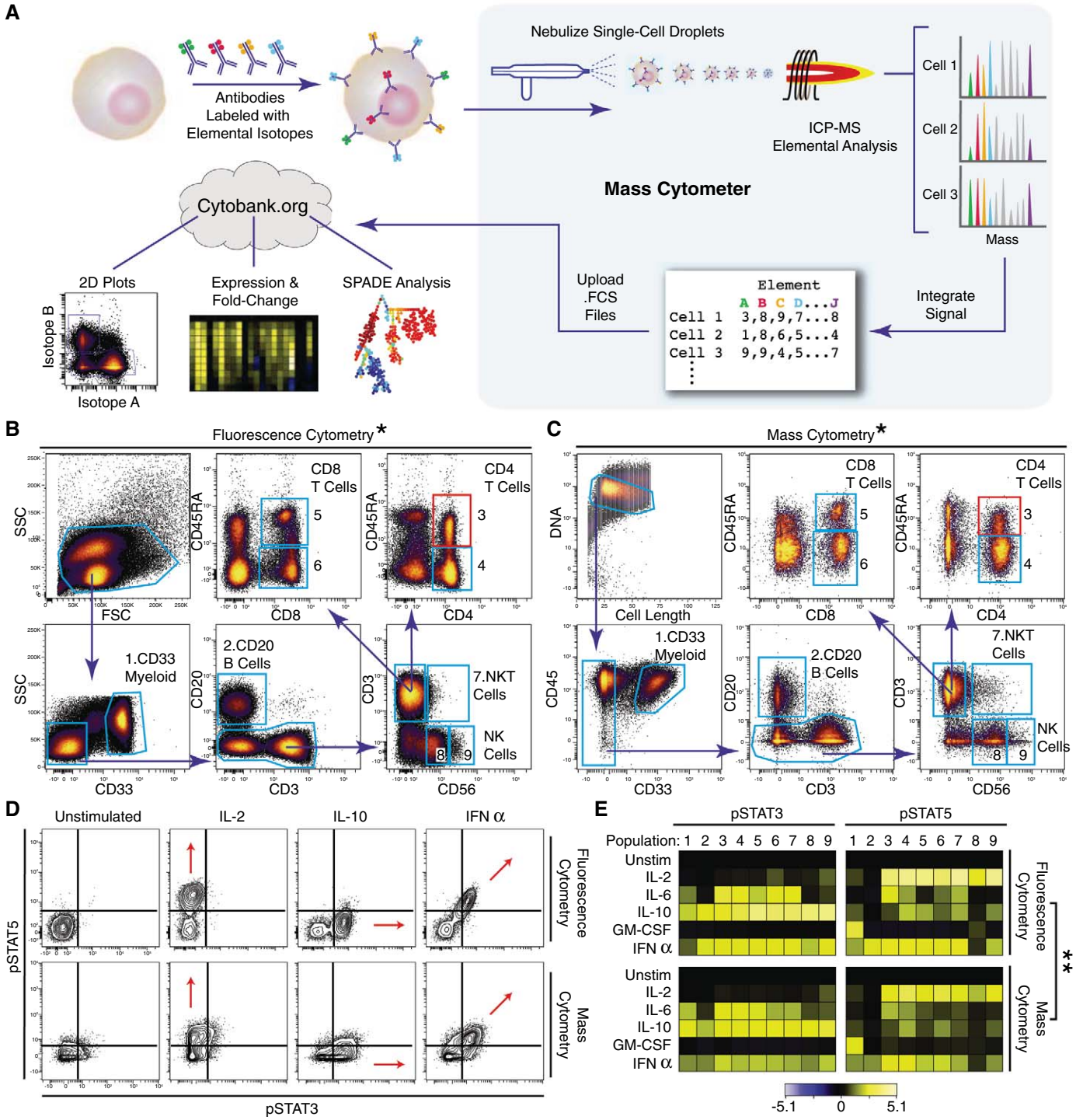

Fig. 1. Mass cytometry profiling of immune cell response patterns. (**A**) Workflow summary of mass cytometry analysis. Cells are stained with epitope-specific antibodies conjugated to transition element isotope reporters, each with a different mass. Cells are nebulized into single-cell droplets, and an elemental mass spectrum is acquired for each. The integrated elemental reporter signals for each cell can then be analyzed by using traditional flow cytometry methods as well as more advanced approaches such as heat maps of induced phosphorylation and tree plots. (**B** and **C**) Representative antibody surface-staining results and cell population definitions ("gating") for (B) fluorescence and (C) mass cytometry analysis of fixed PBMCs from the same donor. Replicate analysis of a second donor is provided in (*21*) (Fig. S1A and S1B). *Pearson correlation between frequencies measured by fluorescence or mass cytometry, including both donors ($r = 0.99$, $P < 0.000001$, two-tailed t test) (table S1 and fig. S1C). (**D**) Induction of STAT3 and 5 phosphorylation by various ex vivo stimuli in naive $CD4^+CD45RA^+$ T cells [(B) and (C), red boxes] as measured by (top) fluorescence and (bottom) mass cytometry. Red arrows indicate the expected shift along the STAT phosphorylation axes. (**E**) Heatmap summary of induced STAT phosphorylation in immune populations from the PBMC donor defined in (B) and (C) [column headers refer to blue polygons in (B) and (C)]. Responses to the indicated stimuli in each row were measured by (top) fluorescence and (bottom) mass cytometry. Color scale indicates the difference in $\log_2$ mean intensity of the stimulated condition compared with the unstimulated control. Signaling responses of a second donor are provided in (*21*) (fig. S1D). **Pearson correlation between signaling induction measured by fluorescence or mass cytometry, including both donors [pSTAT3: $r = 0.92$; $P < 0.000001$, two-tailed t test (fig. S1E); pSTAT5: $r = 0.89$, $P < 0.000001$, two-tailed t test] (figs. S1E and S1F).

T cell population demonstrated that both platforms could equivalently detect pSTAT3, pSTAT5, and dual pSTAT3-pSTAT5 responses to IL-10, IL-2, and IFNα, respectively (Fig. 1D). One qualitative difference between the two platforms was the mathematical correction required to address spectral overlap in the fluorescence data (termed "compensation"), a procedure not required with the atomic mass spectrometer. A second major distinction is the absence of cell-dependent background signal in the mass cytometry data. Thus, although laser-based flow cytometry detects signals from cellular autofluorescence, nonactivated cells had mass cytometric phosphoprotein intensities near zero, indicating very little background antibody binding. This manifests in atomic mass spectrometry as a narrow grouping of cell events at the low end of the dot plot axes. Qualitatively and quantitatively ($P < 0.000001$) similar patterns were revealed by means of fluorescence-based flow cytometry or mass cytometry in terms of magnitude of the pSTAT3 and pSTAT5 responses in cell populations across two healthy peripheral blood samples (Fig. 1E and fig. S1, D to F). An overview of the antibody quality control with testing on cell lines, human PBMCs, and bone marrow is shown in fig. S11. Taken together, mass cytometry and traditional fluorescence based approaches can produce results with equivalent informational value.

Organization and analysis of high-dimensional single-cell data. Taking advantage of the increased dimensionality of mass cytometry, we prepared a set of reagents to capture a system-wide view of immune cell types from a replicate analysis of bone marrow mononuclear cells from two healthy human donors. Thirty-one distinct transition element isotopes were used to label two antibody-staining panels for the study of healthy human bone marrow mononuclear cells. [Data are publicly available at Cytobank (www.cytobank.org/nolanlab). An "immunophenotyping" panel was designed that monitored 13 "core" surface markers and 18 subset-specific cell-surface markers to allow identification of human hematologic cell types. A "functional" panel contained the 13 core surface markers and also 18 intracellular epitopes that reflect intracellular signaling states, such as phosphorylation status of kinase substrates (*21*). These complementary panels allowed simultaneous biochemical analysis of intracellular signaling in rare and diverse cell subsets that were identified through in silico merging of the data. Intracellular signaling responses were determined by treating cells ex vivo with modulators such as cytokines, small molecules, or combinations thereof. Perturbation analysis has proven useful in causality determinations for signaling at the single-cell level (*11*, *22*–*25*) and was applied here to enable cell subset–specific response profiles. An additional three parameters—a DNA intercalator, cell length, and a cell viability dye (*21*)—were included in the analysis panels, creating a total of 34 parameters in each. With an overlap of 13 core surface antibodies between the two analysis panels and the three shared additional cell features, a combined total of 52 unique single-cell parameters were measured. The resulting single-cell data set of bone marrow cells captured a snapshot of the cell types present and their corresponding regulatory signaling responses throughout development from early human hematopoietic progenitors to lineage-committed cells.

A central dogma of immunology is that cells at different stages of maturation can be characterized by the expression of unique sets of proteins on the cell surface. Such "cluster of differentiation" (CD) markers are routinely used for flow cytometric identification of cell populations. Although it is convenient to think of cells in different stages of development as having distinct, regimented profiles, hematopoiesis frequently manifests as a continuum of CD marker expression connecting the cellular lineage stages (*26*). Although cells might pause at recognized stages of development to which we ascribe certain phenotypes, cells also pass through transient intermediate states that connect parent populations to their progeny. As they proceed from one stage of development to the next, CD marker sets rise and fall in accordance with programmed differentiation and environmental contexts. A conventional display of the relationships between the 31 cell surface markers measured here on human bone marrow would require greater than 450 biaxial dot plots (fig. S3), making a comprehensive interpretation of the underlying cellular progression unwieldy, if not impossible.

We hypothesized that the inherent similarity of cell stages and continuity of the transitions between cell differentiation states could be used to organize high-dimensional data into ordered, continuous clusters of similar cell phenotypes that, when projected on a two-dimensional (2D) plane, would convey the relatedness of these cells in a higher dimensional space. We leveraged progressive changes in CD marker expression to organize bone marrow cells in an unsupervised manner, creating a tree-like scaffold for visualization of high-dimensional intracellular signaling behaviors in various cell types present during hematopoietic development in the bone marrow (*27*, *28*). To accomplish this, we used SPADE (spanning-tree progression analysis of density-normalized events), a density normalization, agglomerative clustering, and minimum-spanning tree algorithm to distill multidimensional single-cell data down to interconnected clusters of rare, transitional, and abundant cell populations, which were organized and displayed as a 2D tree plot (Fig. 2A). Such a tree plot from healthy bone marrow represented the clustered expression of the cell-surface antigens that were used to build the tree in 13-dimensional space on the basis of the core surface markers conserved between our two 34-parameter analysis panels (CD3, -4, -8, -11b, -19, -20, -33, -34, -38, -45, -45RA, -90, and -123) (Fig. 2B). Each node of the plot encompasses a cluster of cells that were phenotypically similar in the 13-dimensional space defined by the core surface markers. The approach uses a minimum-spanning tree algorithm, in which each node of cells is connected to its "most related" node of cells as a means to convey the relationships between the cell clusters. The number of nodes and ultimately their boundaries is driven by a user-definable value (*21*). Each node describes an *n*-dimensional boundary encompassing a population of phenotypically similar cells. When connected via the minimum spanning tree, this provides a convenient approach to map complex *n*-dimensional relationships into a representative 2D structure.

As such, related nodes could be mapped into traditionally described immunological cell populations as determined by the localized expression patterns of 13 directly measured surface markers (Fig. 2, B to E, and fig. S4A). A summary of evidence supporting these annotations and boundaries can be found in table S2. For instance, T cell populations were annotated on the far right branch of the tree plot based on the high expression of CD3 (Fig. 2C, bright red). The T cell markers CD4 and CD8 were expressed in mutually exclusive clusters but overlapped with CD3 expression. Density normalization enabled the display of rare cell types, such as $CD34^+$ progenitor cells, in the same space as the more abundant differentiated cell types (Fig. 2E). The unsupervised organization of phenotypically related cell types into adjacent branches, such as CD4 and CD8 T cells (Fig. 2C), mature and immature B cells (Fig. 2D), and different clusters of myeloid cells (Fig. 2E) collectively illustrates that the algorithmic ordering of surface marker similarity can objectively organize cell types into physiologically relevant compartments.

Although they were not used in the tree-building step, the 18 additional surface markers from the "immunophenotype"-staining panel were used to confirm and refine cell subset annotations (Fig. 2F and fig. S4B). These markers were overlaid in an unsupervised fashion onto the existing tree by assigning each cell from the immunophenotyping experiment to whichever node contained analogous cells from the functional data set according to the expression of the shared 13 core surface markers in the registration space. The accuracy of this automated overlaying approach is supported by the agreement of multiple natural killer (NK), monocyte, and B cell markers that localized to the appropriate cell populations (Fig. 2F), even though they were not used to direct the tree's original organization. Although the tree structure derived from bone marrow data recapitulates many features of hematopoietic organization and relatedness, it is interpreted here as a map of the phenotypic relationships between diverse cell types and is not meant to imply a developmental hierarchy. Indeed, even measuring a large number of cells in a single tissue will fail to capture some developmental transitions, including (i) rapid activation (release of cytoplasmically sequestered receptors) (*29*); (ii) uneven surface marker partitioning during asymmetric cell division (*30*); and (iii) organ-specific development outside the assayed organ (matura-

tion of T cells in the thymus). In this bone marrow data set, several well-defined cell types (such as T, NK, B, and monocyte) provide landmarks for the organization of the tree and give context to the nodes encompassing transitional and less-understood cell types. Ultimately, this approach enabled visualization of 34-dimensional bone marrow data in an intuitive graphical format. Although the algorithm over-segregated some cell types into redundant contiguous clusters, this approach has several advantages that complemented the complexity of this data set: (i) increased resolution captured unexpected and transitional cell types that escape standard classification strategies; (ii) Unsupervised analysis helped overcome the bias of subjective gating; and (iii) *n*-dimensional algorithms leveraged the multi-parameter mass cytometry data to define cell types on the basis of previously unappreciated, subtle differences in surface expression. Although we used stochastically selected "seed" cells to initiate the tree generation along with local similarity clustering and minimum-spanning trees, the approach is amenable to incorporation of other more deterministic partitioning approaches that might allow for other standardized tree structure formation.

Ex vivo analysis of healthy human bone marrow signaling. Historically, by detailing immune functions in vivo and in vitro a model of specialized cell types in immunology and hematopoiesis were mapped primarily on the basis of expressed cell surface antigens—many of which were codified by using single-cell analysis and fluorescence-based cytometry (*31*–*34*). Because cell-surface proteins represent only a small proportion of the repertoire of gene products governing cell behavior, intracellular proteins (*33*) are also critical in defining cell types. Because surface and intracellular molecules work together in concert to support different cellular roles, it might be expected that proteins governing specialized immunological cell functions (T cell receptor, B cell receptor, or cytokine receptors) are modulated in a coordinated manner as cells transit developmental pathways from stem cell precursors to differentiated endpoints.

We monitored 13 surface markers to identify immune cell types and 18 intracellular epitopes in order to interrogate intracellular signaling biology in healthy human bone marrow. We examined the signaling dynamics of these 18 intracellular markers in response to 13 ex vivo stimulation conditions (such as IL-7 or GM-CSF), including those shown to have prognostic value in leukemia, lymphoma, and myeloproliferative disorders [such as granulocyte colony stimulating factor (G-CSF)] (*10*, *35*–*37*). Cell populations were first defined on the basis of conventional surface expression gates, ultimately identifying 24 immunological populations in human bone marrow

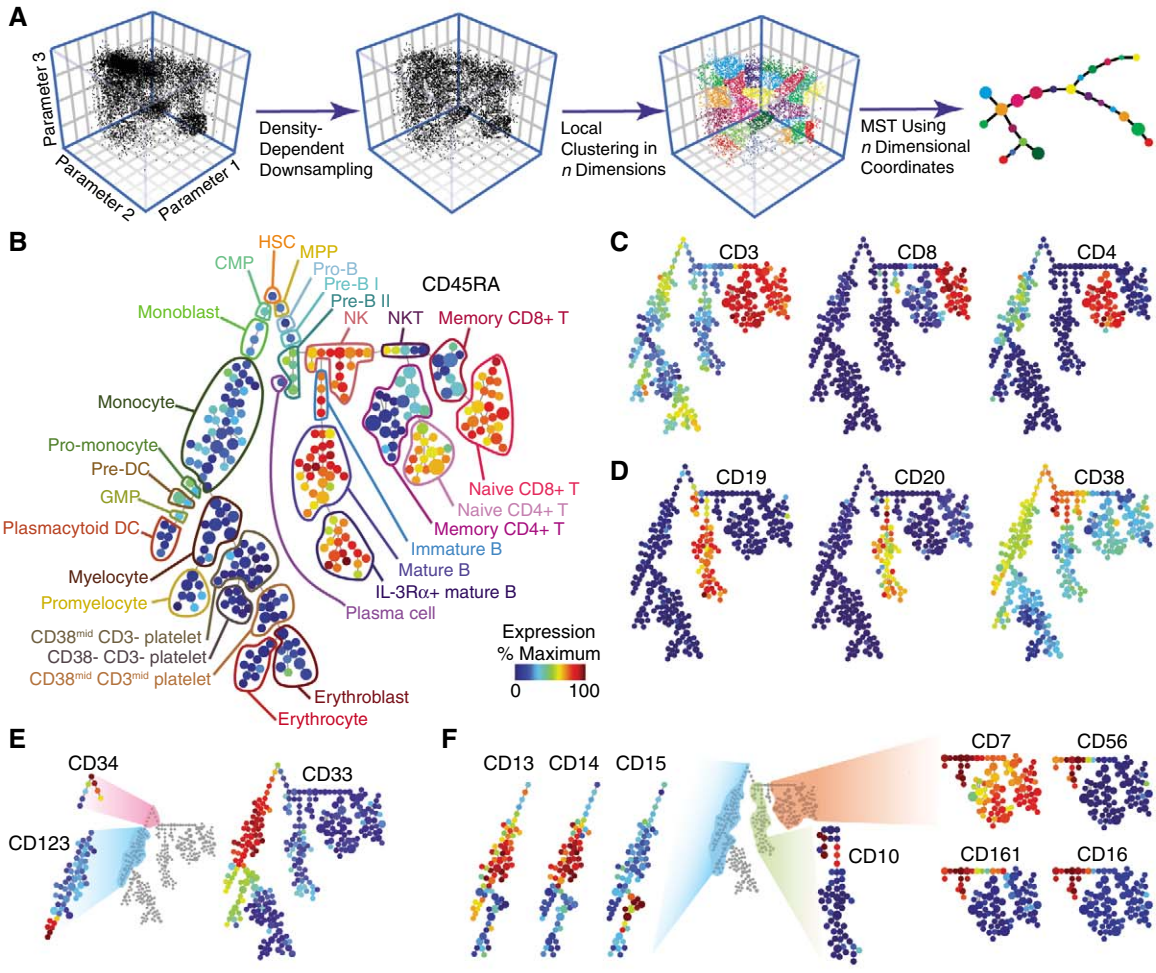

Fig. 2. SPADE links related immune cell types in a multidimensional continuum of marker expression. (**A**) Summary of SPADE analysis. Single-cell data are sampled in a density-dependent fashion so as to reduce the total cell count while maintaining representation of all cell phenotypes. Neighboring cells are then grouped by unsupervised hierarchical clustering. Resulting nodes (defined as those cells within a boundary of an *n*-dimensional hull) are then linked by a minimum-spanning tree, which is flattened for 2D display. (**B**) Immunophenotypic progression in healthy human bone marrow. A tree plot was constructed by using 13 cell-surface antigens in healthy human bone marrow. 18 additional intracellular parameters were acquired concurrently but excluded from tree construction. The size of each circle in the tree indicates relative frequency of cells that fall within the 13-dimensional confines of the node boundaries. Node color is scaled to the median intensity of marker expression of the cells within each node, expressed as a percentage of the maximum value in the data set (CD45RA is shown). Putative cell populations were annotated manually (table S2) and are represented by colored lines encircling sets of nodes that have CD marker expression emblematic of the indicated subset designations. (**C**) Overlaid expression patterns of CD3, CD8, and CD4. Three markers, along with CD45RA (B), were used in clustering that helped define T cell lineages. Color scale is as described in (B). (**D**) Overlaid expression patterns of CD19, CD20, and CD38. Three markers were used in clustering that helped define B cell lineages. Color scale is as described in (B). (**E**) Overlaid expression patterns of CD34, CD123, and CD33. Three markers were used in clustering that helped define myeloid and progenitor cell lineages. Color scale is as described in (B). (**F**) Overlaid expression of complementary surface markers from a staining panel with 18 additional surface markers (fig. S4) by using the 13 core surface markers as landmarks (*21*). Overlaid expression patterns are shown for eight complementary surface markers that helped to further define the myeloid (CD13, CD14, and CD15), B cell (CD10), and NK/T cell (CD7, CD56, CD161, and CD16) portions of the SPADE representation. These markers were not used for tree construction. Color scale is as described in (B).

(fig. S5). The induced intracellular signaling responses (changes in phosphorylation state) in these populations, as compared with those of an untreated control, were summarized as a heatmap (Fig. 3A). Unsupervised, hierarchical clustering of the phosphorylation responses allowed distinction of biologically related cell types (T cell subsets) by their signaling behavior alone, demonstrating that signaling capacities are closely tied to cellular lineage (fig. S6). Several canonical signaling responses that mapped to manually determined cell types are shown in Fig. 3B. These extremely specialized responses, such as the tight restriction of IL-7–mediated pSTAT5 responsiveness in T cells (Fig. 3B, arrow 4) (*38*) or lipopolysaccharide (LPS)–stimulated phosphorylation of the mitogen-activated protein kinase (MAPK) p38 (p-p38) responsiveness in monocytes (Fig. 3B, arrow 5) (*39*), suggest the existence of correlations between signaling events and surface marker–defined boundaries, thus presenting an opportunity to establish a unified view of immune signaling during hematopoiesis.

With ~10^4 signaling observations (Fig. 3A and fig. S10A) for each replicate bone marrow, it was necessary to filter the data set in order to arrive at the most significant and potentially novel observations. Using a one-sample *t*-test, over 500 observations were observed with a Bonferroni-adjusted significance of $P < 0.05$ in each replicate bone marrow for a total of 860 unique responses (fig. S7 and table S3). Of the 248 observations overlapping between patient marrows, 28 belonged exclusively to cells residing in the human hematopoietic progenitor cell compartment [hematopoietic stem cells (HSCs), multipotent progenitors (MPPs), granulocyte/macrophage progenitors (GMPs), and megakaryocyte-erythroid progenitors (MEPs)], including G-CSF induction of pSTAT3 in the most primitive cell types, HSC and MPP (*40*). This same signaling behavior correlated with negative prognosis in acute myeloid leukemia (*10*), suggesting that, as in the case of other malignancies, there may be a selective advantage for cells to mimic the properties of their most primitive counterparts.

For a more objective and fine-grained view of these cell type–specific responses, free of the biases of conventional 1D and 2D surface marker categorization, we overlaid the signaling behavior of the 18 functional epitopes on the tree structure using a similar approach as described for the immunophenotype staining panel (Fig. 2), allowing the intracellular signaling status to be visualized on the previously annotated tree structure (Fig. 3C). Nodes were colored according to the magnitude of the difference in their median responses relative to the untreated control. This effectively eliminated the subjectivity of manual classification and improved the resolution of the heatmap (Fig. 3A), separating the 24 manually assigned cell types into 282 logically connected nodes of phenotypically distinct, but locally similar, cell clusters.

The stimuli that corresponded closely with cell types identified manually in the heatmap also exhibited appropriately specific responses when overlaid on the tree structure—specifically, IL-7/pSTAT5 in T cells, B cell receptor (BCR)/phosphorylated B cell linker protein (pBLNK) exclusively in immature and mature B cells, and LPS/p-p38 restricted to the monocyte compartments (Fig. 3C), with the latter corresponding to the expression of the LPS co-receptor (CD14) (Fig. 2F). A complete set of the effects of 13 stimuli on 18 different functional markers is presented as tree plots (fig. S8) along with a confirmatory analysis of a second bone marrow (fig. S9).

With multiple matching canonical signaling pathways to validate the approach, we examined the data set for previously unidentified or unexpected signaling behaviors. For example, although pSTAT5 activation by IL-3 (Fig. 3D) was commensurate with IL-3Rα (CD123) expression levels (Fig. 3D) in myeloid cells, IL-3–mediated pSTAT3 activation was unexpectedly absent in mature B cells in spite of abundant presence of the receptor (Fig. 3D, blue arrow). This suggests that mature B cells share some, but not all, IL-3 signaling mechanisms with myeloid cell types.

Other responses, such as phosphorylation of the protein tyrosine kinases Btk and Itk mediated by IFNα or ribosomal protein S6 by G-CSF, were less tightly confined, exhibiting a range of activity that spanned multiple cell types (Fig. 3E). Yet other responses showed a signaling "gradient," as exemplified by pervanadate (PVO_4)–mediated disruption of the kinase/phosphatase balance upstream of the adenosine 3′,5′-monophosphate (cAMP) response element–binding protein (CREB) transcription factor. A gradient of responses, highest in HSCs, decreased gradually along the path of B cell maturation (Fig. 3E). A range of NFκB signaling responses, as measured by monitoring total IκBα levels, were observed across monocyte, NK and T cell subsets following TNFα stimulation (Fig. 3E, light blue nodes). As in the CREB response to PVO_4 described above (Fig. 3E), the consistency of responses within the different T cell subsets suggests tightly regulated differences in signaling molecules that underlie the discrete functional roles of these related cell types. Together, these varied signaling responses across algorithmically defined partitions dictated solely by surface marker immunophenotype imply the existence of different classes of developmental transition points: (i) precise transitions, which are characterized by coordinated changes in cell signaling, such as the IL-7/pSTAT5 response in T cells and the LPS/p-p38 response in monocytes (Fig. 3C), and (ii) continuous developmental progressions, which are characterized by gradual gain or loss of expression of certain kinases or phosphatases, as highlighted by PVO_4/pCREB (Fig. 3E) in B cells (*28*). The latter is indicative of fine-grained changes in regulatory architecture that track with immunophenotype within conventionally defined hematopoietic compartments and provides an opportunity to explore the mechanisms that define these distinctive regulatory phenomena.

Confirmation of progression-specific signaling in hematopoietic development. To investigate more closely the signaling transitions and the observed signaling heterogeneity inside seemingly homogeneous cell compartments, we mapped changes in B cell signaling as they coincided with the progression of B cell maturation. Using the cell events comprising the Pre-B II through IL-3Rα$^+$ mature B cell subsets defined in the SPADE plot (Fig. 4A) (see table S2 for surface marker definitions of B lineage stages), we used an independent statistical method—principal component analysis (PCA)—to distill the dimensionality of 13-parameter surface marker data to a single linear "progression axis." Principal component analysis found that the first principal component—the axis of greatest variation in the data (explaining 23% of the variation)—followed known markers of B cell maturation. This progression axis was primarily defined by increasing CD20 expression and decreasing CD38 expression, with smaller contributions from increasing CD45RA (Fig. 4B). The match between the first principal component and the established sequence of B cell development (*26*, *41*) is further supported by additional markers, such as the increase in CD19 and CD123 along this axis of progression. Projecting cells onto this progression trajectory defines a continuum of cells, rather than distinct subsets (Fig. 4A, gray line).

Although no intracellular parameters were used in defining the PCA progression, many intracellular markers demonstrated a smooth and gradual change along this axis of progression, providing the opportunity to explore how signaling changes during B cell development. Abundance of the cell cycle–associated nuclear protein Ki67 at basal state revealed a transition point characterized by a peak in the amount of Ki67 (cycling cells) followed by a concomitant increase in CD20 expression (Fig. 4B). The inverse relationship between these parameters suggests that the continuous production of B cells in bone marrow is paused when CD20 is gained, thus coinciding with the exit of immature B cells from the marrow (*42*). The dramatic increase in the abundance of CD20$^+$ B cells shortly after this transition point (Fig. 4, A and B) may indicate the presence of a reservoir of dormant CD20$^+$ mature B cells in bone marrow awaiting antigen activation (*43*).

Overlaying the basal (untreated) intensities of phosphorylated extracellular signal–regulated kinase 1 and 2 (pERK1/2), Src homology protein tyrosine phosphatase 2 (SHP2), SLP-76/BLNK (SLP-65), pPLCγ2, and CREB onto the PCA axis revealed that basal phosphorylation of these molecules at the measured sites was relatively constant across differentiating B cell types (Fig. 4C). However, induced phosphorylation of these sites by PVO_4 and BCR (Fig. 4C) clarified the heterogeneity of PLCγ2 phosphorylation observed after PVO_4 treatment in the tree plots (Fig. 5B), revealing instead a gradual decline that tracked with maturation. An opposing trend was observed in pPLCγ2 responsiveness to BCR activation, which exhibited an increase that closely tracked with CD20 expression (Fig. 4C). The same trend was observed

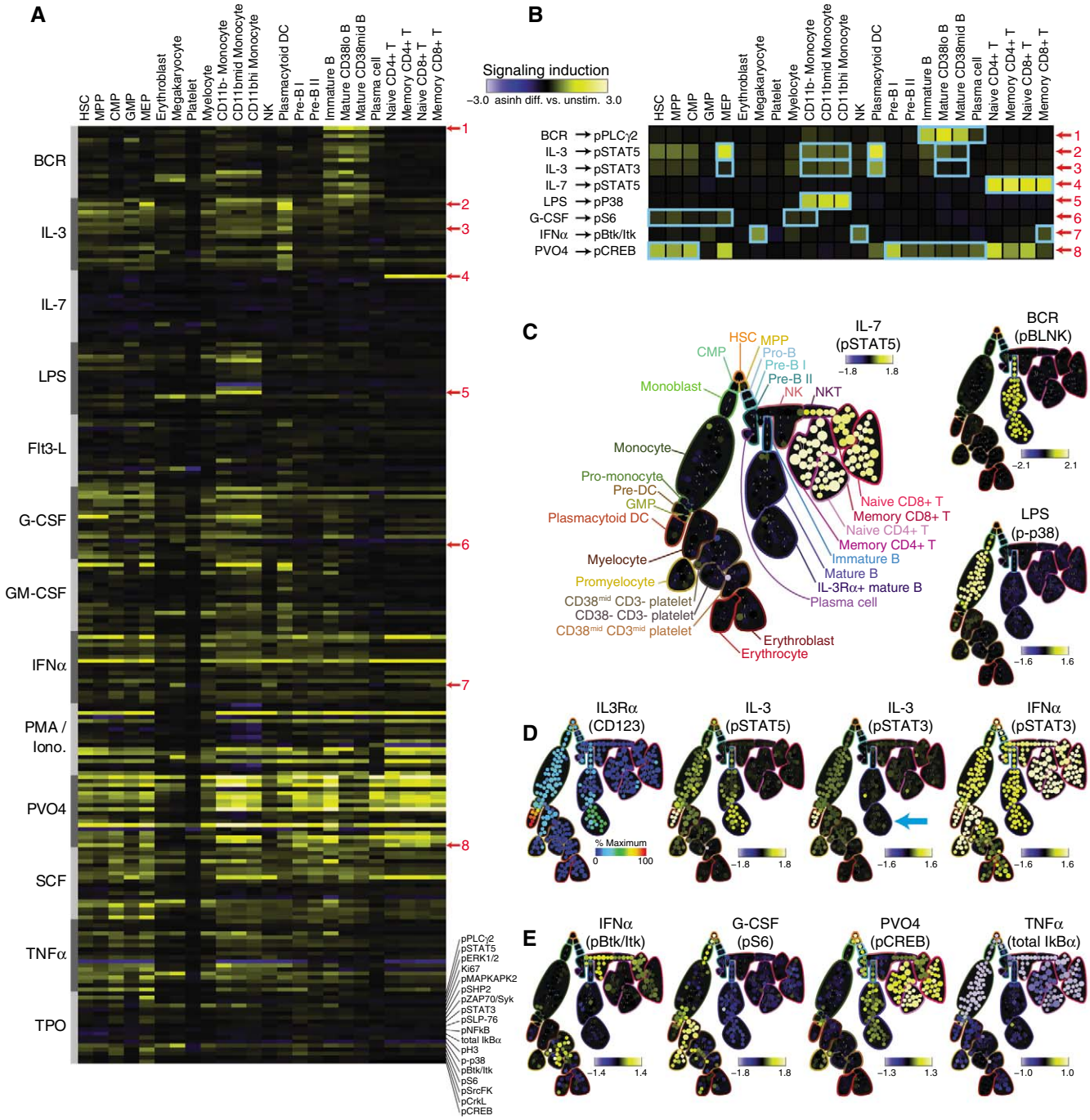

Fig. 3. Signaling functions mark developmental transitions in hematopoietic progression. (**A**) A heatmap summary, ordered developmentally by cell type and stimulation condition, of the status of 18 intracellular functional markers in cells treated with 1 of 13 biological and chemical stimuli. (Left) Abbreviations refer to recombinant human proteins, except BCR, B cell receptor cross-linking; LPS, lipopolysaccharide; PMA/Iono, phorbol-12-myristate-13-acetate with ionomycin; and PVO_4, pervanadate. Single-cell data from healthy human bone marrow were manually divided ("gated") into 24 conventional cell populations (fig. S5) according to 13 surface markers and DNA content. Signaling induction was calculated as the difference of inverse hyperbolic sine (arcsinh) medians of the indicated ex vivo stimulus compared with the untreated control for each manually assigned cell type (*21*). Each row within a given stimulus group (gray bars) indicates the signaling induction of 1 of 18 intracellular functional markers (bottom). A subset of conditions (red numbers) was highlighted for further discussion in (B). (**B**) Magnified view of the conditions marked in (A). A subset of these signaling responses (blue boxes) are shown as SPADE plots [(C) to (E)] to investigate correlations between signaling function and differences in immunophenotype as discussed in the text. (**C**) Canonical, cell type–specific signaling functions. Stimulation by IL-7, BCR, or LPS each induced phosphorylation of STAT5 in T cells, BLNK (SLP-65) [detected with an antibody raised against pSLP-76 (*21*)] in B cells, and p38 MAPK in monocytes, respectively. Signaling induction for each node in the SPADE diagram was calculated as the difference of arcsinh median intensity of the indicated ex vivo stimulus compared with the untreated control. (**D**) Correlation of IL-3–mediated induction of pSTAT3 and pSTAT5 with IL-3Rα expression [(Left) color scale as described in Fig. 2B] in myeloid and B cells. The B cell population that did not phosphorylate STAT3 in response to IL-3 stimulation is indicated (blue arrow). All nucleated cell subsets, including IL-3Rα$^+$ B cells, exhibited pSTAT3 induction in response to IFNα stimulation. Signaling induction calculated as in (C). (**E**) Examples of phosphorylation responses that paralleled immunophenotypic progression identified by the SPADE algorithm. Changes in Btk/Itk, S6, CREB phosphorylation, and total IκBα are shown in response to IFNα, G-CSF, PVO_4, and TNFα, respectively. Signaling induction is calculated as in (C).

for pERK1/2, pSLP-76, and pSHP2, suggesting a parallel and coordinated change in signaling pathways. In contrast, mature B cells lacked a PVO_4-sensitive mechanism, but the same set of signaling mediators appeared to be repurposed in a coordinated phosphorylation response to BCR activation (Fig. 4C). These results suggest that in pre-B II and immature B cells, but not mature B cells, pPLCγ2 activation is increased by an upstream tyrosine kinase with tightly regulated activity. This example supports the existence of parallel signaling mechanisms affecting these nodes (SLP-76, SHP2, PLCγ2, and ERK1/2) that gradually switches along with the expression continuums determined by external immunophenotypic markers. Together, these parallel continuums could define each cell's functional role within the greater hematopoietic system.

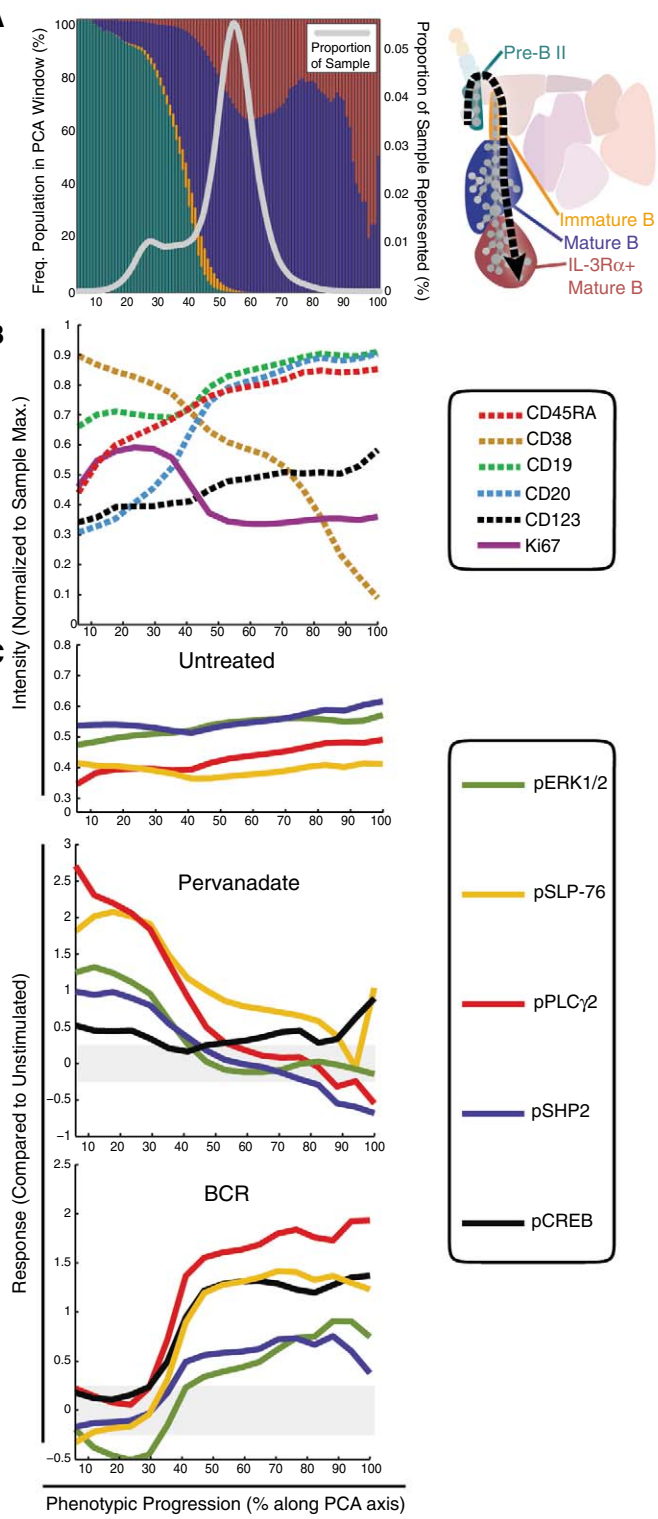

Fig. 4. PCA confirms that cellular signaling potentially tracks with the immunophenotypic continuum in B cell subsets. (**A**) Using the SPADE representation (right), cells assigned to pre-B II, immature B, mature B, and IL-3Rα$^+$ mature B cell populations were selected for PCA in 13 dimensions defined by the core immunophenotypic markers used in both panels. The relative frequencies of the four B cell populations are shown as stacked bars in 1% windows along the phenotypic progression axis (colors correspond to key at right); the number of cells in each window is expressed as a proportion of the sample subjected to PCA (gray line). (**B**) The measured intensities of five immunophenotypic markers (CD45RA, CD19, CD20, CD38, and CD123) along the phenotypic progression axis. These markers captured the majority of the phenotypic changes observed here during B cell maturation. Intracellular Ki67 expression, an indicator of cellular proliferation, was not used in defining the PCA axis but was among the 18 functional markers that were measured concurrently at the single-cell level. (**C**) Phosphorylation of ERK1/2, SLP-76(BLNK/SLP-65), PLCγ2, CREB, and SHP2 overlaid on the PCA progression axis. These and other functional epitopes were not used in the PCA axis construction. The top plot displays the basal levels (untreated) of these phosphorylated epitopes in the untreated sample. Subsequent plots display induced changes in phosphorylation in response to PVO_4 and B cell receptor cross-linking relative to the untreated control.

Effect of pharmacologic kinase inhibition on normal hematopoietic signaling. Having established a baseline of healthy signaling responses to a panel of stimuli, we examined cell type–specific pharmacologic effects of some well-characterized kinase inhibitors. These included the Janus kinase (JAK) I inhibitor and MAPK kinase (MEK) inhibitor U0126. Predictably, when combined respectively with G-CSF and PMA/Ionomycin treatments of human BM (figs. S8 and S9) reliable and specific inhibition, respectively, of STAT3 and ERK1/2 phosphorylation are observed, which is consistent with previously reported observations that used conventional single-cell analysis platforms (*44*). Although interesting results were obtained with these inhibitors, we expanded to focus on dasatinib, a clinically relevant small-molecule kinase inhibitor. Dasatinib was originally introduced as a second-line BCR-ABL kinase inhibitor for imatinib-resistant chronic myelogenous leukemia (CML) (*45*). Unlike imatinib, dasatinib is estimated to inhibit over 100 kinases besides Abl—particularly, Src family kinases (SrcFKs) (*46*). This promiscuity is credited for dasatinib's therapeutic efficacy in other malignancies (*47*). However, both malignant and healthy cells must integrate the effects of a drug with myriad other environmental inputs. We postulated that assessing drug activity in the presence of ex vivo stimuli may reveal interactions that underlie side effects for patients or expose new opportunities for pathway intervention.

Using the same healthy human bone marrow, we selected a panel of ex vivo stimuli that induced signaling in cell subsets either broadly [phorbol 12-myristate 13-acetate (PMA)/ionomycin and PVO_4] or specifically (Flt3-L, IL-7, and BCR), after 30 min of pretreatment with dasatinib. The results showed several examples of pathway-specific inhibition that fit with expected roles of dasatinib (fig. S10). For instance, activation of pERK1/2 in immature and mature B cells through BCR cross-linking was completely suppressed by dasatinib (Fig. 5A), most likely through inhibition of Lyn, a critical SrcFK downstream of the B cell receptor (*48*). In contrast, PMA/ionomycin–mediated activation of pERK1/2 was unaffected by dasatinib, thus confirming the observation that protein kinase C (PKC) signaling is mediated by dasatinib-insensitive kinases (Fig. 5A) (*49*).

Phosphorylation patterns of PLCγ2 after PVO_4 induction (Fig. 5B) were similar to PMA/ionomycin induction of pERK1/2 in the absence of dasatinib. However, dasatinib had a uniformly suppressive effect upon PVO_4 induction of PLCγ2 in all cell types (Fig. 5B), whereas it minimally inhibited induction of Erk1/2 upon PMA/ionomycin stimulation (Fig. 5A). Thus, in contrast to the dasatinib-insensitive PKC pathway described above (Fig. 5A) the PVO_4-sensitive cascade upstream of PLCγ2 was inhibited by dasatinib in all cell types, including platelets. This result may reconcile a clinical

observation of platelet dysfunction in CML patients treated with dasatinib (*50*), in which the inhibition of the SFKs upstream of PLCγ2 (Lyn and Fyn) is the proposed mechanism of dysregulation.

In B cells, dasatinib prevented phosphorylation of all measured components of the BCR signaling cascade (Syk, SHP2, Btk, BLNK, and PLCγ2) regardless of whether activation was through BCR crosslinking or PVO_4 treatment (Fig. 5B and fig. S8C). This off-target activity may underlie the efficacy reported in a patient with chronic lymphocytic leukemia, a B cell malignancy (*51*). However, these effects may also have undesirable consequences. For example, suppression of subtle pro-survival ("tonic") B cell signaling (*52*) may account for the decline of circulating B cells observed in CML patients undergoing high-dose dasatinib therapy (*53*).

Disruption of the tyrosine kinase/phosphatase equilibrium with PVO_4 also caused potent phosphorylation of STAT5 in nearly all cell types, but this was completely abrogated by dasatinib in all but the plasmacytoid dendritic cells (Fig. 5C). This time, dasatinib had no effect on the exclusive induction of STAT5 phosphorylation shown in T cells by IL-7 (Fig. 5C). The suppression of pSTAT5 in PVO_4-treated myeloid cells (Fig. 5C) supports the alternative mechanism of SrcFK activation of STAT5 activity and resembles the effect of dasatinib in a BCR-ABL–positive CML cell line (*54*).

That these pleiotropic downstream signaling molecules (ERK, STAT5, and PLCγ2) can be potently activated via both dasatinib-sensitive and -insensitive pathways highlights the drug's context and cell-type specificity for different signaling mediators. Thus, the unchecked endogenous tyrosine kinase activity revealed by PVO_4 may unveil differences in druggable signaling architecture between cell types by mimicking the dysregulated signaling of cells susceptible to disease or dysfunction. Additionally, as underlined by these limited examples, the dasatinib data set provided a mechanistic blueprint of regulatory cell signaling events that could potentially be exploited in later clinical applications.

Given the diverse cell type–specific effects of dasatinib, we investigated whether drug sensitivity would follow immunophenotypic progressions

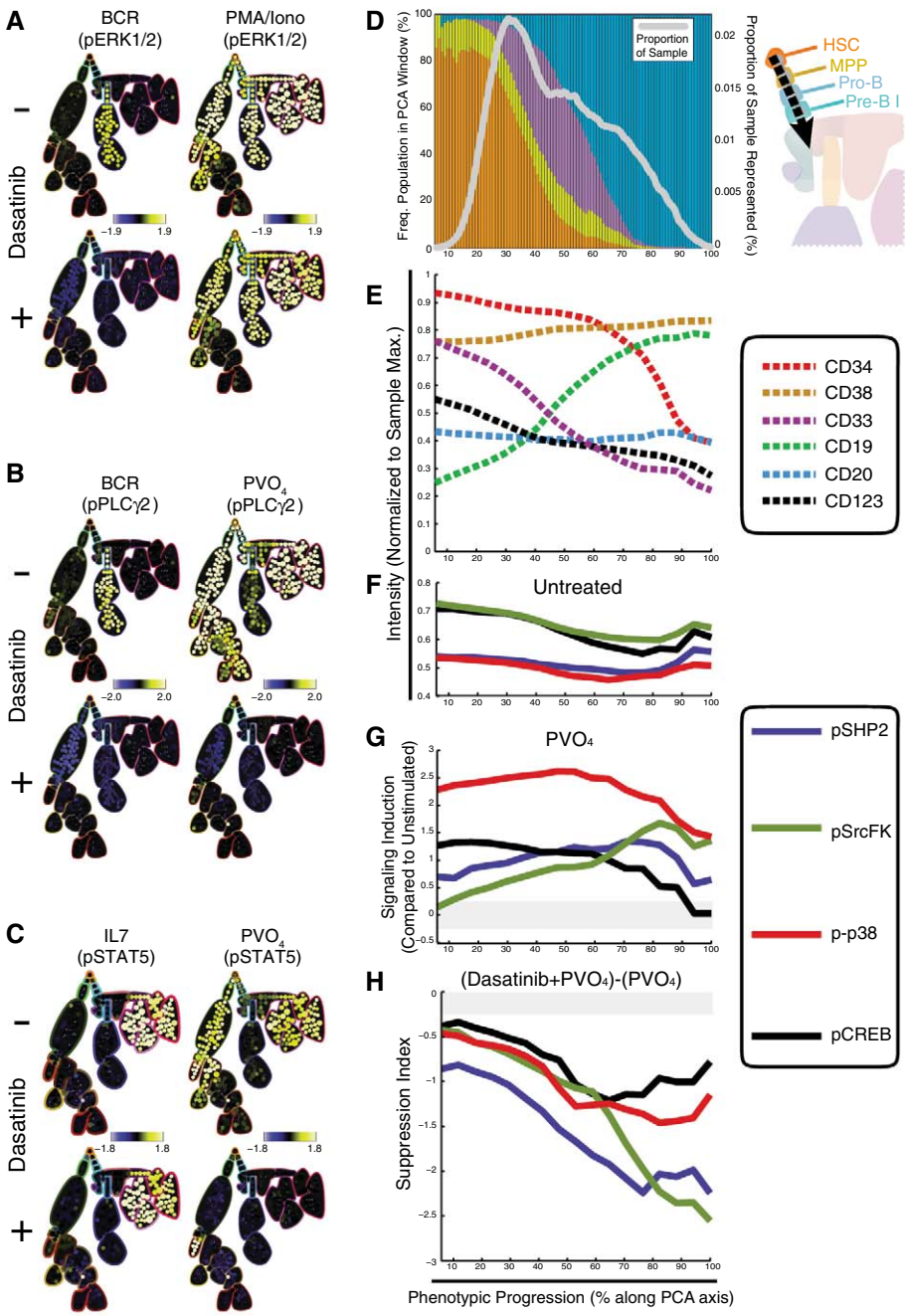

Fig. 5. Multiplexed mass cytometry analysis reveals diverse signaling dynamics in response to the kinase inhibitor agent dasatinib. (**A**) SPADE plots of exemplary cell type–specific inhibitory effects of dasatinib. Phosphorylation of ERK1/2 was sensitive to dasatinib when induced with BCR cross-linking but not when induced with PMA/ionomycin. Signaling induction for each node in the SPADE diagram was calculated as the difference of arcsinh median of the indicated ex vivo stimulus compared with the untreated control. (**B**) T lymphocytes exhibited STAT5 phosphorylation in response to IL-7 in the presence of dasatinib with similar magnitudes as the response observed without drug. PVO_4 induction of STAT5 phosphorylation was inhibited by dasatinib in all but plasmacytoid dendritic cells. Calculated as in (A). (**C**) B lymphocytes exhibited specific PLCγ2 phosphorylation in response to receptor cross-linking that was completely abolished in the presence of dasatinib. PLCγ2 phosphorylation was relatively large in all but B lymphocyte lineages in the presence of PVO_4 but was inhibited completely by dasatinib treament in all cells. Calculated as in (A). (**D**) Using the SPADE representation, cells corresponding to HSC, MPP, pro-B, and pre-B I cell populations were selected for PCA of the 13 core immunophenotypic markers. The relative frequencies of the four progenitor cell populations are shown as stacked bars in 1% windows along the phenotypic progression axis (colors correspond to key at right); the number of cells in each window is expressed as a proportion of the sample subjected to PCA (gray line). (**E**) The measured intensities of six immunophenotypic markers (CD34, CD33, CD19, CD20, CD38, and CD123) along the progression axis. These markers captured the majority of the phenotypic changes observed here during progenitor cell maturation. (**F**) Basal (untreated) phosphorylation levels of p38, SrcFK, CREB, and SHP2 overlaid on the phenotypic progression axis. These and other functional epitopes were not used in the PCA axis construction. (**G**) Induced changes in phosphorylation of p38, SrcFK, CREB, and SHP2 in response to PVO_4 compared with untreated control. Signaling induction is calculated as in (A). (**H**) Suppression of normal PVO_4 response by dasatinib. Suppression index is calculated as the signaling induction by PVO_4 with dasatinib pretreatment, minus the signaling induction by PVO_4 alone.

as observed above (Fig. 4). Cells representing HSC through pre-B I phenotypes were selected from the SPADE plot and subjected to principal component analysis (Fig. 5D). Unsupervised PCA detected the phenotypic progression in early B cell development as a single linear progression axis defined primarily by CD19, CD34, and CD33 intensities (Fig. 5E). This axis recapitulated the expected developmental sequence and independently verified the ordering identified by the SPADE algorithm (Figs. 2 and 5D). The basal intensities of four intracellular signaling mediators (pSHP2, pCREB, pSrcFK, and p-p38) were unchanged throughout the PCA progression axis (Fig. 5F) and exhibited similar potential for activation by PVO_4 (Fig. 5G). In contrast, these same signaling mediators exhibited a gradual increase in sensitivity to dasatinib correlated with maturation (Fig. 5H). This observation may be attributable to high expression of drug efflux pumps in the most immature cell types (HSCs and MPPs) (*55*). Alternatively, because PVO_4 reveals endogenous kinase activity by repressing tyrosine phosphatases these observations may indicate a gradual shift in the phosphatase/kinase balance during early B cell maturation. Altogether, this approach provides insight into how a high dimensional analysis can call attention to potential off-target effects and new therapeutic opportunities that can be leveraged at all stages of the drug development pipeline.

Discussion. In this study of the immune system, coupling classical phenotypic organization to cellular functional responses was unrestricted by the inherent limitations imposed by fluorescence. This merging provided a systems-level view of human hematopoiesis and immunology from the perspective of immunophenotype and coupled it to underlying events as measured through receptor engagement and small-molecule drug actions. Although yielding both qualitatively and quantitatively identical measurements when compared (Fig. 1 and fig. S1), current mass cytometry detection may not be as sensitive as fluorescent detection of the most quantum-efficient dyes (Fig. 1, D to E). However, the differences in sensitivity between mass cytometry isotopes used here are within a twofold range (*19*), whereas quantum yields of routinely used fluorescence dyes vary across a 10-fold range and require compensation for spectral overlap. This combined with the lack of background signal (autofluorescence) and the substantially greater number of parameters that can be simultaneously analyzed makes mass cytometry an attractive platform currently available for highly multiplexed single-cell analysis.

The single-cell functional outcome data set (free to explore and available online) both confirmed expected immunological phenomena and yielded unexpected observations related to the spectrum of cell type–specific signaling faculties and drug responses that arise during hematopoietic development. For instance, there was a lack of IL-3 regulation of STAT3 in mature B cells, despite the presence of CD123 (IL-3 receptor–α chain) (Fig. 3). Additionally, both precise and more gradual continuous signaling transitions observed in the data set across developing cell subtypes (Fig. 3) represent some of the most interesting biological insights. Many of these precise transitions correlate well with receptor expression measured here [IL3/CD123 and LPS/CD14 (Fig. 3 and figs. S4 and S8) and known from previous work (IL7/pSTAT5 based on IL7 receptor expression on T cells (*56*)]. As for the continuous transitions, more broadly acting conditions such as PVO_4 treatment revealed more subtle phosphorylation changes (Figs. 3 to 5) that probably reflect equally subtle changes in the kinase/phosphatase expression levels upstream of each of these measured targets, paralleling the phenotypic transitions.

These observations not only offer an opportunity to investigate the mechanism underlying the differences but may also provide a possibility to design drugs that might more precisely modulate disease states. There were many examples of signaling that corresponded with known distinct hematopoietic stages as well as multiple examples of progressive signaling responses across continuums of related cell types. We expect that a deeper mining of this and additional data sets will reveal many unexpected, system-wide correlations that could initiate new forms of mechanistic inquiry beyond what is currently possible with conventional techniques.

The extension of this analysis pipeline to preclinical settings can provide new insights into the mechanisms of diseases that perturb hematological function and could help pinpoint the true specificity and efficacy of drugs designed to restore the system to homeostasis. Expansion of this technology to additional parameters per cell (*18*, *19*) can be enabled by the use of other isotopes and binding agents—such as with isotopically enriched nanocrystals and new metal chelators. Combination of the increased availability of parameters in this platform with the high-throughput methods previously demonstrated in fluorescence flow cytometry [fluorescent cell barcoding (*57*) and drug screening (*44*)] opens avenues for massively multiplexed single-cell assays. Opportunities exist to extend the repertoire of transition element isotope reporter–enabled reagents to mimic (and potentially improve on) many of the assayable capabilities of fluorophores. Together, these advances offer an opportunity to delve deeper into signaling, studying entire pathways in cellulo, and thus explore the developmental functions of the immune system as a whole. Such studies of normal immune function can act as a backdrop to better understand how cancer, inflammatory, and autoimmune diseases affect or disable system-wide immune functions. An important next step will be the unification of these single-cell systems studies with other "-omic" (such as genomic, epigenomic, metabolomic, and proteomic) approaches to lead to an integrated view of how disease manifests and the ways we can precisely correct pathologic processes.

References and Notes:

1. M. Kondo *et al.*, *Annu. Rev. Immunol. (Paris)* **21**, 759 (2003).
2. S. Doulatov *et al.*, *Nat. Immunol.* **11**, 585 (2010).
3. P. K. Chattopadhyay *et al.*, *Nat. Med.* **12**, 972 (2006).
4. R. Majeti, C. Y. Park, I. L. Weissman, *Cell Stem Cell* **1**, 635 (2007).
5. A. Tárnok, H. Ulrich, J. Bocsi, *Cytometry A* **77**, 6 (2010) (Jan).
6. M. Roederer, S. C. De Rosa, N. Watanabe, L. A. Herzenberg, *Semin. Immunol.* **9**, 389 (1997).
7. C. A. O'Brien, A. Kreso, J. E. Dick, *Semin. Radiat. Oncol.* **19**, 71 (2009).
8. M. A. Krasnow, S. Cumberledge, G. Manning, L. A. Herzenberg, G. P. Nolan, *Science* **251**, 81 (1991).
9. R. Y. Tsien, *Annu. Rev. Biochem.* **67**, 509 (1998).
10. J. M. Irish *et al.*, *Cell* **118**, 217 (2004).
11. K. Sachs, O. Perez, D. Pe'er, D. A. Lauffenburger, G. P. Nolan, *Science* **308**, 523 (2005).
12. P. S. Frisa, J. W. Jacobberger, *PLoS ONE* **4**, e7064 (2009).
13. S. M. Kornblau *et al.*, *Clin. Cancer Res.* **16**, 3721 (2010).
14. D. B. Rosen *et al.*, *PLoS ONE* **5**, e13543 (2010).
15. S. P. Perfetto, P. K. Chattopadhyay, M. Roederer, *Nat. Rev. Immunol.* **4**, 648 (2004).
16. P. Autissier, C. Soulas, T. H. Burdo, K. C. Williams, *Cytometry A* **77**, 410 (2010).
17. X. Lou *et al.*, *Angew. Chem. Int. Ed. Engl.* **46**, 6111 (2007).
18. D. R. Bandura *et al.*, *Anal. Chem.* **81**, 6813 (2009).
19. O. Ornatsky *et al.*, *J. Immunol. Methods* **361**, 1 (2010).
20. O. I. Ornatsky *et al.*, *Anal. Chem.* **80**, 2539 (2008).
21. Materials and methods are available as supporting material on *Science* Online.
22. P. O. Krutzik, G. P. Nolan, *Cytometry A* **55**, 61 (2003).
23. J. G. Albeck *et al.*, *Mol. Cell* **30**, 11 (2008).
24. K. A. Janes *et al.*, *Mol. Cell. Proteomics* **2**, 463 (2003).
25. K. A. Janes *et al.*, *Cell* **124**, 1225 (2006).
26. E. G. van Lochem *et al.*, *Cytom. B Clin. Cytom.* **60**, 1 (2004).
27. I. R. Lemischka, *Ann. N.Y. Acad. Sci.* **1044**, 132 (2005).
28. I. D. C. Fraser, R. N. Germain, *Nat. Immunol.* **10**, 327 (2010).
29. K. Takano *et al.*, *Int. J. Hematol.* **72**, 48 (2000).
30. J. T. Chang *et al.*, *Science* **315**, 1687 (2007).
31. M. J. Fulwyler, *Science* **150**, 910 (1965).
32. L. A. Herzenberg, E. L. Chan, M. M. Ravitch, R. J. Riblet, L. A. Herzenberg, *J. Exp. Med.* **137**, 1311 (1973).
33. H. M. Shapiro, *Practical Flow Cytometry*. (Wiley-Liss, Hoboken, NJ, ed. 4, 2003).
34. M. Fulwyler, *Cytometry A* **67**, 61 (2005).
35. S. T. Oh *et al.*, *Blood* **116**, 988 (2010).
36. J. M. Irish *et al.*, *Proc. Natl. Acad. Sci. U.S.A.* **107**, 12747 (2010).
37. N. Kotecha *et al.*, *Cancer Cell* **14**, 335 (2008).
38. C. D. Surh, J. Sprent, *Immunity* **29**, 848 (2008).
39. R. J. Ulevitch, P. S. Tobias, *Annu. Rev. Immunol.* **13**, 437 (1995).
40. K. D. Gibbs Jr. *et al.*, *Blood*, published online 28 February 2011 (10.1182/blood-2010-07-298232).
41. R. R. Hardy, P. W. Kincade, K. Dorshkind, *Immunity* **26**, 703 (2007).
42. T. W. LeBien, T. F. Tedder, *Blood* **112**, 1570 (2008).
43. T. Kurosaki, H. Shinohara, Y. Baba, *Annu. Rev. Immunol.* **28**, 21 (2010).
44. P. O. Krutzik, J. M. Crane, M. R. Clutter, G. P. Nolan, *Nat. Chem. Biol.* **4**, 132 (2008).
45. B. J. Druker, *Blood* **112**, 4808 (2008).
46. M. W. Karaman *et al.*, *Nat. Biotechnol.* **26**, 127 (2008).
47. M. Lindauer, A. Hochhaus, *Recent Results. Cancer Res.* **184**, 83 (2010).
48. C. Yang *et al.*, *Leukemia* **22**, 1755 (2008).
49. A. E. Schade *et al.*, *Blood* **111**, 1366 (2008).
50. A. Quintás-Cardama, X. Han, H. Kantarjian, J. Cortes, *Blood* **114**, 261 (2009).
51. G. Russwurm *et al.*, *Blood* **116**, 2617 (2010).
52. J. G. Monroe, *Nat. Rev. Immunol.* **6**, 283 (2006).
53. C. Sillaber *et al.*, *Eur. J. Clin. Invest.* **39**, 1098 (2009).
54. S. Nam *et al.*, *Mol. Cancer Ther.* **6**, 1400 (2007).
55. M. Dohse *et al.*, *Drug Metab. Dispos.* **38**, 1371 (2010).
56. J. T. Tan *et al.*, *Proc. Natl. Acad. Sci. U.S.A.* **98**, 8732 (2001).
57. P. O. Krutzik, G. P. Nolan, *Nat. Methods* **3**, 361 (2006).

58. The authors thank W. J. Fantl for critical reading of the manuscript. S.C.B. is supported by the Damon Runyon Cancer Research Foundation Fellowship (DRG-2017-09). This work was supported by NIH grants, U19 AI057229, P01 CA034233, 272200700038C, 1R01CA130826, U54 CA149145, 5U54 CA143907, RB2-01592, PN2 EY018228, NOI-HV-00242,

and HEALTH.2010.1.2-1 (European Commission grant to the Sweden Diatools Consortium), as well as California Institute for Regenerative Medicine (DR-01477, RB2-01592) to G.P.N. G.P.N. is supported by an endowed chair from Rachtford and Carlota A. Harris. S.D.T. was supported by Genome Canada via the Ontario Genomics Institute for Cancer Research and by the Ontario Research Fund ORF-GL2-01-003. D.P. holds a Career Award at the Scientific Interface from the Burroughs Wellcome Fund and Packard Fellowship for Science and Engineering.

Some antibodies were a gift from Becton Dickinson Biosciences. B.B. is a paid employee of Becton Dickinson, and G.P.N. and P.K. are paid consultants for Becton Dickinson Biosciences. G.P.N. is a member of the Board of Directors and a consultant for DVS Sciences. O.O., G.P.N., and S.T. have equity holdings in DVS Biosciences, and S.T. is an employee of DVS Sciences. A patent has been applied for on the SPADE algorithm on behalf of Stanford University. Raw data and SPADE trees can be downloaded open access at www.cytobank.org/nolanlab.

Supporting Online Material
www.sciencemag.org/cgi/content/full/332/6030/687/DC1
Materials and Methods
Figs. S1 to S11
Tables S1 to S3
References

5 October 2010; accepted 22 March 2011
10.1126/science.1198704

REPORTS

Observation of Orbital Currents in CuO

V. Scagnoli,[1]* U. Staub,[1] Y. Bodenthin,[1] R. A. de Souza,[1] M. García-Fernández,[1] M. Garganourakis,[1] A. T. Boothroyd,[2] D. Prabhakaran,[2] S. W. Lovesey[3,4]

Orbital currents are proposed to be the order parameter of the pseudo-gap phase of cuprate high-temperature superconductors. We used resonant x-ray diffraction to observe orbital currents in a copper-oxygen plaquette, the basic building block of cuprate superconductors. The confirmation of the existence of orbital currents is an important step toward the understanding of the cuprates as well as materials lacking inversion symmetry, such as magnetically induced multiferroics. Although observed in the antiferromagnetic state of cupric oxide, we show that orbital currents can occur even in the absence of long-range magnetic moment ordering.

Although high-temperature (T_c) superconductivity was discovered 25 years ago, there is still no consensus on its microscopic origin. The peculiar properties of the normal state are widely thought to hold the key to understanding the electronic behavior of the cuprates, including superconductivity, and for this reason considerable attention has been paid to the pseudo-gap region of the phase diagram (*1*). One theoretical approach to describe the pseudo-gap phase predicts the existence of time-reversal symmetry breaking because of orbital currents (*2*–*4*). An order parameter that can be used to characterize this type of broken symmetry is a polar vector (parity-odd) that is magnetic (time-odd). Such a vector, also known as an anapole or toroidal moment, is a familiar quantity in particle physics (*5*, *6*), where it arises from parity violation inside the nucleus and manifests itself through the magnetoelectric interaction with atomic electrons. The concept has also been extended to the solid state (*7*), where it can be used to describe the antiferromagnetic ordering in crystal without space inversion center. Moreover, the presence of toroidal-moment ordering and its relation to magnetically induced multiferroics is the subject of current debate (*8*). In principle, resonant x-ray diffraction (RXD) can detect orbital current symmetry breaking directly (*9*). RXD takes advantage of resonance effects at an x-ray absorption edge to single out the contribution of the resonant atomic species and enhances weak diffraction signals because of magnetic moments providing information on electrons in the ground state not available in conventional diffraction. The RXD process is a second-order process of electron-photon coupling perturbation. In the electric dipole approximation (E1), the scattering amplitude from a single site is proportional to

$$f(E1-E1) \propto \sum_m \frac{\langle g|\mathrm{R}_{\boldsymbol{\epsilon}'}|m\rangle\langle m|\mathrm{R}_{\boldsymbol{\epsilon}}|g\rangle}{E + E_g - E_m + i\Gamma_m/2} \quad (1)$$

In such a process, a photon with energy E is scattered by being virtually absorbed and emitted with polarization $\boldsymbol{\epsilon}'$ and $\boldsymbol{\epsilon}$, respectively. E_m is the energy of a virtual intermediate state m with lifetime $\hbar/\Gamma_m$, E_g is the energy of an equilibrium state of the electron g belonging to the ground state of the material, $\mathbf{R}$ is the position operator, and $\mathrm{R}_{\boldsymbol{\epsilon}} = \boldsymbol{\epsilon} \cdot \mathbf{R}$. The sum is on the intermediate states m.

When the E1 contribution to the resonant event is small or forbidden, the matrix element $\langle m|\mathrm{R}_{\boldsymbol{\epsilon}}|g\rangle$ must be replaced by (*10*, *11*)

$$(E_m - E_g)m_e\left[\langle m|\mathbf{R}_{\boldsymbol{\epsilon}}|g\rangle + \frac{i}{2}\langle m|\mathbf{R}_{\boldsymbol{\epsilon}}\mathbf{q}\cdot\mathbf{R}|g\rangle\right] + \frac{1}{2}\langle m|\mathbf{q}\times\boldsymbol{\epsilon}\cdot(\mathbf{L}+2\mathbf{S})|g\rangle \quad (2)$$

where the first contribution is the familiar electric dipolar term, the second is due to the electric quadrupole process (E2), and the last is the magnetic dipole term (M1). $\mathbf{q}$ is the photon wave vector, and $\mathbf{L}$ and $\mathbf{S}$ are the orbital and spin angular momentum operators, respectively. Mixed terms (e.g., E1-M1 and E1-E2) may appear in the second-order scattering amplitude, and it is the presence of such terms that allows contributions from orbital currents to be observed (*9*). When mixed terms are present the scattering amplitude is given by, for example, $f = \eta f(\mathrm{E1\text{-}E1}) + f(\mathrm{E1\text{-}M1})$, where the complex parameter η accounts for a possible energy and lifetime difference between the two events.

Despite its simple chemical formula, cupric oxide (CuO) is a material that displays a wealth of interesting properties. It is the building block of the cuprate high-T_c superconductors. Its crystal structure belongs to the non-centrosymmetric monoclinic space group *Cc* (*12*). CuO undergoes two different magnetic transitions, at T_1 = 213 K and T_2 = 230 K (*13*–*15*), between which multiferroic properties have recently been discovered (*16*). Below T_1, CuO is a commensurate antiferromagnetic with ordering wave vector (1/2, 0, –1/2). The low, inversion-lacking symmetry makes it an ideal candidate to detect orbital currents.

We provide evidence of orbital currents through the observation of E1-M1 RXD at the Cu $L_{2,3}$ edges in CuO and suggest the existence of orbital currents in cuprates and multiferroics. Figure 1A shows the resonance enhancement at the copper $L_{2,3}$ edges of the superlattice reflection (1/2, 0, –1/2) associated with the antiferromagnetic motif of the copper magnetic moments. Energies correspond to the 2p → 3d electric dipole excitations. At the L_3 edge there are two resonant features (E_A = 929.5 eV and E_B = 934.8 eV), whereas at the L_2 (E_C = 950 eV) edge there is hardly any resonance. Such a difference might reflect the presence of spin-orbit coupling, leading to a substantial departure from the conventional Mott insulating state.

To confirm the magnetic origin of an observed resonant enhancement, it is standard practice to perform polarization analysis of the diffracted x-rays (fig. S1). Magnetic x-ray diffraction has the property to rotate the polarization of the incident photons by π/2. Therefore, when the incident photon polarization is perpendicular to the diffraction plane (an arrangement known as σ) all diffracted photons are polarized within the diffraction plane (π). The absence of diffracted photons (and the associated Bragg peak) perpendicular

[1]Swiss Light Source, Paul Scherrer Institut, CH 5232 Villigen PSI, Switzerland. [2]Department of Physics, University of Oxford, Clarendon Laboratory, Parks Road, Oxford OX1 3PU, UK. [3]ISIS Facility, RAL, Oxfordshire OX11 0QX, UK. [4]Diamond Light Source Limited, Oxfordshire OX11 0DE, UK.

*To whom correspondence should be addressed. E-mail: valerio.scagnoli@psi.ch

to the scattering plane (the so-called σ-σ′ channel) is a direct proof of the magnetic origin of the diffracted signal.

A distinct Bragg peak is present in the σ-σ′ diffraction channel, incompatible with the known magnetic structure (Fig. 1B). Indeed, such a peak is one of the fingerprints of the presence of orbital currents in the antiferromagnetic phase of CuO. More evidence of an extra contribution in the diffracted intensity comes from its dependence on the helicity of the x-rays around the L_3 edge as a function of the incident x-ray energy for two different azimuthal angles (Fig. 1, C and D). The azimuthal angle ψ represents a rotation of the sample about the diffraction wave vector. Intensity observed for incident circularly left (C_L) photons is not the same as the one gathered with incident circularly right (C_R) polarized incident photons. For this azimuthal angle (ψ = 17°), the first local maximum E_A is more intense for C_R light. However, at the second local maximum E_B it is the C_L light that shows the stronger intensity. Conversely, in Fig. 1D, which corresponds to ψ = –43°, the circular left-to-right intensity ratio is reversed. This dependence cannot be described by the collinear antiferromagnetic order determined by neutron experiments alone, because in this case the intensity does not depend on the helicity of the x-rays.

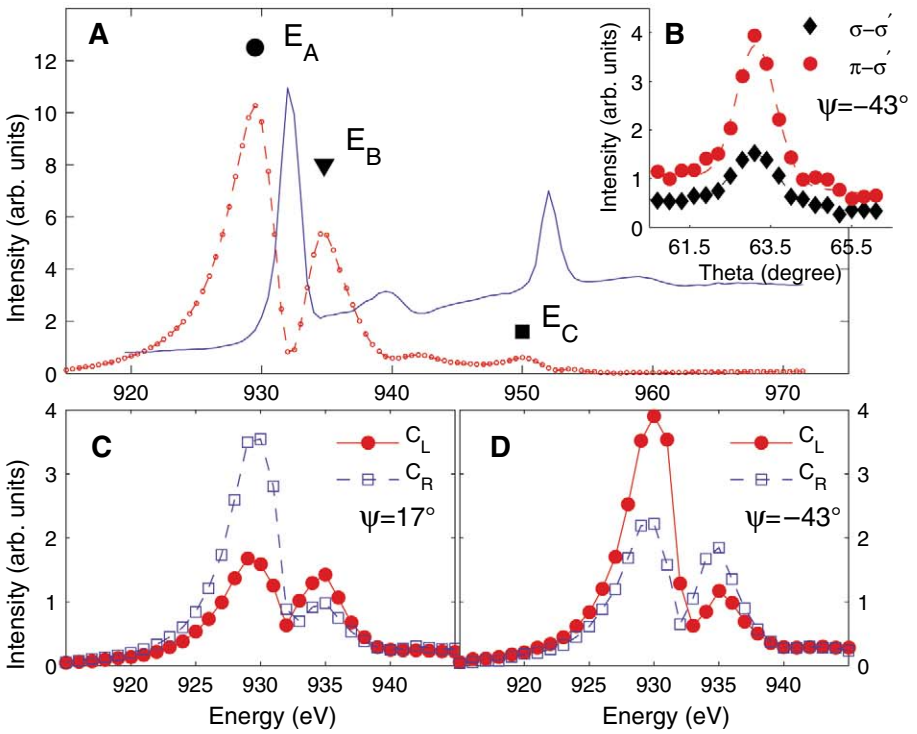

Fig. 1. (**A**) The solid line represents the x-ray absorption spectrum across the $L_{3,2}$ edges. The open (red) dots represent the intensity of the (1/2, 0, –1/2) superlattice reflection for in-plane polarized (π) incident photons. (**B**) Rocking curves of the diffracted intensity recorded with polarization analysis at the L_3 edge corresponding to the energy E_A. (**C** and **D**) Resonant enhancement in the vicinity of the L_3 edge as a function of the helicity of the incident x-rays for two chosen azimuthal angles. Intensities gathered with incident left C_L (right C_R) circularly polarized x-rays are in solid symbols; those gathered with C_R circularly polarized x-rays are shown with open symbols. Lines are guides to the eye. Data were collected at 100 K.

The C_R and C_L intensities modulate as a function of the azimuthal angle (Fig. 2). The intensities show a twofold periodicity and a clear shift of about 45° in the azimuth between the two polarizations collected. Their difference is also a twofold periodic function. Its deviation from a null value is the evidence of an additional contribution that adds in amplitude, causing interference with the resonant magnetic signal. We show that the additional component comes via a magnetic dipole transition M1 resulting from the presence, on the microscopic level, of orbital currents.

Diffracted intensities are particularly sensitive to the linear interfering term E1-M1 appearing in the modulus of the scattering amplitude. This term is analogous to the interference term arising from conventional Thomson charge diffraction and weak nonresonant (ferro-) magnetic diffraction (*17*), which is expected to be six orders of magnitude smaller. In the case of charge-magnetic interference, the reversal of the magnetic field direction clearly singles out the small magnetic contribution. In our case, we reverse the helicity of the incoming x-rays.

Evaluation of the size of the scattering amplitude requires the knowledge of the structure factors using matrix elements appearing in Eq. 2. The latter are usefully written as irreducible spherical tensors with rank K and projection Q ($-K \leq Q \leq K$). The calculation is considerably simplified by the symmetry constrains posed by the crystallographic (*12*) and magnetic structure (*13*). Only one of the nine irreducible tensors associated with the electric dipole event can be different from zero. It is $\langle T_y^1 \rangle = \langle T_b^1 \rangle$ related to the measured magnetic moment along the b axis. For the magnetic dipole term, there are four nonzero tensors whose linear combinations A_Q^K enter the scattering amplitude (*18*). The calculations lead to an appealing expression for the intensity difference between the two circular channels:

$$\Delta = C_L - C_R \propto \langle T_y^1 \rangle A_0^1 \sin(2\psi) \qquad (3)$$

where A_0^1 is the term associated with the presence of the orbital currents.

The introduction of the magnetic dipole amplitude M1 naturally explains the presence of an asymmetry term depending on the helicity of the x-ray. In the absence of an E1-M1 event, the orbital current term, A_0^1, is zero, and we recover the expected result Δ = 0 for a collinear antiferromagnetic structure. The observed ψ dependence is possibly not unique to orbital currents. However, complementary experiments exclude other contributions (*18*). The intensities gathered

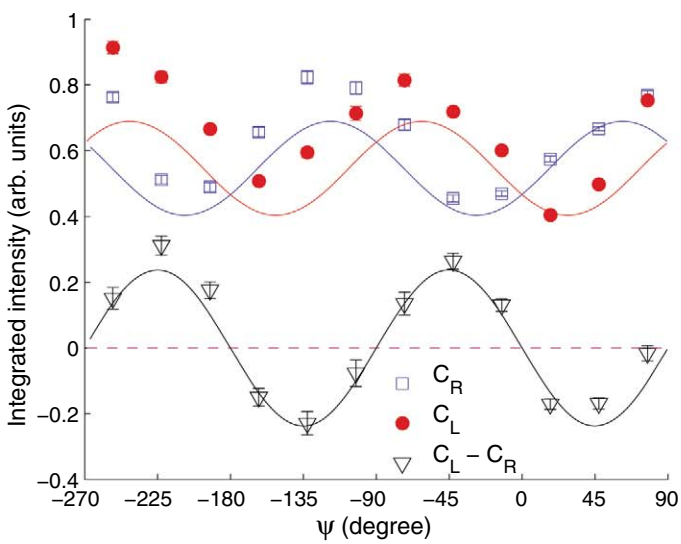

Fig. 2. Azimuthal angle dependence of the (1/2, 0, –1/2) reflection for incident C_R (blue open squares) and C_L (red solid circles) x-rays at 100 K at the energy E_A. The difference $\Delta = C_L - C_R$ is represented by open triangles. Continuous lines represent the fit obtained with the model presented in the text. The dashed line represents the intensity expected for Δ from the ordered Cu spin moments only. Error bars indicate standard deviation.

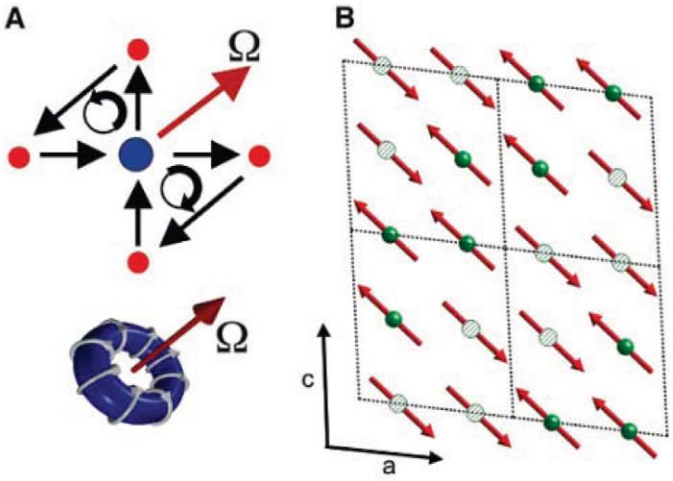

Fig. 3. (**A**) Representation of the relationship between the orbital currents (black curved arrows) flowing between the copper (blue circle) and oxygen (red circles) atoms and the toroidal moment (red arrow). (**B**) Antiferromagnetic-type ordering of the toroidal moments associated with the orbital currents. The orientation of the toroidal moments follows the value of the irreducible tensors obtained from experimental data. The solid green circles represent the Cu magnetic moment parallel to the crystallographic *b* axis. The shaded green circles represent the Cu magnetic moment antiparallel to the crystallographic *b* axis. The latter is perpendicular to the *a*,*c* plane.

with incident horizontal (I_π), vertical (I_σ), C_R, and C_L polarizations were also compared with the corresponding calculated expressions. Figure 2 shows how the E1-M1 contribution leads to a straightforward description of the observed intensities. In particular, the characteristic azimuthal modulation as a function of the x-ray helicity is naturally reproduced. Our model makes it possible to extract quantitative information about the circulating direction of the orbital currents. For illustrative purpose, it is easier to visualize the direction of the toroidal moments associated with such currents. A toroidal moment $\langle\Omega\rangle$ associated with an orbital moment $\mathbf{L}$ or a spin $\mathbf{S}$ is proportional to $\langle\mathbf{R}\times\mathbf{L}\rangle$ or $\langle\mathbf{R}\times\mathbf{S}\rangle$, respectively. Figure 3A illustrates (in the simplest case) the relation between the orbital currents and the toroidal moment associated with a single copper-oxygen plaquette. Figure 3B shows the ordering pattern of the toroidal moments in the extended magnetic unit cell as determined from our model. They lie in the *a*-*c* plane and share the same antiferromagnetic pattern of the magnetic moments. Our observations represent the direct evidence of antiferro ordering of toroidal moments in a material. Such ordering schemes can play an important role for multiferroics materials where the order parameter for the magnetoelectric coupling can be identified with the toroidal moment causing the electric polarization. Because of the subtleness of quantum mechanics, orbital currents can be generalized to a broader phenomenology. The presence of orbital currents is independent of the presence of an ordered atomic magnetic moment $\langle\mathbf{S}\rangle$ as $\langle\mathbf{\Omega}\rangle = \langle\mathbf{R}\times\mathbf{S}\rangle \neq \langle\mathbf{R}\rangle\times\langle\mathbf{S}\rangle$. Therefore, by applying a suitable magnetic (or electric) field an electric polarization (or magnetization) could be induced by the magnetoelectric coupling even in the absence of long-range magnetic order (or electric polarization). Besides multiferroics, another notable realization would be the pseudogap phase of high-T_c cuprates, where magnetic current loops flowing in the Cu-O planes without localized atomic ordered moments are proposed to be a property of the ground-state. In this respect, the observation of orbital currents in CuO, the basic building block of cuprate superconductors, provides strong encouragement for models based on orbital current ordering and related phenomena in high-T_c cuprates.

References and Notes

1. M. R. Norman, D. Pines, C. Kallin, *Adv. Phys.* **54**, 715 (2005).
2. C. M. Varma, *Phys. Rev. B* **55**, 14554 (1997).
3. C. M. Varma, *Phys. Rev. Lett.* **83**, 3538 (1999).
4. M. E. Simon, C. M. Varma, *Phys. Rev. Lett.* **89**, 247003 (2002).
5. Y. B. Zeldovich, *Zh. Eksp. Teor. Fiz.* **6**, 1184 (1958).
6. J. S. M. Ginges, V. V. Flambaum, *Phys. Rep.* **397**, 63 (2004).
7. V. M. Dubovik, V. V. Tugushev, *Phys. Rep.* **187**, 145 (1990).
8. D. I. Khomskii, *Physics* **2**, 20 (2009).
9. S. Di Matteo, C. M. Varma, *Phys. Rev. B* **67**, 134502 (2003).
10. C. Brouder, *J. Phys. Condens. Matter* **2**, 701 (1990).
11. S. W. Lovesey, E. Balcar, K. S. Knight, J. Fernández-Rodriguez, *Phys. Rep.* **411**, 233 (2005).
12. S. Åsbrink, A. Waskowska, *J. Phys. Condens. Matter* **3**, 8173 (1991).
13. J. B. Forsyth, P. J. Brown, B. M. Wanklyn, *J. Phys. C* **21**, 2917 (1988).
14. B. X. Yang, T. R. Thurston, J. M. Tranquada, G. Shirane, *Phys. Rev. B* **39**, 4343 (1989).
15. P. J. Brown, T. Chattopadhyay, J. B. Forsyth, V. Nunez, *J. Phys. Condens. Matter* **3**, 4281 (1991).
16. T. Kimura, Y. Sekio, H. Nakamura, T. Siegrist, A. P. Ramirez, *Nat. Mater.* **7**, 291 (2008).
17. C. Kao *et al.*, *Phys. Rev. Lett.* **65**, 373 (1990).
18. Materials and methods are available as supporting material on *Science* Online.

Acknowledgments: The authors acknowledge stimulating discussions with G. van der Laan, S. Di Matteo, A. Mirone, and F. de Bergevin. This work has been supported by the Swiss National Science Foundation, National Centre of Competence in Research–Materials with Novel Electrical Properties, and the UK Engineering and Physical Sciences Research Council. Part of this work was carried out at the SIM beamline at the Swiss Light Source, Paul Scherrer Institute, Villigen, Switzerland.

Supporting Online Material

www.sciencemag.org/cgi/content/full/science.1201061/DC1
Materials and Methods
Fig. S1
Tables S1 to S5
References

30 November 2010; accepted 22 March 2011
Published online 7 April 2011;
10.1126/science.1201061

Imaging Doped Holes in a Cuprate Superconductor with High-Resolution Compton Scattering

Y. Sakurai,[1]* M. Itou,[1] B. Barbiellini,[2] P. E. Mijnarends,[2,3] R. S. Markiewicz,[2] S. Kaprzyk,[2,4] J.-M. Gillet,[5] S. Wakimoto,[6] M. Fujita,[7] S. Basak,[2] Yung Jui Wang,[2] W. Al-Sawai,[2] H. Lin,[2] A. Bansil,[2] K. Yamada[7,8]

The high-temperature superconducting cuprate $La_{2-x}Sr_xCuO_4$ (LSCO) shows several phases ranging from antiferromagnetic insulator to metal with increasing hole doping. To understand how the nature of the hole state evolves with doping, we have carried out high-resolution Compton scattering measurements at room temperature together with first-principles electronic structure computations on a series of LSCO single crystals in which the hole doping level varies from the underdoped (UD) to the overdoped (OD) regime. Holes in the UD system are found to primarily populate the O $2p_x/p_y$ orbitals. In contrast, the character of holes in the OD system is very different in that these holes mostly enter Cu d orbitals. High-resolution Compton scattering provides a bulk-sensitive method for imaging the orbital character of dopants in complex materials.

The evolution of the electronic structure as well as the orbital character of the doped carriers is a key ingredient for understanding the physics of the cuprates and the mechanism of high-temperature superconductivity. Photoemission has succeeded in obtaining detailed in-

formation on the electronic dispersion and Fermi surface topology (*1*–*3*). Concerning the orbital character, comprehensive studies have concluded that the doped holes predominantly enter the oxygen 2p orbital in the cuprates, at least up to optimal doping (*4*–*7*). As a result, the unusual physical properties of underdoped (UD) cuprates have been analyzed mainly by ascribing a single orbital character to the doped holes. However, in the overdoped (OD) cuprates the orbital character is not fully understood, even though distinct doping dependencies of x-ray absorption (*8*, *6*) and optical reflectivity spectra (*9*) suggest a change in the oxygen 2p orbital character with overdoping. In order to detect changes in orbital character with doping, we need to consider spectral differences, which requires high-quality data for extracting weak wave function effects. Moreover, it is essential to measure a physical quantity that is connected to wave functions, such as the electron momentum density (EMD). Compton scattering is one of the most promising techniques for probing the orbital character of doped holes because it allows direct access to the EMD (*10*). Advantages of Compton scattering over other spectroscopies are that we do not need a nearly defect-free single crystal or a clean surface or ultrahigh vacuum and that the matrix element involved is much simpler than in other highly resolved spectroscopies such as photoemission (*11*), resonant inelastic x-ray scattering (*12*), scanning tunneling (*13*), and positron annihilation (*14*). X-ray Compton scattering has established itself as a viable technique for investigating orbital character (*15*, *16*) and Fermi surface geometry of the bulk system (*17*–*20*) in wide classes of materials.

We have obtained two-dimensional electron momentum densities (2D-EMDs), which represent one-dimensional integrals along the c-axis of three-dimensional EMDs for single crystalline samples of $La_{2-x}Sr_xCuO_4$ (LSCO) with four different hole dopings, $x = 0.0$, 0.08, 0.15, and 0.30 at room temperature. The samples and measurements are described in (*21*), and the experimental 2D-EMDs are presented in fig. S1. To clarify the evolving character of doped holes, we took the differences in 2D-EMDs between two samples with different doping levels. This subtraction technique (Fig. 1) provides information on changes in orbital occupation numbers associated with doped holes (*22*). Subtraction acts as a projector on an energy slice near the Fermi level with the advantage of eliminating the large isotropic contribution of the core as well as irrelevant valence electrons. Each electronic state has its own angular dependence in momentum space, which facilitates the detection of the state. For an atomic

[1]Japan Synchrotron Radiation Research Institute (JASRI), SPring-8,1-1-1 Kouto, Sayo, Hyogo 679-5198, Japan. [2]Physics Department, Northeastern University, Boston, MA 02115, USA. [3]Department of Radiation, Radionuclides, and Reactors, Faculty of Applied Sciences, Delft University of Technology, 2629 JB Delft, Netherlands. [4]Academy of Mining and Metallurgy AGH, 30059 Kraków, Poland. [5]Ecole Centrale Paris, Laboratoire Structures, Propriétés et Modélisation des Solides, UMR CNRS 8580, Grande Voie des Vignes, 92295 Châtenay-Malabry, France. [6]Quantum Beam Science Directorate, Japan Atomic Energy Agency, Tokai, Naka, Ibaraki 319-1195, Japan. [7]Institute for Materials Research, Tohoku University, Sendai 980-8577, Japan. [8]Advanced Institute for Materials Research, Tohoku University, Sendai 980-8577, Japan.

*To whom correspondence should be addressed. E-mail: sakurai@spring8.or.jp

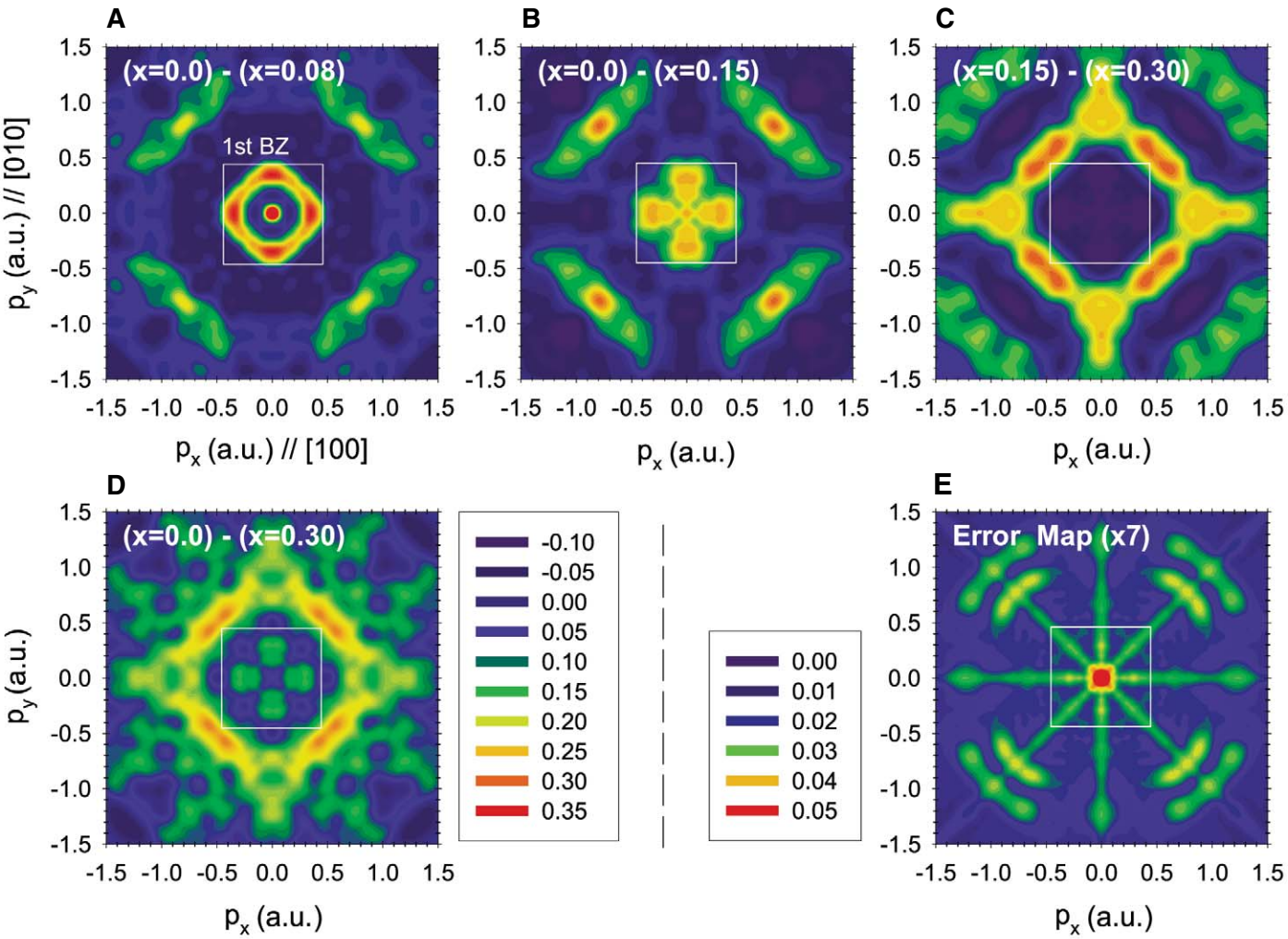

Fig. 1. Experimental difference 2D-EMDs in LSCO between two hole doping concentrations: (**A**) Nondoped ($x = 0.0$) minus UD ($x = 0.08$); (**B**) nondoped ($x = 0.0$) minus optimal-doped ($x = 0.15$); (**C**) optimal-doped ($x = 0.15$) minus heavily OD ($x = 0.30$); and (**D**) nondoped ($x = 0.0$) minus heavily OD ($x = 0.30$). (**E**) Error map of the difference 2D-EMD (the errors are typically 10 times smaller than the amplitudes in the 2D-EMD differences except very close to the origin). a.u., atomic units.

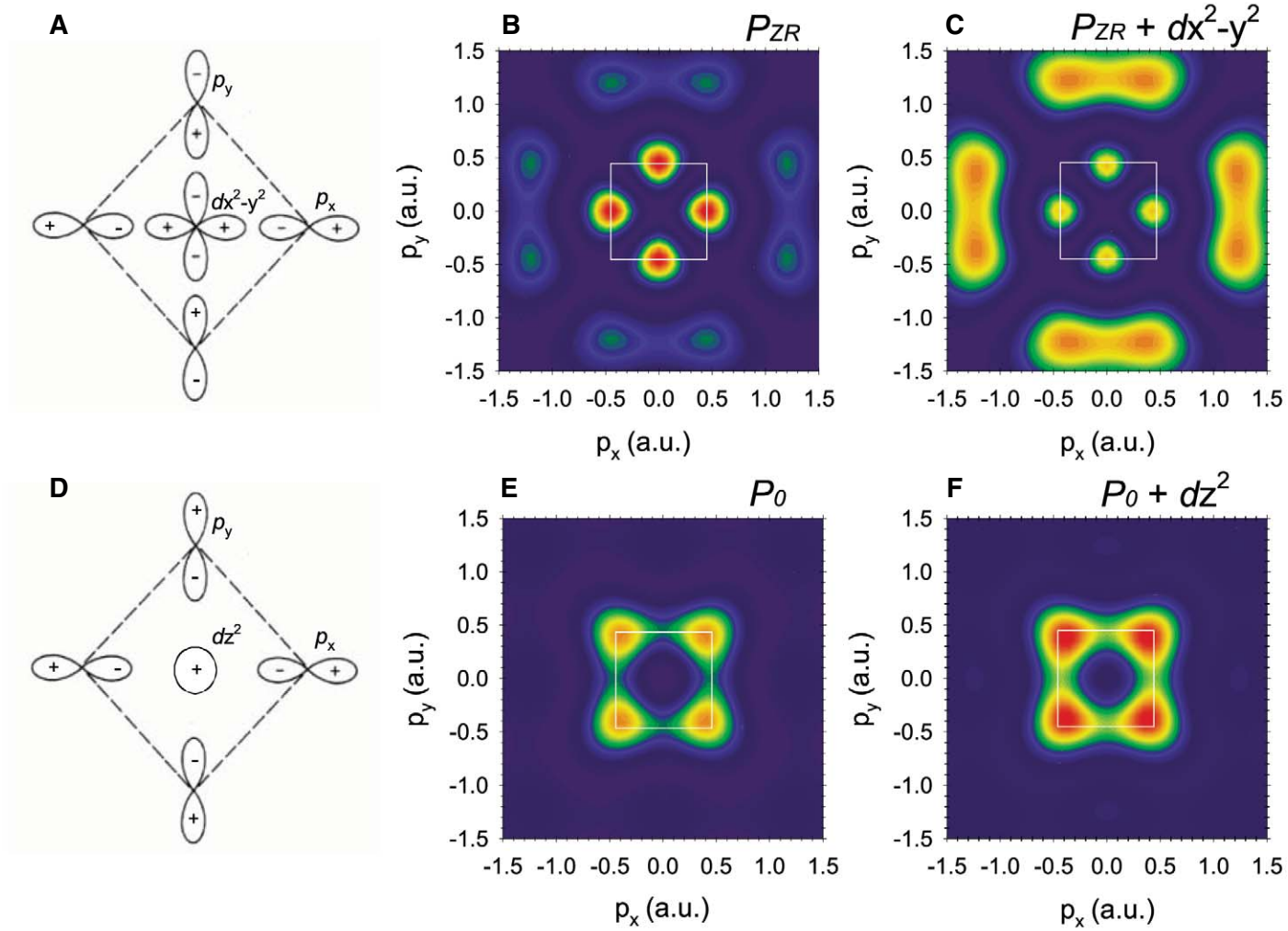

Fig. 2. Directional symmetry of Cu-O octahedral molecular orbitals. 2D-EMD projected onto the *xy* plane of the molecular orbitals: (**A**) Diagram of the $P_{ZR} = P_{1x} - P_{2y} - P_{3x} + P_{4y}$ state; (**B**) P_{ZR} state (only O $2p_{x/y}$ orbitals); (**C**) P_{ZR} state hybridized with Cu $3d_{x^2-y^2}$; (**D**) diagram of the $P_0 = P_{1x} + P_{2y} + P_{3x} + P_{4y}$ state; (**E**) P_0 state (only O $2p_{x/y}$ orbitals); (**F**) P_0 state hybridized with Cu $3d_{z^2}$. a.u., atomic units.

orbital, the EMD, which is the squared modulus of the momentum-space wave function, has the same point symmetry as the corresponding charge density. This result carries over to molecular states (*23*) and is equally applicable to solid-state wave functions (*24*). The radial behavior of the momentum-space wave function for each atomic orbital is determined by the spherical Bessel function, which behaves as p^l at small momenta p, where l is the orbital quantum number (*25*). Therefore, oxygen 2p bands contribute to the EMD at low momenta, whereas the contribution of the Cu 3d bands increases as p^4. This means that O 2p states are more visible in the first Brillouin zone (BZ), whereas Cu 3d states are better seen in higher BZs.

An important question regarding the nature of the electronic ground state of LSCO is the character of the extra holes introduced when we dope the half-filled insulator. Zhang and Rice (*7*) suggested that the holes reside in a molecular orbital state, $P_{ZR} = P_{1x} - P_{2y} - P_{3x} + P_{4y}$ (Fig. 2A), where numbers 1 to 4 label the four O atoms and subscripts x and y denote the direction of the O 2p orbital involved in the plaquette of four O atoms surrounding a Cu atom in the CuO_2 plane. The molecular orbital P_{ZR} couples with the Cu $3d_{x^2-y^2}$ state and forms the so-called Zhang-Rice singlet. By enhancing the O character of the doped hole near half filling, the Zhang-Rice singlet has a strong impact on Compton scattering. In cuprates the angular dependence of the wave functions is primarily set by the d orbitals of Cu, which hybridize with properly symmetrized combinations of p orbitals on nearest-neighbor oxygens. Hence we separate the strong peaks in Fig. 1 into peaks along the [100] axes associated with predominantly Cu $3d_{x^2-y^2}$ states and other peaks along the diagonal directions assigned to the Cu $3d_{z^2}$ orbital hybridized with the molecular orbital $P_0 = P_{1x} + P_{2y} + P_{3x} + P_{4y}$ (Fig. 2D). The Cu $3d_{z^2}$ state can also mix with the p_z atomic orbital from the apical oxygen. A two-orbital model that incorporates both e_g bands, namely the z^2 and the $x^2 - y^2$ hybrid bands, captures several crucial properties of LSCO (*26*).

Figure 2 shows that a number of features of the momentum density of Fig. 1 can be understood in a simple molecular orbital picture (*22*) in which band structure details are neglected. By varying the relative Cu character of the orbital, the model properly describes the doping evolution of the Zhang-Rice characteristics (Fig. 2, B and C) as well as features of the z^2 states (Fig. 2, E and F). However, because of the finite molecular size, the calculations do not quantitatively reproduce the radial positions of O and Cu features in momentum space. These features are more correctly described by band structure calculations, despite the fact that these calculations do not properly reproduce the doping evolution of Cu-O hybridization. Details of the EMD patterns are determined by competition between two opposing tendencies. Coulomb repulsion tends to localize d electrons on the Cu atoms, whereas mixing with the oxygen p electron states tends to delocalize these same electrons. Band structure and molecular orbital calculations are thus both useful for identifying various features in the Compton spectra. The band diagram in Fig. 3A shows the two main bands near the Fermi level. The band with $x^2 - y^2$ symmetry is higher in energy than the band of z^2 symmetry. By calculating difference spectra over

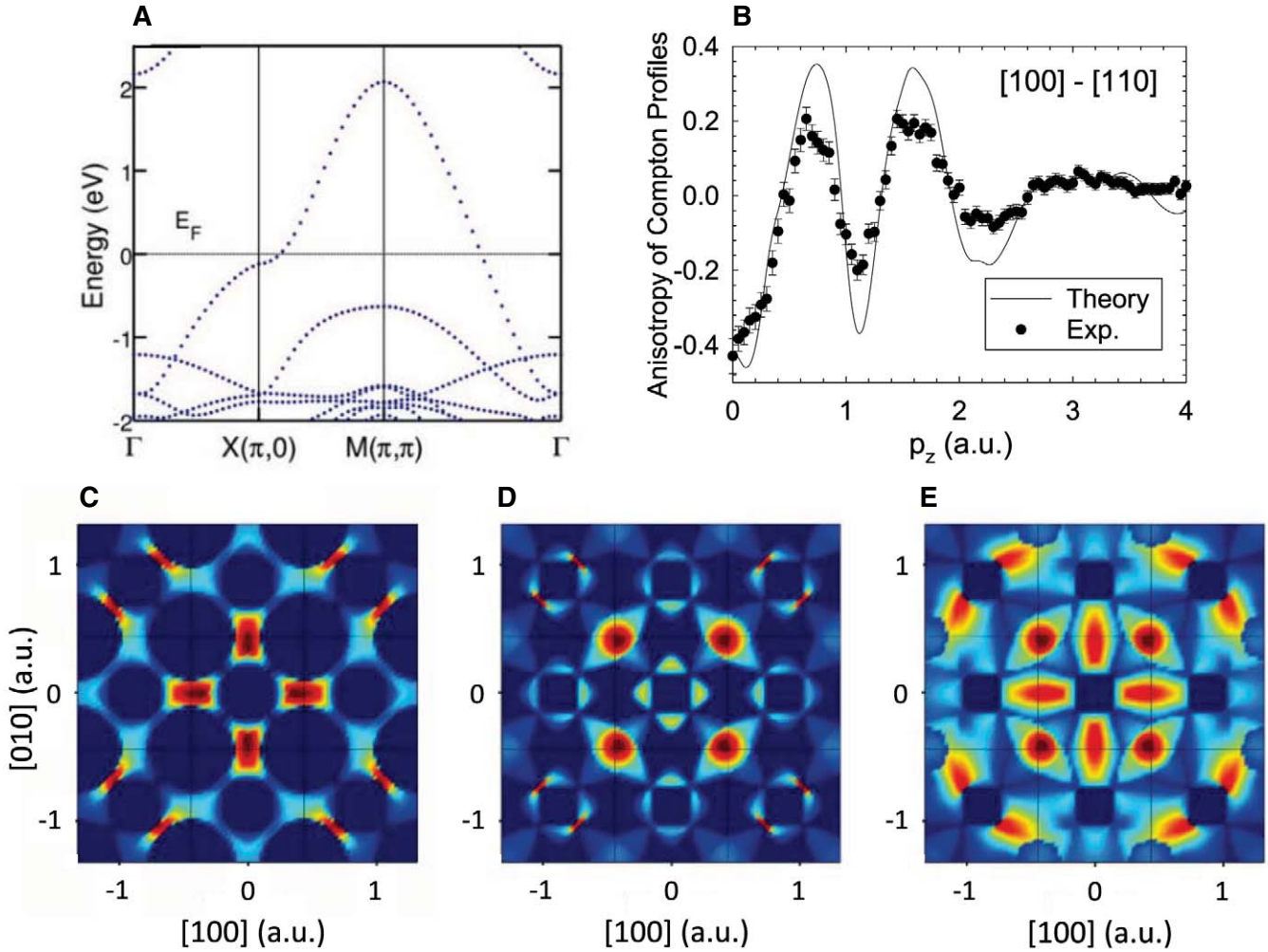

Fig. 3. Theoretical electronic structure: (**A**) Band structure; (**B**) anisotropy of Compton profiles; (**C**) 2D-EMD contribution between –0.4 eV and +0.1 eV; (**D**) 2D-EMD contribution between –0.8 eV and –0.4 eV; and (**E**) 2D-EMD contribution between –0.8 eV and +1.3 eV. Error bars in (B) indicate SEM. a.u., atomic units.

appropriate energy intervals, we can determine the patterns associated with particular orbitals. As shown in Fig. 3B, experiment and theory show a reasonable agreement regarding the difference of the directional Compton profiles [100]-[110] for $x = 0.15$. The present theoretical Compton profiles are computed from the Green functions obtained by Korringa-Kohn-Rostoker coherent potential approximation (KKR-CPA) calculations within the local density approximation (LDA) (*27*, *28*, *21*), which yields Fermi surface properties in agreement with angle-resolved photoemission spectroscopy (ARPES) experiments (*1*). Figure 3 also shows the contribution of the 2D-EMDs between –0.4 eV and +0.1 eV from the $x^2 - y^2$ band (Fig. 3C), between –0.8 eV and –0.4 eV from the z^2 band (Fig. 3D), and between –0.8 eV and +1.3 eV from both bands (Fig. 3E). These calculations reproduce trends related to the Cu-O states. Notably, in Fig. 3E the two diagonal features approximately agree with the experimental Fig. 1C despite some discrepancies regarding the position of the Cu d features along p_x and p_y. Interestingly, other small experimental features along these directions, which are related to d_{xz} and d_{yz} orbitals, could be found at lower energy in the theory. In any event, the present analysis in the energy range between –0.8 eV and +1.3 eV captures the dominant features of the two-orbital band model (*26*). Part of the disagreement between theory and experiment is related to the fact that our LDA computations tend to underestimate the d_z^2 character of states at the Fermi energy (*29*). Our analysis shows that for small Sr concentrations the doped holes have a substantially greater O 2p character than predicted by band theory. These effects are difficult to describe within the conventional Fermi liquid picture and would likely require the treatment of electron correlations involving the formation of Zhang-Rice singlets (*7*). We note as well that lattice perturbations affecting the bonding properties, such as Jahn-Teller distortions and polaronic displacements, are not included in the present calculations.

Our study shows the use of high-resolution Compton scattering for direct, bulk-sensitive imaging of the orbital character of dopants in the ground state of complex materials. This information cannot be obtained from other highly resolved spectroscopies. Features in Compton spectra are extremely robust because they are not significantly affected by defects, surfaces, or impurities.

References and Notes

1. S. Sahrakorpi, M. Lindroos, R. S. Markiewicz, A. Bansil, *Phys. Rev. Lett.* **95**, 157601 (2005).
2. A. Damascelli, Z. Hussain, Z.-X. Shen, *Rev. Mod. Phys.* **75**, 473 (2003).
3. T. Yoshida *et al.*, *Phys. Rev. B* **74**, 224510 (2006).
4. N. Nücker *et al.*, *Phys. Rev. B* **39**, 6619 (1989).
5. A. Bianconi *et al.*, *Solid State Commun.* **63**, 1009 (1987).
6. C. T. Chen *et al.*, *Phys. Rev. Lett.* **68**, 2543 (1992).
7. F. C. Zhang, T. M. Rice, *Phys. Rev. B* **37**, 3759 (1988).
8. D. C. Peets *et al.*, *Phys. Rev. Lett.* **103**, 087402 (2009).
9. S. Uchida, T. Arima, Y. Tokura, S. Tajima, *Phys. Rev. B* **43**, 7942 (1991).
10. M. J. Cooper, P. E. Mijnarends, N. Shiotani, N. Sakai, A. Bansil, Eds., *X-ray Compton Scattering* (Oxford Univ. Press, Oxford, 2004).
11. A. Bansil, M. Lindroos, *Phys. Rev. Lett.* **83**, 5154 (1999).
12. R. S. Markiewicz, A. Bansil, *Phys. Rev. Lett.* **96**, 107005 (2006).
13. J. Nieminen, H. Lin, R. S. Markiewicz, A. Bansil, *Phys. Rev. Lett.* **102**, 037001 (2009).
14. L. C. Smedskjaer, A. Bansil, U. Welp, Y. Fang, K. G. Bailey, *J. Phys. Chem. Solids* **52**, 1541 (1991).
15. A. Koizumi *et al.*, *Phys. Rev. Lett.* **86**, 5589 (2001).
16. B. Barbiellini *et al.*, *Phys. Rev. Lett.* **102**, 206402 (2009).

17. Y. Sakurai *et al.*, *Phys. Rev. Lett.* **74**, 2252 (1995).
18. S. B. Dugdale *et al.*, *Phys. Rev. Lett.* **96**, 046406 (2006).
19. N. Hiraoka, T. Buslaps, V. Honkimäki, J. Ahmad, H. Uwe, *Phys. Rev. B* **75**, 121101(R) (2007).
20. C. Utfeld *et al.*, *Phys. Rev. B* **81**, 064509 (2010).
21. Materials and methods are available as supporting material on *Science* Online.
22. B. Barbiellini *et al.*, *Physica C* **229**, 113 (1994).
23. W. Weyrich, P. Pattison, B. G. Williams, *Chem. Phys.* **41**, 271 (1979).
24. R. Harthoorn, P. E. Mijnarends, *J. Phys. F Met. Phys.* **8**, 1147 (1978).
25. P. E. Mijnarends, *Physica* **63**, 235 (1973).
26. H. Sakakibara, H. Usui, K. Kuroki, R. Arita, H. Aoki, *Phys. Rev. Lett.* **105**, 057003 (2010).
27. A. Bansil, R. S. Rao, P. E. Mijnarends, L. Schwartz, *Phys. Rev. B* **23**, 3608 (1981).
28. A. Bansil, *Z. Naturforsch. A* **48**, 165 (1993).
29. J. B. Goodenough, J. Zhou, *Phys. Rev. B* **42**, 4276 (1990).

Acknowledgments: The work at JASRI was supported by a Grant-in-Aid for Scientific Research (no. 18340111) from the Ministry of Education, Culture, Sports, Science, and Technology (MEXT), Japan, and that at Tohoku University was supported by a Grant-in-Aid for Scientific Research (nos. 16104005, 19340090, and 22244039) from the MEXT, Japan. The work at Northeastern University (NU) was supported by the Division of Materials Science and Engineering, Office of Science, U.S. Department of Energy, and it benefited from the allocation of supercomputer time at the National Energy Research Scientific Computing Center, the NU's Advanced Scientific Computation Center (ASCC), and the Stichting Nationale Computerfaciliteiten (National Computing Facilities Foundation, NCF). The Compton scattering experiments were performed with the approval of JASRI (proposals 2003B0762, 2004A0152, 2007B1413, 2008A1191, and 2010A1907).

Supporting Online Material

www.sciencemag.org/cgi/content/full/science.1199391/DC1
Materials and Methods
Fig. S1

21 October 2010; accepted 22 March 2011
Published online 28 April 2011;
10.1126/science.1199391

Photodetection with Active Optical Antennas

Mark W. Knight,[1,2] Heidar Sobhani,[1,2] Peter Nordlander,[1,2,3] Naomi J. Halas[1,2,3]*

Nanoantennas are key optical components for light harvesting; photodiodes convert light into a current of electrons for photodetection. We show that these two distinct, independent functions can be combined into the same structure. Photons coupled into a metallic nanoantenna excite resonant plasmons, which decay into energetic, "hot" electrons injected over a potential barrier at the nanoantenna-semiconductor interface, resulting in a photocurrent. This dual-function structure is a highly compact, wavelength-resonant, and polarization-specific light detector, with a spectral response extending to energies well below the semiconductor band edge.

Optical antennas are key elements in the conversion of light from free space to ultrasmall, nanometer-scale volumes. The intense light-focusing properties of these structures are due to surface plasmons, oscillations of free electrons in metals that couple to the incident light field. A wide range of applications—in sensing, subwavelength and nonlinear optics, and even novel medical therapies—have arisen for nanoantennas, exploiting the large local electromagnetic fields and intense heating they provide (*1*–*3*). Recent studies have investigated the use of plasmonic antennas to enhance the performance of photoactive devices, such as solar cells, light-emitting diodes, and photodetectors (*4*–*8*). Typically, one or more antennas are placed on or close to the active region of a device, where the near field of the plasmon, the scattering cross section, and the tailored photon density of states may all act to modify and enhance device characteristics.

Another important property of optical antennas is their propensity for generating energetic or "hot" electron-hole pairs by plasmon decay (*9*–*16*). Light not redirected by the antenna is absorbed, forming an energetic electron-hole pair. This process is an additional contribution to plasmon damping, broadening the intrinsic linewidth, and is typically considered deleterious to antenna performance. This process of hot electron generation has been shown to participate in photochemical reactions at noble metal nanoparticle surfaces (*17*–*21*), but it has remained largely unexploited in solid-state devices.

We report an active optical antenna device that uses the hot electron-hole pairs arising from plasmon decay to directly generate a photocurrent, resulting in the detection of light (Fig. 1). This is accomplished by a nanoantenna fabricated on a semiconductor surface where a metal-semiconductor, or Schottky, barrier is formed at the antenna-semiconductor interface. When this type of antenna is photoexcited it generates electron-hole pairs (*9*–*12*) and injects hot electrons into the semiconductor over the Schottky barrier, contributing to a detectable photocurrent (Fig. 1A). In this configuration, photocurrent generation is no longer limited to photon energies above the band gap of the semiconductor, but rather to photon energies above the Schottky barrier height (*22*). Therefore, this device is capable of detecting light well below the band gap of the semiconductor at room temperature and without a bias voltage.

Our initial realization of active optical antenna-diode photodetection consists of an array of independent, rectangular gold nanorods (Fig. 1B) (*23*). Nanorods support both longitudinal and transverse plasmon resonances, with the frequency of these resonances determined by the nanorod geometry: Increasing the nanorod aspect ratio tunes the longitudinal resonance to respond at longer wavelengths (*24*). The resonators studied here had heights and widths of 30 and 50 nm, respectively, and lengths ranging from 110 to 158 nm. Each device array consisted of 300 devices arranged in a 15 × 20 array with a 250-nm interantenna spacing in both the longitudinal and transverse directions, sufficient to ensure that near-field interantenna coupling is absent. The

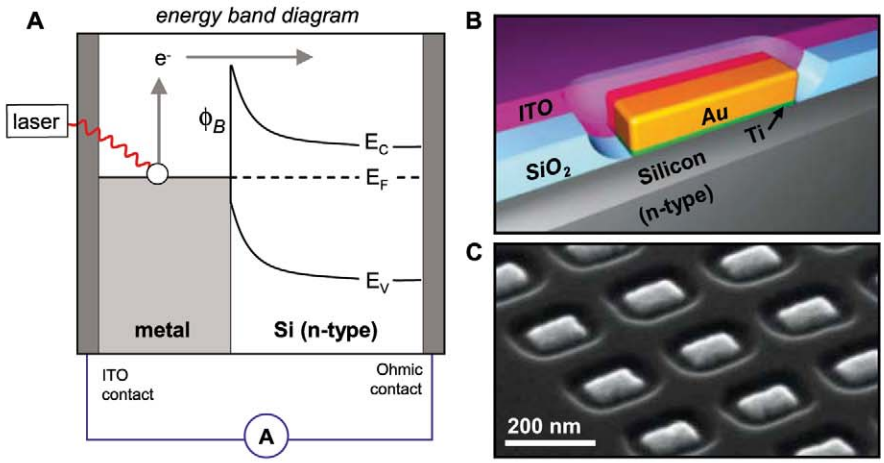

Fig. 1. An optical antenna-diode for photodetection. (**A**) Band diagram for plasmonically driven internal photoemission over a nanoantenna-semiconductor Schottky barrier (ϕ_B). (**B**) Representation of a single Au resonant antenna on an n-type silicon substrate. (**C**) Scanning electron micrograph of a representative device array prior to ITO coating, imaged at a 65° tilt angle.

[1]Department of Electrical and Computer Engineering, Rice University, Houston, TX 77005, USA. [2]Laboratory for Nanophotonics, Rice University, Houston, TX 77005, USA. [3]Department of Physics and Astronomy, Rice University, Houston, TX 77005, USA.

*To whom correspondence should be addressed. E-mail: halas@rice.edu

structure is surrounded by an insulating SiO_2 region (Fig. 1C) and then electrically connected through a top transparent electrode of indium tin oxide (ITO).

The photocurrent obtained from these devices is determined directly by the antenna properties. The photocurrent shows a strong wavelength dependence resulting from the rod geometry, with maximum currents increasing in wavelength with increasing antenna length (Fig. 2A). The spectral response directly follows the longitudinal dipole absorption resonance of the plasmon mode excited on the structure. The polarization dependence of the photocurrent also follows that of the nanoantennas, with a highly polarization-dependent response (Fig. 2B, green points) obeying a $\cos^2\theta$ angular dependence characteristic of a dipole antenna (gray line). For light polarized along the short (transverse) rod axis, we observe >90% attenuation of the photocurrent with respect to the longitudinal polarization. Incident power variation at a single wavelength results in a linear response of the photocurrent, which suggests that the photocurrent is dominated by the conversion of single photons to single hot electrons over this range of incident light intensities (Fig. 2C) (*9*–*12*, *14*).

The responsivity of this device can be understood by first considering a Schottky diode in the absence of a plasmon resonance, where the responsivity depends only on the energy-dependent internal photoemission probability. This quantum transmission probability η_i can be approximated by the modified Fowler theory (*25*, *26*), which describes the number of "available" electrons in the system with sufficient energy to overcome the potential barrier:

$$\eta_i \approx C_F \frac{(h\nu - q\phi_B)^2}{h\nu} \qquad (1)$$

where C_F is the device-specific Fowler emission coefficient (*26*), $h\nu$ is the photon energy, and $q\phi_B$ is the Schottky barrier energy. Fitting the responsivity curve of a planar Schottky device with this equation allows one to extract the material-dependent Schottky barrier height for a given metal-semiconductor interface.

When the Schottky barrier is formed by a plasmon resonant antenna rather than a continuous film, the device responsivity R will show a Fowler response modified by the plasmon absorption spectrum S:

$$R(\nu) = \eta_i S(\nu) \qquad (2)$$

With this extended Fowler relation, we can extract the Schottky barrier height for devices with a known plasmon line shape. In general, $S(\nu)$ will depend on multiple factors, including the geometry, composition, and size of the plasmonic devices. In the quasi-static regime, where the plasmonic particles are significantly smaller than the wavelength of light, the optical response will be dipolar and will exhibit a Lorentzian line shape near the resonance frequency (*13*). Fitting the experimental responsivities (Fig. 2A) with Eq. 2, using a Lorentzian line shape for $S(\nu)$, yields a Schottky barrier height of 0.50 eV. From this analysis we find that the barrier height is determined primarily by the 1-nm Ti adhesion layer and is consistent with Ti/Si Schottky barrier devices (*27*). This low barrier height should permit a detection window covering the entire short-wave infrared spectral range (λ = 1.2 to 2.5 μm).

Conversely, with a known Schottky barrier height, the absorption spectrum of an antenna diode of arbitrary geometry can be extracted from the spectral dependence of the responsivity. For our system, the experimental absorption spectra extracted from the overall responsivity (Fig. 2C) using a barrier height of 0.50 eV are shown in Fig. 2D. These experimental spectra exhibit extremely close agreement with calculated absorption spectra (Fig. 2E); both spectral sequences exhibit similar peak locations for nominally identical geometries, exhibiting a linear redshift with increasing aspect ratio, as is characteristic for nanorods (*24*, *28*). This agreement is notable given that the finite-difference time domain (FDTD) simulations (Fig. 2E) included no adjustable parameters; all calculations were performed with experimental dimensions and literature values for the optical constants of materials (Si, SiO_2, Au, Ti, ITO) (*29*–*31*). This agreement also shows that although the nanoantennas are configured in an array, their response is that of individual, independent nanoantennas and is consistent with the collected photocurrent being generated by hot carriers injected by each discrete nanoscale device.

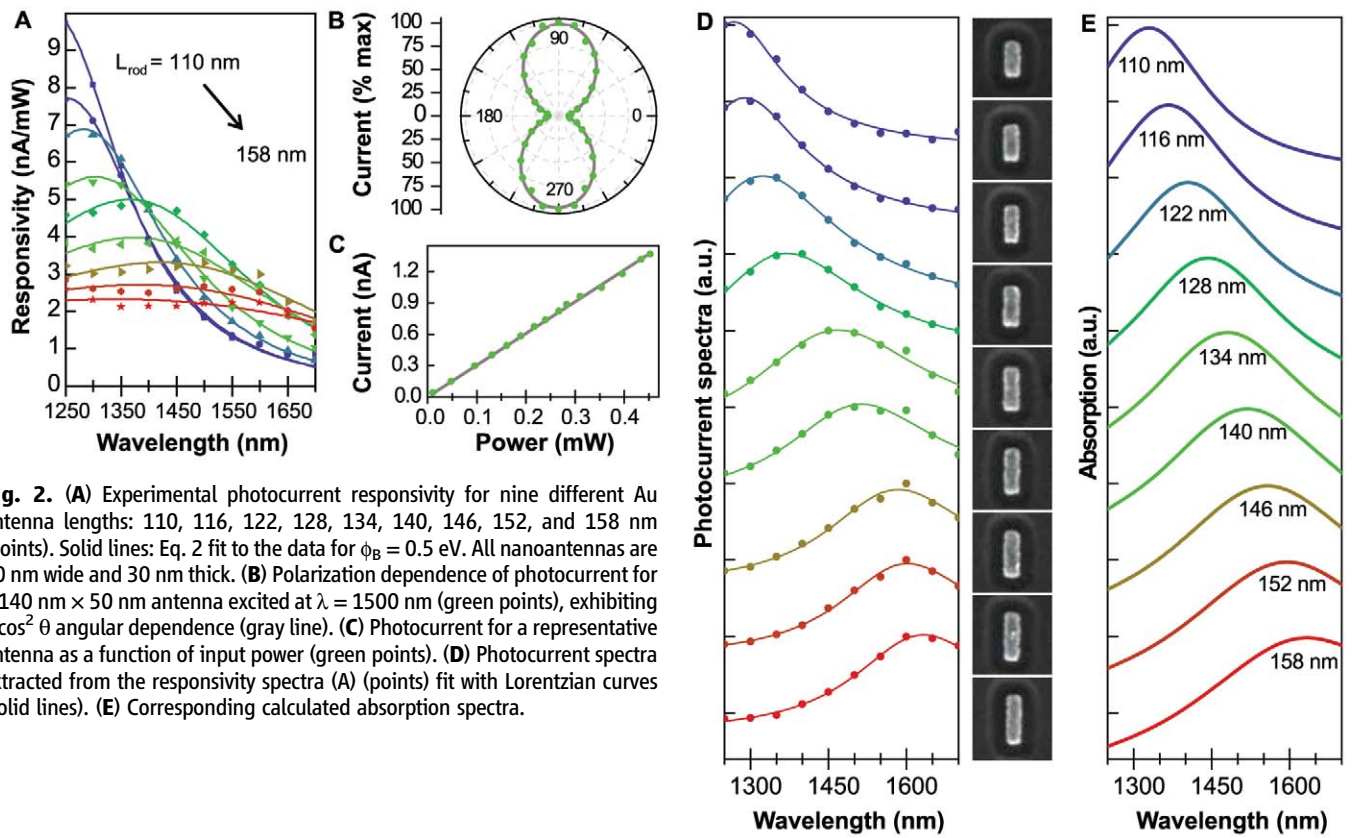

Fig. 2. (**A**) Experimental photocurrent responsivity for nine different Au antenna lengths: 110, 116, 122, 128, 134, 140, 146, 152, and 158 nm (points). Solid lines: Eq. 2 fit to the data for ϕ_B = 0.5 eV. All nanoantennas are 50 nm wide and 30 nm thick. (**B**) Polarization dependence of photocurrent for a 140 nm × 50 nm antenna excited at λ = 1500 nm (green points), exhibiting a $\cos^2\theta$ angular dependence (gray line). (**C**) Photocurrent for a representative antenna as a function of input power (green points). (**D**) Photocurrent spectra extracted from the responsivity spectra (A) (points) fit with Lorentzian curves (solid lines). (**E**) Corresponding calculated absorption spectra.

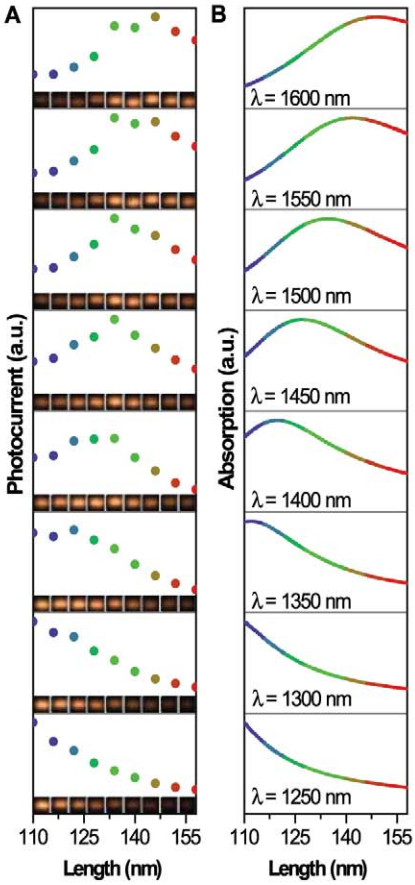

Fig. 3. Sensing the wavelength of incident light. (**A**) Relative photocurrent amplitudes at fixed wavelengths for the nine resonator lengths in Fig. 2. The color coding of the points is the same as in Fig. 2. Insets: Raw photocurrent images (normalized) for each device array. (**B**) Calculated absorption amplitudes for devices that are nominally identical to the experimental system.

When photocurrent measurements are performed on multiple antenna arrays, each with a different resonant frequency, these devices can function as tiny, on-chip spectrometers. This spectroscopic functionality is due to the relationship between photocurrent amplitude and the amplitude of the plasmon resonance at a given frequency. Each antenna array will generate a photocurrent maximum when driven on resonance, with decreasing photocurrent for antennas with a plasmon resonance detuned from the excitation frequency (Fig. 3). The proportionality between photocurrent and relative nanorod resonance amplitudes, expressed in Eq. 2, shows that at a fixed frequency where η_i is nearly constant, the spectral amplitude is directly proportional to device responsivity. Responsivity curves collected using the nine different antenna lengths presented in Fig. 2 are shown in Fig. 3, which illustrates the remarkable agreement between experimental responsivity as a function of antenna resonant frequency and optical absorption amplitudes calculated using the FDTD method. This spectral sensitivity can be used to determine the wavelength of incident light.

The overall quantum efficiency of these nanoantenna-diodes depends on the properties of their constituent materials and the specifics of their device geometry, how these factors affect hot electron generation, and the probability that the hot electrons generated will contribute to the photocurrent. Factors influencing the efficiency of hot electron production include the antenna geometry, the electronic structure of the metal(s) constituting the antenna, and the transmission efficiency of light through the uppermost ITO electrical contact layer. The efficiency of converting hot electrons to photocurrent is affected by the Schottky barrier height, the circuit resistance, and other device-specific parameters. For a device where these factors are known, Eq. 2 permits the direct conversion of experimental photocurrent to absolute absorption cross section.

Although the devices presented here enable us to investigate hot electron generation by plasmonic antennas, further optimization can significantly increase their quantum efficiency (at present, 0.01% of photons absorbed by each nanoantenna are converted into photocurrent). The role of the titanium layer appears to be quite critical: Numerical simulations show that the 1-nm layer is responsible for producing nominally 33% of the hot electrons, which would increase to more than 50% for a 5-nm thickness. Further experimental studies have indicated that reducing extraneous Ti oxidation during the fabrication process, improving ohmic contacts, and increasing the conductivity of the uppermost ITO layer can collectively increase device efficiency by more than an order of magnitude. In addition, a reverse bias of 1 V increases the photocurrent by a factor of 20. Together, these improvements would boost the quantum yield to nearly 2% over the spectral range of the device. A thin dopant layer could also boost efficiency, increase responsivity, and expand the spectral response of the devices by reducing the Schottky barrier height. Applying antireflection coatings or multipass geometries will also further increase the quantum yield.

The range of potential applications of this device concept is extremely diverse. As a silicon-based detector capable of detecting sub–band gap photons, this device could find widespread use in on-chip silicon photonics, ultimately eliminating the need to integrate additional semiconductor materials as detectors into chip designs, which would lower fabrication costs. The photodetection mechanism is compatible with existing, above–band gap photodetectors, which when combined could greatly extend the spectral range of silicon light-harvesting devices, such as silicon-based solar cells, into the infrared region of the spectrum. The broad infrared sensitivity of these devices could enable low-cost silicon infrared imaging detectors that may replace costly InGaAs detectors in this same spectral range. Antenna-diodes also offer functional aspects of photodetection not previously realized. By exploiting nanoantennas as a direct light-harvesting and carrier generation element, both polarization- and wavelength-selective detectors can be realized without additional optical components. We believe this mechanism of photodetection may give rise to additional unforeseen applications in photosensing, energy harvesting, imaging, and light detection technologies.

References and Notes

1. P. Mühlschlegel, H. J. Eisler, O. J. F. Martin, B. Hecht, D. W. Pohl, *Science* **308**, 1607 (2005).
2. S. Lal, S. Link, N. J. Halas, *Nat. Photonics* **1**, 641 (2007).
3. A. M. Gobin *et al.*, *Nano Lett.* **7**, 1929 (2007).
4. H. A. Atwater, A. Polman, *Nat. Mater.* **9**, 205 (2010).
5. T. Ishi, J. Fujikata, K. Makita, T. Baba, K. Ohashi, *Jpn. J. Appl. Phys.* **44**, L364 (2005).
6. N. Yu *et al.*, *Nat. Photonics* **2**, 564 (2008).
7. M. Westphalen, U. Kreibig, J. Rostalski, H. Luth, D. Meissner, *Sol. Energy Mater. Sol. Cells* **61**, 97 (2000).
8. L. Tang *et al.*, *Nat. Photonics* **2**, 226 (2008).
9. J. Hofmann, W. Steinmann, *Phys. Status Solidi* **30**, K53 (1968).
10. J. G. Endriz, W. E. Spicer, *Phys. Rev. Lett.* **24**, 64 (1970).
11. T. Inagaki, K. Kagami, E. T. Arakawa, *Phys. Rev. B* **24**, 3644 (1981).
12. T. Inagaki, K. Kagami, E. T. Arakawa, *Appl. Opt.* **21**, 949 (1982).
13. U. Kreibig, M. Vollmer, *Optical Properties of Metal Clusters* (Springer, New York, 1995).
14. J. Lehmann *et al.*, *Phys. Rev. Lett.* **85**, 2921 (2000).
15. J. T. Stuckless, M. Moskovits, *Phys. Rev. B* **40**, 9997 (1989).
16. V. M. Shalaev, C. Douketis, J. T. Stuckless, M. Moskovits, *Phys. Rev. B* **53**, 11388 (1996).
17. P. L. Redmond, L. E. Brus, *J. Phys. Chem. C* **111**, 14849 (2007).
18. R. Jin *et al.*, *Science* **294**, 1901 (2001).
19. R. Jin *et al.*, *Nature* **425**, 487 (2003).
20. L. Brus, *Acc. Chem. Res.* **41**, 1742 (2008).
21. X. Wu, E. S. Thrall, H. Liu, M. Steigerwald, L. Brus, *J. Phys. Chem. C* **114**, 12896 (2010).
22. C. Scales, P. Berini, *IEEE J. Quantum Electron.* **46**, 633 (2010).
23. See supporting material on *Science* Online.
24. J. Pérez-Juste, I. Pastoriza-Santos, L. M. Liz-Marzan, P. Mulvaney, *Coord. Chem. Rev.* **249**, 1870 (2005).
25. R. H. Fowler, *Phys. Rev.* **38**, 45 (1931).
26. S. M. Sze, K. K. Ng, *Physics of Semiconductor Devices* (Wiley, Hoboken, NJ, ed. 3, 2007).
27. A. M. Cowley, *Solid-State Electron.* **12**, 403 (1970).
28. C. J. Murphy, N. R. Jana, *Adv. Mater.* **14**, 80 (2002).
29. S. Laux *et al.*, *Thin Solid Films* **335**, 1 (1998).
30. E. D. Palik, Ed., *Handbook of Optical Constants of Solids* (Academic Press, San Diego, CA, 1998), vol. 3.
31. P. B. Johnson, R. W. Christy, *Phys. Rev. B* **6**, 4370 (1972).

Acknowledgments: We thank J. B. Lassiter, J. Day, R. Huschka, A. Schlather, and S. Lal for their insight and input. Supported by NSF Integrative Graduate Research and Educational Training program in Nanophotonics grant DGE-0504425 (M.W.K.), National Security Science and Engineering Faculty Fellowship program of the U.S. Department of Defense grant N00244-09-1-0067, Robert A. Welch Foundation grants C-1220 and C-1222, Office of Naval Research grant N00014-10-1-0989, Air Force Office of Scientific Research grant F49620-03-C-0068, and the Center for Advanced Solar Photophysics, an Energy Frontier Research Center funded by the U.S. Department of Energy.

Supporting Online Material

www.sciencemag.org/cgi/content/full/332/6030/702/DC1
Materials and Methods

19 January 2011; accepted 21 March 2011
10.1126/science.1203056

Nocturnality in Dinosaurs Inferred from Scleral Ring and Orbit Morphology

Lars Schmitz[1,2]* and Ryosuke Motani[2]

Variation in daily activity patterns facilitates temporal partitioning of habitat and resources among species. Knowledge of temporal niche partitioning in paleobiological systems has been limited by the difficulty of obtaining reliable information about activity patterns from fossils. On the basis of an analysis of scleral ring and orbit morphology in 33 archosaurs, including dinosaurs and pterosaurs, we show that the eyes of Mesozoic archosaurs were adapted to all major types of diel activity (that is, nocturnal, diurnal, and cathemeral) and provide concrete evidence of temporal niche partitioning in the Mesozoic. Similar to extant amniotes, flyers were predominantly diurnal; terrestrial predators, at least partially, nocturnal; and large herbivores, cathemeral. These similarities suggest that ecology drives the evolution of diel activity patterns.

In animals, bouts of activity are distributed throughout a 24-hour period (diel activity pattern), and the temporal patterns of such activity are classified into four types: diurnal (day-active), nocturnal (night-active), cathemeral (day- and night-active), and crepuscular (twilight-active) (*1*, *2*). Conventional wisdom holds that temporal niche partitioning in the Mesozoic was dictated by phylogeny; that is, nocturnality in mammals evolved as consequence of the dominance of diurnal dinosaurs (*3*–*5*). It has been difficult to test this hypothesis because reliable information on diel activity pattern of fossil taxa was unavailable. However, it recently has been shown that optical information recorded in orbit and scleral ring morphology enables quantitative distinction of activity patterns. We used this approach (*6*) in conjunction with morphological data on extant species with known activity patterns and a time-calibrated phylogeny to make inferences about diel activity pattern in Mesozoic archosaurs.

Our approach is based on optical principles and the relation between form and function of the eye (*7*). Ocular image formation relates to retinal illumination, or the brightness of the projected image. Three groups of ocular image formation, which are correlated with diel activity pattern, exist: (i) photopic (diurnal), with no activity in dim light; (ii) scotopic (nocturnal), with activity in dim light only; and (iii) mesopic (cathemeral), with activity in all light levels. We included crepuscular species, or those that are active during twilight, in the mesopic group, and we classified species that are diurnal plus crepuscular, cathemeral plus crepuscular, or nocturnal plus crepuscular as photopics, mesopics, and scotopics, respectively. Ocular image formation can be identified in fossils that preserve orbit length and diameter of the scleral ring (external and internal) because both are correlated with optical function (*8*, *9*) and informative for classification (*7*).

Ocular image formation corresponds to eye shape (*6*, *7*, *10*). Scotopics improve retinal illumination with a large aperture for given focal length and retinal area. The osteological equivalent is a large internal scleral-ring diameter relative to external diameter and orbit length (Fig. 1). Photopic species have a relatively small aperture and a small internal scleral-ring diameter for a given eye size, emphasizing acuity. Small maximum aperture probably minimizes the energy required to contract the iris for better depth of focus and prevention of retina overstimulation. A large eye facilitates both high acuity and sensitivity, a characteristic important for mesopics. Scleral ring and orbit dimensions in 33 Mesozoic archosaurs (*10*) (Fig. 2, Table 1, and tables S1 and S2) varied, with external diameters of scleral rings ranging from 9.56 mm (*Pterodactylus antiquus*) to 92.6 mm (*Saurolophus osborni*). The latter is more than twice as large as that of the emu (*Dromaius novaehollandiae*, 34.9 mm) (*9*) but is still less than half the size of scleral rings found in ichthyosaurs, marine reptiles of the Mesozoic (*11*). The shape and size diversity of scleral rings and orbits in our sample of fossil archosaurs indicates variety in ocular image formation, which we can confirm quantitatively.

The quantitative discrimination of ocular image formation with osteological features has its foundation in comparative data on extant avians and squamates (*6*). This taxonomic bracket enables analyses of fossil archosaurs that fall between avians and squamates in a phylogenetic tree (*12*). However, there is phylogenetic signal in the correlation between form and ecology of amniote eyes (*6*). This phylogenetic signal can potentially lead to false inferences of activity pattern, and we therefore analyzed the data set with a discriminant analysis accounting for the phylogenetic signal (*10*) (figs. S1 and S2).

To determine the activity pattern of fossil archosaurs, we performed phylogenetic discriminant analysis at Pagel's lambda, a measure of the strength of phylogenetic signal, of 0.08, the optimal value for correlation between ocular image formation and hard-tissue traits (*6*). For classification purposes, we allowed an error of 0.01 around the optimum because the vertex of the likelihood distribution is wide. To make inferences about the activity pattern in fossil archosaurs, we modified a published script to allow inclusion of data with unknown activity pattern (*10*). Prior probabilities are based on proportions of photopics, scotopics, and mesopics among extant amniotes (squamates, avians, and mammals) (*10*) (Fig. 2 and tables S3 and S4). Although archosaurs are nested within the saurian lineage (*12*), the amniote prior is reasonable. A prior based on extant saurians alone would misrepresent the ecological diversity recognized in

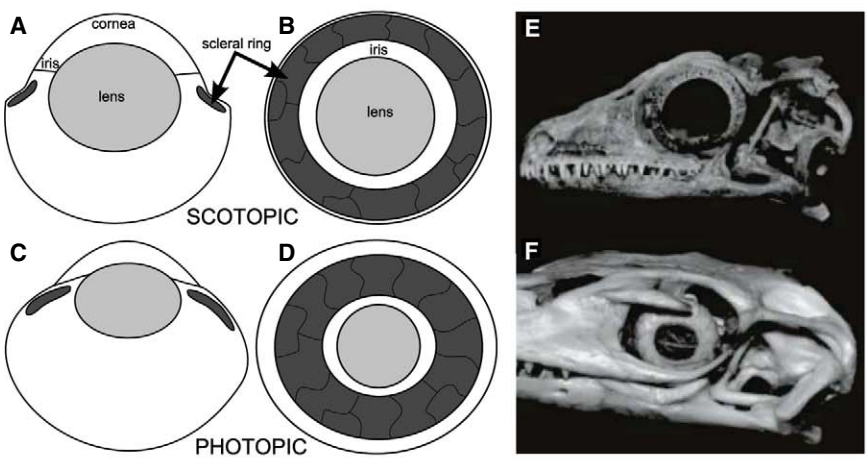

Fig. 1. Scotopic (nocturnal) species [(**A**) cross section, (**B**) lateral view along the optical axis] have a much larger lens and aperture for given eye size compared with photopics [diurnals (**C** and **D**)]. Scotopics and photopics can also be distinguished with skeletal structures alone [(**E**) the scotopic *Rhachodactylus* and (**F**) the photopic *Varanus*]. Not to scale.

[1]Department of Evolution and Ecology, University of California, Davis, CA 95616, USA. [2]Department of Geology, University of California, Davis, CA 95616, USA.

*To whom correspondence should be addressed. E-mail: lschmitz@ucdavis.edu

Mesozoic archosaurs. Ecological niches previously occupied by nonavian dinosaurs are now filled by mammals, and thus the inclusion of mammals is integral for accurate prior probabilities. We estimate that the majority of extant amniotes are photopic (58.5%), followed by scotopics (27.1%) and mesopics (14.4%). Photopics are dominant among active flyers (77.5%), whereas scotopics and photopics form the largest proportions among the terrestrials, or nonflyers (41.6% and 41.0%, respectively) (Fig. 3).

Our results (Table 1) suggest that a variety of ocular image formations existed in the Mesozoic. Fourteen species were identified as mesopics, 9 as scotopics, and 8 as photopics, whereas 2 were ambiguously classified as mesopic/scotopic. There is no clear phylogenetic clustering of ocular image formation. *Euparkeria capensis* and *Proterosuchus vanhoepeni*, both found near the base of the archosaur tree (*13*), were scotopic and mesopic, respectively. This finding is congruent with the hypothesis that archosaur ancestors had visual pigments adapted to dim light (*14*). Given the plasticity of ocular image formation across clades in extant amniotes and fossil archosaurs, however, estimates of ancestral states should be postponed until we have sampled more species. Moreover, *E. capensis* and *P. vanhoepeni* may require further investigation because they occurred near a polar circle (table S5). Polar species experience periods of continuous sunlight or darkness depending on season. However, the majority of the examined archosaurs inhabited low and temperate latitudes (table S5).

Comparisons with extant amniotes suggest that proportions of activity patterns are ecology-specific and largely independent from phylogeny. Similar to extant amniotes, the majority of flyers in our sample, including three pterosaurs and all four avians, were photopic. Four pterosaurs were scotopic; another one, mesopic. *Ctenochasma elegans*, *C. taqueti*, and *Rhamphorhynchus muensteri* were likely piscivorous and possibly had diel activity patterns comparable to those of nocturnal procellariiform birds (*15*). The filter-feeder *Pterodaustro guinazui* may have had diel activity similar to nocturnal filter-feeders among anseriform birds (*16*). Nocturnality in an extinct flyer has been suggested for an ornithurine bird, on the basis of the relative size of brain region impressions (*17*). Anurognath pterosaurs may have been nocturnal as well (*18*), yet we could not test this because a specimen with preserved scleral ring is currently unavailable. Five of the analyzed pterosaurs are part of the Late Jurassic Solnhofen fauna (early Tithonian; Hybonotum Zone, Solnhofen Limestone), which allows for examination of temporal niche partitioning (*19*). Our results suggest that the Solnhofen pterosaur fauna is characterized by a photopic (*Archaeopteryx lithographica*, *Pterodactylus antiquus*, and *Scaphognathus crassirostris*) and a scotopic (*Ctenochasma elegans* and *Rhamphorhynchus muensteri*) group.

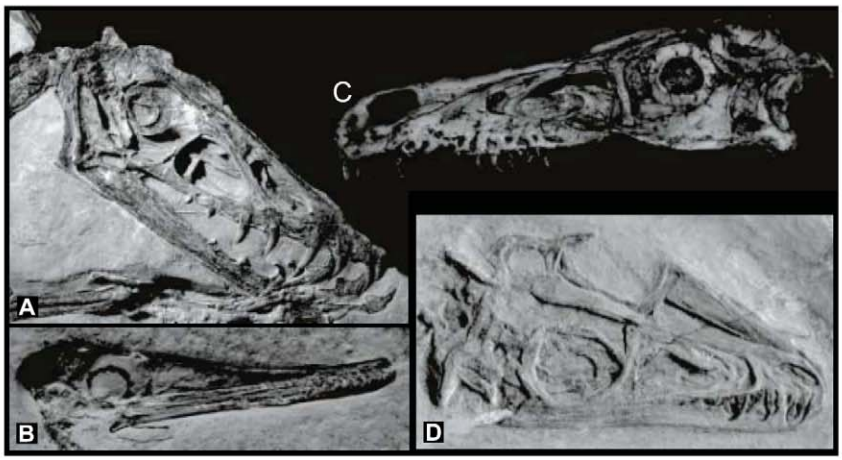

Fig. 2. Scleral rings used to infer diel activity pattern in fossil archosaurs. (**A**) The pterosaur *Scaphognathus crassirostris* was photopic (diurnal), whereas the pterosaur (**B**) *Ctenochasma elegans* and the theropod dinosaurs (**C**) *Velociraptor mongoliensis* and (**D**) *Juravenator starki* were scotopic (nocturnal). Not to scale.

Table 1. Inferred ocular image formation in fossil archosaurs.

	Ocular image formation	Ecology
Basal archosaurs		
Euparkeria capensis	Scotopic	Predator
Proterosuchus vanhoepeni	Mesopic	Predator
Pterosaurs		
Ctenochasma elegans	Scotopic	Flyer
Ctenochasma taqueti	Scotopic	Flyer
Pterodactylus antiquus	Photopic	Flyer
Pterodaustro guinazui	Scotopic	Flyer
Rhamphorhynchus muensteri	Scotopic	Flyer
Scaphognathus crassirostris	Photopic	Flyer
Tapejara wellnhoferi	Mesopic	Flyer
Tupuxuara sp.	Photopic	Flyer
Ornithischian dinosaurs		
Agilisaurus louderbacki	Photopic	Herbivore
Corythosaurus casuarius	Mesopic	Herbivore
Prosaurolophus maximus	Mesopic	Herbivore
Protoceratops andrewsi	Mesopic	Herbivore
Psittacosaurus mongoliensis	Mesopic	Herbivore
Saurolophus osborni	Mesopic	Herbivore
Basal saurischian dinosaur		
Herrerasaurus ischigualestensis	Mesopic	Predator
Sauropodomorph dinosaurs		
Diplodocus longus	Mesopic	Herbivore
Lufengosaurus huenei	Mesopic/scotopic	Herbivore
Nemegtosaurus mongoliensis	Mesopic	Herbivore
Plateosaurus longiceps	Mesopic	Herbivore
Riojasaurus incertus	Mesopic	Herbivore
Nonavian theropods		
Garudimimus brevipes	Mesopic	Herbivore
Juravenator starki	Scotopic	Predator
Megapnosaurus kayentakatae	Scotopic	Predator
Microraptor gui	Scotopic	Predator
Ornithomimus edmontonicus	Mesopic/scotopic	Herbivore
Sinornithosaurus sp.	Mesopic	Predator
Velociraptor mongoliensis	Scotopic	Predator
Avians		
Archaeopteryx lithographica	Photopic	Flyer
Confuciusornis sanctus	Photopic	Flyer
Sapeornis chaoyangensis	Photopic	Flyer
Yixianornis grabaui	Photopic	Flyer

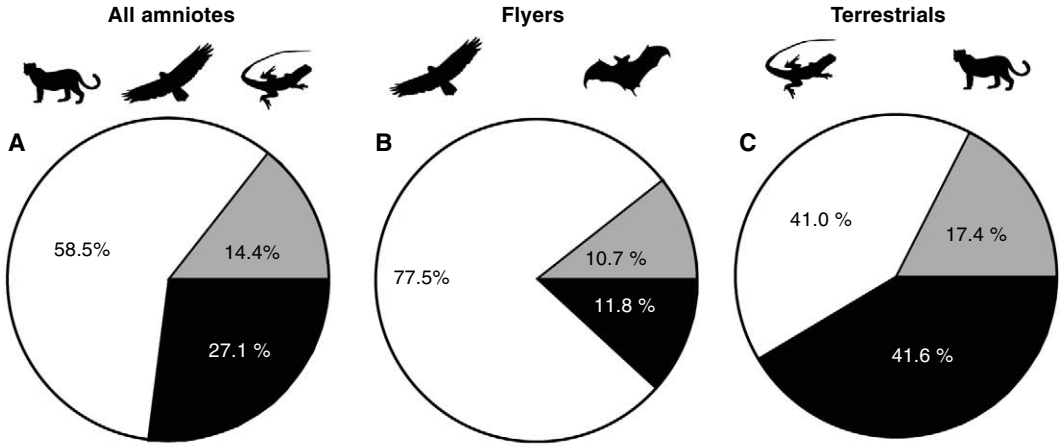

Fig. 3. Estimated proportions of photopic (diurnal, white), scotopic (nocturnal, black), and mesopic (cathemeral, gray) extant mammals, squamates, and avians. Photopics are common when all species are considered (**A**). The dominance of photopics is pronounced among flapping flyers [(**B**) avians and chiropterans combined], whereas photopics and scotopics are equally common among other terrestrial species (**C**). We used proportions in (A) as prior probability for phylogenetic discriminant analysis.

We also recognized similarities between extant and fossil amniote activity patterns for herbivores. All herbivores in our analysis were found to be mesopic, except for the photopic ornithischian *Agilisaurus louderbacki*, the smallest analyzed herbivore, and two, *Lufengosaurus huenei* and *Ornithomimus edmontonicus*, ambiguously classified as mesopic/scotopic. These results confirm previous hypotheses, based on thermoregulatory considerations (*20*), of partially nocturnal behavior in large dinosaurs. Recently, the relatively large orbit size of the ceratopsian dinosaur *Protoceratops andrewsi* was interpreted as a nocturnal adaptation (*21*); however, our results suggest that *P. andrewsi* was adapted to mesopic light levels. Constraints for foraging time and thermoregulation likely influenced diel activity pattern of herbivorous dinosaurs, as is the case for extant herbivores (*22*). The daily foraging budgets of herbivores increase with body mass, and a study (*22*) suggests that herbivorous mammals exceeding a body mass of 423 kg are expected to forage more than 12 hours a day. Constraints on foraging time in herbivorous dinosaurs, often exceeding extant terrestrial vertebrates in size, are reasonable from anatomical and energetic perspectives. Lower metabolic rate (*23*) could decrease food requirement and daily foraging time. Furthermore, sauropodomorphs may have had higher food intake rates and shorter daily foraging time budgets because they did not masticate (*24*). However, thermoregulatory constraints as consequence of size dictate a shift to cathemerality, in particular in the light of high mean annual temperatures in the Mesozoic (*25*). Many terrestrial vertebrates avoid high mid-day temperatures and show bimodal diel activity to minimize overheating (*22*, *26*, *27*), a substantial problem for large animals. The change in diel activity pattern as response to high mid-day temperatures, in combination with the necessity to meet food requirements, can lead to partially nocturnal behavior.

Nocturnal or cathemeral activity was also common among predators, as our results suggest. All terrestrial predators in our sample were either scotopic or mesopic, which matches the pattern seen in extant mammalian carnivores (*28*). Our results are consistent with the interpretation that sensory areas in the brain of the small theropod *Conchoraptor gracilis* were adapted to a crepuscular or nocturnal lifestyle (*29*). Differences in relative orbit size have led to suggestions of niche separation in this group, with small theropods being nocturnal and large theropods being diurnal (*30*). Although we confirm that some small theropods were at least partially scotopic, data on ocular image formation of large theropods are not available yet. However, we can make an inference of predator-prey interaction. *Velociraptor mongoliensis* from the Campanian Djadokhta Formation (Upper Cretaceous) in Mongolia was scotopic, whereas an herbivore of this fauna (*P. andrewsi*) was mesopic. It is plausible that the *Velociraptor* attack on *Protoceratops*, one of the few examples of predatory behavior directly documented in the vertebrate fossil record (*31*), occurred in twilight or low-light conditions.

Our results suggest that the previous assumption of a dichotomous split in temporal habitat and resource use among terrestrial amniotes in the Mesozoic, with archosaurs being diurnal and mammals being nocturnal (*3*–*5*), is inaccurate. Although quantitative inferences of Mesozoic mammals are not available yet, our results show that many Mesozoic archosaurs were active day and night. We reject the hypothesis of a phylogenetic split between nocturnal and diurnal activity patterns. Instead, we argue that partition of diel activity pattern depends on body size, diet, and habitat in both extant amniotes and Mesozoic archosaurs. In conclusion, ecology emerges as major evolutionary driver of diel activity patterns.

References and Notes

1. I. Tattersall, *Folia Primatol.* **77**, 7 (2006).
2. D. J. Curtis, M. A. Rasmussen, *Folia Primatol.* **77**, 178 (2006).
3. A. W. Crompton, C. R. Taylor, J. A. Jagger, *Nature* **272**, 333 (1978).
4. H. J. Jerison, *Evolution of the Brain and Intelligence* (Academic Press, New York, 1973).
5. J. A. Wiens *et al.*, in *Community Ecology*, J. Diamond, J. Case, Eds. (Harper & Row, New York, 1986), pp. 145–153.
6. R. Motani, L. Schmitz, *Evolution*, published online 7 April 2011 (10.1111/j.1558-5646.2011.01271).
7. L. Schmitz, R. Motani, *Vision Res.* **50**, 936 (2010).
8. M. I. Hall, *Anat. Rec.* **292**, 798 (2009).
9. L. Schmitz, *J. Morphol.* **270**, 759 (2009).
10. Materials and methods are available as supporting material on *Science* Online.
11. R. Motani, B. M. Rothschild, W. Wahl, *Nature* **402**, 747 (1999).
12. M. S. Y. Lee *et al.*, in *Assembling the Tree of Life*, J. Cracraft, M. J. Donoghue, Eds. (Oxford Univ. Press, Oxford, 2004), pp. 451–467.
13. D. B. Weishampel *et al.*, Eds., *The Dinosauria* (Univ. of California Press, Berkeley, 2004).
14. B. S. Chang, K. Jönsson, M. A. Kazmi, M. J. Donoghue, T. P. Sakmar, *Mol. Biol. Evol.* **19**, 1483 (2002).
15. F. Mougeot, V. Bretagnolle, *J. Avian Biol.* **31**, 376 (2000).
16. R. McNeil, P. Drapeau, J. D. Goss-Custard, *Biol. Rev. Camb. Philos. Soc.* **67**, 381 (1992).
17. E. N. Kurochkin, G. J. Dyke, S. V. Saveliev, E. M. Pervushov, E. V. Popov, *Biol. Lett.* **3**, 309 (2007).
18. S. C. Bennett, *Paläont. Z.* **81**, 376 (2007).
19. N. Kronfeld-Schor, T. Dayan, *Annu. Rev. Ecol. Syst.* **34**, 153 (2003).
20. F. Seebacher, G. C. Grigg, L. A. Beard, *J. Exp. Biol.* **202**, 77 (1999).
21. N. R. Longrich, in *New Pespectives on Horned Dinosaurs: The Royal Tyrrell Museum Ceratopsian Symposium*, M. J. Ryan, B. J. Chinnery-Allgeier, D. A. Eberth, P. Dodson, Eds. (Indiana Univ. Press, Bloomington, 2010), pp. 308–327.
22. R. N. Owen-Smith, *Megaherbivores: The Influence of Very Large Body Size on Ecology* (Cambridge Univ. Press, Cambridge, 1988).
23. B. K. McNab, *Proc. Natl. Acad. Sci. U.S.A.* **106**, 12184 (2009).
24. P. M. Sander *et al.*, *Biol. Rev. Camb. Philos. Soc.* **86**, 117 (2011).
25. B. W. Sellwood, P. J. Valdes, *Sediment. Geol.* **190**, 269 (2006).
26. S. K. Maloney, G. Moss, T. Cartmell, D. Mitchell, *J. Comp. Physiol. A Neuroethol. Sens. Neural Behav. Physiol.* **191**, 1055 (2005).
27. I. R. Swingland, J. G. Frazier, in *A Handbook on Biotelemetry and Radio Tracking*, C. J. Amlaner, D. W. Macdonald, Eds. (Pergamon, London, 1979), pp. 611–615.
28. J. L. Gittleman, *J. Mammal.* **67**, 23 (1986).
29. M. Kundrát, J. Janácek, *Naturwissenschaften* **94**, 769 (2007).
30. D. J. Chure, *Gaia* **15**, 233 (1998).
31. K. Carpenter, *Gaia* **15**, 135 (1998).

Acknowledgments: We thank D. Brinkmann, S. Carlson, I. Schwab, G. Vermeij, and P. Wainwright for comments. C. Cicero, A. Engilis, I. Engilis, D. Evans, M. Flannery, P. Holroyd, M. Koelbl-Ebert, J. McGuire, C. Mehling,

M. Norell, R. Papendieck, O. Rauhut, M. Sander, K. Seymour, B. Shaffer, D. Unwin, X. Xu, and Z. Zhou granted specimen access. The project was supported by NSF grant EAR 0551024 to R.M. and Durrell Funds of the Department of Geology, University of California Davis, an M. A. Fritz Award of Royal Ontario Museum, a doctoral stipend of German Academic Exchange Service, and a postdoctoral fellowship of German Research Foundation to L.S.

Supporting Online Material

www.sciencemag.org/cgi/content/full/science.1200043/DC1
Materials and Methods
SOM Text
Figs. S1 and S2
Tables S1 to S5
References

5 November 2010; accepted 16 February 2011
Published online 14 April 2011;
10.1126/science.1200043

Saturn's Curiously Corrugated C Ring

M. M. Hedman,[1]* J. A. Burns,[1,2] M. W. Evans,[1] M. S. Tiscareno,[1] C. C. Porco[3]

In August 2009 the Sun illuminated Saturn's rings from almost exactly edge-on, revealing a subtle corrugation that extends across the entire C ring. This corrugation's amplitude is 2 to 20 meters and its wavelength is 30 to 80 kilometers. Radial trends in the corrugation's wavelength indicate that this structure—like a similar corrugation previously identified in the D ring—results from differential nodal regression within a ring that became tilted relative to Saturn's equator plane in 1983. We suggest that this initial tilt arose because interplanetary debris struck the rings. The corrugation's radial extent implies that the impacting material was a dispersed cloud of debris instead of a single object, and the corrugation's amplitude indicates that the debris' total mass was ~10^{11} to 10^{13} kilograms.

The Cassini spacecraft obtained numerous images of Saturn's rings within a few months of Saturn's equinox in August 2009, when the Sun illuminated the rings from almost exactly edge-on. Many of these observations were designed to investigate ring features that would be highlighted by this unusual lighting geometry, such as shadows cast by embedded moonlets or inclined ringlets. Among the most surprising structures revealed by these images was a series of regularly spaced bright and dark bands extending throughout the entire C ring (Fig. 1). Because this periodic banding was not seen in earlier Cassini images, it cannot be ascribed to simple variations in the ring's density or optical depth. Instead, these bands appear to be caused by a vertical corrugation extending across the entire C ring. Broad-scale corrugations have previously been identified in Saturn's D ring (*1*) and Jupiter's main ring (*2*); both these structures appear to have formed within the last few decades when the relevant ring suddenly became tilted relative to its planet's equatorial plane (*1*, *3*). The C-ring corrugation seems to have been similarly generated, and indeed it was probably created by the same ring-tilting event that produced the D-ring's corrugation.

The amplitudes and wavelengths of the C-ring's periodic brightness variations have been measured using Fourier analyses of selected images (SOM text 1). The amplitudes of the observed brightness variations change with viewing and illumination geometries as expected for a vertically corrugated ring (SOM text 2). The corrugation amplitudes derived with a simple photometric model range between 2 and 20 m throughout the C ring (Fig. 2A; SOM text 2 describes systematic uncertainties associated with these estimates), and are thus well below the few-hundred-meter amplitudes of the previously identified D-ring corrugations (*1*). Meanwhile, the corrugation wavenumber systematically decreases with increasing distance from Saturn throughout the entire C ring (Fig. 2B), suggesting that the observed corrugations are part of a single coherent structure. Extrapolating the observed trends interior to the C ring shows that the predicted wavenumber is close to the expected wavenumber of the previously observed, larger-amplitude D-ring corrugation. The latter has been interpreted as the result of differential nodal regression of an initially inclined ring (*1*), which suggests that the C-ring corrugations could have been produced by the same process (Fig. 3). Indeed, the radial trends seen in Fig. 2B are consistent with such a model.

[1]Department of Astronomy, Cornell University, Ithaca, NY 14853, USA. [2]Department of Mechanical Engineering, Cornell University, Ithaca, NY 14853, USA. [3]CICLOPS–Space Science Institute, Boulder, CO 80301, USA.

*To whom correspondence should be addressed. E-mail: mmhedman@astro.cornell.edu

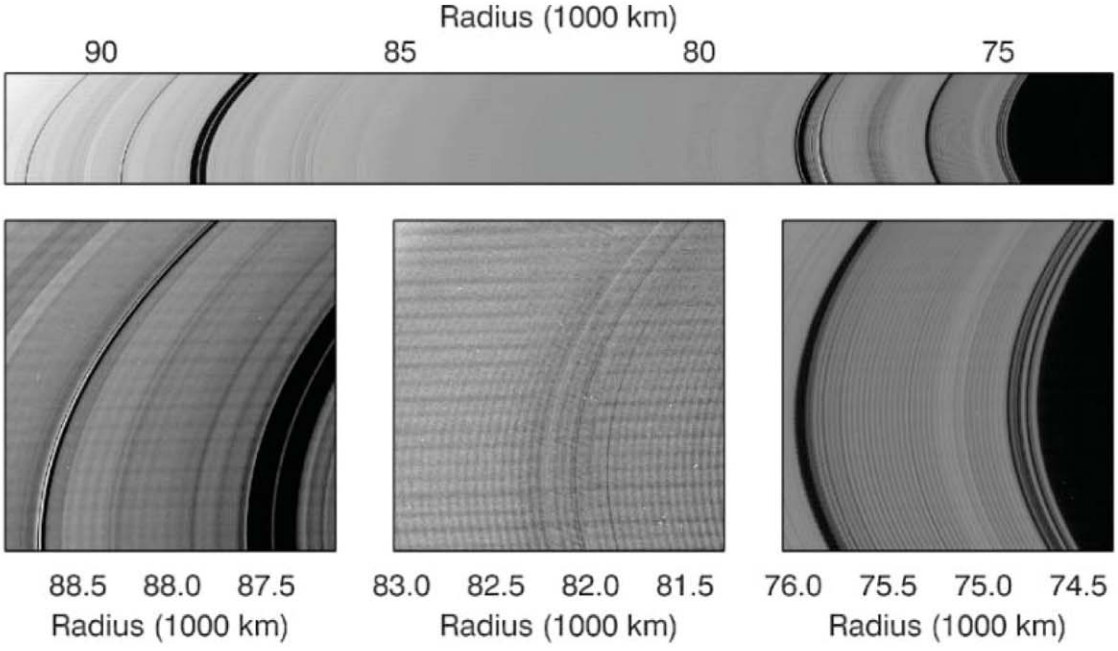

Fig. 1. Mosaic of images of Saturn's C ring obtained during Cassini's orbit 117, along with close-ups of selected radial regions showing the periodic bright and dark bands that extend across the entire C ring. The contrast has been adjusted in each close-up image to better show the periodic structure. Horizontal bands within these close-ups are camera artifacts (*22*).

A corrugation produced by differential nodal regression of an initially inclined ring should have a radial wavenumber given by [SOM text 3 and (*1*)]

$$k_z \approx \left|\frac{\partial \dot{\Omega}}{\partial r}\right| \delta t \qquad (1)$$

where δt is the time that has elapsed since the ring was an inclined sheet, and $\dot{\Omega}$ is the local nodal regression rate. To first order, $\dot{\Omega}$ is determined by Saturn's quadrupole gravitational harmonic J_2 (*4*, *5*), so Eq. 1 can be approximated as

$$k_z \approx \frac{21}{4} J_2 \sqrt{\frac{GM_S}{r^5}} \left(\frac{R_S}{r}\right)^2 \delta t \qquad (2)$$

where G is the gravitational constant, M_S is Saturn's mass, r is the ring radius, and R_S is the assumed Saturn radius used to normalize J_2. Thus, a corrugation produced by differential nodal regression should have $k_z \sim r^{-9/2}$. Including contributions from all Saturn's measured higher-order gravity harmonics (*6*) yields the solid curves in Fig. 2, B and C, which differ slightly from the trend calculated above and match the observed data to within 3%.

The largest deviations from this model include a quasi-periodic wavenumber modulation in the middle C ring and a cluster of low wavenumber values in the outermost C ring ($r >$ 90,000 km, Fig. 2C). These residuals are correlated with the optical depth structure of the ring (compare Fig. 2, C and E) and can be ascribed to the C-ring's finite surface mass density σ. The ring's gravity modifies the local nodal regression rates, producing perturbations to the corrugation wavenumber:

$$\frac{\delta k_z}{k_z} = \frac{\pi G}{2\nu}\left(-\frac{\partial \sigma}{\partial r} + \frac{3\sigma}{r}\right)\delta t \qquad (3)$$

where ν is the vertical epicyclic frequency (SOM text 3). If we assume that the ring's optical depth τ is proportional to its surface mass density σ, then the largest negative residuals in the corrugation wavenumber should occur where the optical depth has the most positive slope and vice versa, as observed. Furthermore, the magnitude of the measured residuals would require that the middle C ring has σ ~ 3 to 6 g/cm^2 (SOM text 4), consistent with previous estimates (*7*, *8*).

If we only consider regions where the predicted $\delta k_z/k_z$ caused by the ring's self-gravity is less than 0.2% (Fig. 2D and SOM text 5), the wavelength estimates are fully consistent with predicted trends based on current estimates of Saturn's gravity field (*6*). We may therefore use Eq. 1 to determine how long ago the C ring was a simple inclined sheet: Julian date (JD) 2445598 ± 40, or day 263 ± 40 of 1983 (*9*). This is within a year of the inclined sheet epoch derived from the previously observed temporal variations in the D-ring's corrugation wavelength (*1*), and the difference between the two estimates may be attributed to the excess variance in the D-ring wavelength estimates derived from images taken in different viewing geometries (*1*). It is therefore reasonable to conclude that the corrugations in both the C and D rings were generated by the same ring-tilting event.

Saturn was near solar conjunction during the latter half of 1983 and thus could not be seen clearly from Earth. Archived images therefore cannot provide direct information about any event that might have caused the rings to become tilted relative to Saturn's gravitational equator. However, any acceptable scenario must be

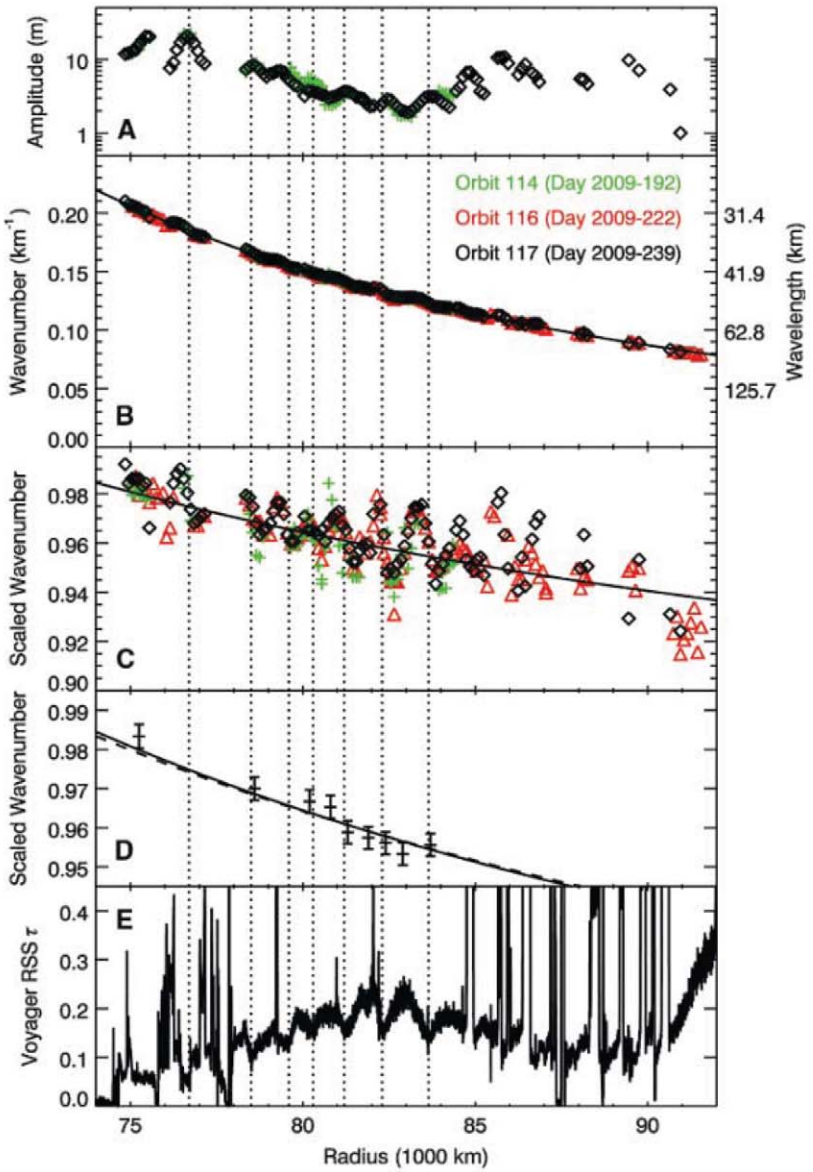

Fig. 2. Corrugation parameters versus radius in the rings (distance from Saturn's spin axis) derived from three observations taken on three different Cassini orbits around the time of Saturn's equinox (see SOM text 1 and 2 for analysis procedures): (**A**) Corrugation amplitude A_z, (**B**) corrugation wavenumber k_z, and (**C**) scaled corrugation wavenumber $k'_z = k_z/k_o \times (r/r_o)^{9/2}$, where $k_o = (2\pi/40)$ km^{-1} r_o = 80,000 km are constants chosen to normalize k'_z to approximately unity at equinox. In these plots, each data point is computed from a Fourier analysis of a 500-km-wide ring region, so adjacent data points from the same observation, which are separated by only 100 km, are not independent. No amplitudes are plotted for the Orbit 116 data because the extremely low Sun-opening angle during these observations complicates the photometry (see SOM text 2). (**D**) Estimates and uncertainties (1 standard deviation) of the rescaled corrugation wavenumber at JD 2455054 at locations in the ring where the finite mass of the ring can be neglected (SOM text 5). The solid curves in (B), (C), and (D) are the predicted wavenumber of a vertical corrugation produced by differential nodal regression of an inclined ring that existed at JD 2445598, assuming the standard model of Saturn's gravity field (*6*) with $J_n = 0$ for $n > 8$. In (D), the dashed curve shows a similar prediction, assuming $J_8 = 0$ instead of $J_8 = -0.00001$. (**E**) Normal optical depth profile of the C ring measured by the Voyager Radio Science Subsystem (obtained from the Planetary Data System rings node).

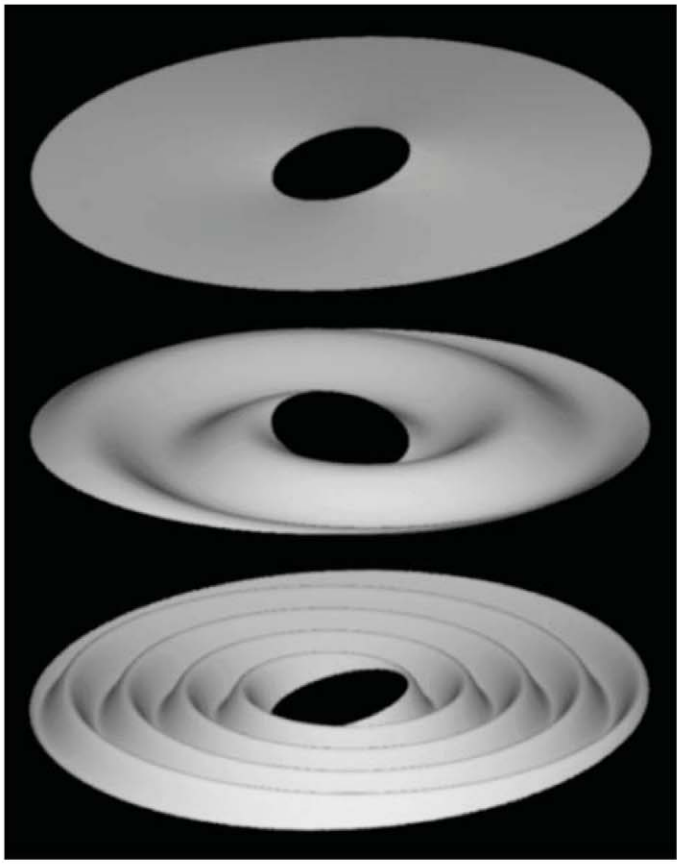

Fig. 3. Cartoon representation of how differential nodal regression produces a vertical corrugation from an initially inclined ring. The top image shows a simple inclined ring (the central planet is omitted for clarity), while the lower two images show the same ring at two later times, where the orbital evolution of the ring particles has sheared this inclined sheet into an increasingly tightly wound spiral corrugation.

able to produce a tilt across a wide swath of the ring in a short period of time compared to the local orbital precession periods (which range between 2 weeks and 1 month). Preliminary calculations suggest that Saturn's equator is unlikely to shift appropriately due to either external torques on Saturn or mass redistribution within the planet (SOM text 6). Furthermore, recent analyses of Galileo data indicate that Jupiter's rings became tilted around the time comet Shoemaker-Levy 9 struck the planet in 1994 (*3*). We therefore investigate scenarios in which the rings became tilted relative to Saturn's equator plane due to interplanetary debris impacting the rings in 1983.

The estimated corrugation amplitudes in the C ring (Fig. 2A) indicate that the entire C ring was initially tilted relative to Saturn's equator plane by an angle $\delta\theta$ between 2×10^{-8} and 3×10^{-7} radians. Assuming a ring surface mass density of ~5 g/cm^2 (see above), the ring's angular momentum would need to reorient by $\delta L_r \sim 10^{23}$ kg m^2/s to produce this tilt. Although a reasonably dense (~1 g/cm^3) 1-km-wide object traveling at typical impact speeds through the rings (~40 km/s, comparable to the escape speed from Saturn) would carry sufficient angular momentum to produce the required δL_r, it is unlikely that an intact comet or meteoroid could have produced a feature as radially extensive as the observed corrugation. A compact object ~1 km across passing through the C ring would only interact with a small patch of the rings containing $<10^{-3}$ the mass of the impactor, so any debris from this collision would follow essentially the same trajectory as that of the pre-impact projectile. Thus, most of the incoming object's momentum would escape in the debris from the collision and not be imparted to the rings, and no large-scale tilt would be established. However, if the rings encountered a diffuse cloud of debris instead of a single solid object, then material would have rained down across a range of radii, producing a tilt that could ultimately form an extensive corrugation. The incoming debris would also interact with a much larger area of the rings and a much greater mass of ring material, so more of the momentum carried by the debris should remain in the ring instead of departing from the Saturn system. Such a scenario could even explain the differences in the corrugation amplitudes between the C and D rings. Assuming the momenta from the incoming particles are efficiently transferred to the rings (SOM text 7), the tilt induced by a given debris flux should be directly proportional to the ring particles' aggregate cross section and inversely proportional to their total mass. The larger amplitude of the D-ring corrugation could therefore arise simply because the submillimeter-wide particles in the D ring (*1*) have much higher surface-area-to-volume ratios than the centimeter-to-meter–sized C-ring particles (*10*).

The viability of this explanation for the ring's initial tilt can be evaluated by estimating the total debris mass required to produce the observed corrugations. For rings of modest optical depth like the C ring, the angular momentum delivered into the rings by a debris cloud of mass m_c can be expressed as

$$L_c = D_F \tau m_c v_c r \quad (4)$$

where v_c is the mean impact speed of the incoming material, r and τ are the orbital radius and normal optical depth of the ring, and D_F is a dimensionless parameter that depends on the longitudinal distribution of the impacting material. For a homogeneous debris cloud, $D_F \sim 0.1$ for a wide range of plausible approach trajectories and speeds (SOM text 7), and it could be higher if the cloud has substantial substructure. Assuming that D_F lies between 1 and 0.01, and further stipulating that $L_c \approx \delta L_r \sim 10^{23}$ kg m^2/s, $v_c \approx 40$ km/s, and $\tau \sim 0.1$ (Fig. 2E), we find that the total mass of the debris cloud would need to be 10^{11} to 10^{13} kg in order to produce the observed C-ring corrugation.

Debris clouds with masses on the order of 10^{12} kg were produced during the break-up of Shoemaker-Levy 9 in 1992 (*11*, *12*) and the major outburst of comet 17P/Holmes in 2007 (*13*). The rate at which Saturn would encounter such massive clouds is quite uncertain, but consider the specific scenario where a 1-km-wide comet nucleus was captured into orbit around Saturn and broke apart during a close periapse passage (due to planetary tides or a collision with the rings), producing ~10^{12} kg of debris on bound orbits that crashed into the rings on a later periapse (*14*). Although the rate at which captured cometary debris impacts Saturn has not yet been thoroughly investigated in numerical simulations, existing studies indicate that roughly 4% of the comets that impact Jupiter had previously passed close enough to the planet to be disrupted (*15*), the impact flux at Saturn is about 40% the flux at Jupiter (*16*, *17*), and the fraction of impactors on bound orbits is about an order of magnitude less for Saturn than it is for Jupiter (*18*–*20*). Together, these results indicate that Saturn should encounter debris clouds derived from comets disrupted by previous planetary encounters at a rate that is roughly 0.2% of Jupiter's impact rate. The 2009 detection of a fresh impact scar at Jupiter suggests that 1-km-wide objects may strike Jupiter as often as once a decade (*21*). In this case, the clouds of orbiting debris created by the disruption of a 1-km-wide comet should rain down on Saturn's rings once every 5000 to 10,000 years. The probability that debris from a previously disrupted comet would hit Saturn's rings in the last 30 years would then be between roughly 1% and 0.1%, which is not very small. Such scenarios therefore provide a reasonable explanation for the origin of the observed corrugation in Saturn's C ring.

References and Notes

1. M. M. Hedman *et al.*, *Icarus* **188**, 89 (2007).
2. M. E. Ockert-Bell *et al.*, *Icarus* **138**, 188 (1999).
3. M. R. Showalter, M. M. Hedman, J. A. Burns, *Science* **332**, 711 (2011).
4. C. D. Murray, S. F. Dermott, *Solar System Dynamics* (Cambridge Univ. Press, Cambridge, 1999).
5. For Saturn's C ring, higher-order gravity harmonics, mainly J_4 (*6*), only contribute a total of <10% to the nodal regression rate and 10 to 15% to the gradient of the nodal regression rate.
6. R. A. Jacobson *et al.*, *Astron. J.* **132**, 2520 (2006).
7. H. A. Zebker, E. A. Marouf, G. L. Tyler, *Icarus* **64**, 531 (1985).
8. P. A. Rosen, G. L. Tyler, E. A. Marouf, J. J. Lissauer, *Icarus* **93**, 25 (1991).
9. The error estimate includes ±10 days of statistical error, ±13 days uncertainty from the published estimate of J_6 (*6*), ±13 days from allowing J_8 to range between 0 and −0.00001, and ±5 days that depends on whether the wavenumbers are corrected for the ring's predicted mass. Additional uncertainty could be introduced if J_{10} and higher-order terms in Saturn's gravity field are sufficiently large.
10. J. N. Cuzzi *et al.*, in *Saturn From Cassini-Huygens*, M. K. Dougherty, L. W. Esposito, S. M. Krimigis, Eds. (Springer, New York, 2009), pp. 459–509.
11. J. V. Scotti, H. J. Melosh, *Nature* **365**, 733 (1993).
12. E. Asphaug, W. Benz, *Icarus* **121**, 225 (1996).
13. M. Montalto, A. Riffeser, U. Hopp, S. Wilke, G. Carraro, *Astron. Astrophys.* **479**, L45 (2008).
14. Scenarios in which the debris from the disrupted comet hits the rings before it can leave the inner Saturn system are explored in SOM text 8 and are found to be less probable.
15. D. M. Kary, L. Dones, *Icarus* **121**, 207 (1996).
16. H. F. Levison, M. J. Duncan, *Icarus* **127**, 13 (1997).
17. K. Zahnle, P. Schenk, H. Levison, L. Dones, *Icarus* **163**, 263 (2003).
18. H. F. Levison, M. J. Duncan, K. Zahnle, M. Holman, L. Dones, *Icarus* **143**, 415 (2000).
19. S. Charnoz, A. Morbidelli, L. Dones, J. Salmon, *Icarus* **199**, 413 (2009).
20. This rate may be conservative because none of the referenced simulations include Saturn's rings, which could not only disrupt incoming comets but also withdraw some momentum from the debris, increasing its chances of being captured into orbit around Saturn.
21. A. Sánchez-Lavega *et al.*, *Astrophys. J.* **715**, L155 (2010).
22. C. C. Porco *et al.*, *Space Sci. Rev.* **115**, 363 (2004).

Acknowledgments: We acknowledge the support of the Imaging Science Subsystem team and the Cassini Project, as well as NASA's Planetary Geology and Geophysics, and Cassini Data Analysis programs. We also thank M. R. Showalter, P. D. Nicholson, S. Charnoz, L. Dones, and D. P. Hamilton for useful conversations.

Supporting Online Material

www.sciencemag.org/cgi/content/full/science.1202238/DC1
SOM Text
Figs. S1 to S5
Tables S1 to S3
References

27 December 2010; accepted 16 March 2011
Published online 31 March 2011;
10.1126/science.1202238

The Impact of Comet Shoemaker-Levy 9 Sends Ripples Through the Rings of Jupiter

Mark R. Showalter,[1]* Matthew M. Hedman,[2] Joseph A. Burns[2]

Jupiter's main ring shows vertical corrugations reminiscent of those recently detected in the rings of Saturn. The Galileo spacecraft imaged a pair of superimposed ripple patterns in 1996 and again in 2000. These patterns behave as two independent spirals, each winding up at a rate defined by Jupiter's gravity field. The dominant pattern originated between July and October 1994, when the entire ring was tilted by about 2 kilometers. We associate this with the Shoemaker-Levy 9 impacts of July 1994. New Horizons images still show this pattern 13 years later and suggest that subsequent events may also have tilted the ring. Impacts by comets or their dust streams are regular occurrences in planetary rings, altering them in ways that remain detectable decades later.

On 9 November 1996, the Galileo spacecraft imaged a systematic, unexplained pattern of brightness variations in Jupiter's main ring, suggesting vertical ripples in the ring's surface (*1*). More recently, Cassini images have revealed a similar pattern in Saturn's rings. The latter pattern arose from an initially inclined ring, which was slowly twisted into a spiral by Saturn's gravity (*2*, *3*). A closer analysis of Galileo data now confirms that the patterns in the rings of Jupiter and Saturn obey identical kinematics, except that Jupiter's ring contains two ripple patterns, not one.

Galileo viewed the rings from nearly edge-on, with opening angle $B = 0.48°$ (Fig. 1 and table S1). The intensity I of an optically thin ring is proportional to the amount of material along the line of sight, so it varies as $\sin(B)^{-1}$. For the jovian ring, optical depth $\tau < 10^{-5}$ (*4*, *5*), so this dependence applies. In this limit, the Sun's opening angle plays no role, because every particle is illuminated equally.

A nonzero surface slope modifies the effective local opening angle, naturally leading to variations in I (*6*).

$$I \propto 1/\sin(B)[1 - \sin(\theta)/\sin(B)Z'(R,\theta)] \quad (1)$$

Here, $Z(R,\theta)$ describes the local height of the ring above the equatorial plane in polar coordinates (R,θ). The radial component of the local slope is $Z'(R,\theta) \equiv \partial Z/\partial R$; we neglect the slope's much smaller tangential component (*6*, *7*). Longitudes are measured from the ansa line passing through the ring's tip, where a radial vector is perpendicular to the line of sight.

The dependence of I on $\sin(\theta)$ naturally predicts the reversals of contrast observed in the Galileo image. We have applied Eq. 1 to derive the function $Z'(R)$ at $\theta = 0$ (Fig. 1C). Slopes approach 3% or ~1.5°. However, unlike the pattern in Saturn's rings (*2*, *3*), this one is not a pure sinusoid; a Fourier transform shows two distinct peaks (Fig. 2A). In a least-squares modeling of $Z'(R)$, two sinusoids successfully account for the location of nearly every peak and trough. Matches to the amplitudes are imperfect, however, suggesting that the ring slope may be modulated by other factors that we have not yet considered. The dominant pattern has a wavelength $\lambda_{long} = 1920 \pm 150$ km and a vertical amplitude $Z_{long} = 2.4 \pm 0.7$ km; the shorter-wavelength pattern has $\lambda_{short} = 630 \pm 20$ km and $Z_{short} = 0.6 \pm 0.2$ km.

If these sinusoidally varying slopes are analogous to the corrugations observed at Saturn (*2*, *3*), then they arose from an initially tilted ring that slowly twisted into a spiral pattern as a result of differential nodal regression. The wavelength of these patterns depends only on the local gravitational field and the amount of time T that has elapsed since the ring became tilted (*2*, *3*). Near the middle of the main jovian ring, the predicted wavelength is

$$\lambda = \sim 4200 \text{ km}/(T/\text{years}) \quad (2)$$

The numerical factor is derived from Jupiter's gravitational harmonics (*8*). It varies by ~15% within the radial limits considered but for practical purposes can be treated as a constant when modeling individual profiles (*6*).

Compared with Saturn's ~30-km periodicity, the longer wavelengths at Jupiter would imply much more recent features. For the long-wavelength pattern, $T = 800 \pm 60$ days, indicating that a ring-tilting event occurred between 1 July and 1 November 1994. The shorter wavelength corresponds to $T = 2430 \pm 80$ days, meaning that the feature originated between early January and early June 1990; the midpoint is 19 March.

Two Galileo images from 21 June 2000 confirm that this pattern is evolving in the predicted

[1]SETI Institute, 189 Bernardo Avenue, Mountain View, CA 94043, USA. [2]Department of Astronomy, Cornell University, Ithaca NY 14853, USA.

*To whom correspondence should be addressed. E-mail: mshowalter@seti.org

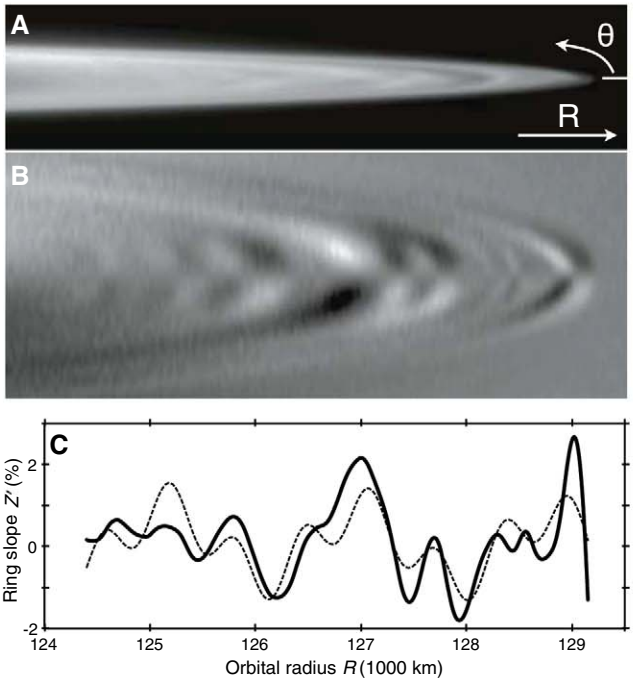

Fig. 1. (**A**) Galileo image C0368974139 from 9 November 1996 shows the jovian ring's tip. Indicated are the directions in which longitude θ and radius *R* are measured. (**B**) We expanded the image vertically, co-added two similar frames for improved signal-to-noise ratio, and subtracted a duplicate of the image after reversing it top-to-bottom. Most of the image nearly cancels itself out, but the signals of the ripples are reinforced. Neutral gray corresponds to zero; darker areas are negative. (**C**) A derived profile of the ring's surface slope versus radius (solid line). For comparison, the dashed line shows a fit involving superimposed patterns triggered on 19 July 19 and 19 March 1990. In this fit, we have neglected the expected variation in λ with *R* (*6*). Panels (A) to (C) have been aligned vertically to employ the same radial/horizontal scale.

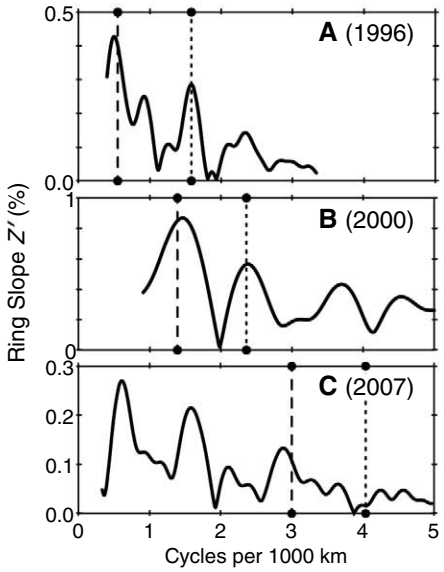

Fig. 2. Fourier transforms of each radial profile of the ring's surface slope, $Z'(R)$. Data are from Galileo in 1996 (**A**) and 2000 (**B**) and from New Horizons in 2007 (**C**). Vertical lines mark the expected wave number (1/λ) for features triggered on 19 July 1994 (dashed) and on 19 March 1990 (dotted). On the vertical axes, the Fourier amplitude values roughly indicate the height of a single sinusoid, of fixed wavelength but variable phase, that best fits the profile.

manner. The images individually have very poor signal-to-noise properties, and charged particle impacts into the camera's charge-coupled device corrupt many pixels (fig. S1). Nevertheless, combined processing of both images has enabled us to identify and eliminate most of the corrupted pixels (Fig. 3A). Contrast reversals show up clearly after processing (Fig. 3B), from which we have derived $Z'(R)$ (Fig. 3C). Fourier processing once more identifies two dominant peaks, but now they are at shorter wavelengths (Fig. 2B). Modeling of the ring profile as a superposition of two sinusoids provides a very good description of the data (Fig. 3C, dashed line), with λ_{long} = 695 ± 55 km; Z_{long} = 1.8 ± 0.4 km; λ_{short} = 414 ± 20 km; Z_{short} = 0.6 ± 0.2 km. For comparison, if we use Eq. 2 to extrapolate forward the patterns seen in 1996 over the intervening 1289 days, we would expect λ_{long} = 734 km and λ_{short} = 412 km. Thus, the wavelengths and amplitudes seen in 2000 are consistent with the expected rate of winding of these spiral features.

To complete our data analysis, we examined four images taken just before New Horizons crossed the jovian ring plane on 1 March 2007 (figs. S2 to S4). Fourier analysis reveals the lingering effects of the 1994 ring-tilting event (Fig. 2C). Although λ_{long} has diminished to ~350 km, this detection attests to the features' longevity. The shorter pattern can no longer be detected. However, two suggestive new patterns appear, with λ ≈ 1315 km and 775 km (fig. S4C). If confirmed by later detections, these would indicate that the rings received additional km-scale tilts around September 2001 and December 2003.

A suitable explanation for ring-tilting events must satisfy some very specific requirements. First, each event must occur within a very brief time span (*2*, *3*). The nodal regression rate for orbits in the main jovian ring is 8.5°/day, enough to smear out the effects of any event lasting more than a few weeks. Second, these events must be infrequent, with 2 to 4 occurrences between ~1985 and ~2006. Within this context, it is natural to associate the long pattern with the Shoemaker-Levy 9 (SL9) impacts of 16 to 20 July 1994. They occurred within the identified window spanning July to October. Although SL9 was earlier regarded as a "once a century" impact, the observed collision of another object into Jupiter on 19 July 2009 suggests that such events may be 5 to 10 times more frequent than previously thought (*9*). The chance of one occurring at random within the identified 4-month window is 1 to 3%.

The triggering event for the secondary pattern in Galileo images is less clear. SL9 fractured during its previous perijove on 7 July 1992. It crossed the equator at R ~ 115,000 km (*10*), apparently producing no measurable effect on the ring less than 15,000 km further out. The perijove before that was in mid-1990, within the window defined by the short wavelength and raising the possibility that SL9 triggered this pattern as well. However, backward integrations of SL9's trajectory place this perijove much farther from Jupiter (*10*, *11*). Such integrations have large uncertainties, arising from the chaotic nature of SL9's orbit, and because we do not know where to position the center of SL9's mass before its breakup (*10*, *11*). Thus, we cannot rule out the possibility that SL9 triggered the 1990 pattern, although it must have passed much closer to the ring than it did in 1992. Alternatively, the secondary pattern may have been triggered by a different, unseen comet; this hypothesis is generally compatible with more recent, higher estimates of the frequency of impacts (*9*). History records other very close passages of Jupiter by comets 16P/Brooks 2 in 1886 and P/Gehrels 3 in 1970 (*12*).

What mechanism might have enabled SL9 to alter the jovian ring so dramatically? In 1994, SL9's solid fragments entered Jupiter at southern latitudes on a north-bound trajectory; they never reached the ring plane. However, dust grains associated with SL9's fragments could have been deflected past the planet and into the ring by solar radiation pressure (Fig. 4) (*6*). Others have explored the effects of radiation pressure on SL9's dust (*13*, *14*), but not with an eye toward the consequences for the ring system. We define β as the ratio of radiation pressure to solar gravity (*15*). Integrations show that grains with β = 0.007 (radius ≈ 50 μm), if released at the time of the 1992 perijove and breakup, would be deflected directly into the main ring in 1994 (*6*). Larger grains can never intercept the ring, but smaller ones, if released later, can. The fragments were emitting dust continuously between the 1992 breakup and the 1994 impact (*14*, *16*), providing a continuous source of potential ring impactors. Regardless of their ejection date, integrations show that all particles crossing the main jovian ring do so within the same ~10° sector of inertial longitude and within a time span of a few days (*6*); thus, they naturally satisfy the requirement to offset the ring quickly and systematically.

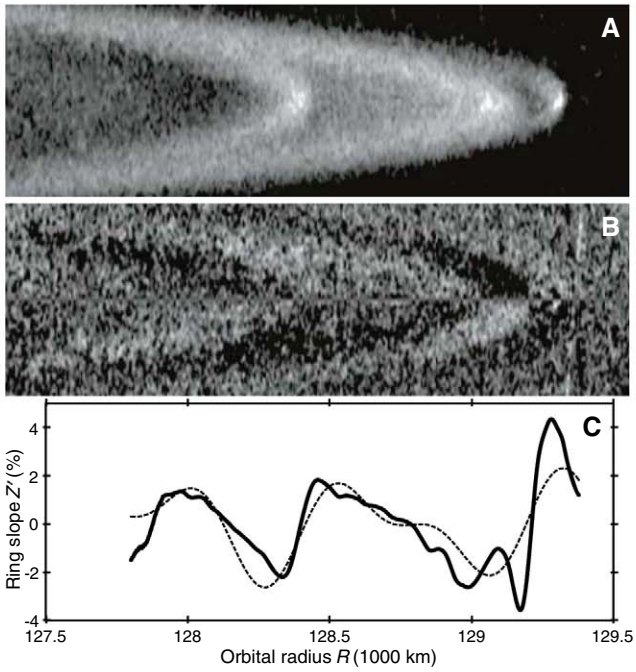

Fig. 3. (**A**) Two Galileo images from 2000 have been overlaid and combined to produce a clear image of the ring's ansa (*6*). (**B**) After flipping the image vertically and subtracting, enhancement reveals the pattern of contrast reversals indicating vertical undulations. (**C**) A derived radial profile of the ring's slope (solid line). For comparison, the dashed line is a best fit using two sinusoidal patterns, with wavelengths defined by our assumed trigger dates of 19 July 1994 and 19 March 1990. The three panels have been aligned to employ the same radial scale; note that this scale is much smaller than that in Fig. 1.

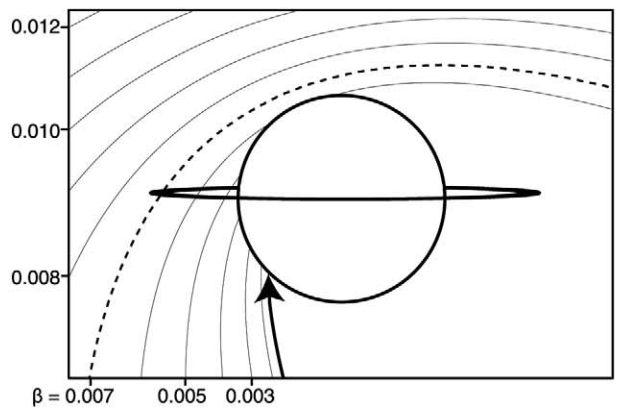

Fig. 4. The influence of solar radiation pressure on the motion of SL9's fragments is shown as a function of β. Integrations assume that the pieces separated at low relative velocity during the 1992 perijove. The heavy arrow (β = 0) shows the path of the large, observed fragments. The trajectories of smaller particles are displaced leftward in the diagram; corresponding β values are labeled around the periphery. Particles with β ≈ 0.007 (heavy dashed line) impact the main ring.

Because Jupiter's ring is optically thin, every ring constituent responds independently to the influx of cometary dust. To tilt an orbit by 2 km requires that, on average, particles intercept ~10^{-6} their own mass (*6*). For a ring of 1-cm particles spanning the orbits of Metis and Adrastea (128,000 to 129,000 km), an integrated fluence of ~10^{-6} g/cm^2 would be required, or ~10^{13} g in total. Our simulations indicate that 0.2 to 0.5% of SL9's ejecta smaller than 50 μm will intercept this ring (*6*). We therefore require SL9 to produce ~2×10^{15} to 5×10^{15} g of dust, amounting to a volume ~2 to 5 km^3. For comparison, estimates of the initial diameter of the intact comet range from $D \sim 1.5$ km (*17*) to 10 km (*18*). Corresponding volume estimates are $V =$ 2 to 500 km^3. A meta-study (*19*) concludes $D =$ 3.5 km ($V \approx 20$ km^3). The fragments of SL9 underwent substantial collisional evolution shortly after the breakup (*13*); this can lead to a steep size distribution in which a substantial fraction of the mass is concentrated in the smallest particles. If so, then the larger estimates for SL9's volume are compatible with our requirements. Our results are difficult to reconcile with the smallest size estimates, which are based on dynamical models of how a loosely bound rubble pile would break apart (*17*).

For a given fluence of cometary dust, larger ring bodies are deflected to smaller tilt angles in inverse proportion to their radii. We chose 1 cm for the above calculation because cm-sized particles are likely to achieve the largest tilts; smaller particles can be shattered by the 50-μm impactors (*6*). Thus, our mass estimate is only valid if the size distribution is steep, so that the ring's appearance is dominated by the smallest surviving particles (and their ejecta). The jovian ring's dust population does steepen markedly above ~30 μm (*5*), suggesting that this assumption is plausible.

The kinematics of these spirals requires that the wavelength be nearly uniform at any given time, but the tilts need not be. In an optically thin ring, they will vary depending on the local ring particle sizes. In Fig. 1C, the inward decrease of the slopes may simply indicate a decreasing population of the cm-sized particles. This is consistent with ring photometry that indicates a rapidly decreasing number of embedded macroscopic bodies interior to the orbit of Metis (*20*, *21*).

We now recognize that impacts by comets and/or their dust clouds are common occurrences in planetary rings. On at least three occasions over the past few decades, these collisions have carried sufficient momentum to tilt a ring of Jupiter or Saturn off its axis by an observable distance. Once such a tilt is established, it can persist for decades, with the passage of time recorded in its ever-tightening spiral. Within these subtle patterns, planetary rings chronicle their own battered histories.

References and Notes

1. M. Ockert-Bell *et al.*, *Icarus* **138**, 188 (1999).
2. M. M. Hedman *et al.*, *Icarus* **188**, 89 (2007).
3. M. M. Hedman, J. A. Burns, M. W. Evans, M. S. Tiscareno, C. C. Porco, *Science* **332**, 708 (2011).
4. M. R. Showalter, J. A. Burns, J. N. Cuzzi, J. B. Pollack, *Icarus* **69**, 458 (1987).
5. S. M. Brooks, L. W. Esposito, M. R. Showalter, H. B. Throop, *Icarus* **170**, 35 (2004).
6. Materials and methods are available as supporting material on *Science* Online.
7. This formula is only valid where both sin(*B*) and sin(θ)/sin(*B*) $Z'(R,\theta)$ are << 1; these constraints are satisfied throughout our analysis.
8. R. A. Jacobson, *Bull. Am. Astron. Soc.* **33**, 1039 (2001).
9. A. Sánchez-Lavega *et al.*, *Astrophys. J.* **715**, L155 (2010).
10. L. A. Benner, W. B. McKinnon, *Icarus* **118**, 155 (1995).
11. P. W. Chodas, D. K. Yeomans, in *The Collision of Comet Shoemaker-Levy 9 and Jupiter*, K. S. Noll, H. A. Weaver, P. D. Feldman, Eds. (Cambridge Univ. Press, Cambridge, 1996), pp. 1–30.
12. K. Zahnle, L. Dones, H. F. Levison, *Icarus* **136**, 202 (1998).
13. Z. Sekanina, P. W. Chodas, D. W. Yeomans, *Astrophys. J.* **289**, 607 (1994).
14. J. M. Hahn, T. W. Rettig, *Icarus* **146**, 501 (2000).
15. J. A. Burns, P. L. Lamy, S. Soter, *Icarus* **40**, 1 (1979).
16. H. A. Weaver *et al.*, *Science* **263**, 787 (1994).
17. E. Asphaug, W. Benz, *Icarus* **121**, 225 (1996).
18. Z. Sekanina, P. W. Chodas, D. K. Yeomans, *Planet. Space Sci.* **46**, 21 (1998).
19. M. Zamarashkina, Y. Medvedev, *Proc. ACM* **500**, 457 (2002).
20. J. A. Burns *et al.*, in *Jupiter: The Planet, Satellites and Magnetosphere*, F. Bagenal, Ed. (Cambridge Univ. Press, Cambridge, 2004), pp. 241–262.
21. M. R. Showalter *et al.*, *Science* **318**, 232 (2007).

Acknowledgments: M.R.S. acknowledges the support of NASA's Jupiter Data Analysis Program through grant NNX09AD97G. J.A.B. has been funded by NASA's Planetary Geology and Geophysics Program.

Supporting Online Material

www.sciencemag.org/cgi/content/full/science.1202241/DC1
Materials and Methods
Figs. S1 to S5
Table S1
References 22 and 23

27 December 2010; accepted 16 March 2011
Published online 31 March 2011;
10.1126/science.1202241

Single-Cell Genomics Reveals Organismal Interactions in Uncultivated Marine Protists

Hwan Su Yoon,[1,2]* Dana C. Price,[3]* Ramunas Stepanauskas,[1] Veeran D. Rajah,[3] Michael E. Sieracki,[1] William H. Wilson,[1] Eun Chan Yang,[1] Siobain Duffy,[3] Debashish Bhattacharya[3]†

Whole-genome shotgun sequence data from three individual cells isolated from seawater, followed by analysis of ribosomal DNA, indicated that the cells represented three divergent clades of picobiliphytes. In contrast with the recent description of this phylum, we found no evidence of plastid DNA nor of nuclear-encoded plastid-targeted proteins, which suggests that these picobiliphytes are heterotrophs. Genome data from one cell were dominated by sequences from a widespread single-stranded DNA virus. This virus was absent from the other two cells, both of which contained non-eukaryote DNA derived from marine Bacteroidetes and large DNA viruses. By using shotgun sequencing of uncultured marine picobiliphytes, we revealed the distinct interactions of individual cells.

Culture-independent analyses of environmental ribosomal DNA (rDNA) clone libraries and metagenomes can uncover unexpected microbial species and gene diversity (e.g., *1*–*3*). These methods cannot, however, reveal in situ interactions among organisms. To achieve this level of resolution, genome data from single cells captured from the wild environment are needed. We used single-cell genomics (*4*–*7*) to study the marine plankton group Picobiliphyta, recently described as a previously unknown lineage of pigmented eukaryotes with a phylogenetic affinity to cryptophytes and katablepharids (*8*, *9*). The cells were originally identified microscopically with the use of 18*S* rDNA-based fluorescent in situ hybridization probes. Although their ultrastructure is unknown, previous studies using autofluorescence and 4′,6-diamidino-2-phenylindole staining data (*9*, *10*) appeared to show that picobiliphytes contain a plastid derived from a cryptophyte alga (owing to the presence of phycobilin proteins; hence the phylum name) and the associated remnant nucleus (nucleomorph). These taxa have not yet been successfully cultivated, leaving open the possibility that the plastid and nucleomorph may not be permanent acquisitions but rather come from a klepto-plastid or a cryptophyte alga

[1]Bigelow Laboratory for Ocean Sciences, West Boothbay Harbor, ME 04575, USA. [2]Department of Biological Sciences, Sungkyunkwan University, Suwon 440-746, South Korea. [3]Department of Ecology, Evolution and Natural Resources, Rutgers University, New Brunswick, NJ 08901, USA.

*These authors contributed equally to this work.
†To whom correspondence should be addressed. E-mail: bhattacharya@aesop.rutgers.edu

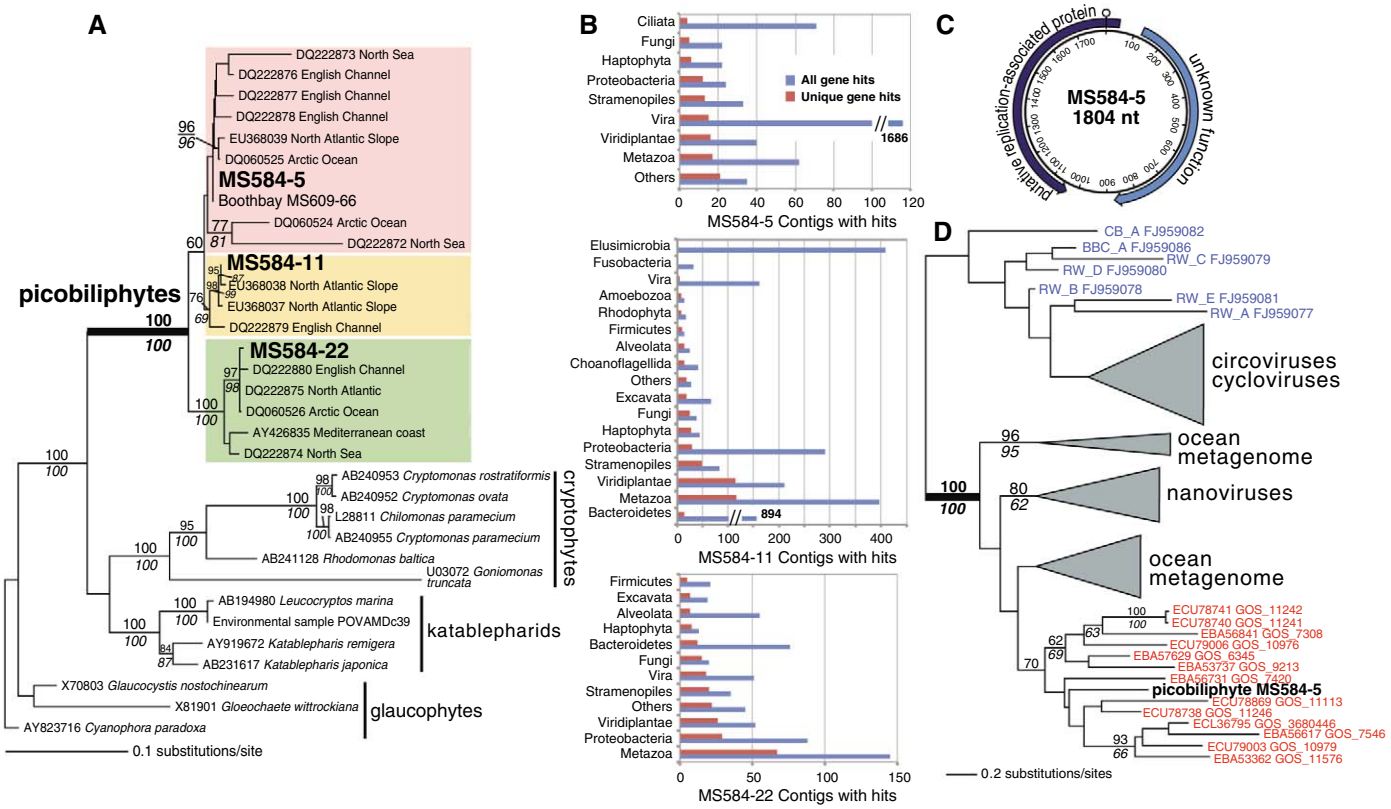

Fig. 1. (**A**) Randomized accelerated maximum likelihood (RAxML) phylogenetic tree of picobiliphyte SSU rDNA coding regions. RAxML bootstrap values are above the branches, and those derived from maximum parsimony (when nodes are shared) are below the branches. Only bootstrap values ≥60% are shown. Sequenced genomes are in bold. GenBank numbers are shown for each taxon. (**B**) Analysis of the taxonomic distribution of BLASTx hits using as query the 454-derived contigs from each SAG assembly (when ≥10; if ≤10, the different hits were grouped under "Others"). The total number of hits (blue bars) and the unique gene hits (red bars) are shown for MS584-5, MS584-11, and MS584-22. Some taxa are overrepresented, such as virus hits in MS584-5 and Bacteroidetes in MS584-22 that are probably explained by MDA bias. (**C**) Genome structure of the previously unknown ssDNA virus. (**D**) Simplified RAxML tree of Rep proteins from representative ssDNA viruses, showing the phylogenetic position of the MS584-5 sequence. Rep from marine ssDNA viruses is shown in blue, whereas sequences derived from ocean metagenome data are shown in red. The bootstrap values (when ≥60%) above the branches are from RAxML, whereas those below are from PhyML. The full tree is shown in fig. S2A.

captured as food. Picobiliphytes are distributed in variable physicochemical habitats (4 to 89 m in depth, 5° to 30°C in temperature) over broad geographical ranges from the Arctic Ocean to the Sargasso Sea and the Mediterranean coast (*8*, *9*, *11*).

We used fluorescence-activated cell sorting to separate individual heterotrophic (lacking chlorophyll fluorescence) protist cells <10 μm in diameter from a single 50-ml seawater sample collected at Boothbay Harbor in the Gulf of Maine. The temperature, amount of chlorophyll, and composition of the microbial community were typical for midsummer at this site (table S1). After whole-genome amplification using multiple displacement amplification (MDA), the taxonomic identity of each single-cell amplified genome (SAG) was determined by sequencing the 18*S* rDNA gene. Of 35 protist SAGs that were analyzed, 6 (17%) were picobiliphytes (*12*) representing three evolutionarily divergent clades, all of which have been previously regarded as photosynthetic (Fig. 1A). The finding of picobiliphytes in the heterotrophic fraction is consistent with the results of another study of 109 SAGs derived from fluorescent and nonfluorescent protists isolated from Boothbay Harbor (table S2). In that analysis of SAG rDNA sequences, picobiliphytes were present only among cells that lacked chlorophyll fluorescence.

Shotgun sequencing of picobiliphyte SAGs MS584-5, MS584-11, and MS584-22 was done using Roche 454 FLX Titanium series reagents and resulted in ~90 mega–base pairs (Mbp) of individual reads and ~5 Mbp of assembled contigs per SAG (table S3). A BLASTx analysis of contigs (Fig. 1B) and unassembled singletons (fig. S1A) revealed many top hits in different eukaryotes. For MS584-5, the majority [85%; 1686 out of 1995 (1686/1995)] of total contig hits were to viral genes. To reduce the impact of possible amplification bias introduced by MDA (*7*, *13*), we reduced the picobiliphyte lists to unique gene hits in each phylum. This was done by reducing multiple hits to the same protein within a single species in our database (table S4) to a single entry. This assumed that each of the duplicated hits represented the same DNA fragment that was overrepresented because of MDA bias. This procedure reduced the overrepresentation of sequences from particular phyla [for example, Elusimicrobia (408 hits to a PBSX phage terminase in *Elusimicrobium minutum* Pei191) and Bacteroidetes in MS584-11] and increased the relative number of hits to Metazoa, Viridiplantae, and Stramenopiles (Fig. 1B and fig. S1A).

Taxonomic analysis of MS584-5 contigs indicated that this SAG contains a previously uncharacterized virus absent in the other two cells (fig. S1A). The assembled genome of this virus (1804 nt; Fig. 1C) was used in a BLASTx search against the NCBI RefSeq viral repository. This showed that the genome encoded a putative replication-associated protein (Rep), with all 58 hits being to Rep proteins in single-stranded DNA (ssDNA) nanoviruses of plants and circoviruses of animals. The top hit was the Rep protein in the Faba bean necrotic yellows virus [expect (*e*) value that by chance another alignment exists with a higher probability = 6.00×10^{-24}; see fig. S1B]. A BLASTn analysis of the individual 454 reads derived from MS584-5 using the assembled viral genome sequence as a query identified 109,748 reads (46.2% of the total data from this SAG) with an *e* value $\leq 1 \times 10^{-20}$, consistent with the large number of virus-derived contigs in this cell. The sequence coverage across this genome was relatively uniform (mean = 22740; standard deviation = 3396). Given the high abundance of shotgun reads spanning the entire genome of a single "nanovirus" genotype in picobiliphyte MS584-5, our data probably indicate virus infection captured in situ by single-cell sequencing. The MS584-5 Rep protein shares no similarity with plasmids of the red alga *Porphyra pulchra* or ssDNA viruses of diatoms (*14*, *15*) or organelle DNA. The virus is larger than any characterized nanovirus genome segment and has a second open reading frame in the opposite sense to Rep (Fig. 1C). Analysis of the Global Ocean Survey metagenome data (*16*) showed that related Rep protein sequences are abundant in the ocean (Fig. 1D).

Contig and singleton BLASTx hits to non-eukaryote DNA from MS584-11 included marine Bacteroidetes, Proteobacteria, and Firmicutes (Fig. 1B and fig. S1A). MS584-22 harbored a diverse range of larger double-stranded DNA viruses, phages, and Proteobacteria (Fig. 1B and

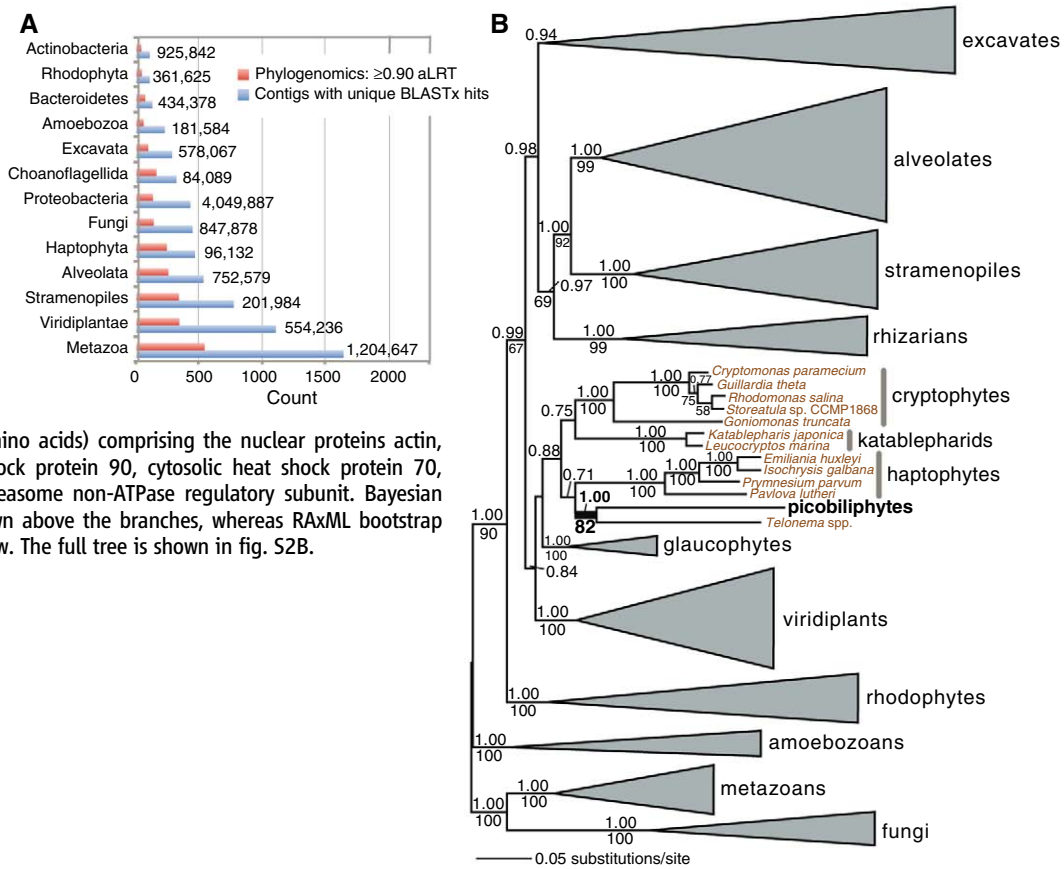

Fig. 2. (**A**) Analysis of the taxonomic distribution of unique BLASTx hits (blue bars) using as query the contigs from the 454 + Illumina assembly of MS584-11. Only phyla with >100 hits are shown. The red bars show the phylogenetic distribution of MS584-11 proteins in PhyML trees at aLRT ≥0.90. The value at the right of the bars is the total number of proteins representing each phylum in our database. (**B**) Simplified phylogeny inferred with Bayesian inference, showing the phylogenetic position of picobiliphytes. This tree was built using a concatenated alignment (2594 amino acids) comprising the nuclear proteins actin, alpha-tubulin, beta-tubulin, heat shock protein 90, cytosolic heat shock protein 70, ribosomal protein L3, and 26*S* proteasome non-ATPase regulatory subunit. Bayesian posterior probability values are shown above the branches, whereas RAxML bootstrap values (when ≥60%) are shown below. The full tree is shown in fig. S2B.

fig. S1A). Presumably, the picobiliphytes feed on Proteobacteria, Bacteroidetes (some apparently phage-infected), and large DNA viruses (*17*), although attachment of viral and bacterial DNA to the picobiliphyte cell surface cannot be ruled out with our approach.

To address the possibility that the picobiliphytes we studied might contain a plastid (*9*) and were sorted as heterotrophs because of a loss of autofluorescence as a result of damage caused by photobleaching, we searched the SAG data for hits to plastid- and mitochondrion-encoded proteins. BLASTx analysis identified 62, 3646, and 102 hits to mitochondrial proteins in the sequence reads from MS584-5, MS584-11, and MS584-22, respectively, but failed to recover plastid proteins (contig hits are shown in table S5). We then generated an additional ~3 Gbp of data from MS584-11 using an Illumina GAIIx sequencer. These data (29.3 million paired-end reads) were coassembled with the existing 454 data, resulting in ~28 Mbp of contigs. Assessment of the two sets of sequence data showed that 94% of the 454 data mapped (at ≤3 mismatches in a 53-bp sliding window of comparison) to the Illumina reads. BLASTx analysis of the combined assembly again failed to identify plastid DNA. As a final step, we generated ~9 Gbp of Illumina data from MS584-22 and used BLASTx to search the assembled ~27 Mbp of contigs for hits to plastid genes; none were found except for a hit to a site-specific DNA endonuclease and to a hypothetical protein that are plastid-encoded in two different green algae (table S6). To assess our ability to identify plastid genes in a SAG-MDA sample, we examined Illumina data derived from a photosynthetic amoeba, *Paulinella chromatophora* [for details, see (*S24*)]. This analysis showed that over one-half of the *P. chromatophora* plastid-encoded genes could be successfully retrieved with BLASTx.

The 454 + Illumina draft genome assembly for MS584-11 afforded assessment of the level of gene homology between the poorly understood picobiliphytes and other eukaryotes. The MS584-11 data were initially analyzed with BLASTx to determine the number of hits of MS584-11 contigs to the total set of predicted proteins in the sequenced genomes of brewer's yeast *Saccharomyces cerevisae* S288c and the model diatom *Phaeodactylum tricornutum* CCAP 1055/1. Using the cutoff *e* value $\leq 1 \times 10^{-5}$, 1866/5863 (31.8%) and 2792/9488 (29.4%) of proteins in the yeast and the diatom, respectively, had hits to picobiliphyte contigs. This suggests that ~2000 picobiliphyte proteins shared detectable similarity with sequences in other eukaryotes. We searched annotations for all diatom protein hits to the picobiliphyte data, now at the more stringent *e* value $\leq 1 \times 10^{-10}$ (1687 proteins) for putative nuclear-encoded plastid-targeted proteins in MS584-11. This analysis turned up a weak hit to a putative chloroplast-targeted nuclear-encoded recombinase and a plastidic inositol phosphatase in *P. tricornutum* (GenBank identification nos. 219111175 and 219110535, respectively). The picobiliphyte recombinase homolog was, however, of bacterial origin, and the inositol phosphatase was of eukaryotic provenance but related to nonplastidic forms of the enzyme. A BLASTx analysis of the MS584-11 contigs against our local database (Fig. 2A) found more unique hits to eukaryote genes in this SAG (with most hits to Metazoa, Viridiplantae, and Stramenopiles) than to prokaryote genes. The large number of hits to Metazoa probably reflects the size of our database (>1.2 million proteins, Fig. 2A), combined with an absence of data from genomes that are closely related to picobiliphytes (Figs. 1A and 2B). Summing the lengths of all MS584-11 contigs with significant BLASTx hits to eukaryote proteins gave an estimate of 7.9 Mbp of detectable, gene-encoding regions of the picobiliphyte genome in our assembly. Given that other picosized eukaryotes such as *Ostreococcus* sp. and *Micromonas* spp. have genome sizes of ~12 to 22 Mbp (*18*), and that picobiliphyte-specific proteins will not be detected by our approach, the MS548-11 assembly probably covers a minimum of 50% of the picobiliphyte genome.

The predicted proteins from the MS584-11 assembly that had significant BLASTx hits (8334 proteins) were used as input for a phylogenomic analysis against our local genome database (see the supporting online material) (*19*). The picobiliphyte data included many highly conserved eukaryotic proteins such as beta-tubulin (contig21336_2; average coverage = 457x) and the second-largest subunit of DNA-directed RNA polymerase I (contig20686_4; average coverage = 11x). We concatenated seven conserved proteins present in the picobiliphyte genome data [actin, alpha-tubulin, beta-tubulin, heat shock protein 90, cytosolic heat shock protein 70, ribosomal protein L3, and 26*S* proteasome non–adenosine triphosphatase (non-ATPase) regulatory subunit] to infer their position in the tree of life. This Bayesian phylogeny (Fig. 2B) shows picobiliphytes to comprise an ancient divergence among eukaryotes with a putative phylogenetic relationship to the plastid-lacking telonemids. The picobiliphyte-telonemid clade is sister to the photosynthetic haptophytes and cryptophytes and the plastid-lacking katablepharids. The union of plastid-containing and plastid-lacking taxa suggests the possibility that picobiliphytes may once have been photosynthetic, as has been suggested for ciliates (*20*) and telonemids (*21*).

Phylogenomics using the MS584-11 data returned 5231 maximum likelihood (PhyML) trees that were sorted (*22*) to determine the taxonomic affinities of the different picobiliphyte proteins at the approximate likelihood-ratio test (aLRT) (*23*) cutoff ≥0.90 (Fig. 2A). This analysis showed that 2228 picobiliphyte proteins (3242 at aLRT ≥0.70) are monophyletic with the eukaryotes tested in our analysis (table S7), which is consistent with the BLASTx analysis described above using the yeast and diatom genome data. Phylogenomics provided a robust estimate of the number of eukaryotic proteins in the MS548-11 data set because it relied on maximum likelihood phylogenetic analysis to assess gene affiliation. The finding that 338, 335, and 240 picobiliphyte proteins group at aLRT ≥0.90 with the Viridiplantae, Stramenopiles, and Haptophyta (table S7), respectively, is consistent with a possible photosynthetic ancestry for picobiliphytes (Fig. 2B). An example of a PhyML tree returned by our pipeline (showing members of the major facilitator superfamily of transporters) that supports a close association of MS584-11 with photosynthetic lineages is shown in fig. S3.

In a final attempt to find potential plastid-targeted proteins in MS584-11, we collected all of the maximum likelihood trees resulting from the phylogenomic analysis that grouped the picobiliphytes with Stramenopiles at aLRT ≥0.70 (1683 individual proteins) and generated gene ontology annotations for these sequences (table S8). Again, we found no evidence for nuclear-encoded plastid-targeted proteins (such as photosystem or light-harvesting proteins) in this data set that included nuclear genome data from photosynthetic diatoms and the pelagophyte *Aureococcus anophagefferens*, which are known to contain these genes. We interpret these different lines of evidence as arguing against a photosynthetic lifestyle for the picobiliphyte SAGs we have studied.

In this study, SAG analysis allowed us to generate significant genome data from three individual, related cells found in a single 50-ml coastal seawater sample. This revealed complex biotic interactions among previously uncharacterized marine microorganisms, with each cell undergoing distinct types of interaction. Our single-cell sequencing approach opens novel opportunities to study protist, prokaryote, and viral interactions in situ, without cultivation artifacts, and has biomedical applications; for example, in determining DNA differences between healthy and diseased cells. The ability to generate substantial amounts of genome data from single cells also opens the possibility of reconstructing the eukaryotic tree of life, using a multitude of uncultured taxa isolated directly from their natural environment.

References and Notes

1. B. J. Baker *et al.*, *Proc. Natl. Acad. Sci. U.S.A.* **107**, 8806 (2010).
2. I. Bodaker *et al.*, *ISME J.* **4**, 399 (2010).
3. P. A. Vaishampayan *et al.*, *Genome Biol. Evol.* **2**, 53 (2010).
4. K. Zhang *et al.*, *Nat. Biotechnol.* **24**, 680 (2006).
5. Y. Marcy *et al.*, *Proc. Natl. Acad. Sci. U.S.A.* **104**, 11889 (2007).
6. R. Stepanauskas, M. E. Sieracki, *Proc. Natl. Acad. Sci. U.S.A.* **104**, 9052 (2007).
7. T. Woyke *et al.*, *PLoS ONE* **4**, e5299 (2009).
8. M. L. Cuvelier *et al.*, *Environ. Microbiol.* **10**, 1621 (2008).
9. F. Not *et al.*, *Science* **315**, 253 (2007).
10. E. Kim *et al.*, *Proc. Natl. Acad. Sci. U.S.A.* **108**, 1496 (2011).
11. C. Lovejoy, R. Massana, C. Pedrós-Alió, *Appl. Environ. Microbiol.* **72**, 3085 (2006).
12. J. L. Heywood, M. E. Sieracki, W. Bellows, N. J. Poulton, R. Stepanauskas, *ISME J.* **5**, 674 (2011).
13. S. Rodrigue *et al.*, *PLoS ONE* **4**, e6864 (2009).
14. D. A. Moon, L. J. Goff, *Curr. Genet.* **32**, 132 (1997).
15. Y. Shirai *et al.*, *Appl. Environ. Microbiol.* **74**, 4022 (2008).
16. S. J. Williamson *et al.*, *PLoS ONE* **3**, e1456 (2008).

17. C. Evans, W. H. Wilson, *Limnol. Oceanogr.* **53**, 2035 (2008).
18. A. Z. Worden *et al.*, *Science* **324**, 268 (2009).
19. A. Moustafa *et al.*, *Science* **324**, 1724 (2009).
20. A. Reyes-Prieto, A. Moustafa, D. Bhattacharya, *Curr. Biol.* **18**, 956 (2008).
21. N. Okamoto, C. Chantangsi, A. Horák, B. S. Leander, P. J. Keeling, *PLoS ONE* **4**, e7080 (2009).
22. A. Moustafa, D. Bhattacharya, *BMC Evol. Biol.* **8**, 6 (2008).
23. M. Anisimova, O. Gascuel, *Syst. Biol.* **55**, 539 (2006).

Acknowledgments: This project was supported by NSF grants EF-0827023, DEB-0936884, OCE-0821374, and OCE-0623288, and by Next-Generation BioGreen 21 (SSAC, 2011), Rural Development Administration, South Korea. The authors thank J. Heywood and N. Poulton for technical support. The genome sequence of the MS584-5 virus is available in GenBank under the accession number HQ322117, whereas the 454 sequence data from SAG MS584-5 and 454 + Illumina reads from MS584-11 and MS584-22 are available at the NCBI Sequence Read Archive under the accession numbers SRR068243.1, SRR068244.2, and SRR068245.2, respectively. The assembled contigs for each SAG, the phylogenomic results (alignments and trees), singleton hit lists, annotations for the 8334 proteins in the MS584-11 joint assembly, protein alignments used for the trees presented in the paper, and the *Paulinella chromatophora* plastid sequence and Illumina genome data used to determine the frequency of plastid genes recovered from these reads are freely available at http://dbdata.rutgers.edu/data/pico.

Supporting Online Material
www.sciencemag.org/cgi/content/full/332/6030/714/DC1
Materials and Methods
SOM Text
Figs. S1 to S3
Tables S1 to S8
References

21 January 2011; accepted 1 April 2011
10.1126/science.1203163

A Family of IFN-γ–Inducible 65-kD GTPases Protects Against Bacterial Infection

Bae-Hoon Kim,[1] Avinash R. Shenoy,[1] Pradeep Kumar,[1] Rituparna Das,[1,2] Sangeeta Tiwari,[1] John D. MacMicking[1]*

Immune interferon gamma (IFN-γ) is essential for mammalian host defense against intracellular pathogens. IFN-γ induces nearly 2000 host genes, yet few have any assigned function. Here, we examined a complete mouse 65-kilodalton (kD) guanylate-binding protein (Gbp) gene family as part of a 43-member IFN-γ–inducible guanosine triphosphatase (GTPase) superfamily in mouse and human genomes. Family-wide loss-of-function analysis found that at least four Gbps—Gbp1, Gbp6, Gbp7, and Gbp10—conferred cell-autonomous immunity to listerial or mycobacterial infection within macrophages and gene-deficient animals. These Gbps solicited host defense proteins, including the phagocyte oxidase, antimicrobial peptides, and autophagy effectors, to kill intracellular bacteria. Thus, specific 65-kD Gbps coordinate a potent oxidative and vesicular trafficking program to protect the host from infection.

Immune interferon gamma (IFN-γ) is critical for resistance to infection, exerting its effects through broad transcriptional programs involving ~2000 genes, many of which remain uncharacterized (*1*, *2*). Prominent within this transcriptional signature are several families of guanosine triphosphatases (GTPases). These include the 47-kD immunity-related GTPases (p47 IRGs), 65- to 73-kD guanylate-binding proteins (p65 Gbps), and 285-kD very large inducible GTPases (Vligs/Gvins) (*2*).

Recent mapping efforts have uncovered 43 members of this IFN-γ–inducible GTPase superfamily within mouse and human genomes (*3*–*7*) (fig. S1, A and B). p47 IRGs represent the largest subgroup (~18 to 21 genes) important for host defense (*8*–*12*). These GTPases bind phosphoinositides, cardiolipin, soluble NSF attachment protein receptor adaptor proteins, and other p47 IRGs to direct their membrane regulatory activities against compartmentalized bacteria and protozoa (*10*–*12*). In contrast, little is known about the p65 Gbp and Gvin subfamilies, despite accounting for ~20% of the relative abundance of all proteins induced by IFN-γ (*2*). Weak antiviral or antibacterial properties have been ascribed individually to Gbp1, Gbp2, and Gbp5 (*13*–*15*); however, integrated family contributions remain untested (*2*, *5*).

We thus conducted loss-of-function screens across the complete 11-member mouse *Gbp* family in macrophages where it is strongly induced by IFN-γ compared with other IFNs (IFN-αβ, IFN-λ, and IFN-Z) and Toll-like receptor (TLR) ligands (fig. S1, C and D) (*6*). These immune cells were infected with two intracellular bacteria particularly sensitive to IFN-γ–mediated killing: *Listeria monocytogenes* (*Lm*), a gram-positive bacterium responsible for food-borne infection in humans, or *Mycobacterium bovis* BCG (*Mb* BCG), which causes lethal mycobacteriosis in IFNγR-deficient patients (*1*). Using short 21-bp (base pair) Gbp small interfering RNA (siRNA) duplexes that gave robust gene-specific silencing (fig. S2, A and B), we found that Gbp1, Gbp6, Gbp7, and Gbp10 were critical for control of virulent *Lm* (EGD strain) or *Mb* BCG (Phipps strain). In resting RAW264.7 macrophages, *Lm* multiplied by a factor of ~85 ($\log10^{1.9}$ growth) over 6 hours after uptake. IFN-γ activation, however, curtailed replication (to a factor of ~18, or $\log10^{1.2}$ growth), a restriction that was reversed with siRNAs for Gbp1, Gbp6, Gbp7, Gbp10 and to a lesser extent Gbp5 (to a factor of 39 to 58 or ~$\log10^{1.5–1.75}$ growth; $P < 0.0062$) (Fig. 1A and fig. S3A). Protective Gbps functioned cooperatively, with siRNA combinations exacerbating the loss of IFN-γ–induced killing (Fig. 1A and fig. S3A). siRNA phenotypes were not attributable to single- and double-stranded RNA sensing. Primary bone-marrow–derived macrophages (BMMs) and RAW264.7 cells defective in either TLR ($MyD88^{-/-}Trif^{-/-}$) or Rig-1/Mda5/Ips-1–dependent RNA recognition (expressing the viral Rig-1/Mda5/Ips-1 inhibitor, NS34A) yielded comparable results (Fig. 1A and fig. S3A).

Mb BCG challenge showed similar Gbp-dependent resistance. In short 48-hour killing assays that were necessitated by waning siRNA effectiveness at 96 hours, IFN-γ reduced *Mb* BCG by ~$\log10^{0.8}$ [72 to 77% reduction in colony-forming units (CFU)] in untreated and scrambled RNA (scRNA)–treated macrophages. Inhibition was partly reversed by Gbp1, Gbp5, Gbp7, or Gbp6/Gbp10 siRNAs (56 to 64% CFU reduction) but not siRNAs for the remaining *Gbp* genes (77 to 82%; $P < 0.0112$) (Fig. 1A and fig. S3B).

To amplify the smaller phenotypes for slow-growing *Mb* BCG, we devised a system of long-term Gbp inhibition. Dominant-negative (DN) mutants were identified and stably expressed under tetracycline-repressible control [tTA-TRE2-Gbp (DN)] to avoid polyketide antibiotics during infection. Two conserved P-loop residues (GxxH/RxKS) required for nucleotide-dependent self-assembly or a C-terminal CaaX box (CVIL) used for C_{20} isoprenyl membrane tethering were mutated (*16*, *17*). All Gbp1 ($Gbp1^{H48P}$, $Gbp1^{S52N}$, and $Gbp1^{SVIL}$) and Gbp7 ($Gbp7^{R48P}$ and $Gbp7^{S52N}$) mutants failed to target vesicle membranes; however, those of Gbp10 ($Gbp10^{R46P}$ and $Gbp10^{S50N}$) showed a less robust phenotype and were not pursued further as potential DN candidates (fig. S4A). Stable expression of Gbp1 and Gbp7 P-loop (S52N) mutants disrupted endogenous Gbp vesicle localization in IFN-γ–activated macrophages (fig. S4B), underscoring their DN action by binding wild-type partners for incorporation into "dead-end" multimeric complexes (fig. S5, A to C). This resembles dynamin-1 P-loop (S52N)

[1]Section of Microbial Pathogenesis, Boyer Centre for Molecular Medicine, Yale University School of Medicine, New Haven, CT 06510, USA. [2]Department of Internal Medicine, Division of Infectious Diseases, Yale University School of Medicine, New Haven, CT 06510, USA.

*To whom correspondence should be addressed. E-mail: john.macmicking@yale.edu

mutants that inhibit self-assembly and endocytic trafficking (*18*). Cell-free assays corroborated these results: α-^{32}P-GTP hydrolyzing activity and nucleotide-dependent homo-tetramerization (*16*) were abolished in recombinant Gbp1^{S52N} and Gbp7^{S52N} proteins, like Dyn^{S45N} (*18*) (fig. S5, D and E).

Subsequent infection of four tTA-TRE2-Gbp1^{S52N} and tTA-TRE2-Gbp7^{S52N} macrophage cell lines showed impaired mycobactericidal activity in each case. *Mb* BCG was reduced 43 to 57% versus 83 to 88% for parental tTA cells over 7 days of IFN-γ treatment ($P < 0.0013$); the DN phenotype exceeded that of 48-hour siRNA assays (Fig. 1B and fig. S6) and was independent of other antimycobacterial pathways [inducible nitric oxide synthase (Nos2)] (*8*) or loss of host cell viability. Defective listerial killing was also seen in all mutant cell lines (57 to 78% versus 83 to 91% reduction in *Lm* CFU of tTA controls; $P < 0.0024$) (Fig. 1B and fig. S6).

Next, we validated bactericidal deficiencies in vivo. We generated Gbp1$^{-/-}$ mice (fig. S7) that exhibited normal T, B, and phagocytic (CD11b^{+}) cell profiles in target lymphoid organs like the spleen and LyG6^{+} granulocytes in peripheral blood (fig. S8). Macrophages from these mice, however, had impaired killing activities despite intact responses to IFN-γ as shown by NO release (*8*) (Fig. 1B and fig. S9A). Such killing defects also manifested in vivo. Gbp1$^{-/-}$ mice allowed Lm to replicate by a factor of 100 to 1000 in livers and spleens after natural orogastric challenge, whereas Gbp1$^{+/+}$ mice curtailed replication despite initial colonization of these organs being similar for both groups (0.8- to 9-fold growth during days 1 to 3) (Fig. 1C). Genotypic differences persisted through day 8 postinfection (p.i.), by which stage Gbp1$^{-/-}$ mice exhibited discernible weight loss and sporadic diarrhea (Fig. 1, C and D, and fig. S9B).

Mb BCG infection yielded similar results. Gbp1$^{-/-}$ mice had increased mycobacterial burdens as early as 5 weeks p.i. before becoming moribund at ~10 to 14 weeks, with up to 350 times more *Mb* BCG in their lungs than Gbp1$^{+/+}$ controls (Fig. 1, E and F, and fig. S9, C to E). Susceptibility to either *Lm* or *Mb* BCG was not attributable to impaired granuloma formation (fig. S9, D and E) or to global IFN-γ defects, because production of this cytokine (fig. S9F) and responses to it (macrophage NO secretion) (fig. S9A) were intact in Gbp1$^{-/-}$ mice. Thus, our three independent loss-of-function approaches—siRNA silencing, DN inhibition, and chromosomal deletion—implicate the 65-kD Gbps as a class of bacterial host defense proteins that operate in vitro and in vivo.

To understand how the protective Gbps conferred host resistance, we focused on trafficking to the bacterial compartment because pathogen-susceptible S52N mutations interfered with mem-

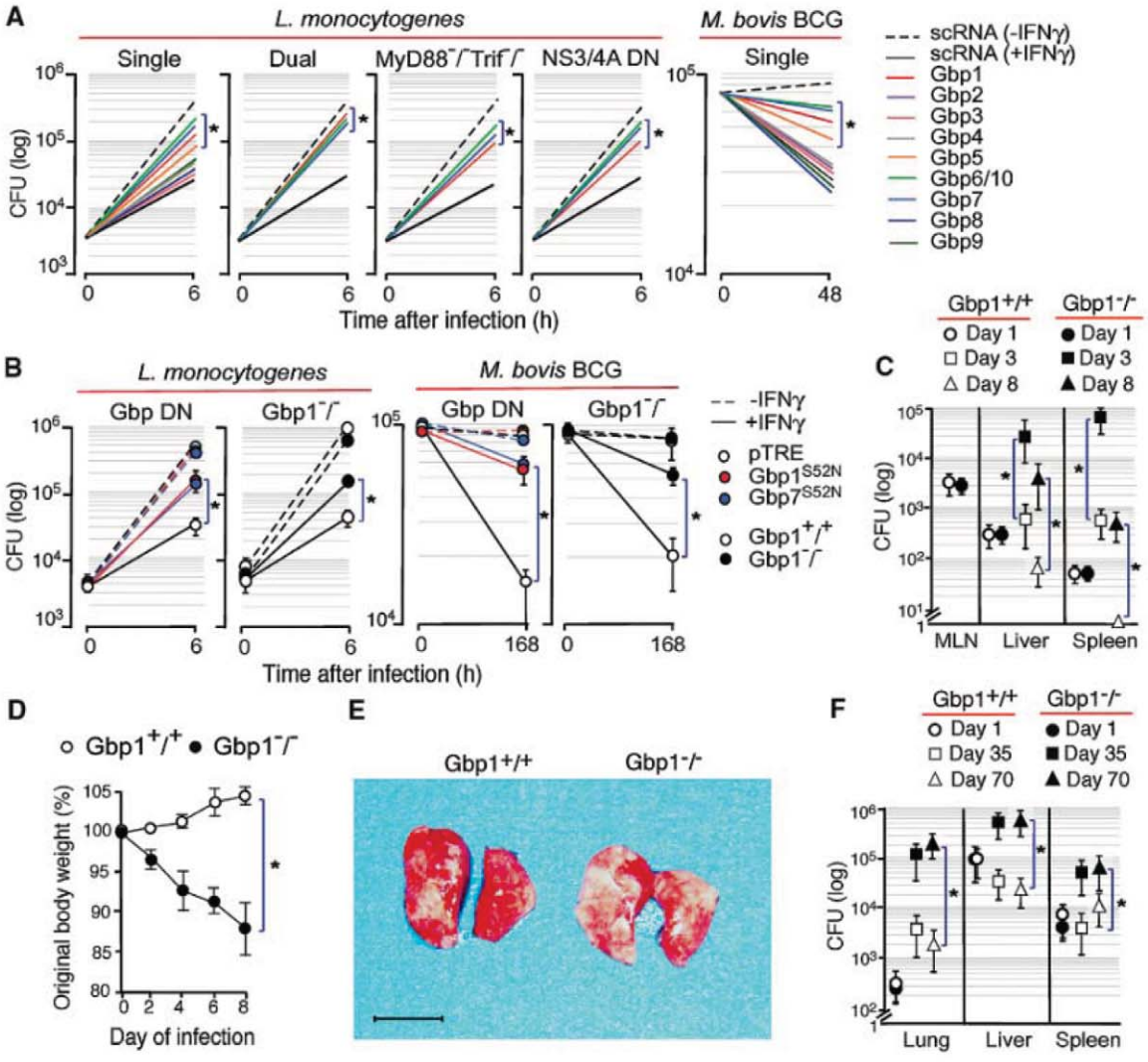

Fig. 1. IFN-γ–inducible Gbps protect against bacterial infection. (**A**) Gbp siRNA screen for loss of *Lm* or *Mb* BCG killing in IFN-γ–activated macrophages. Mean (triplicate wells) for each siRNA shown (SD removed for clarity; see fig. S3). Gbp10 siRNAs also silence Gbp6 due to 99.1% nucleotide identity. Dual silencing: Gbp1+Gbp7 (red); Gbp7+Gbp10 (blue); Gbp10+Gbp1 (green). Control, scRNA (2x). *, $P < 0.0112$, analysis of variance (ANOVA). 1 of 14 similar experiments. (**B**) Antibacterial activity in RAW264.7 cell lines expressing GbpDN mutants or BMMs lacking Gbp1 (fig. S6). Mean ± SD, some values falling within symbols. *, $P < 0.046$, ANOVA. $N = 3$ experiments each. (**C**) *Lm* burdens in orally infected (10^9 CFU) Gbp1$^{+/+}$ and Gbp1$^{-/-}$ mice. Day 1 colonization included local mesenteric lymph nodes (MLNs). $N = 8$ to 12 mice per group per time point. Error bars, mean ± SD. *, $P < 0.040$, ANOVA. $N = 3$ experiments. (**D**) Listeriosis-induced weight loss (% of starting weight) over 8 days (8 to 12 per group). Error bars, mean ± SD. *, $P < 0.039$, ANOVA. One of three experiments shown. (**E**) Diseased lungs of Gbp1$^{+/+}$ and Gbp1$^{-/-}$ mice infected with *Mb* BCG Phipps (10^5 CFU intravenously) at day 70 p.i. Scale bar, 1 cm. (**F**) Organ mycobacterial burdens at 1, 35, and 70 days p.i. $N = 6$ mice per group. Error bars, mean ± SD. *, $P < 0.025$, ANOVA. One of two similar experiments shown.

brane targeting (figs. S4, A and B, and S10A). All the protective Gbps translocated to mycobacteria-containing vacuoles (MCVs) and *Lm*-containing vacuoles (LCVs) within 0.5 to 2 hours of uptake (Fig. 2, A and B), which correlates with the known ability of IFN-γ–activated macrophages to sequester *Lm* or *Mb* BCG inside phagosomes for lysosomal delivery and killing (*8*–*10*, *19*). Live imaging showed that Gbps arrived on ~50- to 100-nm vesicles over a 20- to 30-min period before fusing with MCVs (Fig. 2C, fig. S10B, and movie S1). This parallels *Toxoplasma gondii* infection, where different Gbps target the parasitophorous vacuole (*6*), potentially helping deliver antimicrobial cargo to the pathogen compartment.

To identify the type of cargo Gbps transport, we combined three unbiased partner interactive screens with microscopic analysis of Gbp-containing vesicles. Macrophages stably expressing doxycycline-repressible Gbp1, Gbp7, or Gbp10 with different N-terminal tags for single-step or two-step capture via tandem affinity purification (TAP) were generated. In addition, glutathione *S*-transferase (GST)–Gbps were immobilized to ensure sufficient bait for isolating partners from stringent detergent-liberated fractions enriched for membrane complexes (*10*). Each method identified interacting proteins involved in the antimicrobial effects of the Gbps.

Most abundant among these partners was the membrane-bound gp91^{phox}-p22^{phox} (cytochrome b_{558}) component of NADPH (reduced form of nicotinamide adenine dinucleotide phosphate) oxidase that generates superoxide (O_2^-) for killing listeria and mycobacteria (*19*, *20*) (Fig. 3A and table S6). Gbp7 coprecipitated endogenous p22^{phox} and both shared a subpopulation of vesicles that targeted MCVs (Fig. 3B and fig. S11A). Gbp7 also bound other NADPH oxidase subunits—principally p67^{phox}, which is recruited as a heterodimer with p40^{phox} to the cytochrome b_{558} complex for assembling the holoenzyme (Fig. 3B). An N-terminal G domain of Gbp7 bound p67^{phox}, whereas its C-terminal helix engaged gp91^{phox}-p22^{phox} (Fig. 3A and fig. S11B). This suggested that Gbp7 could act as a bridging protein to help deliver cytosolic p67^{phox}-p40^{phox} to gp91^{phox}-p22^{phox} for NADPH oxidase assembly on phagosomal membranes.

We tested this proposal in IFN-γ–treated macrophages stably expressing hemagglutinin (HA)–tagged p67^{phox} that allows robust coprecipitation of endogenous gp91^{phox}; Gbp7 siRNAs largely abolished this interaction, without altering p67^{phox}-HA binding to cytosolic p40^{phox} or the expression of NADPH oxidase subunits (Fig. 3C). Gbp7 siRNAs and Gbp7^{252N} DN mutants both diminished p67^{phox}-p40^{phox} targeting to MCVs as well as IFN-γ–induced O_2^- production

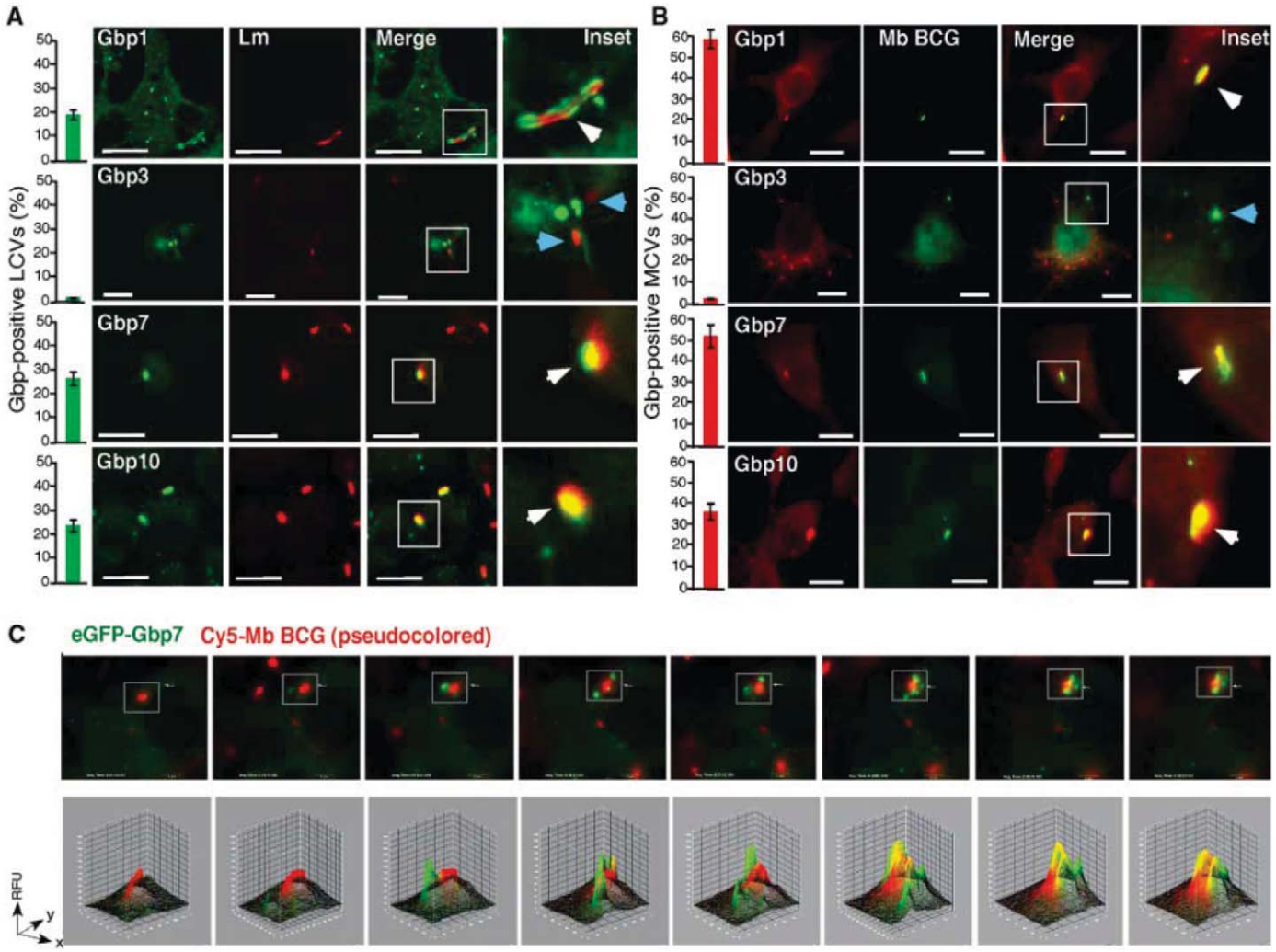

Fig. 2. Protective Gbps target bacteria-containing vacuoles. (**A**) Vesicular Gbp1, Gbp7, and Gbp10, but not Gbp3, recruited to 30-min LCVs (antibody to *Lm*, Alexa 594) or (**B**) 2 hours MCVs (GFP^{S65T}-*Mb* BCG) in IFN-γ–activated RAW264.7 macrophages. Scale bar, 5 μm. Gbp1 detected with antibody to M18 (Alexa 488); remaining Gbps as (A) enhanced yellow fluorescent protein (eYFP)– or (B) monomeric red fluorescent protein (mRFP)–tagged constructs. Colocalization (mean ± SD) from 120 to 270 confocal images. *N* = 8 experiments. (**C**) Live imaging (frames 7.41 to 38.21 min) of IFN-γ–activated macrophages stably expressing eGFP-Gbp7 given Cy5-labeled *Mb* BCG. Scale bar, 5 μm. Three-dimensional surface intensity plots (boxed area) shown below. One of four experiments shown.

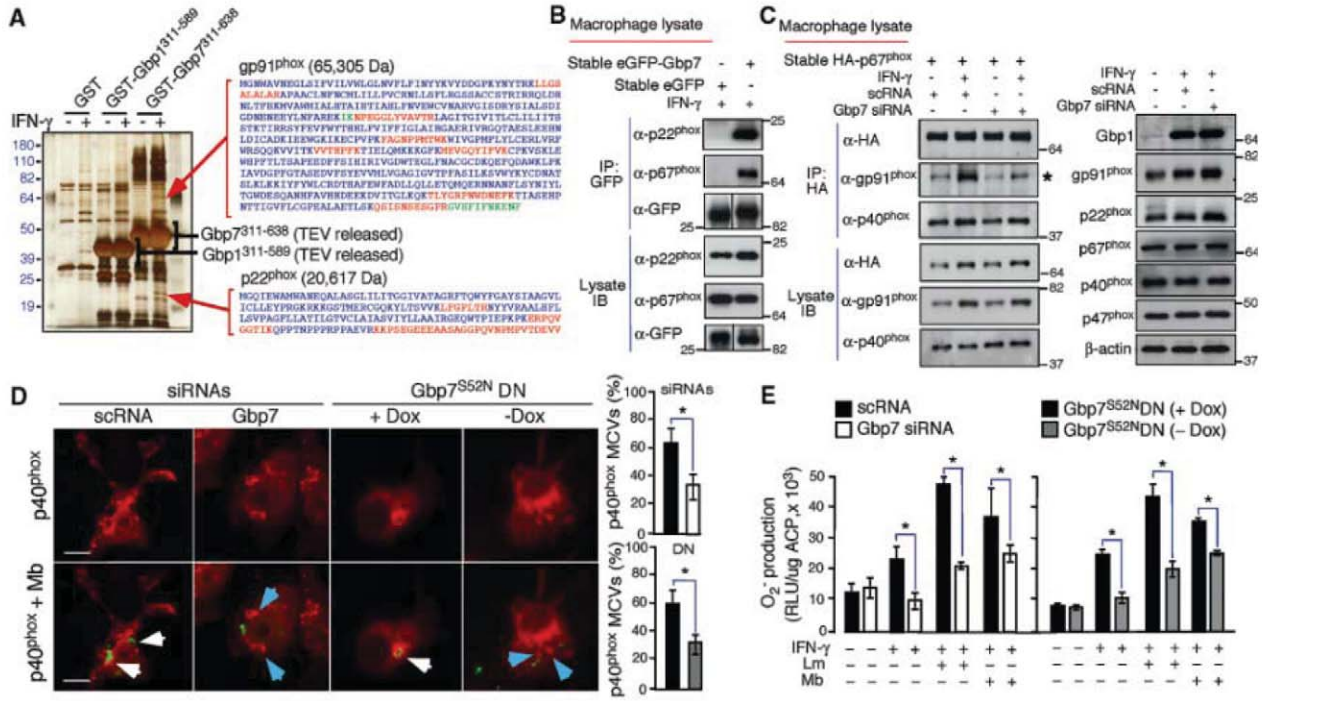

Fig. 3. Gbp7-dependent oxidative host defense. (**A**) Silver-stained gel of macrophage membrane-enriched fractions incubated with the GST-Gbp7 C-terminal helical domain (amino acids 311 to 636). Controls, GST-Gbp1 (amino acids 311 to 589) and GST. TEV protease-released Gbps, $p22^{phox}$, and $gp91^{phox}$ plus liquid chromatography–tandem mass spectrometry peptides (red font, overlapping peptides in green) are shown. (**B**) Coprecipitation of endogenous $p22^{phox}$ and $p67^{phox}$ by stable eGFP-Gbp7 in IFN-γ–activated macrophages. One of three experiments shown. (**C**) (Left) Gbp7 siRNAs disrupted $p67^{phox}$-HA interaction with endogenous $gp91^{phox}$ (asterisk) but not $p40^{phox}$; (Right) NADPH oxidase subunit and Gbp1 expression. One of two experiments shown. (**D**) Impaired $p40^{phox}$-HA targeting to MCVs (blue arrows) with Gbp7 siRNAs or $Gbp7^{S52N}$ DN mutant at peak 2 hours recruitment time using GFP^{S65T}-Mb BCG. 280 to 430 MCVs (mean ± SD) per condition. $P < 0.012$, ANOVA. siRNA treatment: scRNA (black bars); Gbp7 siRNAs (white bars). DN expression: tTA control (black bars); $Gbp7^{S52N}$ DN (gray bars). (**E**) Diminished O_2^- production in Gbp7 siRNA-treated or DN RAW264.7 cells given IFN-γ (100 U/ml, 16 hours) ± *Lm* (multiplicity of infection, 1:1; 30 min) or *Mb* BCG (MOI, 2:1; 3 hours). ACP, adherent cell protein. $P < 0.017$, ANOVA. $N = 3$ experiments.

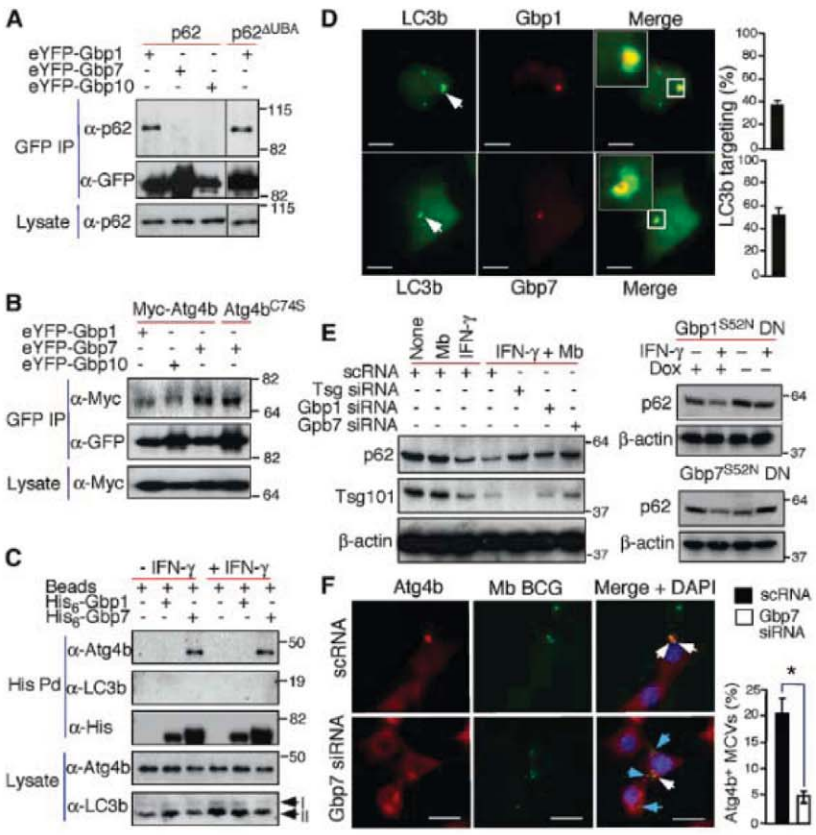

Fig. 4. Gbp1 and Gbp7 traffic antimicrobial peptides. (**A**) eYFP-Gbp1 coprecipitated full-length or UBA-deleted DsRed-p62, and (**B**) eYFP-Gbp7 captured Myc-Atg4b or Myc-$Atg4B^{S74A}$ in mammalian cell (HeLa) extracts. One of four experiments shown. (**C**) His_6-Gbp7 retrieved endogenous Atg4b from RAW264.7 lysates. One of three pulldown (Pd) experiments shown. (**D**) Targeting endogenous Gbp1 (top) or eGFP-Gbp7 vesicles (bottom) to LC3b autophagic membranes in IFN-γ–activated macrophages. 245 to 260 images counted. Scale bar, 10μm. (**E**) Impaired p62 degradation in 1% triton-X 100 extracted fractions of Gbp-deficient macrophages activated with IFN-γ (100 U/m; 48 hours) ± *Mb* BCG (MOI, 2:1, 3 hours) at peak p62 turnover (fig. S13D). One of three experiments shown. (**F**) Impaired MCV targeting by Atg4b (K25 antibody, Alexa 594) at peak 4 hours recruitment time. Targeted MCVs (white arrows); non-targeted MCVs (blue arrows). Scale bar, 15μm. 220 to 240 MCVs (mean ± SD) for each condition. $P < 0.009$, ANOVA. One of two experiments shown.

(Fig. 3, D and E). Such defects were complemented by provision of an O_2^- donor that helped restore *Lm* killing in Gbp7-deficient cells (fig. S11C). Thus, Gbp7 exerts its action in part by downstream O_2^- production. Enforced Gbp7 expression also increased O_2^- release by a factor of ~10, like $p67^{phox}$-HA but not $Gbp7^{S52N}$, which served as positive and negative controls, respectively (fig. S11D). $p67^{phox}$-HA–mediated O_2^- secretion was inhibited by Gbp7 but not Gbp1 or Gbp10 siRNAs, further underlining the specific role of Gbp7 in $p67^{phox}$ translocation. Thus, Gbp7 is important for IFN-γ–induced oxidant protection against intracellular bacteria.

Our Gbp-interaction screens also identified a second antimicrobial pathway that generates bacteriolytic peptides (*21*–*23*). Here, Gbp1 bound p62/Sqstm1 and Gbp7 captured Atg4b, respectively (Fig. 4, A to C). p62 delivers ubiquitinated cargo to autolysosomes, generating ubiquitin-derived peptides that kill mycobacteria once MCVs fuse with this compartment (*21*, *22*). Gbp1 vesicles harbored p62 and monoubiquitinated proteins (fig. S12) that were delivered to larger $LC3b^+$ vacuoles (Fig. 4D) for liberating mycobactericidal peptides (detected in Gbp1 TAP screens) (fig. S13A and table S6). Lysosomal delivery was blocked in Gbp1-deficient cells or with siRNAs against Tsg101 (also required for p62 targeting and mycobacterial killing) (*23*) because large amounts of p62 went undigested (Fig. 4E). Gbp1 deficiency did not affect proteasomal degradation of inhibitor of nuclear factor κB (IκB) for p62-stimulated nuclear factor κB (NF-κB) signaling (fig. S13B), nor was Gbp1 itself ubiquinated (fig. S13C), degraded (fig. S13D), or targeted to lysosomes (fig. S12). Thus, Gbp1 probably recycles off this compartment before enclosure, consistent with a lack of LC3b coprecipitation along with p62, the latter of which Gbp1 bound outside its ubiquitin-associated (UBA) domain (Fig. 4A). Such binding could promote p62 oligomerization through Gbp1 self-assembly to capture monoubiquitinated proteins (*24*).

Gbp7 appeared to regulate the next step—cargo engulfment by autophagic membranes—because it bound native Atg4b (Fig. 4C), localized to sites of LC3b membrane elongation (Fig. 4D), and promoted p62 degradation (Fig. 4E). Gbp7 siRNAs disrupted membrane closure; here, incomplete ubiquinated ring structures were evident (fig. S14A) along with Atg5-Atg12, which normally disassembles after membrane closure, like $Atg4b^{C74A}$ mutants that prevent LC3b processing (*25*) (fig. S14, B to D). Gbp7, but not $Gbp7^{S52N}$, rescued these defects and accelerated LC3b lipidation plus p62 turnover, probably by recruiting native Atg4b to unoccupied sites of LC3b attachment (fig. S14, D to G). Indeed, Atg4b recruitment to early MCVs was also blocked by Gbp7 siRNAs, reminiscent of $p67^{phox}$-$p40^{phox}$ translocation (Fig. 4F). Hence, we favor Gbp7 operating as a membrane trafficking protein rather than protease cofactor (it bound both active and inactive Atg4b equally well) (Fig. 4B) that transports different substrates, like NADPH oxidase subunits or Atg4b, to the site of infection.

In sum, the IFN-γ–inducible Gbps promote oxidative killing and deliver antimicrobial peptides to autophagolysosomes (fig. S15). Such cooperative effects could provide broad host protection against different pathogen classes (*2*, *5*).

References and Notes

1. S. Y. Zhang *et al.*, *Immunol. Rev.* **226**, 29 (2008).
2. S. Martens, J. Howard, *Annu. Rev. Cell Dev. Biol.* **22**, 559 (2006).
3. C. Bekpen *et al.*, *Genome Biol.* **6**, R92 (2005).
4. M. A. Olszewski, J. Gray, D. J. Vestal, *J. Interferon Cytokine Res.* **26**, 328 (2006).
5. A. R. Shenoy *et al.*, *Immunobiology* **8**, 771 (2007).
6. D. Degrandi *et al.*, *J. Immunol.* **179**, 7729 (2007).
7. Materials and methods are available as supporting material on *Science* Online.
8. J. D. MacMicking, G. A. Taylor, J. D. McKinney, *Science* **302**, 654 (2003).
9. S. B. Singh, A. S. Davis, G. A. Taylor, V. Deretic, *Science* **313**, 1438 (2006).
10. S. Tiwari, H. P. Choi, T. Matsuzawa, M. Pypaert, J. D. MacMicking, *Nat. Immunol.* **10**, 907 (2009).
11. S. B. Singh *et al.*, *Nat. Cell Biol.* **12**, 1154 (2010).
12. J. P. Hunn *et al.*, *EMBO J.* **27**, 2495 (2008).
13. A. C. Rupper, J. A. Cardelli, *Infect. Immun.* **76**, 2304 (2008).
14. I. Tietzel, C. El-Haibi, R. A. Carabeo, *PLoS ONE* **4**, e6499 (2009).
15. Y. Itsui *et al.*, *Hepatology* **50**, 1727 (2009).
16. B. Prakash, G. J. Praefcke, L. Renault, A. Wittinghofer, C. Herrmann, *Nature* **403**, 567 (2000).
17. N. Modiano, Y. E. Lu, P. Cresswell, *Proc. Natl. Acad. Sci. U.S.A.* **102**, 8680 (2005).
18. S. Sever, A. B. Muhlberg, S. L. Schmidt, *Nature* **398**, 481 (1999).
19. J. T. Myers, A. W. Tsang, J. A. Swanson, *J. Leukoc. Biol.* **171**, 5447 (2003).
20. J. Bustamante *et al.*, *Nat. Immunol.* **12**, 213 (2011).
21. S. Alonso, K. Pethe, D. G. Russell, G. E. Purdy, *Proc. Natl. Acad. Sci. U.S.A.* **104**, 6031 (2007).
22. M. Ponpuak *et al.*, *Immunity* **32**, 329 (2010).
23. J. A. Philips, M. C. Porto, H. Wang, E. J. Rubin, N. Perrimon, *Proc. Natl. Acad. Sci. U.S.A.* **105**, 3070 (2008).
24. E. Itakura, N. Mizushima, *J. Cell Biol.* **192**, 17 (2011).
25. N. Fujita *et al.*, *Mol. Biol. Cell* **19**, 4651 (2008).

Acknowledgments: We thank Y. Matsuura (NS34A DN cells); S. Ivanov (Ub-K63-GFP cells); R. Medzhitov ($MyD88^{-/-}$ $Trif^{-/-}$ mice); M. Pypaert (electron microscopy); and P. Cresswell, W. Mothes, C. Roy, G. Superti-Furga, T. Yoshimori, and H. Zhu (plasmids and antibodies). Supported by NIH National Institute of Allergy and Infectious Diseases (R01 AI068041-01A1), Burroughs Wellcome Fund Investigator in Pathogenesis of Infectious Disease Award, Searle Scholars Program, Cancer Research Institute Investigator Award, W.W. Winchester Foundation (to J.D.M.) and Browne-Cox Fellowship (to A.R.S.).

Supporting Online Material

www.sciencemag.org/cgi/content/full/332/6030/717/DC1
Materials and Methods
Figs. S1 to S15
Tables S1 to S6
Movie S1
References

14 December 2010; accepted 29 March 2011
10.1126/science.1201711

Normalization for Sparse Encoding of Odors by a Wide-Field Interneuron

Maria Papadopoulou,[1] Stijn Cassenaer,[1,2] Thomas Nowotny,[3] Gilles Laurent[1,4]*

Sparse coding presents practical advantages for sensory representations and memory storage. In the insect olfactory system, the representation of general odors is dense in the antennal lobes but sparse in the mushroom bodies, only one synapse downstream. In locusts, this transformation relies on the oscillatory structure of antennal lobe output, feed-forward inhibitory circuits, intrinsic properties of mushroom body neurons, and connectivity between antennal lobe and mushroom bodies. Here we show the existence of a normalizing negative-feedback loop within the mushroom body to maintain sparse output over a wide range of input conditions. This loop consists of an identifiable "giant" nonspiking inhibitory interneuron with ubiquitous connectivity and graded release properties.

Sparse coding, the properties and advantages of which have been known for decades (*1*–*3*) has recently found experimental support in a number of systems (*4*–*8*). In such representations, information is encoded by neurons that express rare, though not exclusive, responses. In some sparse encoding systems, such as the insect mushroom bodies (*7*, *9*) or zebra-finch song control nuclei (*6*), the responses of individual neurons are also very brief (one or two action potentials over a background of 0), making these representations difficult to discover, but the spikes produced extremely informative. In locust, the principal neurons of the mushroom bodies, called Kenyon cells (KCs), respond to odors with high specificity (*7*, *10*) and can express concentration- (*11*) and

[1]Division of Biology, Computation and Neural Systems Program, California Institute of Technology, Pasadena, CA 91125, USA. [2]Broad Fellows Program in Brain Circuitry, California Institute of Technology, Pasadena, CA 91125, USA. [3]Centre for Computational Neuroscience and Robotics (CCNR), School of Informatics, University of Sussex, Falmer, Brighton BN1 9QJ, UK. [4]Max Planck Institute for Brain Research, 60528 Frankfurt, Germany.

*To whom correspondence should be addressed. E-mail: gilles.laurent@brain.mpg.de

category-invariant properties. The baseline activity of KCs is close to 0 (*7*, *10*, *12, 13*), their responses to odors typically contain fewer than three action potentials, and the gain of their output synapses (the effectiveness of their rarely elicited spikes) is both high on average and modifiable by a Hebbian learning rule (*14*). Because each KC is, on average, connected to about half of its presynaptic population (the projection neurons or PNs) (*15*), small changes in the PN population's output could affect the reliability of the KCs' sparse output [supporting online material (SOM) text], inconsistent with experimental observations (*11*).

Earlier anatomical studies (*16*) identified a single "giant GABAergic neuron" (GGN) in each mushroom body—[that is, GGN contains and releases the neurotransmitter γ-aminobutyric acid (GABA)]—with extensive overlap with KC projections [Fig. 1A (i)]: the neurites of GGN in the peduncle and α lobe are fine and highly branched, consistent with dendrites—but varicose in the calyx, consistent with axonal projections (*17*) [Fig. 1A (ii)]. [This neuron appears similar to neuron APL recently described in *Drosophila* (*18*)]. Morphological data thus suggest that GGN is well suited to form a negative-feedback loop with KCs. Using numerical simulations, we verified that an all-to-all feedback system between KCs and GGN could solve the normalization problem described above (SOM text). We show experimentally that GGN in fact fulfills this role.

All experiments were conducted in vivo, in immobilized, nonanesthetized animals (*19*). GGN was impaled from one (sometimes two) neurite(s) in the calyx or peduncle with a sharp microelectrode after blind search (*19*). Our results are based on 80 such recordings in 55 animals. GGN, is a nonspiking neuron with a resting potential of –51 ± 5 mV. It responded to every odor tested (fig. S4) with graded potentials composed of superimposed excitatory and inhibitory postsynaptic potentials (E- and I-PSPS, respectively) [Fig. 1B (i)]. Overall, excitation dominated, and depolarization grew with stimulus concentration (tested over a million-fold) with a peak depolarization of 15 to 20 mV above rest [Fig. 1, B and C (i)]. The oscillatory power (15 to 30 Hz) of the mushroom body local field potential (LFP) increased with odor concentration [Fig. 1B (iii and iv)] (*11*). Simultaneously recorded LFP (power) and V_{GGN} ($\int Vdt$) covaried over this concentration range (n = 364 pairs, linear fit, r = 0.93) [Fig. 1C (ii)]. In

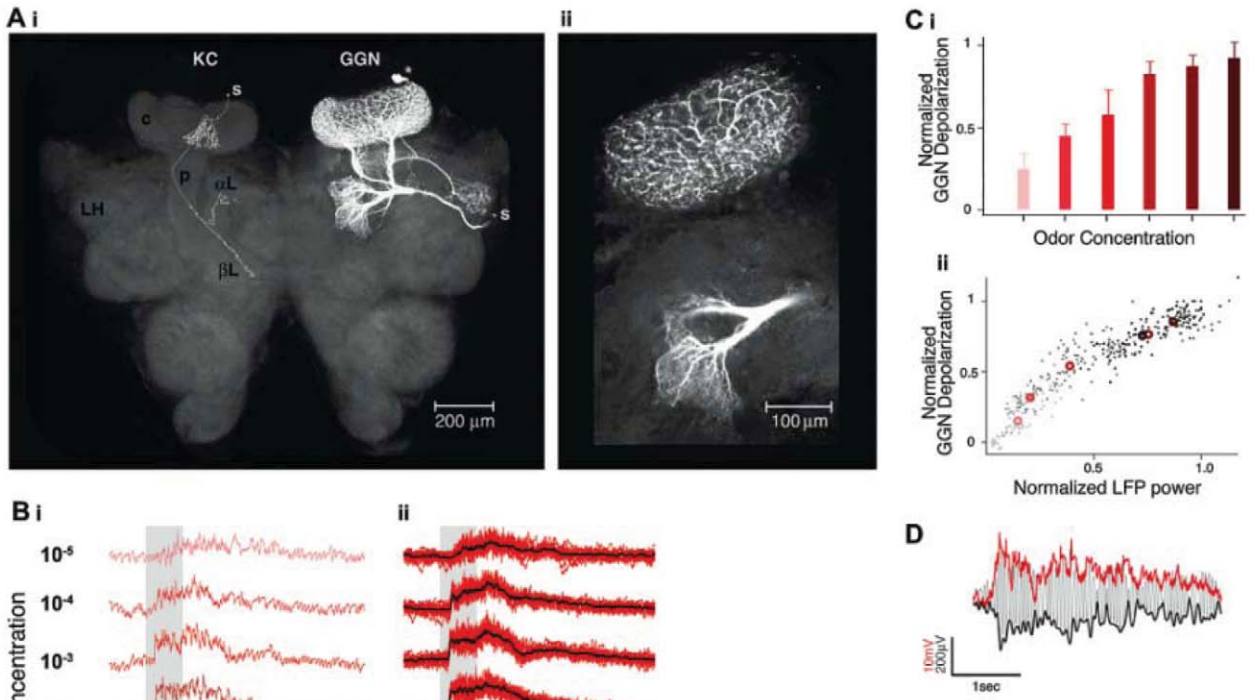

Fig. 1. Morphology of and responses to odors by GGN. (**A**) (i) GGN intracellular fill (5% biocytin) reveals extensive arbor in mushroom body calyx (c), α lobe (αL), and in the lateral horn (LH). (Left) Pasted intracellularly labeled KC image for comparison. p, pedunculus; β-L, β lobe; s, soma. (ii) Higher magnification of GGN axonal (top) and dendritic (bottom) fields. (**B**). GGN membrane voltage: (i) single traces, (ii) 14 superimposed trials (average in black) and mushroom body LFP, (iii) single trials, and (iv) spectral power in 10- to 30-Hz band (single trials are gray; average is black) recorded simultaneously in response to octanol concentration series (gray bar is odor). (**C**) (i) Cumulative integral of GGN voltage (mean and SD) in (B) (ii) against odor concentration. (ii) Scatter plot of LFP power versus GGN intracellular voltage integral over response duration. Dots represent single trials for each odor concentration (five experiments); circles represent averages for each concentration; light-to-dark gray or red shows increasing odor concentration. (**D**) GGN intracellular voltage (single trial, red) superimposed with simultaneous LFP (gray) and corresponding negative LFP envelope (black).

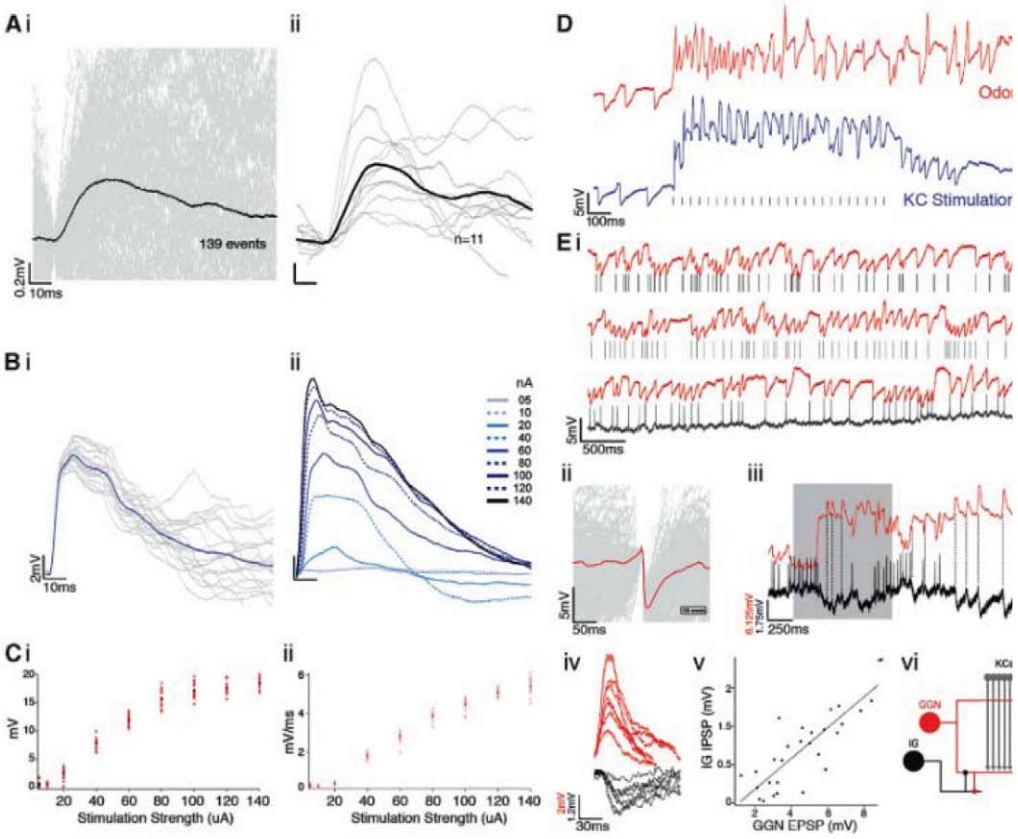

Fig. 2. Synaptic inputs to GGN. (**A**) (i) Single (gray) and averaged (black) EPSPs caused by a single KC on GGN; spike-triggered sweeps and average (STA) from dual intracellular recording from KC soma and GGN neurite. KC spikes caused by direct current injection in KC soma. (ii) STA of 11 different KC-GGN pairs (gray), and their own average (black). Calibration as in (i). (**B**) (i) Compound GGN EPSP caused by extracellular stimulation of KCs (gray represents single sweeps; blue shows average). (ii) Same as (i), across stimulation intensities. Calibration as in (i). (**C**) Peak amplitude (i) and slope (ii) of compound EPSPs in (B) as a function of KC stimulation amplitude. (**D**) Comparison of GGN responses to odor (red) and 20-Hz KC stimulation train (blue). (**E**) Simultaneous intradendritic recordings of GGN (red) and of the source of its large, discrete IPSPs (neuron named IG, gray) (i) Spontaneous activity. (ii) Spike-triggered single (gray) and averaged (red) sweeps of GGN intracellular voltage, triggered on IG spikes. (iii) Response of simultaneously recorded GGN and IG to odor (gray bar), indicating antagonistic membrane potential fluctuations. Stippled lines indicate IG hyperpolarizing potentials coinciding with GGN EPSPs. (iv) Single sweeps of IG membrane potential (gray) triggered on GGN EPSPs, showing nonspiking, inhibitory synaptic transfer. (v) IG IPSP (absolute value) against GGN EPSP amplitude, showing positive correlation, which indicates graded release. (vi) Schematic of inferred KC-GGN-IG interconnectivity.

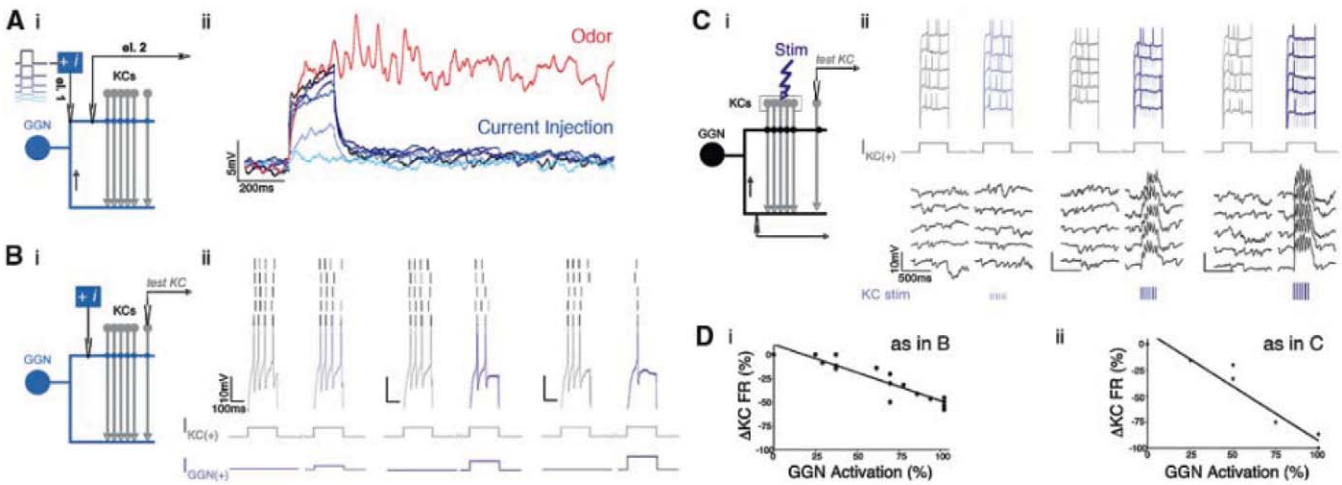

Fig. 3. Action of GGN on KC responses to direct or synaptic depolarization. (**A**) (i) Schematic of experiment in (ii): GGN is impaled simultaneously with two intraneurite microelectrodes: One is used to inject direct current and the other to record resulting transmembrane voltage. (ii) Calibration of intracellular current pulse amplitude needed to depolarize GGN membrane (blue series) to values comparable to odor-evoked response (red; octanol, concentration 0.1). Current injected in GGN: 1.5, 5.5, 13.5, 15.5, 17.5, and 19.5 nA. (**B**) (i) Schematic of experiment in (ii): one intracellular electrode is used to depolarize GGN [to values determined in (A) (ii)]; another is used to record and depolarize a single test-KC above spike threshold. (ii) Pairing GGN and test-KC depolarizations reduces current-induced firing of KCs, which indicates graded postsynaptic inhibitory action of GGN onto KCs. Current injected in GGN from left to right: 3.5, 11.5, and 19.5 nA. (**C**) Similar experiment to that in (B), but GGN direct depolarization has been replaced with electrical stimulation of many KCs, the firing of which causes GGN depolarization by synaptic excitation. Current-evoked firing of test-KC is again reduced by KC-induced GGN depolarization, in a graded manner (left to right). Stimulation intensity (from left to right): 10, 20, and 30 μA. Downward deflections in KC traces (blue) are stimulation artifacts. (**D**) Quantification of the relation between KC firing rate reduction and GGN depolarization for experiments in (B) [D (i) five KCs] and (C) [D (ii) three KCs)]. See fig. S6 for *x*-axis calibration in (D) (i). For each experiment in (D) (ii), stimulation strength is expressed as percent of the observed odor-induced depolarization in the same location.

addition, the instantaneous variations of V_{GGN} matched those of the LFP envelope (Fig. 1D). Hence, GGN output covaries with the global drive provided to the mushroom body.

We next tested the synaptic connections between KCs and GGN. Paired intracellular recordings were made from randomly chosen KC somata and a neurite of GGN. Superimposed V_{GGN} sweeps (n = 139) triggered from the spikes of one KC are shown in Fig. 2A (i), together with their average (black). The spike-triggered averages for this and 10 other pairs are shown in Fig. 2A (ii). They all revealed waveforms typical of unitary EPSPs, with latencies consistent with monosynaptic connections after accounting for KC spike conduction delay (n = 1302 events). Unitary EPSPs were 1 ± 0.50 mV (n = 11 KCs), with some nearing 2 mV. Using extracellular stimulation of KC somata, we could progressively recruit increasing numbers of KCs, and record increasingly large postsynaptic potentials in GGN, with a mean peak of 15 to 20 mV (Fig. 2, B and C, and fig. S5). These compound potentials had nonmonotonic falling phases, explained by an additional indirect inhibitory component (see below). We compared GGN responses evoked by odors—generated by periodic KC population input at the LFP frequency (~20 Hz) (red in Fig. 2D)—to ones evoked by direct extracellular electrical stimulation of KCs at the same frequency (blue in Fig. 2D). This comparison revealed a common depolarization and large unitary IPSPs, that counteracted depolarizing summation especially in the odor-evoked response (red trace, Fig. 2D). The discrete nature of these IPSPs suggested that they might originate from a single inhibitory interneuron. We found this putative interneuron (named IG, for "inhibitor of GGN"); its action potentials led with a consistent latency the IPSPs in GGN, whether at baseline or during responses to odors [Fig. 2E (i to iii)]. IG itself received phasic inhibitory inputs that each corresponded to phasic depolarizations (compound EPSPs) of GGN [Fig. 2E (iii and iv)]. The amplitudes of the E- and I-PSPS

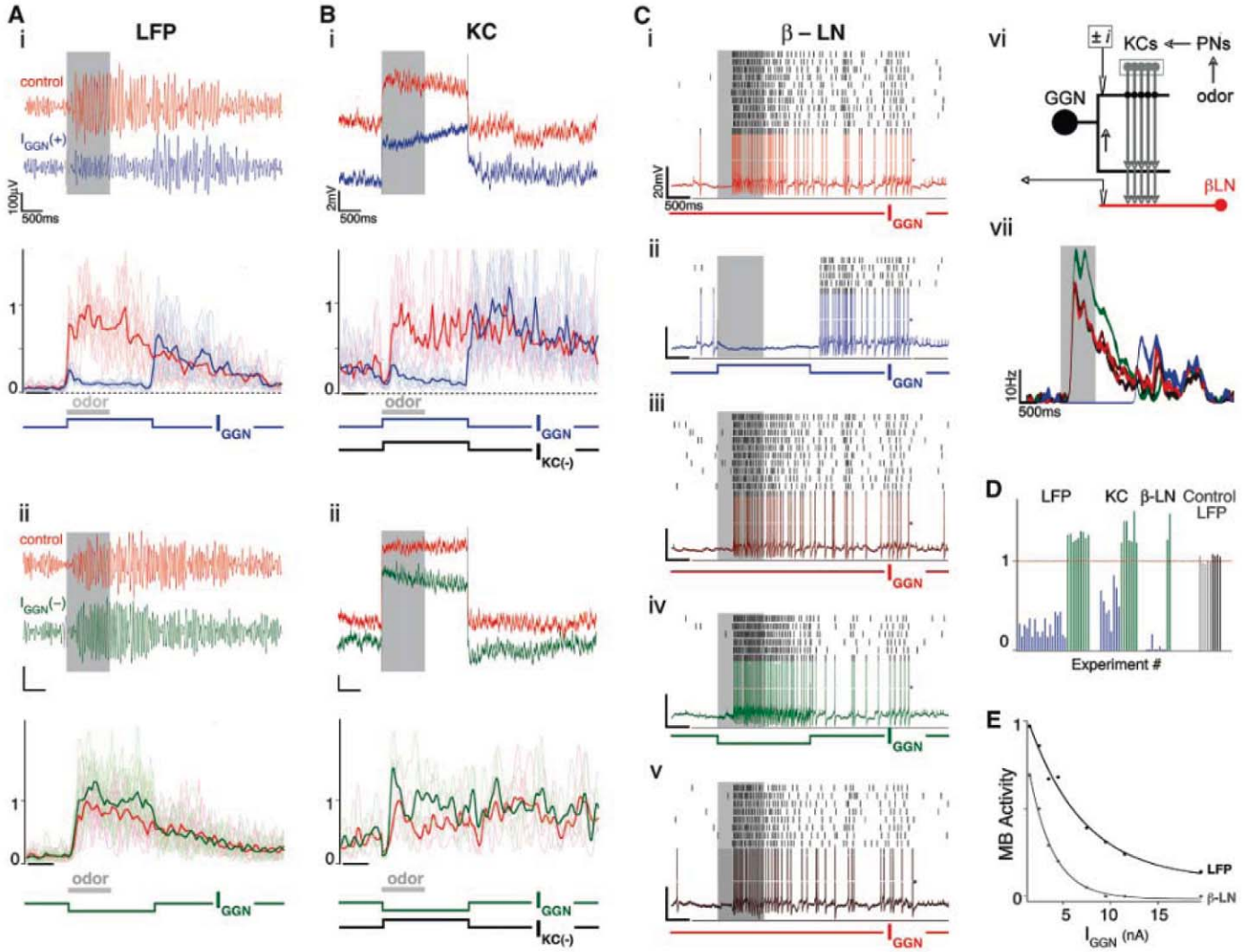

Fig. 4. Nature of GGN action on KCs and consequences on mushroom body output. (**A**) Action of GGN on odor-evoked LFP oscillations. (i) LFP traces (top) and spectral power in 10- to 30-Hz band (bottom) in control and GGN-depolarized conditions (20 interleaved trials; individual trials and averages are shown in lighter and darker colors, respectively). Note massive reduction in LFP amplitude and power. (ii) Same as (i) but with intracellular hyperpolarization of GGN. Note enhancement of LFP, indicating graded release of GABA at rest. (Artifacts caused by GGN current pulses are grayed out.) (**B**) Same as in (A), but with single KC intracellular membrane potential replacing LFP. Note the effect of GGN on KC membrane potential oscillations, indicative of postsynaptic shunt. [(B) (i): 18 trials, (B) (ii): 8 trials; (19).] (**C**) Intracellular recording of βLN responses to odors in control conditions [red in (i), (iii), and (v)] and during GGN current injections [depolarizing, blue in (ii); and hyperpolarizing, green in (iv)]. Asterisks: spikes have been clipped. (vi) Schematic of the experiment. (vii) Quantification of effect of GGN polarization on βLN instantaneous firing rate in response to odor (19). (**D**) Summary of all experiments in (A) to (C), as well as control experiments evaluating the effect of positive (light gray) or negative (dark gray) current injection from 50 to 100 µm outside of GGN on LFP, after withdrawal of GGN microelectrode. (**E**) Relation and fit between LFP or βLN outputs and depolarizing current injected in GGN. Note the steeper action on βLN.

in the two neurons were positively correlated [Fig. 2E (v)]. We conclude that GGN receives direct input from the KC population, that GGN is an inhibitory neuron [consistent with its GABA immunoreactivity (*16*)], that it releases neurotransmitter in a graded manner, and that GGN is itself reciprocally connected to a spiking inhibitory interneuron [Fig. 2E (vi)]. During an odor response, GGN receives both excitatory input (from KCs) and inhibitory input from IG, itself driven by KCs and possibly also antennal lobe projection neurons. Overall, the response of GGN to odors is depolarizing, but significantly less than the pure summation of KC-evoked EPSPs would suggest, at least in part, because of the action of IG on GGN. We now turn to the action of GGN on KCs.

Because GGN is a nonspiking neuron, we first performed double dendritic impalements (one for current injection, the other for voltage recording) and calibrated current injections to generate depolarizations commensurate with those evoked by odors (Fig. 3A and fig. S6). We could then assess the effect of depolarizing GGN on KC firing thresholds. A KC was impaled in the soma, and a short 70 to 300 pA pulse was injected to produce a few action potentials (n = 9 KCs, 85 trials) (Fig. 3B). This manipulation was subsequently combined with a depolarization of GGN, using increasing intensities [Fig. 3B (ii)]. In every pair, GGN depolarization beyond 5 mV reduced current-evoked firing of the recorded KC [Fig. 3, B and D (i)]. GGN thus exerts a direct, postsynaptic inhibitory effect on KCs. We then depolarized one KC (as in Fig. 3B) but depolarized GGN indirectly, by extracellular stimulation of other, unrelated KCs. A microelectrode was used to monitor simultaneously GGN membrane potential (Fig. 3C). As above, GGN depolarization counteracted current-induced spiking of the KC (indeed activating GGN synaptically was nearly twice as effective as via direct current injection) [Fig. 3, C and D (ii)]. Thus, GGN inhibits KCs postsynaptically in degrees correlated with membrane depolarization, itself a function of total KC population output.

We next sought to manipulate GGN during odor presentation. During these experiments, we monitored LFPs in the mushroom body calyx. These LFPs result mainly from synaptic currents caused (directly and indirectly) by PN input onto KCs, and are strongly oscillating in the 20-Hz range during odor stimulation (*12*). Current-evoked depolarization of GGN during odor stimulation caused a strong and immediate reduction of the odor-evoked LFP oscillatory power [Fig. 4A (i), and fig. S7]. GGN hyperpolarization had a weaker but opposite effect [Fig. 4, A (ii) and D]. Replacing LFPs with intracellular KC recordings, we observed that odor-evoked KC membrane-potential oscillations were similarly affected by GGN polarization (Fig. 4B). One simple interpretation is that GABA released by GGN depolarization causes a conductance increase in KCs, shunting the odor-evoked synaptic currents (Fig. 4B) and the current loops responsible for the LFPs (Fig. 4A). It is possible, however, that GGN also affects KCs by presynaptic action on PN axons. Thus, although the results in Figs. 3 and 4 indicate a postsynaptic (shunting) action of GGN onto KCs, we cannot exclude the possibility that GGN also inhibits KCs presynaptically, by action ono PN axons.

Thus far, we have assessed the effects of GGN only on individual KCs. Because thousands of KCs converge on a small number of extrinsic neurons in the output lobes of the mushroom body (*14*, *20*), we can use β-lobe neurons (βLNs) as assays of GGN action onto the KC population. We impaled βLNs in a dendrite (n = 10 βLNs) to monitor odor-evoked activity. Manipulating GGN membrane potential during the odor pulse changed the recorded βLN's responses to the odor (Fig. 4, C to E): A large GGN depolarization could silence the βLN [Fig. 4C (ii)]; conversely, hyperpolarizing GGN (moderately) increased βLN firing rate [Fig. 4C (iv and vii)]. The action of GGN on the βLN was not direct, for GGN had no effect on βLN firing evoked by current injection (fig. S8). Increasing depolarization of GGN during an odor caused a progressive reduction of βLN firing and LFP power (Fig. 4E), consistent with GGN's effect on current-induced firing of KCs (Fig. 3, B to D). Hence, GGN affects βLNs indirectly by its actions on the KC population output.

Using simultaneous intradendritic, intrasomatic, and extracellular recordings in vivo and in nonanesthetized animals, we assessed directly and specifically the functional connectivity and actions of a single, identifiable wide-field interneuron (GGN) in a structure implicated in learning and memory in insects. This single neuron forms the negative arm of a feedback loop by KCs onto themselves and thus regulates KC excitability adaptively, a function required to maintain the sparseness of odor representations by KCs (SOM text, figs. S1 to S3). The effects of this neuron are such that it can, on its own, shut down entirely the output of the mushroom body. Conversely, its hyperpolarization can increase mushroom body output. Because GGN is also under the influence of at least one other inhibitory neuron (IG), however, the gain of the KC negative-feedback loop can, in principle, itself be modulated. This attribute is highly desirable in a circuit involved in memory for it could allow the lowering or raising of KC firing threshold and thereby increase the probability of—and degrees of refinement in—object recognition during recall.

GGN lacks action potentials, a property common in insect interneurons (*21*). Although the implementation we described may be specific to invertebrate brains (see fig. S9 for intracellular recordings from the *Drosophila* analog of GGN, for example), the underlying principles may be widespread among circuits with equivalent requirements for sparse representations. GGN acts as an integrator, similar in function to that of a population of spiking neurons: the membrane potential of GGN can be thought of as equivalent to the poststimulus time histogram of a population of spiking interneurons, smoothed with an EPSP-like kernel. Just as functionally equivalent feed-forward inhibitory loops have been found in insect mushroom bodies (*7*) and in mammalian piriform cortex (*22*), we may find in mammalian olfactory cortex a global negative-feedback loop comparable to the one we describe here.

References and Notes

1. D. Marr, *J. Physiol.* **202**, 437 (1969).
2. B. A. Olshausen, D. J. Field, *Curr. Opin. Neurobiol.* **14**, 481 (2004).
3. P. Kanerva, *Sparse Distributed Memory* (MIT Press, Cambridge, MA, 1988).
4. W. E. Vinje, J. L. Gallant, *Science* **287**, 1273 (2000).
5. M. P. Young, S. Yamane, *Science* **256**, 1327 (1992).
6. R. H. Hahnloser, A. A. Kozhevnikov, M. S. Fee, *Nature* **419**, 65 (2002).
7. J. Perez-Orive *et al.*, *Science* **297**, 359 (2002).
8. M. R. DeWeese, M. Wehr, A. M. Zador, *J. Neurosci.* **23**, 7940 (2003).
9. G. C. Turner, M. Bazhenov, G. Laurent, *J. Neurophysiol.* **99**, 734 (2008).
10. B. M. Broome, V. Jayaraman, G. Laurent, *Neuron* **51**, 467 (2006).
11. M. Stopfer, V. Jayaraman, G. Laurent, *Neuron* **39**, 991 (2003).
12. G. Laurent, M. Naraghi, *J. Neurosci.* **14**, 2993 (1994).
13. O. Mazor, G. Laurent, *Neuron* **48**, 661 (2005).
14. S. Cassenaer, G. Laurent, *Nature* **448**, 709 (2007).
15. R. A. Jortner, S. S. Farivar, G. Laurent, *J. Neurosci.* **27**, 1659 (2007).
16. B. Leitch, G. Laurent, *J. Comp. Neurol.* **372**, 487 (1996).
17. A. H. Watson, M. Burrows, *J. Comp. Neurol.* **240**, 219 (1985).
18. X. Liu, R. L. Davis, *Nat. Neurosci.* **12**, 53 (2009).
19. Materials and methods are available as supporting material on *Science* Online.
20. Y. Li, N. J. Strausfeld, *J. Comp. Neurol.* **387**, 631 (1997).
21. M. Burrows, M. V. Siegler, *J. Physiol.* **285**, 231 (1978).
22. C. Poo, J. S. Isaacson, *Neuron* **62**, 850 (2009).

Acknowledgments: We thank G. Turner for help with early locust experiments; V. Jayaraman, G. Turner, and G. Jefferis for help with the *Drosophila* recordings (fig. S9); and the Caltech Imaging Center for use of a confocal microscope. This work was funded by the National Institute for Deafness and Communications Disorders (G.L.), the Lawrence Hanson Fund (G.L.), the Max Planck Society (G.L.), the Office of Naval Research (grants N00014-07-1-0741 and N00014-10-1-0735 to G.L. and S.C.), a grant from Evolved Machines, Inc. (G.L. and M.P.), a Research Council of UK Academic Fellowship, and a grant from the Biotechnology and Biological Sciences Research Council (UK grant number BB/F005113/1) (T.N.).

Supporting Online Material

www.sciencemag.org/cgi/content/full/332/6030/721/DC1
Materials and Methods
SOM Text
Figs. S1 to S9
References

17 December 2010; accepted 28 March 2011
10.1126/science.1201835

Relationship Between Clinical Signs and Transmission of an Infectious Disease and the Implications for Control

Bryan Charleston,[1]* Bartlomies M. Bankowski,[1] Simon Gubbins,[1] Margo E. Chase-Topping,[2] David Schley,[1] Richard Howey,[2] Paul V. Barnett,[1] Debi Gibson,[1] Nicholas D. Juleff,[1] Mark E. J. Woolhouse[2]

Control of many infectious diseases relies on the detection of clinical cases and the isolation, removal, or treatment of cases and their contacts. The success of such "reactive" strategies is influenced by the fraction of transmission occurring before signs appear. We performed experimental studies of foot-and-mouth disease transmission in cattle and estimated this fraction at less than half the value expected from detecting virus in body fluids, the standard proxy measure of infectiousness. This is because the infectious period is shorter (mean 1.7 days) than currently realized, and animals are not infectious until, on average, 0.5 days after clinical signs appear. These results imply that controversial preemptive control measures may be unnecessary; instead, efforts should be directed at early detection of infection and rapid intervention.

Strategies to control the spread of many infectious diseases rely wholly or partly on reactive measures implemented upon the detection of a clinical case. Examples include human influenza, diphtheria, pertussis, pneumonic plague, severe acute respiratory syndrome (SARS), and viral haemorrhagic fevers, as well as major animal diseases such as classical swine fever, foot-and-mouth disease, highly pathogenic avian influenza, and swine vesicular disease (*1*). For these diseases, once a clinical case is detected the affected individual may be treated or isolated or (for livestock diseases) culled with the aim of limiting opportunities for further transmission. In some circumstances, prophylaxis, quarantine, or culling of at-risk individuals (usually those in close physical proximity to a case or identified by contact tracing) is also implemented. Such measures are often contentious (*2*, *3*) and are defended on the grounds of their perceived contribution to reducing transmission rates and so protecting public or animal health.

The success of reactive disease control strategies has previously been shown to depend on the timing of the onset of infectiousness relative to the onset of detectable clinical signs (*4*). The key variable is θ, the fraction of transmission that occurs during the overlap of the incubation period (time from exposure to onset of signs) and the infectious period. If θ is small, then reactive control targeted only at clinical cases may be effective. For moderate values of θ (or for low values of θ if there is a substantial delay implementing control measures), additionally targeting at-risk individuals may be warranted. However, if θ is too large—if most transmission occurs before disease is apparent (such as in the case of HIV/AIDS)—reactive control measures will be ineffective. Three successful disease eradication campaigns—smallpox, SARS, and rinderpest—were facilitated by low θ values (*4*, *5*).

The means and distributions of incubation, latent, and infectious periods are key determinants of θ and have been estimated for many infectious diseases (*6*–*9*), but the value of θ also depends on their joint distributions, which are less well studied. Here, we report how we quantified these distributions for foot-and-mouth disease (FMD) in cattle and assess the implications of the results for the design of control strategies. We go on to consider the relevance of the findings to other infectious diseases.

Foot-and-mouth disease virus (FMDV) is a RNA virus of the Picornaviridae family (a group containing a number of animal and human pathogens) that naturally infects cattle and other livestock species, causing an acute illness characterized by fever, nasal discharge, and lesions on the tongue and/or feet. It is one of the world's most important animal pathogens, responsible for huge global losses to livestock production and trade, as well as frequent and highly disruptive large-scale epidemics (*10*).

We carried out an experimental study of direct transmission of FMDV between pairs of cattle kept indoors in close proximity for 8 hours, with room temperature, humidity, and air circulation optimized during pilot studies for transmission to occur. Briefly, eight "source" cows were successfully exposed to infection by direct contact with cattle injected with the FMDV serotype O isolate circulating in the UK in 2001, and transmissions to naïve cows were attempted at 2-day intervals post exposure (*11*). This design allowed us to study individual transmission events occurring at specific time points after exposure, in contrast to previous studies that estimated net FMDV transmission rates for small groups of animals in contact for extended periods (*12*, *13*).

There were only eight successful transmissions (from seven of the cows) in 28 attempts, even though we detected FMDV in blood (viraemia), nasal fluid (NF), and/or oesophageal-pharyngeal fluid (OPF) on all but one occasion (table S1). We quantified a set of 23 virological, immunological, and clinical variables for each of the source cows (table S2). From these, we created composite variables using the data reduction method nonmetric multidimensional scaling (NMS) (*11*). NMS score was strongly associated with infectiousness (P = 0.0002) (Fig. 1A and table S3). Moreover, NMS axis 1 and 2 together provided an informative representation of the sequence of events that occur during FMDV infection and, crucially, how these relate to infectiousness (Fig. 1B). We depict these in relation to a reference time point, day P, which corresponds to the day of peak NMS axis 1 score for each infected cow. There is an initial quiescent phase lasting 1 to 4 days; previous studies suggest the variation is due to differences in the infectious dose received (*14*). Day P-1 is marked by the first appearance of high levels of viraemia. On day P, there is a rapid cascade of events including the detection of live virus in nasal fluid and the onset of clinical signs and a type-1 interferon response, all of which are heavily weighted components of NMS axis 1 (fig. S1). On day P+1, there is a decrease in the amount of detectable virus because a sharp peak in the level of type-1 interferon prevents virus from infecting additional epithelial cells where most replication occurs (*15*), although some clinical signs persist. From day P+2 onwards, only low levels of virus and interferon are detectable, but FMDV-specific antibodies are present. Six out of eight successful transmissions occurred on day P, a highly significant association (exact P = 0.0064). These results suggest that conditions promoting transmission exist for only a brief period and clearly show that infectiousness is a complex phenomenon related not just to virus dynamics but also to host responses and clinical signs, which is consistent with a general but rarely tested expectation that disease signs may be functionally linked to infectiousness (*16*).

The experimental data allowed us to make formal estimates of the infectious period, the latent period, and the incubation period; clinical signs were defined here as any visible lesions or body temperature above 39.5°C. We did this using a Bayesian framework that allowed us to draw inferences about the unobserved latent and infectious periods according to the outcome of each transmission attempt. The mean latent and incubation periods were estimated to be 4.6 days [95% credible interval (CI): 3.1 to 7.2 days] and 4.1 days (2.9 to 5.9 days), respectively (Fig. 2, A and B). These variables were significantly correlated (correlation ρ = 0.77, 95% CI: 0.30 to 0.96) (Fig. 2C), and the mean infectious period was short: 1.7 days (0.3 to 4.8 days) (Fig. 2D). Both of these results are consistent with the NMS analysis. The statistical model was a good description of the transmission data (Fig. 2E).

Previous estimates of the latent and infectious periods for FMDV have used indicators such as the detection of virus in blood, NF, or OPF as

[1]Institute for Animal Health, Pirbright Laboratory, Ash Road, Woking, Surrey GU24 0NF, UK. [2]Centre for Immunity, Infection and Evolution, University of Edinburgh, Ashworth Laboratories, Kings Buildings, West Mains Road, Edinburgh EH9 3JT, UK.

*To whom correspondence should be addressed. E-mail: bryan.charleston@bbsrc.ac.uk

proxy measures of infectiousness (*13*) rather than directly demonstrating transmission to another animal. Using these measures from our experimental data gave significantly shorter estimates of the mean latent period (0.5 to 2.7 days) (Fig. 2A) and much longer estimates of the mean infectious period (4.2 to 8.2 days) (Fig. 2D). These estimates are very similar to the results of a recently published meta-analysis of data on FMDV serotype O in cattle (*17*). Additionally, when we used proxy measures of infectiousness the latent period appeared longer than the incubation period [whereas the transmission data suggested it was shorter (Fig. 2, A and 2)], and the correlation between latent and incubation periods was weaker or entirely absent (Fig. 2C). Similar proxies for infectiousness are routinely used in studies of not just FMDV but many other human and animal pathogens (*6*–*8*).

Extending previous analyses (*4*) to allow for jointly distributed latent and incubation periods, the proportion of transmission occurring before the onset of clinical signs is given by

$$\theta = \frac{\int_0^{\infty}\int_0^{\tau}\left\{\int_{\tau}^{\infty} f(E,C)\,\mathrm{d}C\right\}\left\{\int_{\tau-E}^{\infty} g(I)\,\mathrm{d}I\right\}\mathrm{d}E\,\mathrm{d}\tau}{\int_0^{\infty}\int_0^{\tau} f_E(E)\left\{\int_{\tau-E}^{\infty} g(I)\,\mathrm{d}I\right\}\mathrm{d}E\,\mathrm{d}\tau} \quad (1)$$

where $f(E,C)$ is the joint probability distribution function (PDF) for the latent and incubation periods, $f_E(E)$ is the marginal PDF for the latent period, and $g(I)$ is the PDF for the infectious period [see (*11*) for derivation of this expression]. As shown in Fig. 3A, with parameters based on virus isolation in blood, NF, or OPF, the median estimate of θ was 0.43, 0.27, or 0.44, respectively (see Fig. 3A for PDFs), with the possibility that a cow could be infectious for several days before showing clinical signs. Using a direct measure of infectiousness, the median estimate of θ was only 0.13 (Fig. 3A), and an animal that was infectious before clinical onset would most likely be so for only a few hours.

Sensitivity analysis of Eq. 1 indicates that the effects reported here for FMD could potentially apply to any acute infectious disease (*11*). The crucial factor is whether the variance of the timing of the onset of infectiousness relative to signs is large in comparison with the infectious period. For human influenza, for example, the value of θ has been reported as 0.3 to 0.5 (*4*), yet several authors have suggested, on the basis of observational data, that it could be much lower (*8*, *9*, *18*). Resolving this debate for influenza or any other acute infection will require experimen-

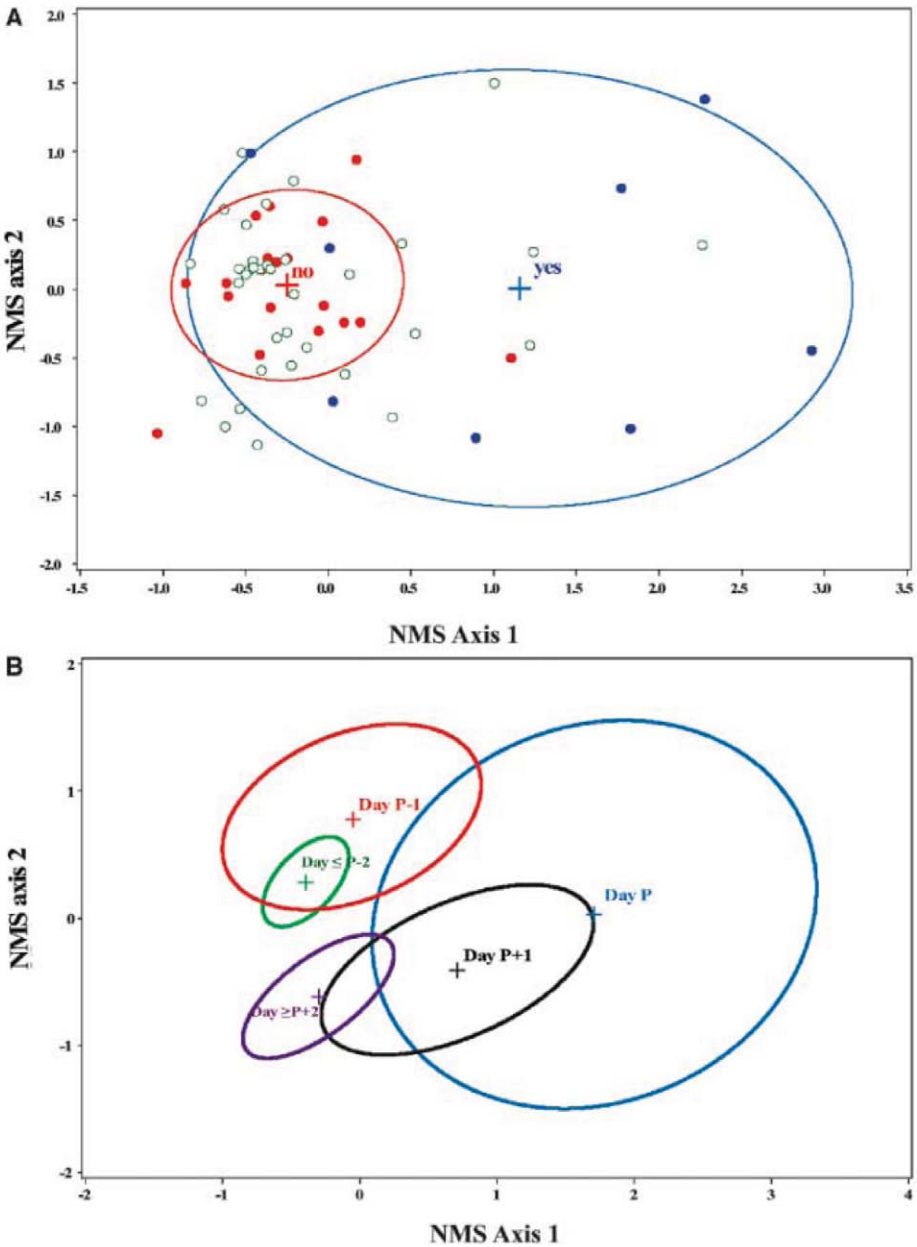

Fig. 1. NMS ordination of transmission data. The NMS final solution was two dimensional and explained 86.1% of the variation in FMD transmission success. Correlations between variables used (table S2) and NMS scores are shown in fig. S1. (**A**) Blue circles represent days when transmission occurred, red circles when no transmission occurred, and green open circles when transmission was not attempted. Ovals indicate the mean ±1 SD bivariate interval for successful and unsuccessful transmission attempts only. (**B**) Ovals indicate the mean ±1 SD bivariate interval for each day, where day P is the day of peak NMS axis 1 score. Days ≥P+2 and ≤P−2 have been grouped.

tal and/or epidemiological studies of transmission in natural hosts designed to quantify transmission rates at different times after exposure.

The combined effect of the differences between our findings and previous work based on proxy measures of infectiousness is that cattle infected with FMDV are substantially less likely to be infectious before showing clinical signs than is currently realized, implying that the need for reactive control measures targeted at "at-risk" farms, notably pre-emptive culling (*19*), has been overestimated. The likelihood of transmission is dramatically decreased if control can be implemented just 24 hours earlier; this effect is greatly underestimated if proxy measures of infectiousness are used (Fig. 3B). This result provides strong support for investment in the development of practical tools for preclinical diagnosis (*20*, *21*) because the onset of detectable viraemia typically occurs at ≥1 day before infected cows become infectious and/or show clinical signs (Fig. 1B and table S1). The same argument also suggests that the penalties for delayed detection of cases and/or implementation of control are even greater than is currently realized (Fig. 3B). Also, for the future our results suggest that prophylaxis, such as antiviral therapy, targeted at contacts could be used preclinically with greater confidence of preventing transmission. Lastly, we suggest that there is a need for more robust empirical evidence on relationships between clinical signs and infectiousness to underpin policy, not only for FMDV but also other acute infections for which reactive

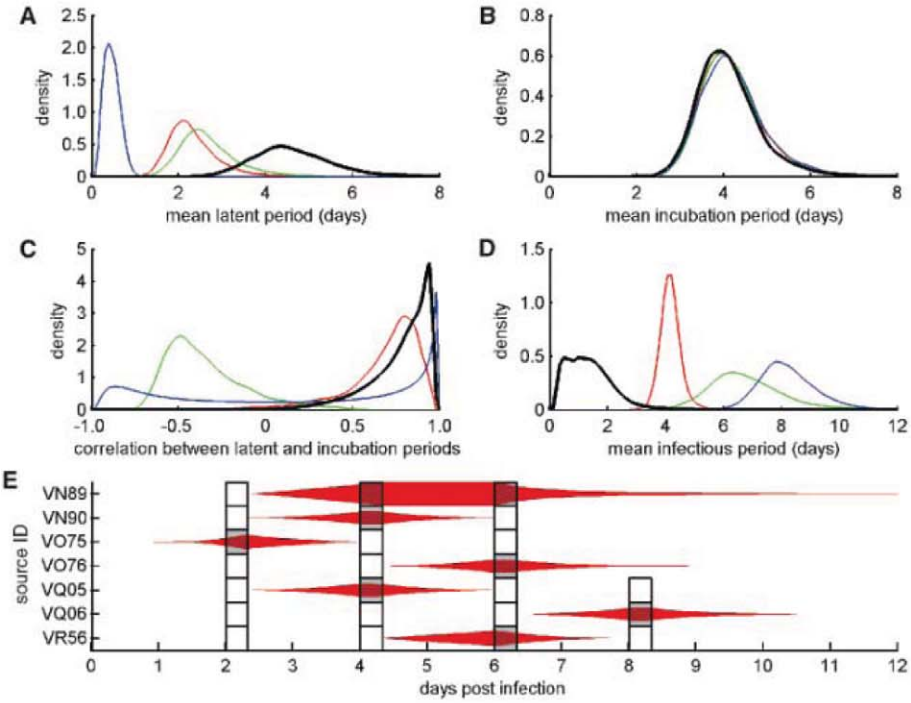

Fig. 2. Bayesian analysis of FMDV transmission data. (**A** to **D**) Marginal posterior densities for the mean duration (in days) of the (A) latent and (B) incubation periods, (C) the correlation between the latent and incubation periods, and (D) the infectious period. Results for the analysis based on transmission attempt outcome only (black lines) were compared with results for virus isolation from NF (green lines), blood (red lines), or OPF (blue lines). There were significant ($P < 0.05$) differences for latent period (blood and OPF), latent period minus incubation period (blood and OPF), their correlation (NF), and infectious period (NF, blood, and OPF). (**E**) Posterior estimates for the (unobserved) latent and infectious periods in relation to the experimental transmission attempts (indicated by boxes marked gray if the attempt was successful and white if it was not). The thickness of the red shapes indicates the proportion of Markov chain Monte Carlo samples for which an animal was infectious at that time (with the symbol occupying the full width of the box if it was infectious for all samples). Cow VR57 was excluded from these analyses because although infected, it was apparently never infectious.

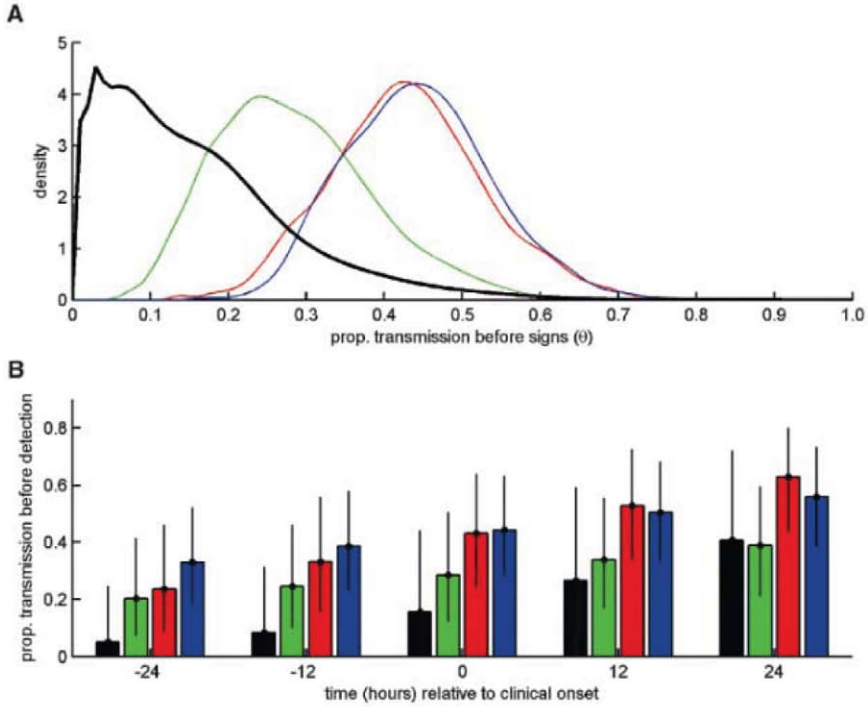

Fig. 3. Implications of results for detection and control of FMDV. (**A**) Marginal posterior density for the proportion of transmission that occurs before the onset of clinical signs, θ. (**B**) Posterior means (bars) and 95% credible intervals (error bars) for the proportion of transmission that occurs before detection assuming infected animals are detected at −24, −12, 0, +12, or +24 hours relative to the onset of clinical signs. In each plot, results are shown for the analysis based on transmission attempt outcome only (black) and virus isolation from NF (green), blood (red), or OPF (blue).

measures are an important component of control strategies.

References and Notes

1. See World Health Organization (WHO) Factsheets, http://www.who.int/mediacentre/factsheets/en/ (accessed 21 April 2011) and World Organisation for Animal Health (OIE) Animal diseases data, www.oie.int/animal-health-in-the-world/oie-listed-diseases-2011 (accessed 21 April 2011).
2. J. Zinsstag, M. G. Weiss, *Science* **294**, 477 (2001).
3. C. S. Tracey, E. Rea, R. E. G. Upshur, *BMC Public Health* **9**, 470 (2009).
4. C. Fraser, S. Riley, R. M. Anderson, N. M. Ferguson, *Proc. Natl. Acad. Sci. U.S.A.* **101**, 6146 (2004).
5. G. R. Scott, in *Virus Diseases of Food Animals,* E. P. J. Gibbs, Ed. (Academic Press, New York, 1981), vol. 2, pp. 401–425.
6. M. Lipsitch *et al.*, *Science* **300**, 1966 (2003).
7. F. Carrat *et al.*, *Am. J. Epidemiol.* **167**, 775 (2008).
8. L. L. H. Lau *et al.*, *J. Infect. Dis.* **201**, 1509 (2010).
9. T. Yamagishi *et al.*, *Jpn. J. Infect. Dis.* **63**, 327 (2010).
10. D. J. Paton, D. P. King, N. J. Knowles, J. Hammond, *Vet. Rec.* **166**, 569 (2010).
11. Materials and methods are available as supporting material on *Science* Online.
12. K. Orsel, A. Bouma, A. Dekker, J. A. Stegeman, M. C. M. de Jong, *Prev. Vet. Med.* **88**, 158 (2009).
13. K. Orsel, M. C. M. de Jong, A. Bouma, J. A. Stegeman, A. Dekker, *Vaccine* **25**, 327 (2007).
14. R. Howey *et al.*, *J. R. Soc. Interface* **6**, 835 (2009).
15. J. Chinsangaram, M. E. Piccone, M. J. Grubman, *J. Virol.* **73**, 9891 (1999).
16. G. C. Williams, R. M. Nesse, *Q. Rev. Biol.* **66**, 1 (1991).
17. F. O. Mardones, A. Perez, J. Sanchez, M. Alkhamis, T. E. Carpenter, *Vet. Res.* **41**, 45 (2010).
18. E. Patrozou, L. A. Mermel, *Public Health Rep.* **124**, 193 (2009).
19. M. J. Tildesley, P. R. Bessell, M. J. Keeling, M. E. J. Woolhouse, *Proc. Biol. Sci.* **276**, 3239 (2009).
20. D. A. King, C. Peckham, J. K. Waage, J. Brownlie, M. E. J. Woolhouse, *Science* **313**, 1392 (2006).
21. D. J. Paton, K. J. Sumption, B. Charleston, *Philos. Trans. R. Soc. London Ser. B* **27**, 2657 (2009).

22. We thank L. Fitzpatrick, C. Randal, and M. Jenkins for their assistance with the handling and management of experimental animals; P. Hamblin and P. Keel for help and advice with serology assays; L. Reid, M. Windsor, and S. Cox for assistance with laboratory assays; S. Alexandersen, D. Paton, and N. Savill for valuable advice on study design; and B. Grenfell, M. Keeling, M. de Jong, A. Graham, C. Dye, and four anonymous referees for insightful comments. The work was funded by the Biotechnology and Biological Sciences Research Council (grant BBSB00549), UK. B.C. and P.V.B. are Jenner Investigators. S.G. and D.S. acknowledge funding from the Biotechnology and Biological Sciences Research Council (grant BBSEI00001444). M.E.C.T. is partly supported by the Wellcome Trust.

Supporting Online Material

www.sciencemag.org/cgi/content/full/332/6030/726/DC1
Materials and Methods
SOM Text
Figs. S1 and S2
Tables S1 to S5
References

2 November 2010; accepted 18 March 2011
10.1126/science.1199884

Neuronal GPCR Controls Innate Immunity by Regulating Noncanonical Unfolded Protein Response Genes

Jingru Sun, Varsha Singh, Rie Kajino-Sakamoto, Alejandro Aballay*

The unfolded protein response (UPR), which is activated when unfolded or misfolded proteins accumulate in the endoplasmic reticulum, has been implicated in the normal physiology of immune defense and in several human diseases, including diabetes, cancer, neurodegenerative disease, and inflammatory disease. In this study, we found that the nervous system controlled the activity of a noncanonical UPR pathway required for innate immunity in *Caenorhabditis elegans*. OCTR-1, a putative octopamine G protein–coupled catecholamine receptor (GPCR, G protein–coupled receptor), functioned in sensory neurons designated ASH and ASI to actively suppress innate immune responses by down-regulating the expression of noncanonical UPR genes *pqn/abu* in nonneuronal tissues. Our findings suggest a molecular mechanism by which the nervous system may sense inflammatory responses and respond by controlling stress-response pathways at the organismal level.

Endoplasmic reticulum (ER) stress has been linked to several human diseases, including diabetes, cancer, neurodegenerative disease, and inflammatory disease (*1*–*3*). The ER has developed specific signaling pathways, known as the unfolded protein response (UPR), to cope with ER stress and restore ER homeostasis. Recent studies indicate that increased demand on protein folding in the ER, which may occur during bacterial infections, must be alleviated by UPR pathways for a complete immune response to be mounted (*4*–*8*).

We took advantage of the simple nervous and immune systems of the nematode *Caenorhabditis elegans* to investigate the role of the nervous system in the organismal control of pathways involved in innate immune responses. Three sensory neurons (AQR, PQR, and URX) are known to regulate resistance to pathogen infections by controlling the activation of a p38 mitogen-activated protein kinase (MAPK) pathway and the *C. elegans* avoidance to certain pathogens (*9*, *10*). In addition, a range of chemosensory neurons that penetrate the cuticle and directly detect and respond to different environmental cues have the potential to control innate immune responses.

To elucidate the molecular mechanism by which these neurons regulate innate immunity in response to pathogen infection, we first determined the susceptibility to the human opportunistic pathogen *Pseudomonas aeruginosa* of *octr-1(ok371)* animals, which lack a G protein–coupled catecholamine receptor normally expressed in the cilia of neurons located in sensory openings, including ASH, ASI, AIY, and dopaminergic ADE/CEP neurons (*11*, *12*). *octr-1(ok371)* animals exhibited enhanced resistance to killing by *P. aeruginosa* (Fig. 1A), which suggests that the loss of OCTR-1 signaling increases the general immune function of the nematodes. We observed no difference in survival between *octr-1(ok371)* and wild-type (WT) animals that were fed heat-killed *P. aeruginosa* or *Escherichia coli* (Fig. 1B and fig. S1). Thus, *octr-1* mutation affects the immune response to living pathogenic bacteria without altering the basic life span of the nematodes.

Because pathogen avoidance is part of the *C. elegans* defense response to *P. aeruginosa* (*9*), we examined the susceptibility to *P. aeruginosa*–mediated killing of *octr-1(ok371)* animals on agar plates that were completely covered in bacteria, a condition that eliminates pathogen avoidance. *octr-1(ok371)* animals died at a slower rate than did WT animals (Fig. 1C), indicating that pathogen avoidance does not play a role in *octr-1(ok371)*–enhanced resistance to *P. aeruginosa.* In addition, the magnitude of pathogen avoidance of *octr-1(ok371)* and WT animals was similar (Fig. 1D). The enhanced resistance of *octr-1(ok371)* to *S. enterica* (fig. S2), a pathogen that does not elicit an avoidance behavior (*13*), further supports the function of OCTR-1 in the regulation of immune responses.

Certain mutants resistant to pathogen infection exhibit resistance to pathogen accumulation (*14*). Therefore, we examined whether *octr-1* mutation affected bacterial accumulation in the intestine. Compared to WT animals, *octr-1(ok371)* animals exhibited a similar accumulation pattern of *P. aeruginosa*/green fluorescent protein (GFP) or *S. enterica*/GFP (Fig. 1E and fig. S3). In addition, the number of bacterial cells in *octr-1(ok371)* animals was similar to that in WT animals (Fig. 1F and fig. S4). Thus, the bacterial load to which the animals were exposed was comparable, and reduced bacterial accumulation levels in the intestine did not contribute to the enhanced immunity of *octr-1(ok371)* animals, indicating that *octr-1(ok371)* animals exhibit enhanced endurance to *P. aeruginosa* infection.

To provide insights into the mechanism underlying the enhanced immunity of *octr-1(ok371)* ani-

Department of Molecular Genetics and Microbiology, Duke University Medical Center, Durham, NC 27705, USA.

*To whom correspondence should be addressed. E-mail: a.aballay@duke.edu

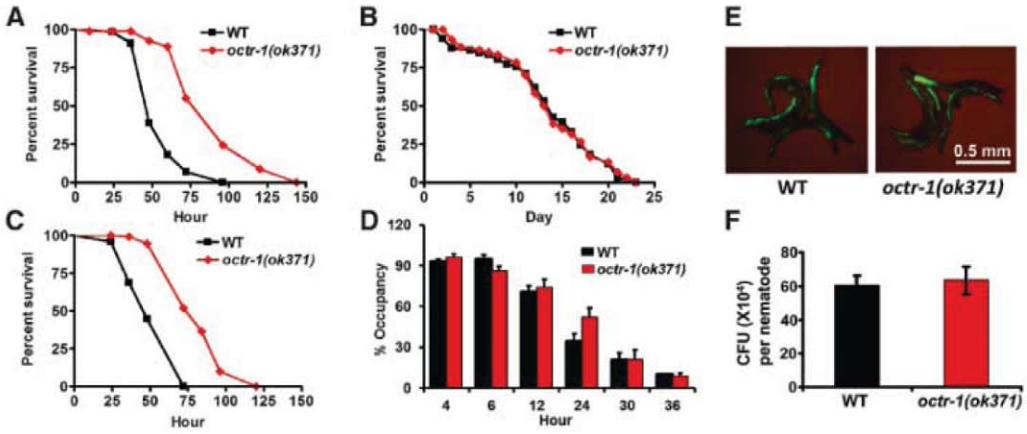

Fig. 1. *C. elegans* G protein–coupled receptor OCTR-1 is involved in immunity to *P. aeruginosa*. (**A**) WT and *octr-1(ok371)* animals were exposed to *P. aeruginosa*. (**B**) WT and *octr-1(ok371)* animals were exposed to heat-killed *P. aeruginosa*. (**C**) WT and *octr-1(ok371)* animals were exposed to a full lawn of *P. aeruginosa*. The survival graphs represent combined results of two independent experiments. $n = 90$ adult animals per strain. (**D**) Animals were placed on a small spot of *P. aeruginosa* in a 3.5-cm plate and monitored over time for their presence or absence on the lawn. The graph represents combined results of three independent experiments. $n = 60$ adult animals per strain. (**E**) WT and *octr-1(ok371)* animals were exposed to *P. aeruginosa* expressing GFP for 48 hours and then visualized using a MZ FLIII Leica stereomicroscope. (**F**) WT and *octr-1(ok371)* animals were exposed to *P. aeruginosa* expressing GFP for 48 hours, and the colony forming units (CFU) were quantified. Ten animals were used for each condition. The graph represents combined results of three independent experiments. Bars represent mean ± SEM.

mals, we used genome microarrays to find clusters of genes commonly misregulated in *octr-1(ok371)* relative to WT animals grown on live *P. aeruginosa*. OCTR-1–regulated genes previously known to be regulated by pathways involved in *C. elegans* innate immunity—including a DAF-2/DAF-16 insulin pathway, a p38/PMK-1 MAPK pathway, and a CED-1 pathway—were enriched (Fig. 2A and tables S1 and S2). Unexpectedly, the enhanced resistance to *P. aeruginosa*–mediated killing of *octr-1(ok371)* animals was suppressed by *pmk-1* RNA interference (RNAi) or mutation, but not by *daf-16* RNAi or mutation (Fig. 2, B and C, and fig. S5). Mutation in *sek-1*, which encodes for a MAPK kinase essential for PMK-1 activation, also suppressed the enhanced resistance of *octr-1(ok371)* animals (fig. S6). Consistent with the idea that derepression of PMK-1 transcriptional activity by lack of OCTR-1 signaling activates innate immunity, *octr-1(ok371)* animals exhibited higher levels of active PMK-1 than WT animals (Fig. 2D). Thus, in contrast to AQR, PQR, and URX neurons, which control not only PMK-1 activity but also pathogen avoidance, OCTR-1–expressing neurons control PMK-1 activity without affecting pathogen avoidance.

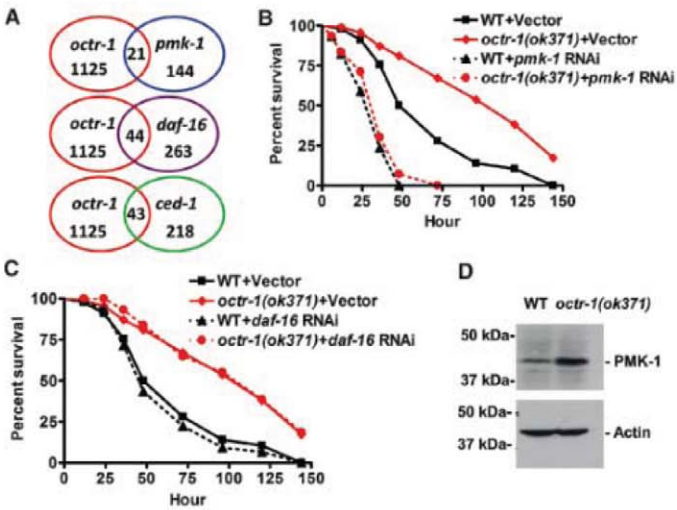

Fig. 2. OCTR-1 controls pathways required for *C. elegans* innate immunity. (**A**) Venn diagrams of genes that are up-regulated in *octr-1(ok371)* animals and positively regulated by *daf-16*, *pmk-1*, and *ced-1*. (**B**) WT and *octr-1(ok371)* animals grown on double-stranded RNA (dsRNA) for vector control or dsRNA for *pmk-1* were exposed to *P. aeruginosa*. (**C**) WT and *octr-1(ok371)* animals grown on dsRNA for vector control or dsRNA for *daf-16* were exposed to *P. aeruginosa*. The survival graphs represent combined results of two independent experiments. $n = 90$ adult animals per strain. (**D**) Active PMK-1 was detected in WT and *octr-1(ok371)* animals. Animals were grown at 20°C until 1-day-old adult and whole-worm lysates were used to detect active PMK-1 with an antibody against human p38 from Promega (Madison, WI). Actin was used as loading control. kDa, kilodaltons.

Among genes up-regulated in *octr-1(ok371)* animals, a group of 43 genes transcriptionally regulated by the phagocyte receptor CED-1 (*4*) was significantly enriched (Fig. 2A and table S2). Indeed, 7 out of 14 genes (Fig. 3A) that were up-regulated greater than twofold in *octr-1(ok371)* animals correspond to a family of *pqn* (*prionlike glutamine[Q]/asparagine[N]-rich domain-bearing protein*) genes that are controlled by CED-1 (*4*). Eleven genes in the *pqn* family are classified as *abu* (*activated in blocked unfolded protein response*) (*15*), because they are activated in *xbp-1* mutant animals when ER stress is induced by tunicamycin treatment. The *abu* genes encode UPR proteins that function in parallel with the canonical UPR pathway (*15*). We studied whether the most highly up-regulated *pqn* genes in *octr-1(ok371)* mutants could be induced by tunicamycin in an *xbp-1* mutant background. Indeed, *pqn-40*, *pqn-46*, *pqn-95*, and *pqn-5* genes were found to be activated by ER stress in animals with blocked UPR (table S3) and were named *abu-12*, *abu-13*, *abu-14*, and *abu-15*. *abu-1*, *-7*, *-8*, *-12*, *-13*, *-14*, and *-15* were significantly up-regulated in *octr-1(ok371)* animals (Fig. 3B), suggesting that the noncanonical UPR pathway is inhibited by OCTR-1. Consistent with this idea that *abu* genes encode noncanonical UPR proteins that may interact with abnormal ER client proteins, ABU-1 is retained in the ER by its transmembrane domain (*15*). Furthermore, with the exception of *pqn-46*, all *pqn/abu* genes that were up-regulated in *octr-1(ok371)* animals encode proteins that have both an ER signal sequence and a transmembrane domain (table S4).

Nine out of thirteen *pqn/abu* genes up-regulated in *octr-1(ok371)* animals are strongly expressed in the pharynx and the intestine, primary interfaces between host cells involved in immune responses and bacterial pathogens. Transgenic animals show expression of ABU-1::GFP in vesicular structures corresponding to the pharyngeal cells (*15*). In situ hybridizations completed as part of NEXTDB (The Nematode Expression Pattern Database) reveal expression of eight *pqn/abu* genes in the pharynx and the intestine from L3 to adult stages (http://nematode.lab.nig.ac.jp). To investigate the relation between the noncanonical UPR pathway and host responses to *P. aeruginosa* infection, we tested whether exposure to this pathogen would up-regulate *abu* genes. Indeed, *P. aeruginosa* exposure up-regulated *abu* genes (fig. S7 and table S5), indicating that the noncanonical UPR pathway may be required for *C. elegans* immune response against this pathogen. We then studied the resistance to *P. aeruginosa*–mediated

killing of WT and *octr-1(ok371)* animals where *abu* genes were inhibited by RNAi. Inhibition of *abu-1*, *-7*, *-8*, *-12*, and *-13* partially suppressed the enhanced immunity of *octr-1(ok371)* animals (Fig. 3C). RNAi-mediated inhibition of *abu* genes also resulted in enhanced susceptibility to *P. aeruginosa*–mediated killing (fig. S8).

Because *ced-1* is part of a pathway that transcriptionally controls the expression of *pqn/abu* genes (*4*), we asked whether *ced-1* mutation suppresses the enhanced immunity of *octr-1(ok371)* animals. The survival of *octr-1(ok371);ced-1(e1735)* animals was comparable to that of WT animals (Fig. 3D). We observed no additive effect of *abu* RNAi ablation on *octr-1(ok371);ced-1(e1735)* animals (Fig. 3E), confirming that *ced-1* and *abu* genes are part of the same pathway responsible for the enhanced resistance to pathogen infection of *octr-1(ok371)* animals. Furthermore, *abu-1* overexpression protected *octr-1(ok371);ced-1(e1735)* animals from *P. aeruginosa*–mediated killing (Fig. 3F). Thus, higher CED-1–mediated signaling is responsible for the enhanced resistance to *P. aeruginosa*–mediated killing in animals with impaired neural function due to mutation in *octr-1*.

To determine the specific foci of OCTR-1 activity involved in the control of innate immunity, we studied the pathogen susceptibility of *octr-1(ok371)* animals expressing *octr-1* under the control of the *sra-6* promoter, which drives the expression of *octr-1* to the ASH, ASI, and PVQ neurons (*16*). Expression of *octr-1* under the control of the *sra-6* promoter fully rescued the mutant phenotype of *octr-1(ok371)* animals (Fig. 4A), indicating that OCTR-1–expressing neurons regulate innate immunity in *C. elegans*. Consistent with this idea, OCTR-1 expression under the regulation of its own promoter also fully rescued the mutant phenotype of *octr-1(ok371)* animals (Fig. 4B). Because PVQ neurons do not express *octr-1*, our results suggest that ASH and ASI neurons negatively regulate innate immunity. Thus, we studied the susceptibility to *P. aeruginosa* of a strain in which mutation in *polyQ enhancer-1* promotes early onset degeneration of ASH neurons caused by polyQ toxicity (*17*). The strain lacking ASH neurons exhibited a significantly increased survival on *P. aeruginosa* (fig. S9), indicating that ASH neurons suppress innate immunity.

We confirmed that ASH and ASI neurons negatively regulate *abu* genes required for appropriate innate immunity by studying the gene expression levels of *abu-1*, *-12*, *-13*, *-14*, and *-15* in WT, *octr-1(ok371)*, and *octr-1(ok371)* animals expressing *octr-1* under the control of the *sra-6* promoter. Whereas the expression levels of *abu* genes in *octr-1(ok371)* animals are higher than those in WT animals, their expression levels are close to those of the wild type in *octr-1(ok371)* animals where *octr-1* expression in ASH and ASI was restored (Fig. 4C).

We have shown that OCTR-1–expressing neurons ASH and ASI negatively regulate innate immunity, at least in part, by controlling the expression of a family of genes that are part of a noncanonical UPR pathway regulated by the

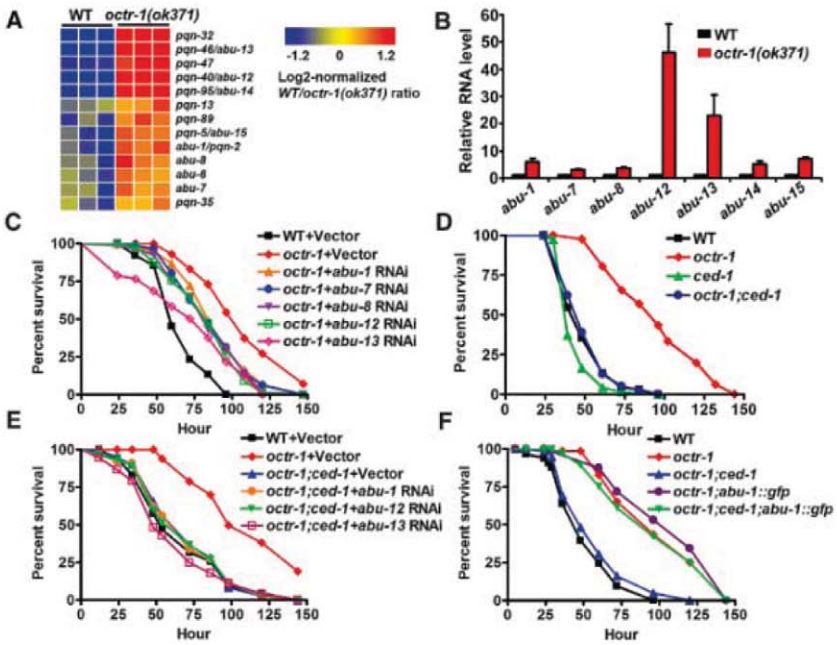

Fig. 3. *pqn/abu* genes are required for the enhanced immunity of *octr-1(ok371)* animals to *P. aeruginosa*. (**A**) Cluster of *pqn/abu* genes that are up-regulated in *octr-1(ok371)* mutants. (**B**) Quantitative reverse transcription polymerase chain reaction (RT-PCR) analysis of *abu-1*, *abu-7*, *abu-8*, *abu-12*, *abu-13*, *abu-14*, and *abu-15* expression in *octr-1(ok371)* relative to WT animals exposed to *P. aeruginosa*. $n = 3$ independent experiments; bar graphs correspond to mean ± SEM (error bars). (**C**) WT animals grown on dsRNA for vector control and *octr-1(ok371)* animals grown on dsRNA for vector control or dsRNA for *abu* genes were exposed to *P. aeruginosa*. (**D**) WT, *octr-1(ok371)*, *ced-1(e1735)*, and *octr-1(ok371);ced-1(e1735)* animals were exposed to *P. aeruginosa*. (**E**) WT and *octr-1(ok371)* animals grown on dsRNA for vector control and *octr-1(ok371);ced-1(e1735)* animals grown on dsRNA for vector control or dsRNA for *abu* genes were exposed to *P. aeruginosa*. (**F**) WT, *octr-1(ok371)*, *octr-1(ok371);ced-1(e1735)*, *octr-1(ok371);abu-1::gfp(zcEx8)*, and *octr-1(ok371);ced-1(e1735);abu-1::gfp(zcEx8)* animals were exposed to *P. aeruginosa*. The survival graphs represent combined results of two independent experiments. $n = 90$ adult animals per strain.

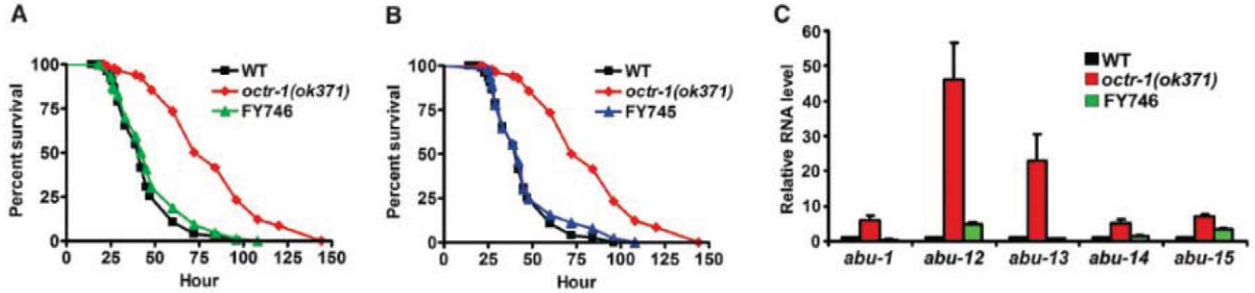

Fig. 4. OCTR-1–expressing neurons ASH and ASI suppress innate immunity by controlling the expression of *pqn/abu* genes. (**A**) WT, *octr-1(ok371)*, and FY746 *octr-1(ok371);grEx158[Psra-6::octr-1]* animals were exposed to *P. aeruginosa*. (**B**) WT, *octr-1(ok371)*, and FY745 *octr-1(ok371);grEx157 [Poctr-1::octr-1::gfp]* animals were exposed to *P. aeruginosa*. The survival graphs represent the combined results of two independent experiments. $n = 90$ adult animals per strain. (**C**) Quantitative RT-PCR analysis of *abu-1*, *abu-12*, *abu-13*, *abu-14*, and *abu-15* expression in *octr-1(ok371)* and FY746 *octr-1(ok371);grEx158[Psra-6::octr-1]* relative to WT animals exposed to *P. aeruginosa*. $n = 3$ independent experiments; bars represent mean ± SEM.

apoptotic receptor CED-1. Furthermore, the conserved p38 MAPK pathway is under the control of OCTR-1–expressing neurons. Recent studies indicate that the murine nervous system, through the vomeronasal organ, has the potential to "smell" molecules related to disease or inflammation in the outside world (*18*). Even though the mammalian nervous system plays a key role in the regulation of inflammation (*19*), the specific role of neurons in contact with the outside world in the control of immune responses remains unclear.

References and Notes

1. G. S. Hotamisligil, *Cell* **140**, 900 (2010).
2. D. J. Todd, A. H. Lee, L. H. Glimcher, *Nat. Rev. Immunol.* **8**, 663 (2008).
3. I. Kim, W. Xu, J. C. Reed, *Nat. Rev. Drug Discov.* **7**, 1013 (2008).
4. K. A. Haskins, J. F. Russell, N. Gaddis, H. K. Dressman, A. Aballay, *Dev. Cell* **15**, 87 (2008).
5. C. E. Richardson, T. Kooistra, D. H. Kim, *Nature* **463**, 1092 (2010).
6. L. J. Bischof *et al.*, *PLoS Pathog.* **4**, e1000176 (2008).
7. F. Martinon, X. Chen, A. H. Lee, L. H. Glimcher, *Nat. Immunol.* **11**, 411 (2010).
8. C. W. Woo *et al.*, *Nat. Cell Biol.* **11**, 1473 (2009).
9. K. L. Styer *et al.*, *Science* **322**, 460 (2008); 10.1126/science.1163673.
10. A. Aballay, *Cell Cycle* **8**, 966 (2009).
11. R. T. Wragg *et al.*, *J. Neurosci.* **27**, 13402 (2007).
12. Materials and methods are available as supporting material on *Science* Online.
13. J. L. Tenor, A. Aballay, *EMBO Rep.* **9**, 103 (2008).
14. L. E. Fuhrman, A. K. Goel, J. Smith, K. V. Shianna, A. Aballay, *PLoS Genet.* **5**, e1000657 (2009).
15. F. Urano *et al.*, *J. Cell Biol.* **158**, 639 (2002).
16. E. R. Troemel, J. H. Chou, N. D. Dwyer, H. A. Colbert, C. I. Bargmann, *Cell* **83**, 207 (1995).
17. P. W. Faber, C. Voisine, D. C. King, E. A. Bates, A. C. Hart, *Proc. Natl. Acad. Sci. U.S.A.* **99**, 17131 (2002).
18. S. Rivière, L. Challet, D. Fluegge, M. Spehr, I. Rodriguez, *Nature* **459**, 574 (2009).
19. K. J. Tracey, *Nat. Immunol.* **11**, 561 (2010).

Acknowledgments: We thank the Caenorhabditis Genetics Center (Univ. of Minnesota) for strains used in this study, R. Komuniecki (Univ. of Toledo) for providing FY745 and FY746, and D. Ron for providing the *abu-1* transgenic strain. A.A. is funded by the Dana Foundation and the NIH (grant GM070977).

Supporting Online Material

www.sciencemag.org/cgi/content/full/science.1203411/DC1
Materials and Methods
Figs. S1 to S9
Tables S1 to S6
References 19 to 26

26 January 2011; accepted 24 March 2011
Published online 7 April 2011;
10.1126/science.1203411

Transient Activation of the HOG MAPK Pathway Regulates Bimodal Gene Expression

Serge Pelet,[1]* Fabian Rudolf,[1]† Mariona Nadal-Ribelles,[2] Eulàlia de Nadal,[2] Francesc Posas,[2] Matthias Peter[1]*

Mitogen-activated protein kinase (MAPK) cascades are conserved signaling modules that control many cellular processes by integrating intra- and extracellular cues. The p38/Hog1 MAPK is transiently activated in response to osmotic stress, leading to rapid translocation into the nucleus and induction of a specific transcriptional program. When investigating the dynamic interplay between Hog1 activation and Hog1-driven gene expression, we found that Hog1 activation increases linearly with stimulus, whereas the transcriptional output is bimodal. Modeling predictions, corroborated by single-cell experiments, established that a slow stochastic transition from a repressed to an activated transcriptional state in conjunction with transient Hog1 activation generates this behavior. Together, these findings provide a molecular mechanism by which a cell can impose a transcriptional threshold in response to a linear signaling behavior.

Mitogen-activated protein kinase (MAPK) cascades orchestrate many cellular processes including cell growth, division, and differentiation (*1*). In *Saccharomyces cerevisiae*, the high osmolarity glycerol (HOG) pathway is needed to reestablish the balance between internal and external pressures upon osmotic shock (*2*). Osmosensors at the cell membrane activate either the MAPK kinase kinases (MAPKKKs) Ste11 or Ssk2,22, which converge on the MAPKK Pbs2. In turn, Pbs2 doubly phosphorylates the MAPK Hog1, leading to rapid translocation into the nucleus to launch a transcriptional program. Although increased transcription is essential to survive very high osmotic stress (0.8 M NaCl), it is not required for milder stress conditions (0.4 M NaCl) (*3*), under which Hog1 kinase activity alone is sufficient to drive cellular adaptation. By contrast, in the yeast mating MAPK pathway, transcription and new protein expression are required for cell cycle arrest and mating (*4*).

Transcriptional activation of mating genes occurs with linear kinetics and high fidelity (*5*, *6*), and the observed cell-to-cell variation in protein expression is governed by the ability of cells to express proteins (expression capacity) (*5*). Whereas the mating pathway can be compared to a cell-fate decision system with sustained MAPK activity, the HOG pathway is an adaptation response, which is only transiently induced like other stress-activated pathways (*7*). We therefore investigated whether this transient response would trigger different expression behavior.

To quantify the transcriptional output induced by osmotic stress, we engineered a reporter system based on a quadruple Venus (qV) fluorescent protein expressed under the control of specific osmostress-inducible promoters dependent on the three main transcription factors orchestrating the transcriptional response to osmotic stress (Hot1 and Sko1: p*STL1*; Msn2,4: p*ALD3*; or Msn2,4 and Hot1: p*HSP12*) (*8*). Flow cytometry revealed a Pbs2-dependent 20-fold increase in p*STL1*-qV reporter expression when 0.4 M NaCl was added to the growth medium (Fig. 1, A and B). No expression was detected at low salt concentrations (below 0.05 M), while above 0.15 M, all cells expressed the reporter and the amount of fluorescence increased linearly with stress. However, at intermediate concentrations, we observed histograms with two distinct subpopulations representing nonexpressing cells with basal autofluorescence levels and expressing cells with higher intensities. These distributions are termed bimodal. The p*ALD3*-qV and p*HSP12*-qV reporters displayed a similar bimodal expression behavior (Fig. 1B and fig. S1A). Induction of the mating pathway for 45 min with α-factor also generated a bimodal expression output of the Ste12-specific reporter p*FIG1*-qV. However, signaling in the mating pathway is prevented from "start" through S phase (*9*), and expression output became unimodal after relieving this cell cycle–dependent restriction (Fig. 1B and fig. S1B).

To investigate the source of the HOG pathway bimodal expression behavior, we integrated two reporters driving the expression of a quadruple cyan fluorescent protein (qCFP) and a qV construct in the same cell. Correlation of the cyan and yellow intensities measures the contribution of cell-to-cell (extrinsic) and intracellular (intrinsic) variability to the overall expression noise (*5*, *10*). The two p*FIG1* reporters induced by α-factor demonstrated that the mating pathway is governed by extrinsic noise. By contrast, we observed a lack of correlation between the two p*STL1* reporters (Fig. 1, C to E, and fig. S2), demonstrating that the bimodal expression behavior of the HOG pathway is independent of cell-to-cell variability caused by extrinsic factors such as expression capacity or cell-cycle stage.

To assess the observed bimodality and Hog1 signaling simultaneously, we combined a Hog1-relocation assay (*11*, *12*) with the p*STL1*-qV ex-

[1]ETH-Zurich, Department of Biology, Institute of Biochemistry, Schafmattstrasse 18, CH-8093 Zurich, Switzerland. [2]Cell Signaling Unit, Departament de Ciències Experimentals i de la Salut, Universitat Pompeu Fabra, E-08003 Barcelona, Spain.

*To whom correspondence should be addressed. E-mail: serge.pelet@bc.biol.ethz.ch (S.P.); matthias.peter@bc.biol.ethz.ch (M.P.)

†Present address: D-BSSE, ETH-Zurich, Mattenstrasse 26, CH-4058 Basel, Switzerland.

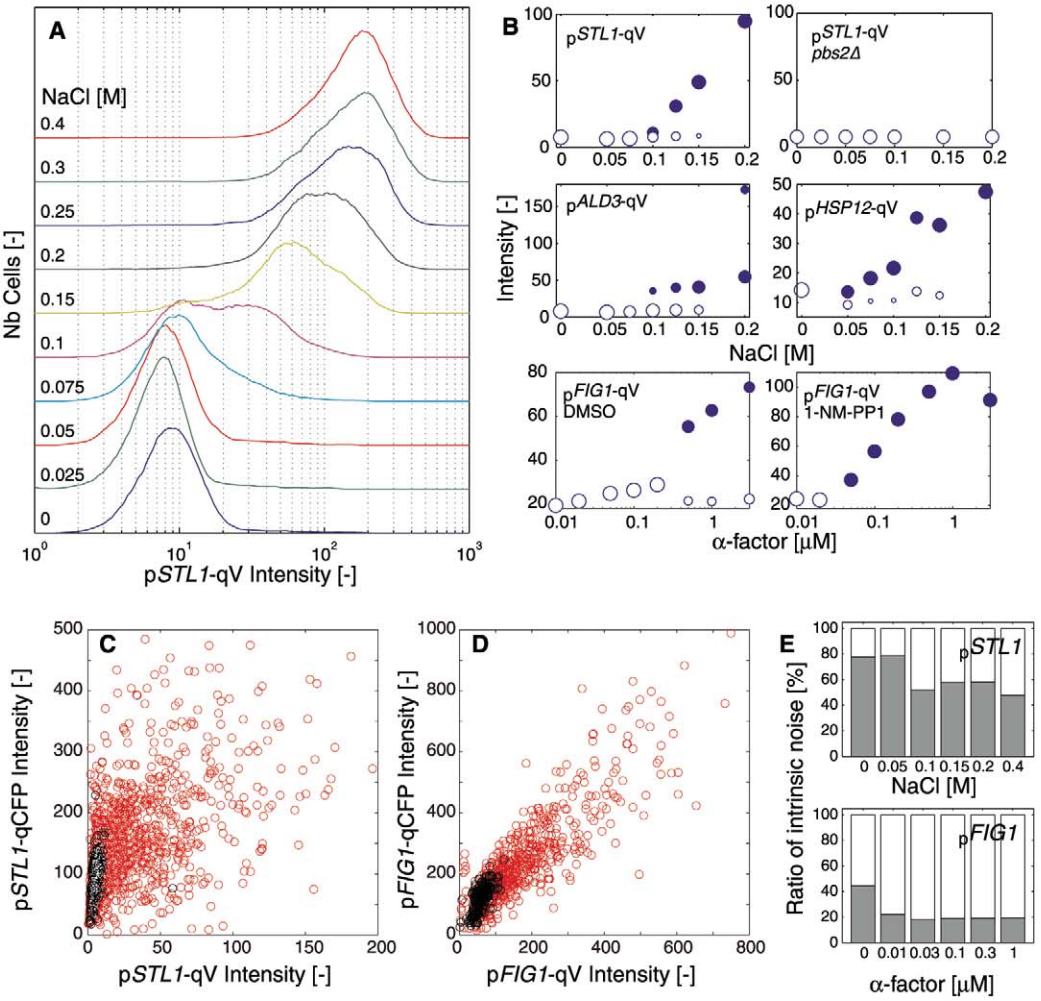

Fig. 1. Bimodal expression of fluorescent reporters upon osmotic stress. (**A**) Dose response of the quadruple-Venus (qV) fluorescence reporter driven by the *STL1* promoter (p*STL1*) measured by flow cytometry. (**B**) Dose responses of wild-type or *pbs2*Δ cells harboring the indicated osmostress-inducible reporters driven by the *STL1*, *ALD3*, or *HSP12* promoters, or α-factor–inducible reporter p*FIG1*-qV in a *cdc28-as* background with 1-NM-PP1 inhibitor (10 μM) or dimethyl sulfoxide (DMSO). The mean of the log-normal distribution fitted to the flow cytometry histograms is plotted. The best fit between single or double log-normal distributions was selected for each curve. The open and closed circles represent, respectively, the population of nonreacting and reacting cells. Circle size is proportional to the population under each distribution. (**C** and **D**) Intrinsic and extrinsic noise revealed by microscopy in a strain that contains both CFP (cyan fluorescent protein) and YFP (yellow fluorescent protein) expression reporters driven by the p*STL1* promoter stressed with 0.1 M (red) or no (black) NaCl (C), or in *cdc28-as* cells inhibited by 1-NM-PP1 with expression reporters driven by the p*FIG1* promoter treated with 0.03 μM (red) or no (black) α-factor (D). (**E**) Percentage of intrinsic (gray) and extrinsic (white) noise over total noise quantified for osmotic stress or α-factor treatment in cells bearing two p*STL1* or p*FIG1* expression reporters, respectively.

pression reporter (Fig. 2A). Because nuclear accumulation of Hog1 is linked to its kinase activity (*13*), this assay allows one to correlate in each cell the signaling and expression outputs (Fig. 2, B and C). When cells were stressed with increasing salt concentrations, Hog1 nuclear accumulation gradually augmented both in magnitude and retention time. At the single-cell level, a clear discrepancy was apparent between the linear increase in signaling output versus the bimodal behavior observed in the expression output (Fig. 2, D to F, and fig. S3). We conclude that Hog1 activation as measured by its nuclear translocation is not sufficient to induce a defined transcriptional output, indicating that an unknown intracellular factor (or factors) sets a threshold for gene expression.

Hog1 has been implicated at various steps in the complex mechanisms leading to gene transcription (*14*, *15*). First, Hog1 associates with transcription factors that bind at specific promoters (*16*). The MAPK then recruits RNA polymerase II (Pol II) as well as chromatin-remodeling complexes such as SAGA (Spt-Ada-Gcn5 acetyltransferase) and RSC (chromatin structure remodeling), which evict nucleosomes (*17*–*19*). During active transcription, the INO80 complex and histone chaperones are involved in redeposition of histones, and therefore help in silencing these genes once stress has been overcome (*20*).

To test if bimodality is reflected in chromatin remodeling, we used chromatin immunoprecipitation (ChIP) to monitor the occupancy of histone H3 on the *STL1*, *HSP12*, and *ALD3* promoters. Histone eviction occurred in a Hog1-dependent manner (fig. S4A) (*18*) and was complete from 0.15 M (*STL1*, *ALD3*) or 0.2 M NaCl (*HSP12*) (Fig. 3A). The partial eviction observed at low stress levels suggests that only a fraction of the population could remodel chromatin to allow for efficient transcription. In contrast to other transcription regulators such as Asf1, Cyc8, or Htz1, the bimodal behavior of the p*STL1*-qV stress reporter was already present in the absence of stress in cells deleted for the INO80 subunit Arp8 (Fig. 3B; fig. S5, A and B; and table S1). Conversely, bimodality was markedly increased in cells with impaired SAGA or RSC function (Fig. 3B and fig. S6), indicating that chromatin remodeling activity affects the threshold of gene expression. We verified that eviction of histone H3 is incomplete in *gcn5*Δ cells (Fig. 3C and fig. S4B), reinforcing the notion that the partial histone eviction observed at the population level is linked to the bimodal expression measured in single cells.

Deletion of either of the two transcription factors Sko1 or Hot1 strongly reduced p*STL1*-qV expression and led to a bimodal expression pattern at high stress levels (fig. S5C). This behavior could be partially rescued by the additional deletion of *ARP8*. Moreover, cells grown at low glucose concentration (0.05%), where glucose repression is alleviated, display a bimodal transition around 0.05 M NaCl (fig. S7, A to C). The bimodal transition shifts to higher stress levels as glucose repression increases with the amount of glucose in the medium. Together, these results suggest that the bimodality depends on a number of dynamic processes cooperating at stress-induced promoters to regulate the activation of the transcription.

To better understand the dynamics of gene activation, we designed a simple stochastic model of Hog1-induced transcription (fig. S8 and SOM Text), which identified the formation of an active gene complex (i.e., a gene with open

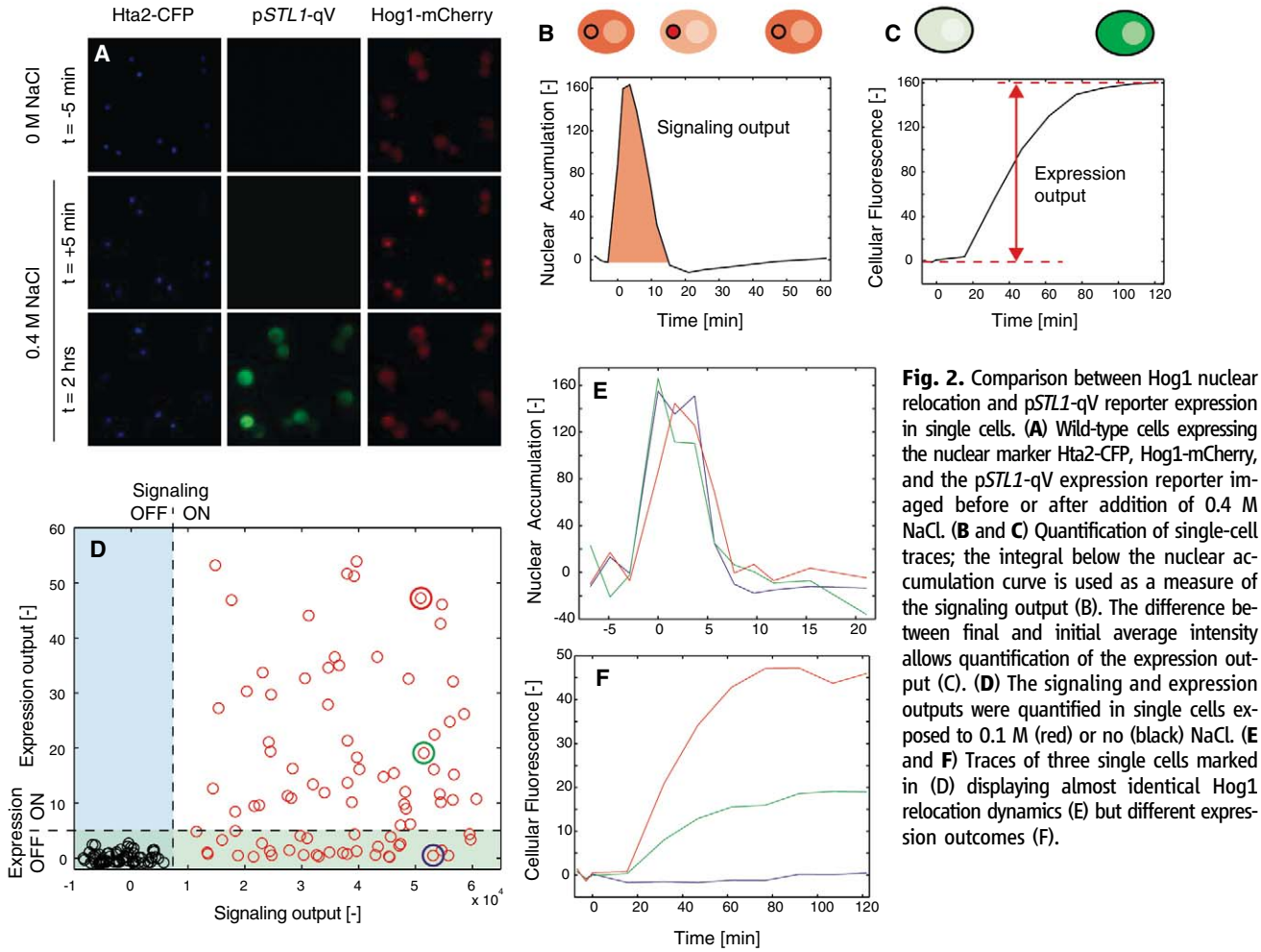

Fig. 2. Comparison between Hog1 nuclear relocation and p*STL1*-qV reporter expression in single cells. (**A**) Wild-type cells expressing the nuclear marker Hta2-CFP, Hog1-mCherry, and the p*STL1*-qV expression reporter imaged before or after addition of 0.4 M NaCl. (**B** and **C**) Quantification of single-cell traces; the integral below the nuclear accumulation curve is used as a measure of the signaling output (B). The difference between final and initial average intensity allows quantification of the expression output (C). (**D**) The signaling and expression outputs were quantified in single cells exposed to 0.1 M (red) or no (black) NaCl. (**E** and **F**) Traces of three single cells marked in (D) displaying almost identical Hog1 relocation dynamics (E) but different expression outcomes (F).

chromatin, which can be efficiently transcribed) as the crucial step governing the bimodal expression pattern. As predicted by the model, a transient activation of the HOG pathway for specific lengths of time with high stresses revealed a bimodal distribution of p*STL1*-qV reporter expression at early time points (Fig. 4, A and C). Microscopy analysis confirmed that these conditions result in short-lived nuclear relocation of Hog1 in all cells and a bimodal expression response of the population (Fig. 4, D and E). Conversely, sustained activation of Hog1 with low stresses with a ramping protocol resulted in a transition from nonexpressing to fully expressing cells going through a bimodal stage (Fig. 4, B to E). We conclude that both the retention time and concentration of Hog1 in the nucleus are critical parameters that control bimodality of the transcription of stress-activated genes.

Stress genes must fulfill two contradictory requirements, which may explain their large noise in expression (*21*, *22*). First, under normal growth conditions these genes are silenced, although basal pathway activity can be present (*23*, *24*). Second, upon stress, these genes must be expressed at a high rate to contribute to the adaptation of the cell during the short period of activity of the pathway. Notably, bimodal gene expression may

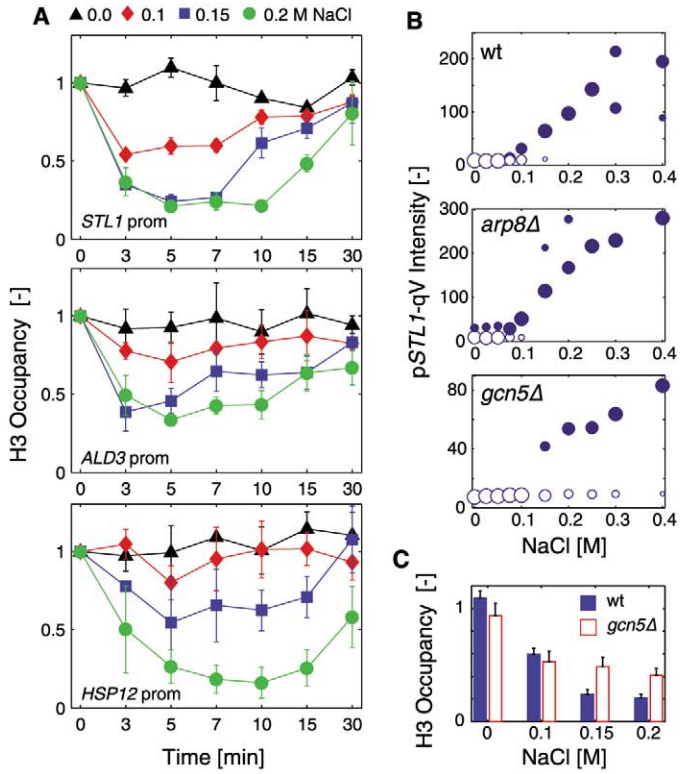

Fig. 3. Influence of chromatin remodeling on reporter expression. (**A**) Dynamics of histone H3 eviction at the *STL1*, *ALD3*, and *HSP12* promoters was measured by quantitative ChIP experiments after addition of the indicated NaCl concentration. Histone H3 binding was normalized to a *TEL2* sequence control. The error bars correspond to the standard deviation of three independent measurements. (**B**) Mean of the log-normal fit of flow cytometry histograms of p*STL1*-qVenus expression quantified in wild-type (wt), *arp8*Δ, and *gcn5*Δ cells after addition of NaCl. (**C**) Histone H3 occupancy in wt and *gcn5*Δ cells was quantified as in (A) 5 min after osmotic stress.

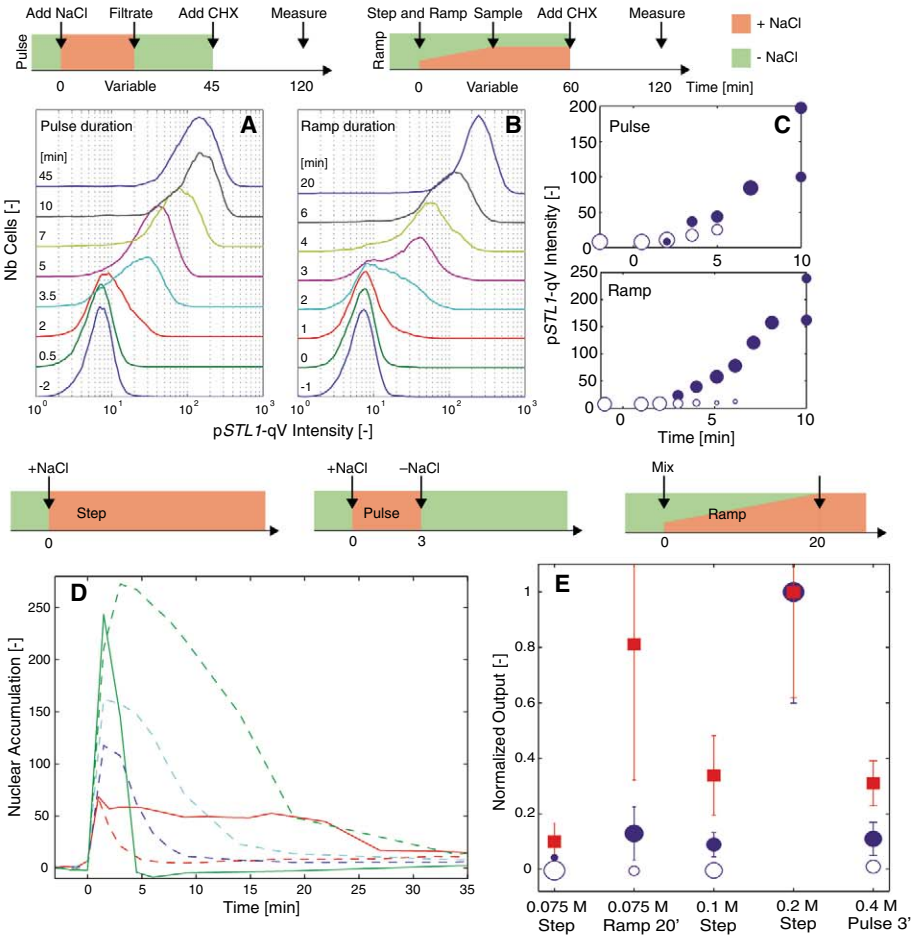

Fig. 4. Duration and intensity of Hog1 nuclear accumulation controls bimodality. (**A** to **C**) Flow cytometric measurement of p*STL1*-qV expression and mean of log-normal fits of the histograms (C) upon transient or sustained activation with a pulse of 0.2 M NaCl (A) or a ramp from 0.05 to 0.4 M NaCl (B) Cycloheximide (CHX) is added after 45 min to block protein synthesis. (**D**) Modulation of the Hog1 activation pattern in flow chambers studied by microscopy. Mean Hog1 nuclear accumulation upon transient (0.4 M NaCl for 3 min, green) and sustained (from 0.075 to 0.4 M NaCl in 20 min, red) activation of the pathway. Stepwise activation (dashed lines) for 0.075 M (red), 0.1 M (blue), 0.2 M (cyan), and 0.4 M NaCl (green) are shown for comparison. (**E**) Average signaling (red) and expression outputs (blue) for different activation patterns. The open and closed circles represent, respectively, the population of nonreacting and reacting cells. Circle size is proportional to the population under each distribution. The error bars show the standard deviation of 40 to 130 single cells.

be a general feature of stress-induced genes, because oxidative or heat stresses also generated a bimodal expression pattern (fig. S9).

If the approximately 300 genes induced by osmotic stress (*8*) were expressed in a stochastic fashion, a unique set of 150 genes would be present in each cell. Fluorescence reporter expression can therefore not be linked to increased resistance to osmotic stress, and we failed to detect a pattern in reporter expression in cells subjected to two subsequent mild osmotic stresses (fig. S10). However, this broad diversity in expression pattern will result in a large variability in protein content of the cells, which could be advantageous to survive in changing environments (*25*). Thus, noise in stress gene expression may confer an evolutionary advantage to a population by increasing fitness to face a large range of stress events.

References and Notes

1. R. E. Chen, J. Thorner, *Biochim. Biophys. Acta* **1773**, 1311 (2007).
2. S. Hohmann, M. Krantz, B. Nordlander, *Methods Enzymol.* **428**, 29 (2007).
3. P. J. Westfall, J. C. Patterson, R. E. Chen, J. Thorner, *Proc. Natl. Acad. Sci. U.S.A.* **105**, 12212 (2008).
4. L. J. Oehlen, J. D. McKinney, F. R. Cross, *Mol. Cell. Biol.* **16**, 2830 (1996).
5. A. Colman-Lerner *et al.*, *Nature* **437**, 699 (2005).
6. R. C. Yu *et al.*, *Nature* **456**, 755 (2008).
7. A. P. Gasch *et al.*, *Mol. Biol. Cell* **11**, 4241 (2000).
8. A. P. Capaldi *et al.*, *Nat. Genet.* **40**, 1300 (2008).
9. S. C. Strickfaden *et al.*, *Cell* **128**, 519 (2007).
10. M. B. Elowitz, A. J. Levine, E. D. Siggia, P. S. Swain, *Science* **297**, 1183 (2002).
11. D. Muzzey, C. A. Gómez-Uribe, J. T. Mettetal, A. van Oudenaarden, *Cell* **138**, 160 (2009).
12. P. Hersen, M. N. McClean, L. Mahadevan, S. Ramanathan, *Proc. Natl. Acad. Sci. U.S.A.* **105**, 7165 (2008).
13. P. Ferrigno, F. Posas, D. Koepp, H. Saito, P. A. Silver, *EMBO J.* **17**, 5606 (1998).
14. E. de Nadal, F. Posas, *EMBO J.* **29**, 4 (2010).
15. V. M. Weake, J. L. Workman, *Nat. Rev. Genet.* **11**, 426 (2010).
16. E. de Nadal, L. Casadome, F. Posas, *Mol. Cell. Biol.* **23**, 229 (2003).
17. P. M. Alepuz, E. de Nadal, M. Zapater, G. Ammerer, F. Posas, *EMBO J.* **22**, 2433 (2003).
18. G. Mas *et al.*, *EMBO J.* **28**, 326 (2009).
19. M. Zapater, M. Sohrmann, M. Peter, F. Posas, E. de Nadal, *Mol. Cell. Biol.* **27**, 3900 (2007).
20. E. Klopf *et al.*, *Mol. Cell. Biol.* **29**, 4994 (2009).
21. A. Bar-Even *et al.*, *Nat. Genet.* **38**, 636 (2006).
22. J. R. S. Newman *et al.*, *Nature* **441**, 840 (2006).
23. J. Macia *et al.*, *Sci. Signal.* **2**, ra13 (2009).
24. A. Loewer, E. Batchelor, G. Gaglia, G. Lahav, *Cell* **142**, 89 (2010).
25. L. López-Maury, S. Marguerat, J. Bähler, *Nat. Rev. Genet.* **9**, 583 (2008).

Acknowledgments: We thank R. Dechant, C. Schüller, G. Ammerer, A Colman-Lerner, and A. Smith for strains, plasmids, and helpful discussions, and S.-S. Lee and H. Koeppl for help with flow chamber experiments and model design, respectively. We are grateful to C. Rupp and D. Condé for technical assistance. This work was supported by QUASI, UNICELLSYS, the SystemsX.ch organization, and the Competence Centre "Systems Physiology and Metabolic Disease" (CC-SPMD). M.N.-R. is supported by ISCIII, and F.P is recipient of an ICREA Acadèmia (Generalitat de Catalunya) award. Work in the Posas and de Nadal laboratories is funded by the Fundación Marcelino Botín (FMB) and the Ministerio de Ciéncia y Innovación (BFU2008-00530 to E.N. and BIO2009-07762 to F.P.). The Peter laboratory is supported by the Swiss National Science Foundation and ETHZ. The authors declare that they have no competing financial interests.

Supporting Online Material

www.sciencemag.org/cgi/content/full/332/6030/732/DC1
Materials and Methods
SOM Text
Figs. S1 to S11
Tables S1 to S5
References

8 October 2010; accepted 25 March 2011
10.1126/science.1198851

SORTING CELLS FOR MEDICINE

The basic technology for cell separation hasn't changed much over the past several years. What has changed dramatically is what those cells are being used for: treating patients. As the promise of cell therapy is gradually realized, researchers are searching for cell separation technologies that can solve some basic problems, such as improving cell processing speed and making processing as sterile as possible. Researchers already use a mix of density-gradient separation, magnetic separation, and flow cytometry to prep cells for clinical use but hope for newer chip-based technologies to help advance the field. By Anne Harding

"Given the rigid regulatory environment, the manufacturers in this clinical space need to have a long-term outlook and a commitment to cellular therapy and regenerative medicine."

Cell therapy has technically been around for decades—think bone marrow transplants—but now researchers are finding evermore sophisticated ways to manipulate and use cells for medicine. Physicians and scientists are harvesting dendritic cells, T cells, stem cells, and more from patients' bodies and identifying and separating those with the strongest potential for helping patients. Once isolated, these cells can be grown in large quantity and returned to a patient's body to treat various diseases.

Though cell therapy remains a lively area of research, commercially available treatments have been slow to enter the clinic. The **U.S. Food and Drug Administration** (FDA) approved the first-ever autologous cell therapy (which manipulates the patient's own cells and returns them to his or her body), **Genzyme**'s Carticel, for treating damaged knee cartilage in 2007. The second, Provenge, for treating metastatic prostate cancer, followed in 2010. Last March, the **Centers for Medicare and Medicaid Services** announced that it plans to cover this $93,000 prostate treatment, a major boost for **Dendreon,** the Seattle-based company that makes the drug.

Allogeneic cell therapies, made from cells harvested from donors rather than the patient, offer the possibility of "off the shelf" use. Dozens of candidates are currently in clinical trials for applications ranging from boosting wound healing to treating graft-versus-host disease to supplementing blood cancer chemotherapy treatments.

Because these cells are being used for medicinal purposes, the FDA regulates the entire process under the same rules that govern the production of pharmaceuticals, known as good manufacturing practice (GMP). Given the vast potential for cell therapy, many companies making instruments, reagents, and other tools for cell separation have shifted their focus away from the research lab and into the translational and clinical research space.

But researchers in the field say many gaps remain in what's available to develop clinically viable cell therapies, from instruments to antibodies. And because the payoffs so far have been relatively few and far between, some companies making these instruments or reagents have had to pull their products off the market, such as with **Baxter**'s Isolex 300 Magnetic Cell Selection System—leaving researchers who use their products high and dry, especially those with open clinical trials under way.

"It's really hard to depend on a single manufacturer," says Lynn O'Donnell, who directs the Cell Therapy Laboratory at the **Ohio State University**'s **James Cancer Hospital** in Columbus. "Given the rigid regulatory environment, the manufacturers in this clinical space need to have a long-term outlook and a commitment to cellular therapy and regenerative medicine."

BACK TO BASICS: CELLS OUT OF TISSUE

Separating cells from their tissue of origin is one of the real bottlenecks for developing cell therapies for clinical use, says Firman Ghouze, director for cell therapy within **GE Healthcare Life Sciences.** While sorting cells out of blood is fairly easy, isolating them from fat—which has turned out to be a very rich source of stem cells—is another matter.

UPCOMING FEATURES

Food Safety—June 24

Proteomics: Protein Folding—August 26

qPCR—October 7

Companies are putting a lot of effort towards developing simpler high volume, high throughput processes for separating cells from tissue that can be handled by technicians and not only Ph.D.s, according to Ghouze.

To this end, GE offers the StemSource 900/MB Tissue Processing System, which was developed by **Cytori Therapeutics.** This sterile, closed centrifugation system can be used for extracting several different regenerative cell types from connective tissue, yielding an average of 4.6 x 10^7 nucleated cells per 100 grams of tissue. GE's Res-Q 60 Bone Marrow Concentration System, also centrifuge-based, can be used at the patient's bedside to isolate mononuclear cells from bone marrow in less than 20 minutes.

"In the case of magnetic bead systems, a whole new series of reagents and equipment have been developed that allow for more automated processing and more closed operation, so you can get a sterile cell product."

O'Donnell and her colleagues separate islet cells out of pancreatic tissue using another popular centrifuge-based instrument, **CaridianBCT**'s COBE 2991 Cell Processor. The instrument uses a closed fluid path and single-use disposable set for cell centrifugation—a vast improvement over traditional centrifuges and conical tubes because it allows various fractions to be collected within a closed system, O'Donnell explains.

But the density gradient system has limitations when it comes to coping with pancreatic islets, which "are kind of like mini-organs because they are clusters of cells," she adds. The instrument is nonspecific and variable between islet isolations.

"It's challenging to come up with a purification technique that works for large clusters of cells and variably sized cells," O'Donnell says. And given the nature of islets, "you end up sacrificing yield in order to gain purity because the separation isn't great."

CLOSED SYSTEMS ARE KEY FOR CLINICAL PRODUCTS

Most researchers in the field, including O'Donnell, use a combination of centrifugation, magnetic bead separation, and flow cytometry to develop their cell therapies. Magnetic separation has the advantage of speed, while cell sorting allows for the use of multiple markers and results in a purer end product.

"In the case of magnetic bead systems, a whole new series of reagents and equipment have been developed that allow for more automated processing and more closed operation, so you can get a sterile cell product," says Shelly Heimfeld, who directs the Cellular Therapy Laboratory and cGMP Cell Processing Facility at the **Fred Hutchinson Cancer Research Center** in Seattle. Heimfeld is also past president of the **International Society for Cellular Therapy,** an organization that supports the translation of cell therapy research into clinical use.

Such instruments include **Miltenyi Biotec**'s CliniMACS platform, which uses magnetic-based technology for enriching target cells or depleting unwanted cells. Miltenyi is about to introduce a second-generation version of the instrument, the CliniMACS Prodigy. "The idea is to have the entire GMP-conformed process for cell manufacturing integrated into one device," explains Jurgen Schmitz, head of research and development at the Bergisch-Gladbach, Germany-based company. This closed system can wash, separate (with density gradient cell separation or magnetic bead cell separation), and formulate the cells of interest, Schmitz explains.

"That is something quite complex in terms of logistics," he adds. "Such an instrument can really help make things easier and less expensive, for example by reducing clean-room requirements."

Because companies are focused on making cell-sorting instrumentation and reagents that are suitable for use in clinical products, they are now "thinking about how to comply with GMP-manufacturing guidelines," says Tim Fong, technical director of cell therapy at **BD Biosciences.**

Maintaining the sterility of cell products is key. BD Biosciences, for example, offers a replaceable gamma-irradiated fluidics kit for the Influx cell-sorting platform. "All the tubing that the cell sample comes into contact with on the instrument is single use and gamma irradiated, which mitigates the prospect of serial contamination," explains Jack Dunne, who leads the company's cell-therapy research team.

ACCELERATING CELL SORTING WITH MULTI-MICROFLUIDICS

The ideal technology for producing cell therapeutics, says O'Donnell, would be a speedier version of flow cytometry since "you can look at multiple markers and purify very specific kinds of cells." But, she points out, there's the challenge of engineering a single-use fluid path that allows cell sorting under sterile conditions. One solution, she says, is to put a box around a standard flow sorter that would provide clean, HEPA-filtered air, "but you still have cross-contamination questions, like what do you do between processing for patient A and patient B."

Another possibility researchers foresee is the use of microfluidics chips that sort cells via microscopic channels and gates that open and close to determine the cells' flow path. With several flow paths running in parallel on a single chip, the sorting process could be sped up continued »

considerably. What's more, the system could be entirely closed and aseptic. Feasibility studies by developers, including **Owl Biomedical,** have been promising, according to David DiGiusto, who directs the Laboratory for Cellular Medicine at the **Beckman Research Institute** of the City of Hope in Duarte, California.

Yet another advantage of electrostatic cell sorting on chips is that it would be "label-free." While centrifugation techniques are label-free also, both magnetic cell separation and flow cytometry require tagging cells of interest with antibodies or dyes, creating another challenge for researchers: finding ways to remove the labels such as using enzymes that can "clip off" antibodies after sorting or designing biodegradable labels that simply fall apart.

"We're still in an era where we're using the [same] methods that identify the cells to mediate their separation," says Adrian Gee, a professor in the Department of Cell and Gene Therapy at the **Texas Children's Hospital.**

EVADING REJECTION TO MAKE 'OFF-THE-SHELF' PRODUCTS

So far, large pharmaceutical companies seem to have held back from getting involved in cell therapeutics, which remains pretty much the province of startup biotechs and translational research institutions.

"It's much more attractive for companies to have a generalized cell product that could be used to treat a wide variety of patients," says Gee. But developing such generalized products requires figuring out a way to ensure that the recipient's immune system accepts the donated cells. Just as with blood transfusions and organ donations, cell therapies can be rejected by a patient's body. Solving this problem may, in some cases, require using tissue matching techniques like those used for blood donation or organ transplantation.

Investigators have also learned that some cells, such as mesenchymal stromal cells and nerve cells, do not provoke the rejection responses seen with other cell types. Gee and his colleagues found that T cells primed to attack viruses can circumvent human leukocyte antigen (HLA) barriers, the immune-system "tissue types" that must match between donor and recipient to prevent rejection. "We used to think that these [T cells] could only be used in essentially closely matched tissue recipients, but it appears they can be used across some tissue types," he explained.

FEATURED PARTICIPANTS

Aastrom Biosciences
www.aastrom.com

Baxter
www.baxter.com

BD Biosciences
www.bdbiosciences.com

CaridianBCT
www.caridianbct.com

Centers for Medicare and Medicaid Services
www.cms.gov

City of Hope's Beckman Research Institute
www.cityofhope.org/research/beckman-research-institute

Cytori Therapeutics
www.cytori.com

Dendreon
www.dendreon.com

Fred Hutchinson Cancer Research Center
www.fhcrc.org

GE Healthcare Life Sciences
www.gelifesciences.com

Genzyme
www.genzyme.com

Geron
www.geron.com

International Society for Cellular Therapy
www.celltherapysociety.org

Miltenyi Biotec
www.miltenyibiotec.com

Ohio State University's James Cancer Hospital
cancer.osu.edu

Osiris Therapeutics
www.osiristx.com

Owl Biomedical
www.owlbiomedical.com

Stanford University
www.stanford.edu

Texas Children's Hospital
www.texaschildrens.org

U.S. Food and Drug Administration
www.fda.gov

LOTS OF PROMISE, BUT SLOW PROGRESS TO THE CLINIC

"There's a lot of things going on" in the development of cellular therapies, but progress is "slow and painful," says Robert S. Negrin, a professor of medicine at **Stanford University,** director of the university's Bone Marrow Transplant Program, and medical director for the Stanford Cell Therapeutics Laboratory.

One factor delaying things, explains Negrin, is the scarcity of antibodies that are made to GMP standards for magnetic cell separation. He estimates that there are currently a dozen or so antibodies, made by BD, Miltenyi, and other companies, that are suitable for preparing cells for clinical use. "That's where we often get stuck, is having the proper reagents," Negrin says. Just having more antibodies available for clinical use could give the field a major push forward, he adds. Yet, as with many other technologies related to the field, investors and companies are shying away from such investments until they see some real success.

However, investments in products that support cell therapy research is just as essential as the research itself, says DiGiusto, since "one without the other does no good."

Despite the challenges of developing commercially available cell therapies, more than a dozen companies have allogeneic or autologous products in various stages of clinical trials, including **Geron, Osiris Therapeutics,** Cytori Therapeutics, and **Aastrom Biosciences.**

And with each success story, such as Dendreon's prostate cancer drug therapy, Provenge, the field as a whole benefits, explains DiGiusto. "It's at least a sign to the investment community that [success] can happen," he adds. "And it's really a critical thing that the investment community continues to have confidence in the field."

Anne Harding is a freelance science writer based near New York City.

DOI: 10.1126/science.opms.p1100055

MAGNETIC BEADS

Streptavidin Mag Sepharose magnetic beads have a high binding capacity for efficient purification of biotinylated biomolecules and enrichment of target proteins. The magnetic beads provide simplified handling, as rapid capture is facilitated by magnetic devices while delivering scalability and high yield, from low microliter- to high milliliter-scale sample volumes. Streptavidin Mag Sepharose beads support reliable sample preparation for downstream analysis and have more than a 400-fold enrichment factor to enable an increased identification rate of target proteins. The magnetic beads are hydrophilic with a high density to ensure the beads do not aggregate, avoiding sample loss and increasing yield. Additionally, the MagRack Maxi magnetic rack provides easy handling and supports sample capacities of up to 50 ml, to provide capture of low-expressed target proteins from larger sample volumes. The MagRack Maxi consists of an anodized aluminium housing with a detachable plastic bar containing a neodymium magnet.

GE Healthcare

For info: 800-526-3593 | www.gelifesciences.com

PLATE WASHER/COATER

SQUIRT can wash any 96-, 384-, and 1536-well SBS formatted plate without manifold exchange or adjustment. SQUIRT's unique design sweeps a blade of liquid across the whole surface of the plate. This is followed by an air blade to dry the plate. This unique blade design eliminates clogging and the 'corona effect' (where cells are selectively removed from the center of the wells with traditional probe based instruments). SQUIRT microplate washers are perfect for any lab performing cell-based assays, enzyme-linked immunosorbent assays (ELISA), coating microplates, high content screening, and proteomics and genomics research. The SQUIRT can be fitted with a magnetic plate insert for applications using magnetic beads.

Matrical Bioscience

For info: 509-343-6225 | www.matrical.com

EX-VIVO CELL-THERAPY EXPANSION

The Cellbase CT system, which was developed in collaboration with cell-therapy experts, can be used in a good manufacturing practice (GMP) facility for rapid scale-up of existing manual cell-culture processes in T flasks. Cellbase CT provides researchers with a fully contained, aseptic cell-expansion area where the risk of external contamination or internal cross-contamination has been eliminated. This enables scientists to manufacture multiple autologous cell therapies from many individual patients in parallel, making the Cellbase CT a cost-effective alternative to labor-intensive manual cell culture. Cellbase CT comes with a range of tools to support validation in a GMP-regulated environment and has been developed and extensively tested to enable clean, reproducible expansion of clinically applicable stem cells and other cell types.

TAP Biosystems

For info: 302-478-9060 | www.tapbiosystems.com

MONOCLONAL ANTIBODIES

Monoclonal antibodies have become invaluable tools for researchers developing diagnostic tests and novel therapeutics. The 1,500 new mouse monoclonal TrueMAB antibodies have been specifically developed with full-length human proteins produced in HEK293T cells and validated for critical research and diagnostic needs that require improved antibody sensitivity and specificity. TrueMAB antibodies and hybridoma cell lines are generated using OriGene's large collection of full-length human proteins as primary antigens that have been affinity purified under native conditions to preserve natural protein conformations. As a result, TrueMAB antibodies provide high sensitivity and specificity for the recognition of native epitopes on the protein's natural conformational structure. All TrueMAB antibodies are routinely validated for critical applications such as immunohistochemistry, immunofluorescent staining, flow cytometry, immunoprecipitation, and Western blot analysis.

OriGene Technologies

For info: 888-267-4436 | www.origene.com

AUTOMATED CELL EXPANSION

The Quantum Cell Expansion System is designed to automate cell culture in a closed system. The cutting-edge technology is intended to support advancements in the field of cell therapy by streamlining cell culture processes while reducing the risk of contamination for large-scale cell manufacturing. Current methods used to culture cells are manual and complex, which can limit the ability to provide cellular therapy to a large number of patients. As an integrated, closed system, the Quantum Cell Expansion System improves the efficiency of the cell culture process—allowing for larger scale manufacturing of cells under good manufacturing practice (GMP) process control and with less risk of contamination.

CaridianBCT

For info: 877-339-4228 | www.caridianbct.com

Electronically submit your new product description or product literature information! Go to **www.sciencemag.org/products/newproducts.dtl** for more information.

Newly offered instrumentation, apparatus, and laboratory materials of interest to researchers in all disciplines in academic, industrial, and governmental organizations are featured in this space. Emphasis is given to purpose, chief characteristics, and availability of products and materials. Endorsement by *Science* or AAAS of any products or materials mentioned is not implied. Additional information may be obtained from the manufacturer or supplier.

Living cells are dynamic entities, dependent on an enormous range of spatially and temporally coordinated molecular processes. Defects in cellular dynamics are a major cause of disease and the physical properties of membranes and the mechanisms that underlie re-organisation of sub-cellular structures are of fundamental scientific interest.

The University of Exeter is embarking on a major interdisciplinary initiative to investigate cellular dynamics and to develop a quantitative understanding of cell behaviour and the underlying biochemical and biophysical properties of cells. We aim to address this challenge by recruitment of world-leading researchers in the areas of Molecular Cell Biology, Biophysics, Bioengineering and Medical Sciences. Together with existing staff, these individuals will pursue an integrated, interdisciplinary research programme investigating cellular dynamics using model systems or primary cell lines. They will develop new techniques for bio-imaging, address cellular processes in a quantitative manner and investigate the molecular basis of disease.

The available positions include:

- Biosciences, College of Life and Environmental Sciences

  Professor in Functional Cell Biology Ref R10320

  Senior Lecturer in Functional Cell Biology Ref R10321

  Lecturer in Functional Cell Biology Ref R10322

- College of Engineering, Mathematics and Physical Sciences

  Professor in Cell Mechanics Ref R10323

  Professor in Physical Cell Biology Ref R10324

  Lecturer in Medical Systems Biology Ref R10325

- A complementary position is also available to develop physical methods of disease detection and clinical monitoring:

  Professor in Biosensing Ref R10326

PENINSULA
COLLEGE OF MEDICINE & DENTISTRY
UNIVERSITIES OF EXETER & PLYMOUTH

- Peninsula College of Medicine and Dentistry

  Professor in Functional Cell Biology Ref R10327

  Associate Professor/Senior Lecturer in Functional Cell Biology Ref R10328

Prospective candidates should be innovative researchers with a strong track record of research funding and international quality publications in cell biology. Additionally, they should show a clear commitment to interdisciplinary research and the desire to contribute to a significant large-scale research programme spanning three of the Colleges of the University of Exeter.

The University of Exeter and the Peninsula College of Medicine and Dentistry are equal opportunity employers and promote diversity in their workforce and, whilst all applicants will be judged on merit alone, are particularly keen to consider applications from groups currently underrepresented in the workforce.

UNIVERSITY OF EXETER

For more information about these exciting opportunities visit **www.exeter.ac.uk/jobs**

Positions @ NIH

THE NATIONAL INSTITUTES OF HEALTH

Tenure-Eligible/Tenure-Track Position in Viral Disease Ecology Laboratory of Virology

The National Institute of Allergy and Infectious Diseases (NIAID), Division of Intramural Research (DIR), Laboratory of Virology (LV) at Rocky Mountain Laboratories (RML) in Hamilton, MT, seeks applicants for a tenure-eligible/tenure-track position (assistant/associate professor equivalent) to conduct independent research on viral agents requiring high or maximum containment.

LV conducts high-impact, innovative scientific research on viral agents requiring high or maximum containment, including arenaviruses, bunyaviruses, filoviruses, flaviviruses, paramyxoviruses, and orthomyxoviruses, with the goal of developing diagnostics, vaccines, and therapeutics. The research conducted in LV includes studies of vector/reservoir transmission and the pathogenesis, pathophysiology, and host immune response of high containment viral pathogens. Candidates must be able to develop an independent research program in infectious disease ecology, supervise staff and fellows, and collaborate with RML/DIR researchers working on other infectious diseases. An interest in and commitment to research in the field and a high-containment biosafety level 3 and 4 (BSL-3 and BSL-4) environment is essential. Other requirements are listed below.

The selected candidate is expected to implement and direct a vigorous, independent research program in viral disease ecology, including field and laboratory studies targeted toward understanding virus persistence in natural reservoirs, transmission from natural reservoirs and/or intermediate hosts to end hosts, and reservoir ecology. This program is expected to include studies in animals, and preference will be given to candidates with experience in infectious disease animal models.

Facilities at existing NIAID field sites in Africa and Asia are available to the incumbent. In addition, LV currently operates established field sites in Mali and the Republic of the Congo. An interest and ability to develop programs at established field sites is highly desirable.

Candidates must hold a Ph.D., D.V.M., M.D., or equivalent degree and have relevant post-doctoral experience. Independent resources including space, support personnel, and an annual budget for services, supplies, and salaries are committed to the position. These are appointments under Title 42. Salary is dependent on experience and qualifications.

RML's state-of-the-art facilities include an operational BSL-3 facility; a BSL-4 laboratory and animal facility that can accommodate work with both small animal and nonhuman primate models; and outstanding support facilities for genomics, electron microscopy, flow cytometry, and other advanced techniques dedicated to scientific collaboration.

Other RML research programs focus on prions, retroviruses, pathogenic prokaryotic organisms, and pathogen transmission by arthropod vectors. RML is located in the scenic Bitterroot Valley of western Montana within easy access to some of the finest outdoor recreational opportunities in North America.

To apply, e-mail curriculum vitae, bibliography, and a two- to three-page description of your proposed research program to Ms. Bao-Hanh Ngo at **lvsearch@mail.nih.gov**. In addition, three letters of recommendation must be sent directly from the referees to Dr. Tom Schwan, Chair, NIAID Search Committee, c/o Ms. Bao-Hanh Ngo at **lvsearch@mail.nih.gov** or 10 Center Drive, MSC 1356, Building 10, Room 4A30, Bethesda, MD 20892-1356. E-mail is preferred.

The selected candidate may be asked for additional references.

Key Requirements:

- Applicants must be U.S. citizens, resident aliens, or nonresident aliens with or eligible to obtain a valid employment-authorizing visa.
- Applicants must be able to fulfill, acquire, and maintain a favorable Access National Agency Check and Inquiries (ANACI) background investigation, select agent clearance, and other NIH biosecurity requirements.

Applications will be reviewed starting **May 31, 2011**, and will be accepted until the position is filled. Additional information on this position can be obtained by contacting Dr. Heinz Feldmann at **feldmannh@niaid.nih.gov**.

Further information about LV is available at **www.niaid.nih.gov/labs/aboutlabs/lv**, information about DIR laboratories is available at **www.niaid.nih.gov/about/organization/dir**, and information about working at NIAID is available at **www.niaid.nih.gov/careers/ve**.

NIAID

National Institute of Allergy and Infectious Diseases

US DEPARTMENT OF HEALTH AND HUMAN SERVICES
National Institutes of Health

National Institute of Allergy and Infectious Diseases
Proud to be Equal Opportunity Employers

THE NIH IS DEDICATED TO BUILDING A DIVERSE COMMUNITY IN ITS TRAINING AND EMPLOYMENT PROGRAMS

WWW.NIH.GOV

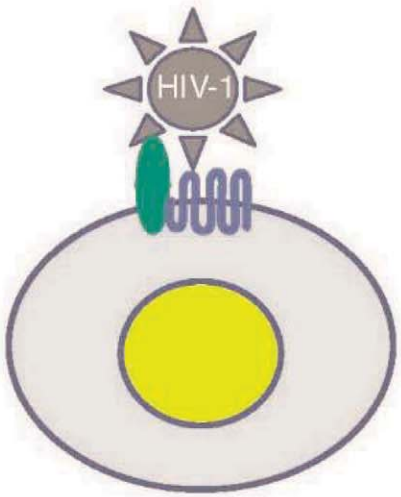

Postdoctoral Fellow
HIV Viral and Host Cell Interaction

A postdoctoral position is available at the National Institute of Allergy and Infectious Diseases (NIAID) to study the molecular mechanisms of HIV viral and host cell receptor interactions and their contribution to viral infection.

The available position is in the Laboratory of Immunogenetics, located at the Twinbrook campus of NIH in Rockville, MD.

Candidates with relevant research background are preferred. Starting salary is between $44,000 and $50,000, depending on experience. Interested candidates should send a detailed curriculum vitae and names of three references (including e-mail addresses and telephone numbers) to psun@nih.gov.

For more information, contact Peter D. Sun, Ph.D., Chief, Structural Immunology Section, Laboratory of Immunogenetics, NIAID, NIH, at 301-496-3230 (phone), 301-402-0284 (fax), or psun@nih.gov.

Visit us on the web at www.niaid.nih.gov/careers/td2
Follow us on Twitter: Twitter.com/NIAIDCareers
Become a fan on Facebook: Facebook.com/niaid.nih

National Institute of Allergy and Infectious Diseases

NIAID

US DEPARTMENT OF HEALTH AND HUMAN SERVICES
National Institutes of Health

National Institute of Allergy and Infectious Diseases
Proud to be Equal Opportunity Employers

NCCAM
NATIONAL CENTER FOR COMPLEMENTARY AND ALTERNATIVE MEDICINE

NATIONAL INSTITUTES OF HEALTH
National Center for Complementary and Alternative Medicine
Scientific Director - Neuroscientist

The National Center for Complementary and Alternative Medicine (NCCAM), a component of the National Institutes of Health (NIH), Department of Health and Human Services, seeks an accomplished, innovative neuroscientist to serve as Scientific Director of its Division of Intramural Research (DIR). The Scientific Director will build and lead a vibrant research program focused on the mechanisms and management of pain. This Scientific Director reports to the Director, NCCAM, and will also serve as a member of the NCCAM senior leadership team.

The Scientific Director will develop an overall vision for, and implement a research program focused on increasing understanding of the mechanisms of pain and its central modulation, with the long term goal of strengthening clinical management of chronic pain through the integration of pharmacological and non-pharmacological approaches. Topics of special interest include pathways and mechanisms by which emotion, attention, and other processes modulate pain or pain processing, and mechanisms of the placebo effect. The research program will be highly collaborative with, and leverage the basic and clinical research talent and resources of other ongoing neuroscience and imaging programs of the larger NIH intramural research community.

This exceptional opportunity is available to an accomplished neuroscientist who has a demonstrated track record of internationally recognized research on pain, a commitment to both basic and clinical research, and the leadership and management skills to build and sustain vibrant, collaborative team efforts with colleagues within intramural programs across the NIH. Applicants must possess an M.D., Ph.D., or equivalent degree in the biomedical sciences, and have professional experience reflecting a broad scientific background and experience in basic and/or clinical neuroscience research. Applicants should be known and respected within their profession, both nationally and internationally, as distinguished individuals of outstanding scientific accomplishment. Salary is commensurate with experience and a full package of Civil Service benefits is available including retirement, health and life insurance, long term care insurance, leave and savings plan (401 K equivalent).

Application Process: Interested candidates should send a letter of interest, including a brief description of research and administrative experience, CV, bibliography, and a list of up to five individuals who can serve as references to: Ms. Belinda Davis at nccamsrrecruits@mail.nih.gov. Email receipt of applications and inquiries is preferred; however, candidates needing reasonable accommodation may fax application materials to 301-402-4741.

Applications will be reviewed starting June 27, 2011, and will be accepted until the position is filled. All information provided by applicants will remain confidential and will not be released outside the NCCAM search process without a signed release from the applicant.

The NIH encourages the application and nomination of qualified women, minorities, and individuals with disabilities.
NIH AND DHHS ARE EQUAL OPPORTUNITY EMPLOYERS

Tenure-track Associate Professor
Bio-AFM Frontier Research Center
Kanazawa University, Japan

The Bio-AFM Frontier Research Center at Kanazawa University is seeking to hire a full-time tenure-track associate professor to conduct research in the Imaging Research Division and teach graduate and undergraduate courses.

The Research Center was recently founded in Kanazawa University to promote biological research with the use of advanced atomic force microscopy (AFM) techniques and technological development of bio-AFM. The Center comprises four Divisions. The Imaging Research Division focuses on the elucidation of structure and dynamics of biological molecules using high-speed AFM and super-resolution in-liquid AFM, collaborating with the other Divisions.

Candidates should have an earned doctorate and outstanding research records in at least one of the following areas; Biology, Biochemistry, Molecular Biology, and Biophysics. Experience of AFM studies is not necessarily required of candidates.

The tenure-track associate professor can be promoted to a full tenure professor position through reviewing. Detailed information on the position and the Center is available at the web site (**http://www.se.kanazawa-u.ac.jp/bioafm_center/open_position.htm**).

Applications (in free format) including a curriculum vitae, a list of publications, electronic copies of the 5 most important papers, a list of research grants acquired, details of research experience, a statement on research interests, a brief three-year plan of research to conduct at the Center, and a list of two references should be sent to the following e-mail address;

Prof. Toshio Ando, Director of the Bio-AFM Frontier Research Center
E-mail: **tando@staff.kanazawa-u.ac.jp**

Deadline for application is June 30, 2011. An appointee is expected on duty on October 1, 2011 or earlier.

Kanazawa University is an equal opportunity employer, and encourages international and female applications.

Invest your career where you can
Make a Difference!

Associate/Full Professor

Duke University School of Medicine

The Duke Cancer Institute invites applications from basic scientists working in the broad area of Cancer and the Environment for a tenured appointment as an Associate or Full Professor in the Duke University School of Medicine. This position will bridge ongoing multidisciplinary efforts with the School of Medicine and, particularly, forge strong ties to the Nicholas School of the Environment. The successful candidate must have a Ph.D. and/or M.D. degree and a demonstrated dynamic cutting-edge research program.

Applicants should submit a current curriculum vitae, a brief statement of past research accomplishments and future research interests, and a list of three references as a single PDF (please, also arrange to have letters of recommendation forwarded), to Duke Cancer and the Environment search committee 2011 at: **DCEsearch@duke.edu**

Review of applications and letters will begin June 15, 2011 and continue until the position is filled.

DUKE CANCER INSTITUTE
A National Cancer Institute-designated Comprehensive Cancer Center

Duke University is an equal opportunity/affirmative action employer.

Faculty Positions
Assistant and Associate Professors
Center for Cell Biology and Cancer Research
Albany Medical College

The Center for Cell Biology and Cancer Research at the Albany Medical College announces the availability of tenure-track faculty positions at the Assistant and Associate Professor levels. The successful candidates' research will interface with scientific programs within the Center which has a strong focus on tissue remodeling, tumor microenvironment, inflammation and fibrosis, tumor growth/metastasis and gene regulation. Candidates will have the opportunity to be affiliated with the Cancer Genomics Center at the State University of New York's East Campus. The Albany area is also home to Taconic Farms, Rensselaer Polytechnic Institute, the College of Nanoscale Science & Engineering at the University of Albany (SUNY) and General Electric Health Care Research, all of which contribute significantly to the collaborative environment in the Capital District. Studies by Center faculty concentrate on molecular mechanisms regulating cell adhesion and motility, angiogenesis, growth factor- and matrix-dependent signal transduction, transcriptional control of cell fate, tumor-stroma interactions and targeted therapy of cancer. The applicant will be expected to develop an extramurally-funded research program emphasizing molecular and/or genetic approaches to problems relating to these focus areas. Candidates using animal models that mimic stages in human cancer progression are particularly encouraged to apply.

Qualifications include a Ph.D. degree and a demonstrated track record of excellence in research. Associate Professor candidates are expected to have an externally-funded research program. All faculty in the Center participate in the teaching missions of the College Graduate and Medical School curricula. Full consideration will be given to those applications received by July 1, 2011. Curriculum vitae, description of research interests, and at least three letters of recommendation are required; providing copies of published papers is strongly encouraged. All materials should be submitted to: **Paul J. Higgins, Ph.D., Center for Cell Biology and Cancer Research (MC-165), Albany Medical College, 47 New Scotland Avenue, Albany, New York 12208.**

The Albany Medical College is an Equal Opportunity, Affirmative Action Employer.

MEDICAL SCHOOL FACULTY
Microbiology with Biochemistry
St. Kitts Medical Campus

The University of Medicine and Health Sciences is a premier, for-profit boutique off shore medical school located on the exotic Caribbean Island of St. Kitts. Our ocean front state of the art campus is comparable to the best medical schools in the United States. We maintain small classes and provide a personalized education catering to the individual needs of the students. To date we have invested over 50 million dollars into our campus facilities and infrastructure.

We are seeking a full time medical microbiologist preferably with a minimum of 4 years experience teaching in a U.S. or Canadian medical school. Candidates must have a minimum of an earned PhD in microbiology. Candidates additionally holding an M.D. degree will be given preference. Candidate should also be able to teach portions of biochemistry as well. Salaries and benefits are competitive and commensurate with experience. A significant portion of the salary is offered tax free.

Candidates should forward their CV's and cover letter to: **hr@umhs-sk.net**
For further details about

The University of Medicine and Health Sciences
For further details about our university please visit **www.umhs-sk.org**

EDUCATING THE NEXT GENERATION OF PHYSICIANS

UMHS

ETH

Eidgenössische Technische Hochschule Zürich
Swiss Federal Institute of Technology Zurich

Professor of Energy Homeostasis / Movement Biomechanics / Neural Control of Movement

The preservation of health and quality of life is a challenge for society and especially for the health care system, given the demographic development, a progressively aging population and an increasing proportion of obese individuals. Preventing age- and weight-related diseases, developing effective therapies and technological help, and training of competent students requires a systematic and multidisciplinary approach. ETH Zurich therefore decided to form a new department of «Health Sciences and Technology» (D-HEST; www.hest.ethz.ch), which brings together scientists and engineers in food, nutrition, exercise, neuroscience, and medical technology. D-HEST, which will be established 1 January 2012, invites applications for three new professorships in:

- **Energy Homeostasis**
- **Movement Biomechanics**
- **Neural Control of Movement**

Candidates should demonstrate an exceptional potential to develop an innovative and collaborative research program at the interfaces of movement sciences and sport, molecular health sciences, neurosciences, nutritional biology, biomechanics, rehabilitation technology, physiology, and medicine.

Professor of Energy Homeostasis
The successful candidate is expected to establish an interdisciplinary research group focused on energy homeostasis at large. Possible research topics may include integrative aspects such as understanding how the status of an organism with respect to physical activity, nutrition, and age impacts cellular and molecular processes of energy homeostasis. Beside a formal education in physiology, biology or a closely related discipline, the candidate should have a proven track record in solving problems on the organ/tissue/cellular/molecular level.

Professor of Movement Biomechanics
The successful candidate is expected to establish an interdisciplinary research program focused on movement biomechanics in the aging musculoskeletal system. Possible research areas focus on: multi-scale simulation techniques from organ to cells; imaging of tissue deformations; mechanobiological adaptation; virtual physiology of the healthy and pathological musculoskeletal system; or computational modeling and evaluation through movement measurements. Beside a formal education in mechanical engineering or closely related disciplines, the candidate should have a proven track record in the development of computational models for biomechanical problems on the organ/tissue/cellular/molecular level, incorporating experimental aspects of movement analysis.

Professor of Neural Control of Movement
The successful candidate is expected to establish an interdisciplinary research group focused on neural control of movement in the normal or disabled population from young up to old age. Possible research areas focus on: neuronal macro- and microcircuit structure and function, the role of nerve fiber growth in the adult brain under conditions of learning and repair, the analysis of the interaction of large populations of neurons in the sensory/motor networks on the various levels of the nervous system, mechanisms that cause central and peripheral fatigue, neuroimaging and human-machine interaction for the investigation of motor control and neuroplasticity or biofeedback for movement learning and neurorehabilitation. The candidate should have a proven track record in successful research on human and animal experimentation from the system to the cellular level, using most advanced technology.

Additional prerequisites for all three positions are a strong motivation and an undisputable commitment to undergraduate and graduate student education. The professorships will be embedded in the Department's undergraduate and graduate program in Health Sciences and Technology. The professors will be expected to teach both undergraduate (in German or English) and graduate level courses (in English).

Each professorship comes with several salary lines for academic and technical assistants, start-up funds and annual allocations to establish a world-class research program. Access to excellent animal facilities and several technology platforms of ETH and the University of Zurich (Functional Genomics Centre, Imaging, Mass spectrometry, etc.) is ensured.

Please apply online at **www.facultyaffairs.ethz.ch.** Your application should include your curriculum vitae and a list of refereed publications. The letter of application should be addressed **to the President of ETH Zurich, Prof. Dr. Ralph Eichler. The closing date for applications is June 30, 2011**. With a view towards increasing the number of women in leading academic positions, ETH Zurich specifically encourages women to apply.

universität wien

The Faculty of Life Sciences of the University of Vienna announces the position of three Full Professors. The appointments are full-time, permanent positions under private law.

The professorships are announced for the following fields:

Vegetation Science (20/1-2011)

Systematic and Evolutionary Botany (20/2-2011)

Anthropology (20/3-2011)

The official and legally relevant text of the job announcements can be found at the web page http://www.univie.ac.at/persadmin/lifesciences.

Applications, written in English and in electronic form (preferably as a pdf file), should be sent to the Dean of the Faculty of Life Sciences of the University of Vienna (O. Univ.-Prof. Dr. Horst Seidler; e-mail: dorothea.prenner@univie.ac.at), not later than **June 10th, 2011**.

The University of Vienna intends to increase the number of women on its faculty, particularly in high-level positions, and therefore specifically invites applications by women. Among equally qualified applicants women will receive preferential consideration.

The University of Vienna, one of Europe's oldest universities, offers approximately 8,900 employees manifold opportunities in research, teaching and administration.

Lamont-Doherty Earth Observatory

COLUMBIA UNIVERSITY | EARTH INSTITUTE

Search for the Director of Lamont-Doherty

The Lamont-Doherty Earth Observatory (LDEO) of Columbia University, one of the world's premier earth science research institutes, seeks outstanding candidates for the position of Director.

LDEO is recognized internationally for its breadth of research, range of inquiry and exploration, and imaginative science. The next Director will have the opportunity to continue to expand the breadth and scale of intellectual inquiry that is emblematic of the Observatory, enhance instructional and research faculty, and develop a robust program to build endowment, support research, and improve the physical plant. The Director is part of the senior leadership of the University, with responsibilities for the operation of Columbia's Lamont Campus, and reports to the Director of Columbia's Earth Institute.From this position, the Director will provide scientific leadership in the earth sciences internationally and within the University.

LDEO seeks acclaimed earth scientists with an exemplary record of scholarship and the leadership ability to secure LDEO's many accomplishments and direct the institution to new levels of success. The Director should uphold the values of collaboration, transparency, and the rigorous and entrepreneurial pursuit of scientific excellence.

Please send applications along with a letter of interest and qualifications and current curriculum vitae electronically to the address below; nominations should be sent to the same address.

Nicholas Brill
Brill Neumann Associates
Boston, MA 02116
Email: ldeo@brillneumann.com

Please visit the LDEO website www.ldeo.columbia.edu/ for additional information about LDEO and the University. In employment as in education, Columbia University is committed to equal opportunity and affirmative action.

brillneumann Executive Search Consulting

Aker/Zvonkovic Photography

Our World-Class Research Institute Is Looking for Scientific Leaders

Since its inception, The Methodist Hospital Research Institute has challenged the notion of "by-the-book" medical research. Led by Mauro Ferrari, Ph.D., President and CEO, the Research Institute is a 440,000-square-foot research enterprise for The Methodist Hospital System in Houston, TX, and is affiliated with the Weill Cornell Medical College in New York City. Methodist is transforming medicine with emerging techniques, and a staff that is developing real treatments and cures every day. Our laboratories are equipped with advanced technology and facilities that include a cyclotron, pre-clinical and clinical imaging, flow cytometry and microscopy, small and large animal vivariums; and a GMP facility for nanoparticles, contrast agents, vaccines, and therapeutic molecules. Our facility is a vertically integrated state-of-the-art laboratory for translational and clinical research where translational researchers and physician scientists bring ideas to clinical applications.

We are now searching for research professionals to serve in a variety of capacities.

Program leaders in the fields of:

- *Neurodegenerative Diseases and Repair of the Nervous System (Methodist Neurological Institute)*
- *Cardiovascular Science (Methodist DeBakey Heart & Vascular Center)*
- *Cancer Biology (Methodist Cancer Center)*

Senior scientists in the fields of:

- *Diabetes and Metabolic Disorders (Methodist Center for Diabetes, Obesity and Lipids)*
- *Transplant Immunology (Methodist Transplant Center)*

Candidates should be nationally and internationally recognized leaders with an outstanding track record of scientific discovery, funded research, programmatic leadership and academic mentorship. We will provide you with a position in the epicenter of medical research. You'll discover an excellent research environment, state-of-the-art equipment, and the chance to follow your research from discovery to clinical application in a single facility.

Applicants should submit a Statement of Scientific Interest, a Curriculum Vitae, and the names of three references to: Tong Sun, Director of Central Research Administration, The Methodist Hospital Research Institute, 6670 Bertner St., M.S. R2-216, Houston, TX 77030, or email facultyapplications@tmhs.org (please specify applying field in the subject line of email). Our success as an organization is due to the diversity of our team. We are an equal opportunity employer.

www.tmhri.org www.MethodistHealth.com

Methodist The Methodist Hospital Research Institute

Houston, TX

LEADING MEDICINE

The Methodist Hospital System is the official health care provider of the Houston Texans, Houston Astros, Houston Dynamo, Rice Athletics, Houston Ballet, Houston Grand Opera and Houston Symphony.

GOVERNMENT OF INDIA
MINISTRY OF SCIENCE & TECHNOLOGY
DEPARTMENT OF BIOTECHNOLOGY

NOMINATIONS/APPLICATIONS ARE INVITED FOR THE POST OF
DIRECTOR, NATIONAL INSTITUTE OF IMMUNOLOGY (NII),
NEW DELHI, INDIA

National Institute of Immunology, an autonomous institute under the Department of Biotechnology, Government of India, with a mandate of carrying out high quality basic and applied research, is looking for an eminent scientist from India or abroad and Non-Resident Indians (NRIs) having proven scientific record in the areas such as immunology/cell biology/molecular biology/disease biology, excellent leadership ability.

The applicants/nominees should be below 55 years of age but for exceptional candidates, age can be extended. The appointment will be on contract basis for a period of 5 years which will be extended for a further term, as per rules of the institute. The post carries basic pay of ₹80,000/- p.m. (fixed) and usual allowances as per Govt. of India rules.

The applications/nominations alongwith detailed curriculum vitae indicating the date of birth, address for correspondence including telephone, fax and email address, qualifications acquired, professional and research experience, present position and scale of pay with total emoluments, publication details and a 500 word write-up on the candidate's vision on NII for the next ten years may be sent to **Shri K.M. Kutty, Deputy Secretary, Department of Biotechnology, Block-2, CGO Complex, Lodi Road, New Delhi-110003 (Email: km.kutty@nic.in)** superscribing the cover "Application for the post of Director, NII" so as to reach him by **15th June, 2011**.

The Department reserves the right to relax any of the requirements prescribed above.

AWARDS

POSITIONS OPEN

FACULTY POSITIONS
Virology and Bacterial Pathogenesis (Bacterial/Host Interactions)

The Microbiology department at UT Southwestern Medical Center at Dallas is seeking new faculty, at the **ASSISTANT PROFESSOR** (tenure track) level, in virology and bacterial pathogenesis (including bacterial/host interactions). This will be a rolling search until positions are filled. Appointees will be expected to develop front-rank, competitive, independent research programs on medically relevant pathogens. For virology, some preference will be given to candidates working on RNA viruses and/or viral pathogenesis. The appointees will contribute to the teaching of medical and graduate students. Attractive startup packages, including a competitive salary and generous laboratory space in a new building, are available to conduct research in an expanding, dynamic environment. Candidates also will be considered for UT Southwestern's $1.2M Endowed Scholars (startup) Program. Candidates should have a Ph.D. and/or M.D. degree with at least three to four years of postdoctoral experience and an exceptional publication record. Candidates should send a cover letter, curriculum vitae, contact information for three letters of recommendation, and a brief summary of future research to either **e-mail: virologysearchcommittee@utsouthwestern.edu** or **bacterialpathogenesissearchcommittee@utsouthwestern.edu.** *U.T. Southwestern is an Equal Opportunity/Affirmative Action Employer.*

ASSISTANT or ASSOCIATE PROFESSOR of Ecosystem Health

The College of Veterinary Medicine & Biomedical Sciences, Department of Veterinary Pathobiology at Texas A&M University, invites applications for an Assistant or Associate Professor in the field of Ecosystem Health. This is a 12-month, tenure-track, fully funded position with primary responsibility for development of an externally funded program focused on the health, biology, conservation, and aviculture of exotic birds. Preference given to candidates with research experience in the conservation of Neotropical psittacines. Candidate will participate in teaching and ornithological research with the Schubot Exotic Bird Health Center. Requirements: D.V.M. or Ph.D. in biology, wildlife sciences, ecosystem health, or related fields. Review of applications will begin immediately and continue until the position is filled. Send electronic applications to the attention of: **Ms. Cindy Voelker** (**e-mail: cvoelker@cvm.tamu.edu**) or **Veterinary Pathobiology, 4467 TAMU, College Station, Texas 77843-4467.** Include a letter of application, current and planned research initiatives/direction and proposed funding sources, outline of teaching interests/experience, curriculum vitae, and three references, including names, addresses, e-mail, telephone, and fax number. Further detailed information **website: http://vetmed.tamu.edu/vtpb/employment-opportunities.** *Texas A&M University is an Equal Opportunity/Affirmative Action Employer/Educator.*

POSTDOCTORAL POSITIONS supported by the NIH are available in the Section of Nephrology at the University of Chicago. A diversity of research mentors are available investigating immune and pathological mechanisms of experimental renal diseases and transport physiology. Applicant MUST have a Ph.D. and/or M.D. degree and be a U.S. citizen or permanent resident. Expertise in cellular and molecular biology, signal transduction, and/or immunology is essential. The start date can be as early as July 1, 2011. Submit curriculum vitae including three references to **Dr. Richard Quigg** at **e-mail: rquigg@uchicago.edu.** *Affirmative Action/Equal Opportunity Employer.*

SCIENTIST, NMR Spectroscopy (Full-time) nuclear magnetic resonance (NMR) to work on polysaccharides and glycoproteins to include multidimensional NMR techniques. Need Ph.D. or foreign equivalent (Chemistry/Biochemistry) plus NMR knowledge for polysaccharide analysis (including glycosaminoglycans) and knowledge of multidimensional NMR techniques. Resumes to: **Laurie Travers, Momenta Pharmaceuticals, 675 W. Kendall Street, Cambridge, MA 02142.**

Jumpstart your biomarker research

with a Biomarker Discovery Pilot Grant

Discover more. Publish faster.

RayBiotech offers the widest selection of protein profiling tools in today's market. Our product line-up includes protein arrays for detecting over 500 proteins, including cytokines, growth factors, receptors, and other molecules related to

- Alzheimer's disease
- Obesity & diabetes
- Cardiovascular disease
- Cancer
- Angiogenesis
- Inflammation
- Apoptosis
- and many more

More data with less sample.

- High content screening
- Adaptable to high throughput
- Compatible with most sample types
- Multiple formats available
- Proven technology, hundreds of publications

APPLY TODAY to win up to $20,000 worth of Raybiotech products and services.

Complete your application **for Raybiotech's Biomarker** Discovery Grant Program **TODAY and get a 10% discount on** all Raybiotech products and services (good through the end of 2011). DEADLINE FOR APPLICATIONS IS AUGUST 1, 2011.

For more details, visit our website:
www.Raybiotech.com/Grant_sci
or email grant@raybiotech.com.

RayBiotech, Inc.
the protein array pioneer company

+1 888 494 8555 +1 770 729 2992 http://www.RayBiotech.com/Grant_sci grant@raybiotech.com